Seasonal flow variability of Greenlandic glaciers : satellite observations and numerical modeling to study driving processes

Anna Derkacheva

THÈSE

Pour obtenir le grade de

DOCTEUR DE L'UNIVERSITÉ GRENOBLE ALPES

Spécialité : **Sciences de la Terre et de l'Univers et de l'Environnement**

Arrêté ministériel : 25 mai 2016

Présentée par

Anna DERKACHEVA

Thèse dirigée par **Jérémie MOUGINOT** et
co-encadrée par **Fabien GILLET-CHAULET**

préparée au sein de l'**Institut des Géosciences de l'Environnement**
dans **l'École Doctorale Sciences de la Terre de l'Environnement et des Planètes**

Variabilité saisonnière de l'écoulement des glaciers groenlandais : observations par satellite et modélisation numérique pour étudier les processus moteurs

Seasonal flow variability of Greenlandic glaciers: satellite observations and numerical modeling to study driving processes

Thèse soutenue publiquement le **23 septembre 2021**,
devant le jury composé de :

Monsieur, Jérémie, MOUGINOT
CHARGÉ DE RECHERCHE, CNRS, Directeur de thèse
Madame, Hélène, SEROUSSI
DOCTEUR EN SCIENCES, Dartmouth College, Rapporteure
Monsieur, Andreas, KÄÄB
PROFESSEUR, University of Oslo, Rapporteur
Monsieur, Olivier, GAGLIARDINI
PROFESSEUR, Université Grenoble Alpes, Président du jury

en présence de
Monsieur, Fabien, GILLET-CHAULET
CHARGÉ DE RECHERCHE, CNRS, Co-encadrant
Monsieur, Poul, CHRISTOFFERSEN
PROFESSEUR, University of Cambridge, Invité

Abstract

The recent changes of outlet glaciers flow speed have vast control on the undergoing mass loss of the Greenland ice sheet. The processes driving the flow variability on different time scales, as well as the associated consequences and feedbacks, are not yet entirely understood. This is partly because the lack of frequent, precise, and large-scale observations limits the development of numerical models. It is particularly difficult to resolve seasonal speed fluctuations, yet it is crucial to better constrain the physical processes controlling the ice flow.

This thesis aims to address (i) the difficulties that exist in establishing robust seasonal time-series of Greenland glacier surface velocities from satellite observations, and (ii) the use of these time-series in numerical models for better understanding of the flow drivers.

Satellites are able to cover large areas in a relatively short time and uniform way. Continuous time-series with seasonal temporal resolution have only started to be used recently, due to the limited number of image acquisitions made previously. Nevertheless, the time-series of ice surface velocity derived from individual sensors remain temporally incomplete and relatively noisy. Taking together three suitable satellites (Landsat-8, Sentinel-2, and Sentinel-1) across three case study sites in Greenland (Russell sector, Upernavik Isstrøm and Petermann Gletscher), we demonstrate that it is possible to obtain continuous year-around time-series only by combining results from multiple satellites. It is also shown here that by applying post-processing based on the data redundancy to such multi-sensor datasets, we are able to achieve persistent tracking of ice surface motion with a temporal resolution of about 2 weeks and mean accuracy of about 10 m/yr. With such parameters, we can resolve the seasonal variability of greenlandic glaciers where previous studies had limited success.

Elaboration of reliable numerical models which would correctly represent the ice flow processes requires suitable observations for the calibration and validation. In the land-terminating sector around Russell Gletscher, we explore the ability of an existing numerical modelling method to use advantageously the obtained high-frequency satellite-derived maps of surface velocity to infer seasonal variations in subglacial conditions. It is widely recognized that they exert a major control on the flow variability, however, despite recent theoretical and modelling developments, constraining the processes in situ remains a key question in Glaciology. By applying the inverse control method implemented in Elmer/Ice on biweekly velocity maps, we estimate the year-around evolution of glacier basal sliding speed, basal traction, and subglacial water pressure with an unprecedented spatial and temporal resolution. Our analysis shows that such results can be successfully used to reveal the functioning of the subglacial environment over different timescales and its influence on glacier speed. These results also could serve as an intermediate validation for more complex ice-flow/subglacial-hydrology coupled models.

Résumé

Les changements récents de la vitesse d'écoulement des glaciers ont une grande influence sur la perte de masse actuelle de la calotte glaciaire du Groenland. Les processus à l'origine de la variabilité de l'écoulement à différentes échelles de temps, ainsi que les conséquences et les rétroactions associées, ne sont pas encore entièrement compris. Ceci est partiellement dû au fait que le manque d'observations fréquentes, précises et à grande échelle limite le développement des modèles numériques. Il est particulièrement difficile de résoudre les fluctuations saisonnières de vitesse, mais il est crucial de mieux contraindre des processus physiques contrôlant l'écoulement de la glace.

Cette thèse se concentre donc sur (i) les difficultés qui existent dans l'établissement de séries temporelles saisonnières robustes de la vitesse de surface des glaciers du Groenland à partir d'observations satellitaires, et (ii) l'utilisation de ces séries temporelles dans les modèles numériques pour une meilleure compréhension des facteurs affectant l'écoulement.

Les satellites sont capables de couvrir de vastes zones en un temps relativement court et de manière uniforme. Les séries temporelles continues avec une résolution temporelle saisonnière n'ont commencé à être utilisées que récemment, en raison du nombre limité d'acquisitions d'images réalisées auparavant. De plus, les séries temporelles des vitesses dérivées de capteurs individuels restent temporellement incomplètes et relativement bruitées. En combinant trois satellites appropriés (Landsat-8, Sentinel-2 et Sentinel-1) sur trois sites d'étude au Groenland (les secteurs de Russell, Upernavik Isstrøm et Petermann Gletscher), nous démontrons qu'il est possible d'obtenir des séries temporelles continues sur toute l'année. Nous montrons également ici qu'en appliquant un post-traitement basé sur la redondance des données à ces ensembles de mesures multi-capteurs, nous sommes en mesure d'obtenir un suivi du mouvement de la surface de la glace avec une résolution temporelle d'environ 2 semaines et une précision moyenne d'environ 10 m/an. Avec de tels paramètres, nous pouvons résoudre la variabilité saisonnière des glaciers du Groenland où les études précédentes n'ont eu qu'un succès limité.

L'élaboration de modèles numériques fiables représentant correctement les processus affectant l'écoulement de la glace nécessite des observations appropriées pour leurs calibrations et validations. Dans le secteur autour de Russell Gletscher, nous explorons la capacité d'une méthode de modélisation numérique existante à utiliser avantageusement les séries temporelles obtenues précédemment pour en déduire les variations saisonnières des conditions sous-glaciaires. Il est largement reconnu qu'elles exercent un contrôle majeur sur la variabilité des débits, cependant, malgré des développements théoriques et de modélisation récente, la contrainte du processus in situ reste une question clé en glaciologie. En appliquant la méthode de contrôle inverse mis en œuvre dans le modèle d'écoulement glaciaire Elmer/Ice sur des cartes de vitesse bimensuel, nous estimons l'évolution tout au long de l'année de la vitesse de glissement basale des glaciers, de la traction basale et de la pression d'eau sous-glaciaire avec une résolution spatiale détaillée. Notre analyse montre que ces résultats peuvent être utilisés avec succès pour révéler le fonctionnement de l'environnement sous-glaciaire sur différentes échelles de temps et son influence sur la vitesse des glaciers. Ces résultats pourraient également servir de validation intermédiaire pour des modèles couplés plus complexes entre l'écoulement glaciaire et l'hydrologie sous-glaciaire.

Аннотация

Колебания скорости течения выводных ледников оказывают значительное влияние на современную потерю массы ледяным щитом Гренландии. Процессы, определяющие флуктуации скорости в различных временных масштабах, и связанные с этим последствия, еще не полностью поняты. Отчасти это связано с отсутствием частых, качественных и обширных наблюдений, что ограничивает развитие численного моделирования. Особенно сложно вести наблюдения за сезонными флуктуациями скорости, в то время как они являются критичными для улучшения нашего понимания физических процессов, контролирующих течение ледников.

Это исследование фокусируется на: (i) создании качественных временных рядов наблюдений за поверхностными скоростями гренландских ледников по данным спутниковой съемки, и (ii) использовании таких временных рядов в численном моделировании для углубления понимания процессов, контролирующих движение ледников.

Ранее получение непрерывных спутниковых наблюдений с суб-сезонным временным разрешением было ограничено частотой получения изображений. Современные съемочные системы способны охватывать большие площади за относительно короткое время. Однако наблюдения, полученные с помощью отдельных спутников, остаются эпизодическими во времени и зашумленными. Используя совместно три спутника с подходящими характеристиками (Landsat-8, Sentinel-2 и Sentinel-1) на трех тестовых участках в Гренландии (ледники Рассела, Петерманна и Упернавик Исстром), мы продемонстрировали, что непрерывные в течении года наблюдения с высоким временным разрешением можно получить только путем объединения результатов с нескольких спутников. Мы также показали, что, применяя к таким комплексным наблюдениям алгоритмы постобработки, основанные на избыточности данных, мы можем создавать карты скорости с повторяемостью около 2 недель и точностью около 10 м/год. Ряды наблюдений с такими характеристиками позволили нам выявить наличие сезонной динамики скорости там, где предыдущие исследования констатировали ее отсутствие.

Разработка надежных численных моделей течения льда требует подходящих наблюдений для калибровки и валидации. На примере ледника Рассела мы исследовали способность одного из существующих методов численного моделирования использовать с наибольшей отдачей полученные карты поверхностной скорости для определения сезонной эволюции подледных условий, которые являются одним из ключевых факторов, регулирующим скорость. Применив на двухнедельные измерения скорости метод инверсии, реализованный в модели Elmer/Ice, мы получили воспроизведение годовой эволюции скорости скольжения, базального трения и давления базальной воды с недостижимым ранее временным и пространственным разрешением. Анализ показал, что такие результаты могут быть успешно использованы для концептуализации функционирования подледниковой среды в различных временных масштабах и ее влияния на скорость движения ледника. Эти результаты также могут служить промежуточным звеном для построения более сложных моделей, связывающих динамику движения льда и подледную гидрологию.

Acknowledgements

First of all, I would like to thank my thesis directors, *Jérémie Mouginot* and *Fabien Gillet-Chaulet*, who managed this research as well as all kind of problems during three years. When I have posted for the position, I've known nobody who could warranty me that you are nice to work with, but finally this adventure has been fully successful! According to several studies, from 30 to 50 % of PhD-students finish with a clinical depression; so cool that finally I do not. At this point I also want to thanks the *lab administration* who is very humane-oriented and open for the flexible solving of personal situations.

Thanks to my committee members and especially the reviewers - *Helene Seroussi, Andreas Kaab, Olivier Gagliardini, and Poul Christoffersen* - to accept this time-consuming task. I am glad to have so international and high-level jury.

The story of this thesis would be started with a phrase: "Long-long time ago, far-far from away, I have quarreled with my best friend and have changed my summer internship plans...". That was 2013. So, thanks to my master-study supervisor *Olga Tutubalina* (Lomonosov Moscow State University) and to my supervisor of the first abroad internship *Yvette Vaguet* (Université de Rouen), with whom my international adventures started.

Well, I would also to give a special thanks to the *Swiss government* and particularly *Geneva airport*, who have been keeping the air connection during the most of COVID-restrictions time, when endless closure of borders has been applied by EU and France (and this is still partly a case, more than 1.5 years later).

The last, but absolutely not the least: my huge thanks to *P.S.* who has been waited me back all these three years. That was and that is enormously supportive.

Table of content

Introduction

…The accuracy (or "skill") that can be achieved by predictive models rests as much on the quality of data available for testing as it does on the insightful representation of the physical processes. Weather prediction models exhibit a good deal of skill, not because the atmosphere is simpler or better understood than ice flow, but because those models are run and tested with different starting conditions every day and are modified when proved inadequate…

Why Is It Hard to Predict the Future of Ice Sheets?
David G. Vaughan and Robert Arthern, Science, 2007

Observed sea-level rise (SLR) over the last few decades is the result of the current climate warming. The primary contributors to SLR are the ocean thermal expansion (42%), the mountain glaciers (21%), as well as the Greenland (15%) and Antarctic (8%) ice sheets (Cazenave et al., 2018). In particular, the ice sheets are now contributing faster than it was anticipated even 20 years ago. The changes of the ice sheet mass balance are still the main source of uncertainty in the SLR future projections. While the future rate of mass loss through surface melting controlled by climate conditions is predicted with higher certainty, the processes that control glaciers flow responsible for the ice transfer towards the melting area and discharge fronts, are still insufficiently understood and weakly constrained in numerical models.

To access the net values of an ice sheet contribution to SLR, which is in fact the "displacement" of water from cryosphere to the ocean, changes in the total mass in time or net mass fluxes coming in and out of an ice-sheet system should be investigated. Total mass balance (MB) of an ice sheet is a net sum of the surface mass balance (SMB), the ice discharge into the ocean (D), and the basal mass balance (BMB) that is usually ignored because its first estimations appeared only recently. SMB is the mass flux that is exchanged through the upper free surface and results from the difference between accumulation terms (mostly from snow falls) and ablation terms (melt water runoff, sublimation). It can have a negative value, meaning that more ice melted than was accumulated in a given time. It is driven by precipitations and air temperature and thus directly depends on climate conditions. To estimate and forecast the evolution of SMB over entire ice sheets, the mentioned elements are commonly derived from climate models, meaning that the projections are highly dependent on the chosen climate scenario of greenhouse gases emission (IPCC Working Group 1 et al., 2013). BMB has a similar idea to SMB but refers to the basal glacier surface. The main process happening here is basal melting. D, oppositely to two other terms, is the dynamic output of ice, meaning that it is happening due to the ice flow. As floating ice already contributes to sea level, D usually represents the ice flux of ice that detaches from the ground and goes afloat either to form an ice shelf or to be calved. Being the flux toward the front, D depends on the flow speed and glacier

terminus geometry including ice thickness, and is influenced over time by flow dynamics and glacier interaction with ocean and atmosphere which can intensify calving. This is the component that currently brings the highest uncertainty into MB projections of the ice sheets.

In this study, we will focus on the Greenland ice sheet (GrIS). In the last decade, a number of investigations have done the estimations of its SMB, D or total MB with different technics – altimetry, gravimetry, or input/output fluxes. All of them agree that during the last decades GrIS has been losing mass at an increasing rate (Figure 1), and that since about the 2000s SMB has become persistently negative, while D demonstrates a general increase (Shepherd et al., 2020). For instance, one of the studies (which did not account for BMB) shows that Greenland was losing mass in 1990–2000 at a relatively small rate -41±17 Gt/yr, but this process has accelerated and MB decreased to -286±20 Gt/yr in 2010–2018 (Mouginot et al., 2019). The same study has found that D was the major driver of mass loss during the previous century (66±8% of MB), but in the last two decades SMB dominates (55±5%). Thus, both mass balance components change in absolute values, but SMB does it almost twice as fast. The latter became more negative, first of all, due to a strong rise in surface melting which is provoked now by the air temperature increase and ice surface darkening in the ablation zone (Bevis et al., 2018). The D grow up due to the glacier flow acceleration that brings more ice towards the ocean. In turn, BMB was currently estimated only once, by the input/output fluxes approach, and is presently about -21.4±~4 Gt/yr or almost 8% of the mentioned MB estimation (Karlsson et al., 2021). Together with other MB components, it is currently intensifying the mass loss, which became 10% more negative during the first decade of the 2000s due to the glaciers flow acceleration (Karlsson et al., 2021).

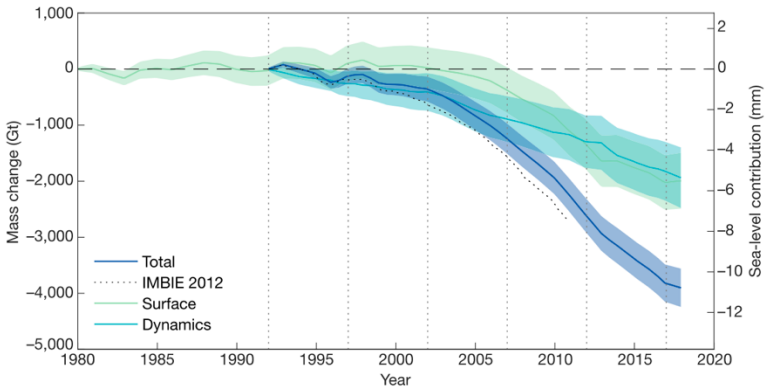

Figure 1 Cumulative anomalies in the total mass, SMB and D of the Greenland Ice Sheet, averaged from multiples modelling studies, with corresponding 1σ uncertainty; dotted line is MB satellite-observation-based estimation; the arbitrary 0 corresponds to the 5-years average MB since the start of the authors' satellite observations in 1992. From (Shepherd et al., 2020).

Changes in glacier flow speed are important for the total mass loss of the GrIS. Speed increase, usually initially provoked by increasing surface melt and/or ice front retreat, is able to trigger negative feedbacks on MB. This is because flow acceleration means that more ice per time is transferred from higher accumulation zone to the lower melting-exposed areas and towards discharge fronts; being not compensated by a raised snow accumulation, this will lead to a deficit MB. For instance, just two sectors, North-West and South-East, contribute now to over 80% of the total Greenlandic D, after a significant recent increase in the rate of calving rate of glaciers in these sectors (Bunce et al., 2018). The latter was caused by the ice motion destabilization,

manifested in significant speed-ups, accompanied by ice front retreats of more than 95% of the marine-terminating glaciers in these sectors (Bjørk et al., 2012; Bunce et al., 2018; Khan et al., 2014a; Moon and Joughin, 2008). Currently, such large-scale and dramatic-rate changes in glacier flow dynamics are hardly predictable, that is why ice sheets are the major source of SLR uncertainties.

The processes driving the flow speed fluctuations on land- and marine-terminating glaciers, as well as the associated consequences and feedbacks, are still not entirely understood, especially when it comes to specific glaciers. The major reason for that is the spatio-temporal multi-scale variability of processes, which complicates the investigations. To estimate the current state of glacier dynamics, better conceptualize the physics of flow acceleration drivers, or make more accurate projections of GrIS future and SLR, extensive observations and realistic models are required. Herewith, elaboration of good models itself requires observations for the calibration and validation. At present, the modelling studies operating on a large scale and high temporal resolution usually involve many assumptions and synthetic data to represent ice flow speed and boundary conditions. On the other hand, the observations-based studies stay local or investigate the multi-annual flow dynamics. Thus, one of the critical points for further advances is the limited space coverage and time duration of suitable observations of the glaciers state and surrounding environment conditions (Vaughan and Arthern, 2007). At the actual state-of-the-art, this is especially true for the flow speed variability occurring at seasonal time-scales.

One of the most required and most easily accessible parameters for observation is ice surface speed. For instance, in contrast with measurements of basal environment conditions or ice material properties, it does not require complex manipulations like borehole drilling. Nevertheless, making speed observations in a continuous, frequent and spatially-extended way across Greenland is challenging due to its size and limited accessibility. The in-situ measurements by GPS are very valuable as they are very precise and have high temporal resolution. However, they remain spatially local and usually are not extended more than few years. This limits our ability to observe and understand dynamic changes over large areas and long periods of time. In contrast, the satellite observations are able to cover large areas in a relatively short time (several days) and uniformly, being also a more cost-effective solution for the end user than deploying a large-cover GPS network. While generally their precision and frequency are lower, they remain suitable for a vast majority of common ice-sheet-investigation tasks, from the simple monitoring of velocity changes (e.g. Tedstone et al., 2015) to complex model-involving estimation of D (e.g. Mouginot et al., 2019) or indirect retrieval of basal environment state (e.g. Karlsson et al., 2021).

The satellite-derived measurements of surface speed for the last 4-5 decades have been widely used to assess the contemporary evolution of the ice sheets. These measurements have been typically made at an annual or multi-annual frequency. Only recently, continuous time-series at seasonal temporal resolution have started to be used to monitor and understand glacier dynamics. Hitherto, such observations have been hard to derive, mainly due to satellites-coming limitations. The lack of observations at high temporal resolution, in turn, has limited the progress in understanding seasonal ice flow dynamics, its leading physical processes and their influence on large-scale glacier stability in the changing environment. In addition, some physical drivers of the seasonal flow variability are the same as the ones playing a role in the long-term. Thus, relatively short-term investigations would certainly help to develop a more robust longer-term projection

of glacier's near future evolution. With the state-of-the-art constellations in orbit such as Landsat or Sentinel, satellite imaging became the forefront of the remote sensing approaches in the sense of spatial coverage, temporal repeatability and the simplicity of data access by the end user, compared to other aero-based solutions. Additionally, technical and methodological advances now provide relatively high precision and accuracy of the derived measurements. Indeed, changes in ice flow can be actually tracked on monthly to weekly timescales, when they are relatively well pronounced. Since the 2010s, we have entered a new era of spaceborne ice sheet observations with the launch of Landsat-8, Sentinel-2, and Sentinel-1. These sensors achieve an unprecedented rate of data acquisition, with a revisit up to 5 days for optical Sentinel-2 and 6 days for radar Sentinel-1. The speed observations now are more frequent, precise, and spatially extended, allowing to overcome the existing limits.

Nevertheless, raw ice velocity data from individual sensors remain sparse and noisy in some specific periods of the year or across challenging regions. Recent studies have shown that it still remains challenging to capture the subtle changes in ice speed over relatively slowly flowing glaciers or events with short duration by using individual measurements from the mentioned sensors and actual processing techniques. Relatively high uncertainties of output velocity products are the main issue for that. Thereby, an increase in the spatio-temporal coverage and accuracy of products, compared to existing products, is still needed to capture in details the seasonal ice flow variability across the GrIS.

In this thesis, we address both challenges of seasonal glacier dynamics investigation:

(i) the retrieval of robust and detailed surface velocity time-series, which would be able to resolve the short-duration variations, from satellite imagery, and

(ii) the analysis of these time-series in terms of the physical processes, to explain the causes of the observed fluctuations.

First, we focus on the generation of surface velocity measurements with high precision and temporal resolution. To overcome the existing quality and frequency issues, we design velocity data creation, storage, and manipulation methodologies based on the joint usage of imagery from the multiple satellite constellations. We then demonstrate the capability of the obtained velocity time-series for the observations of short-duration dynamics events across three selected sites. Thereafter, we explore the opportunities of numerical modelling constrained by such temporally-dense velocity data to study the drivers of seasonal motion variability. For one case study site, we design the modelling framework, which assimilates in the best way the collected velocity dataset and makes the most of its richness. Close attention has been paid to this assimilation issue, since the rarity of similar datasets limits familiarity with the best practices of their use. After that, a detailed interpretation of model's outputs is done to investigate the driving processes of seasonal flow variability and attendant changes in basal environment. Finally, we conclude on the capability of modern satellite remote sensing to advance and refine the understanding of cryosphere dynamics.

1. Glaciers

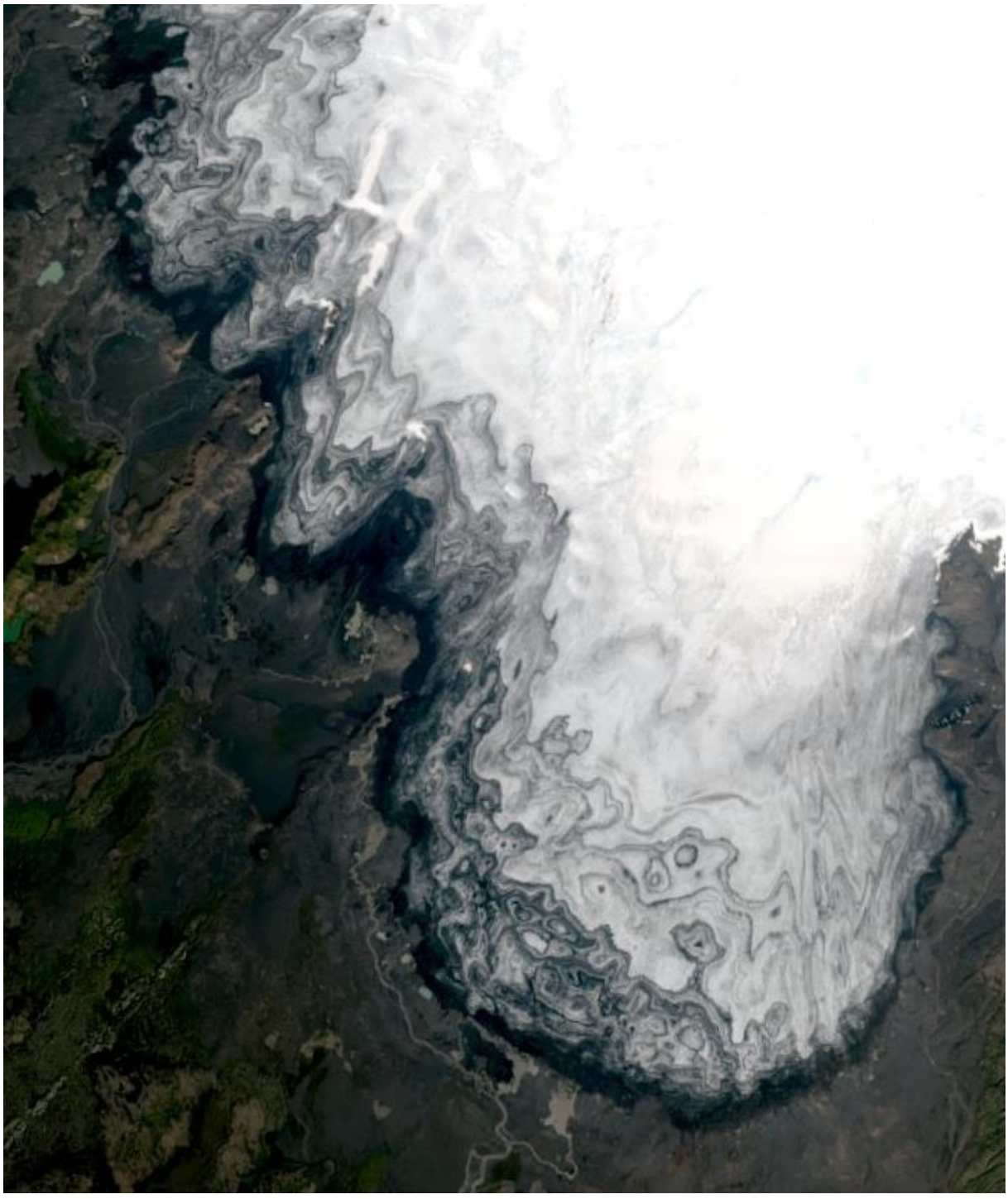

Vatnajokull Ice Cap, Island – Sentinel-2 satellite image, 18 Jul 2021

1.1 Glacier definitions

Glaciers are large masses of ice which form in favorable climate conditions through accumulation and consolidation of snow which became capable of coherent motion under its own weight. They appear when the snow accumulation rate exceeds the melting rate over a long period of time. Currently, this is the part of cryosphere which contains the absolute majority of ice on Earth.

Depending on average size, placement, and relation between geometric dimensions, ice masses are usually divided into (i) mountain glaciers that are relatively small, placed on mountain slopes, and typically have an elongated shape with commensurate length and thickness (Figure 2, left); (ii) ice caps that are larger, have more a dome-like shape which usually entirely covers the solid topography, and can have many tongues forming radial flows (Figure 2, right); and (iii) ice sheets that are huge ice caps with the planar sizes orders of magnitude bigger than the thickness.

Figure 2 A Caucasus mountain glacier (left, by A. Derkacheva) and the Spitsbergen ice cap (right, by S. Mostieva).

Currently there are two ice sheets on Earth: Greenland and Antarctica. In this thesis, we focus on Greenland, although many of the results obtained could be applied to Antarctica as well. The Greenland Ice Sheet (GrIS) with an area of 1 710 000 km² covers almost entirely the island of Greenland. It contains about 7.3 m sea-level-equivalent of water (Morlighem et al., 2017). Generalizing, GrIS has a dome-like shape, meaning that the ice is much thicker in the inland central areas compared to the margins where it thins over short distance. This shapes the universal radial gravity-driven ice flow from the center towards the ice sheet margins, regardless of the predominantly inverse direction of the bed slope. The ice flow is relatively slow (several tens of meters per year) and uniform over inland areas and increases toward the margin in a non-uniform way, forming distinct *outlet glaciers* with a velocity that ranges from tens of meters to several kilometers per year. As for rivers, they have *drainage basins* defining the catchment area where the ice comes from and usually follow the subglacial topographical valleys near the ice-sheet margin.

Two types of outlet glaciers can be distinguished in regards to how they terminate. The *land-terminating* type (Figure 3-a) corresponds to glaciers that terminate on land and not in contact

with water. If a glacier terminates in contact with an ocean, it is called *marine-terminating* (or *tidewater*). As ice is less dense than water, some glaciers start floating at the ending section when ice reaches hydrostatic equilibrium. Thus, two subtypes of marine-terminating glaciers can be defined: *grounded tidewater glaciers* terminating in a vertical ice cliff and *floating tidewater glaciers* ending with a floating *ice shelf* (Figure 3-b). At a land-terminating glacier, the speed decreases to zero at the terminus, while at a marine-terminating glacier speed usually stays fast or even increases towards the calving front.

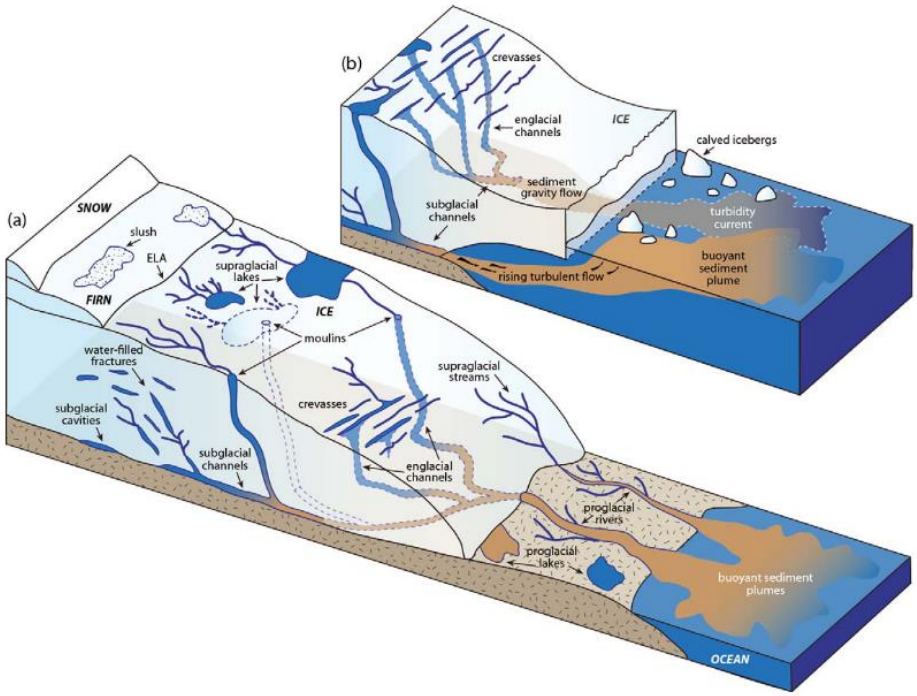

Figure 3 Schematic view of (a) land- and (b) marine-terminating glaciers (Chu, 2014).

Glaciers are often composed of two specific zones depending on the experienced surface mass regimes. The upper one is the *accumulation zone* where the annual accumulation rate of snow is greater than the melting rate, meaning that surface mass is gained. From there, ice mass is transferred by the ice *flow* process toward the *ablation zone,* where the annual surface *ablation* rate, mainly consisting of surface melting, exceeds accumulation. The elevation where the two processes of accumulation and ablation compensate each other defines the limit between these two zones or the *equilibrium line*. The *surface mass balance* (SMB) of a glacier defines the net difference over a time period between total snow accumulation and total surface ice melting. The total *mass balance* (MB) is the difference between accumulation and all "ice-removing" processes, i.e. surface ablation, ice discharge (D) into lakes or the ocean, and, not yet commonly included in this concept, basal melting. The latter is a key process of *basal mass balance* (BMB) which describes ice mass loss and gain processes happening at the bedrock interface, its first estimations only start to appear (e.g. Karlsson et al., 2020). Note that D term is commonly estimated as a flux across the grounding line, thereby floating sections do not account in the mass budget.

By definition a land-terminating glacier does not discharge ice, and so its MB is equal to mass exchanges on the top and bottom surfaces. In contrast, a marine-terminating glacier

discharges ice directly into ocean through *calving* (detachment of ice blocks at the front) and submarine melting. As the discharge rate depends on the ice flow speed, MB of such glaciers is highly influenced by their dynamics. The glacier flow causes the displacement of ice from accumulation to ablation areas and calving front; thereby, the glacier shape, speed and mass balance are closely related and cross-influencing. For a glacier in a steady state, the annual MB is null, and the mean annual speed and geometry are relatively stable.

The glacier geometry is partly shaped by external constraints and partly depends on the mass balance. The upper *surface* of a glacier corresponds to the free, unrestricted upper face of the ice mass which adapts over short and long terms being a result of the balance between local melting, local accumulation, and mass transfer by the ice flow from one area to others. In contrast, the *basal surface* under grounded ice is restricted and on a large scale follows the bedrock topography. Its change depends on the evolution of underlying rocks, mainly due to glacier erosion, which is usually considered as a relatively slow process with typical time scales of tens to hundreds of years. The *front line* (or *terminus*) is the furthest downstream extension limit of a glacier where the whole incoming ice volume melts or where icebergs calving happens. Sometimes, on the line of a faster flow the elongated *tongue* is shaped, clearly outstanding downstream from the main ice field (Figure 2, left). When a glacier ends in an ice shelf, the *grounding line* delimits the location where the ice detaches from the bed. Both the front and grounding lines are highly dynamic borders which can advance and retreat over time. Depending on the mutual displacement of both lines which is semi-independent and can be in opposite directions, the same tidewater glacier can switch between grounded and floating types during its lifetime.

The melt water produced at the surface or base of a glacier is routed outside through a *hydrological system* which develops on, in and below the ice (Figure 3). The majority of melting happens on the top surface, where water can be captured by snow and firn, filling the surface depressions creating lakes, being routed by supraglacial rivers toward the margin or by vertical *crevasses* and *moulins* to the bed. Some water can be generated as well right at the bed thanks to the local heat sources such as geothermal flux or basal friction. Together with surface water, it is routed more or less efficiently in the direction of hydraulic potential which at the scale of the entire glacier follows the surface slope. If the local area of water input or generation has the opportune connection, the water from there will be finally discharged out from the subglacial environment; otherwise it accumulates in cavities under the glacier.

1.2 Glacier motion

Generalizing, the main driver of glacier motion is gravity. The uneven distribution of ice mass generates the gradient of pressure exerted by it. This causes the ice to deform and slide at the bed. In this section, the physics basis behind the ice flow processes are explained first for an idealistic block of ice and then developed for the more realistic glacier configurations. Note that in this section we do not consider the details and equations of the mentioned phenomena; however, some of them can be found in Chapter 3.2.

1.2.1 Ice mechanics and rheology

After a certain threshold, under a pool of *forces* acting in different directions per area unit (*stresses*), a unit of ice starts to deform (*strain*) with changes in the shape. The ice strain mainly occurs as a *permanent deformation*, meaning that it keeps its new configuration after the stress is removed. The opposite *elastic deformation* can be important to explain the glaciers' behavior in the specific situations like ice shelf response to the ocean tides, but usually it can be neglected. If the deformation happens in the failure way, a crack appears in the matter block; otherwise, the ductile deformation causes a *flow* of matter (or *creep*). The second type of reaction is the key process of the glacier's motion; in turn, the former is responsible for crevasses appearance, including calving events.

The ability of a material to deform within time is its *strain rate,* which can be measured as the motion of different parts of material relative to each other. The relation between applied stress and strain rate, especially how the latter varies with respect to changes in the stress or its duration, is defined by *rheological properties* of the material. For ice, it was experimentally established (Duval et al., 1983; Glen, 1952; Lliboutry and Duval, 1985) that this relation is non-linear and that ice can be considered as a highly-viscous incomprehensible (non-Newtonian) fluid. Its *viscosity* (resistance to motion) depends non-linearly on temperature and also demonstrates the *anisotropy* (easier deformation in a preferred direction predefined by crystals orientation).

The force component acting perpendicular to the matter surface (*normal stress*) causes the compressive and tensile actions (Figure 4-b), while the component acting parallel to the matter surface (*shear stress*) leads to the shearing between the matter layers (Figure 4-c). A block of ice exerts a persistent force by its weight on the underlying bed. When considered parallel to the gravity, *ice pressure force* is directly proportional to the ice column thickness. In the same way all overlying ice layers exert pressure force on the underlying layers. Acting on the horizontal bed, pressure is equivalent to the normal stress (Figure 4-d); on the inclined bed (or, equivalent in the turned coordinate system, under a top-surface inclined ice block) it can be decomposed, and each of the components becomes dependent on ice thickness (measured vertically) and ice surface slope. The shear component, acting parallel to the bed in the slope direction, is the gravitational *driving stress* (Figure 4-e). It can be considered as the pressure force gradient in the bed-face plane which defines the rate and direction of the deformation and sliding on the ice-bed interface. Thereby, it is a key forcing of the glaciers motion, i.e. the coherent displacement of the entire ice mass in the same direction. Pressure forces exerted on other faces can also be important for flow occurrence in specific cases, for instance, on the marine-exposed face of the glacier, where the

ice-to-sea difference of ice- and water-generated pressures creates a "pulling action" which causes the ice to flow towards the ocean.

The *resistive forces* act in the direction opposite to the driving stress. They occur due to the drag on the ice block boundaries and by the matter viscosity. These can be *basal drag* or *lateral drag*, depending on the boundary considered, or *longitudinal stress gradient* which occurs from the spatial variations in pushing and pulling forces along the flow. In the majority of glacier configurations, the former is the most important one. The *basal shear stress*, commonly called *basal friction*, results from it as a stress component parallel to the bed and, thus, complementary to the driving stress (Figure 4-e). In the idealistic case of a small, uniformly moving, side-free ice block, where any other resistive stresses are neglected, both will be equal.

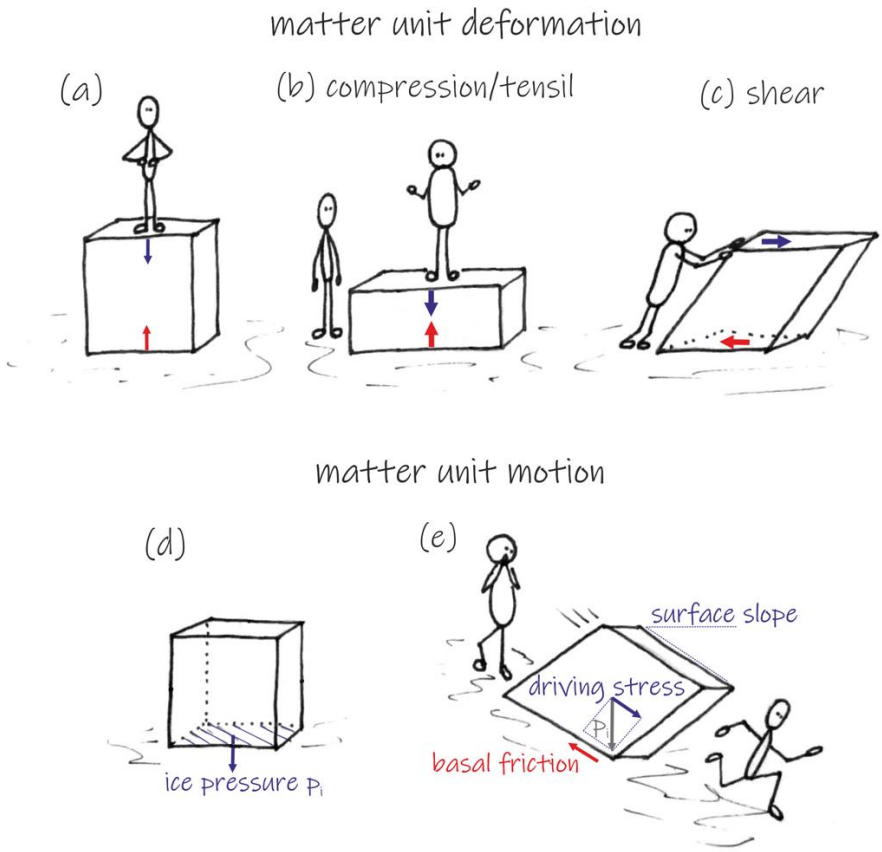

Figure 4 (a)-(c) types of matter deformation under the stresses; (d)-(e) ice pressure generates the stress for the ice block motion.

The motion resulting from ice matter deformation has a relatively slow rate. The inertial forces of such flow are very small and can be neglected, meaning that the internal velocity field of an ice block in each next moment does not depend on the previous state and is governed only by the matter properties and current conditions on the external boundaries. Such motion satisfies the principles of mass and momentum conservation; thus, its internal fields of velocity and pressure can be derived from the matter properties and boundary conditions alone, using the Stokes equation from fluid mechanics.

1.2.2 Glacier flow

Figure 5 Greenlandic glacier *Elephant Foot* is a good demonstration that ice behaves as a highly-viscous fluid (by N. Larsen)

The flow of a glacier, meaning the ice mass displacement in space, is the same process of ice deformation as described above, which happens uniformly across the glacier and is accompanied by some additional processes on the ice-bed interface. The ice temperature across the glacier and the boundary conditions can vary is space and time, therefore, a field of acting stresses is complex.

Depending on the glacier's shape and bed type, the relative contribution of various stresses changes. To simplify the problem and bring to the fore the principal mechanisms in a specific situation, the approach of *force budget* is widely used (Van Der Veen and Whillans, 1989). It assumes that despite the complexity of a real glacier, its average driving stress is closely balanced by a limited number of the most important resistive stresses, with the possibility to neglect some of them according to the required accuracy. For instance, for a glacier grounded on a relatively flat topography the most simplistic approximation is that resistive forcings can be approximated by the basal friction alone, which thereby is equal to the driving stress. Another example: under a floating shelf the basal drag on the bottom ice-water interface is zero, thus, one can simplify the resistive stresses to the drag on the shelf's lateral borders in contact with the bedrocks.

The fact that different glacier faces experience unequal stresses leads to the more pronounced deformations concentrated on specific locations. Usually in the case of a grounded glacier, the majority of processes which drive the glacier motion occurs close to the bottom face, where the major stress – basal friction – acts. To simplify the further considerations, we decompose the internal ice-motion field into two components (Figure 6): *internal shear deformation component* related to the deformation occurring along the entire ice column, and the *basal sliding component* related to the cumulative effect of all processes occurring close to the ice-bed interface.

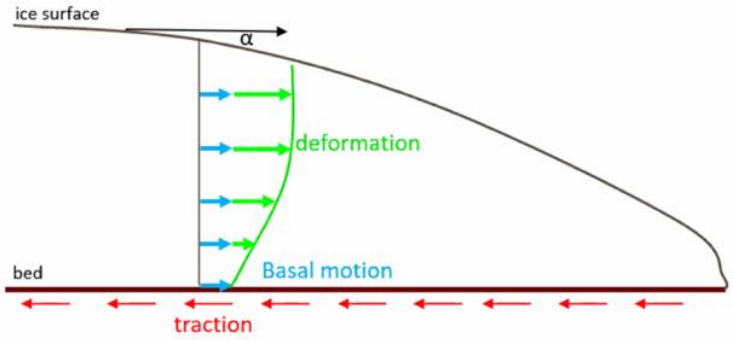

Figure 6 Simplified schematic view of glacier motion with internal velocity field decomposed into *internal shear deformation* (green) and *basal sliding* components (blue), and the basal drag opposing the flow (red).

The "internal shear deformation" component refers to the ice creep which occurs along the entire vertical profile of the ice column. Its cumulative effect causes slow displacement of ice layers relative to the basal face with certain *deformation speed* u_d (Figure 6, green line). Deformation speed has a non-uniform vertical profile along the ice column, because the shear rate increases towards the bed, where the weight of the overlying ice is larger. Additionally, it is typical for Greenland that the lower ice layers have a higher temperature, so they are easily deformable (e.g. Maier et al., 2019; Young et al., 2019). Thereby, a faster creep develops on the lower section of the ice column, while it is negligible in the upper ice layers.

Under the term "basal sliding", we consider the cumulative effect of all micro-scale processes taking place near the ice-bed interface and resulting in the uniform - at the scale of the ice column - motion of the entire upper ice column with a certain *basal speed* u_b (Figure 6, blue line). The list of corresponding processes includes enhanced deformation of the basal ice layers around large obstacles, "displacement" of ice by melting and refreezing around small-scale obstacles, sliding on a water film at bedrock the interface, and others (Benn and Evans, 2010). Note that usually the presence of a water film on the ice-bed interface is assumed to exist, so no "true" dry friction directly between materials takes place; instead, the term "basal friction" refers to the general flow retention effect of bedrock's obstacles. Except the slip on water film, those processes involve the local deformation of ice or its state change. The appearance and dominance of some of them depend on the glaciers' underlying bed type, which can be *hard* non-deformable rocks and frozen sediments or *soft* deformable sediments (*till*). In the latter case, under a certain shear stress at the till interface, till also starts to deform in the direction of the glacier flow. For simplification, we will also include this process in the "basal sliding" component of the glacier motion, as it provides additional speed to the underlying glacier with a uniform contribution across the ice column.

Note that while the discussion above considers only the basal face, similar processes take place on the lateral sides of a glacier between ice and rocks (e.g. a glacier confined in a valley or fjord), under the analogical *lateral friction*.

The speed of motion observed at the glacier surface u_s (*surface speed*) is a cumulative sum of creep and sliding components. Usually they occur together (Figure 7-c). However, limit cases of glacier motion can be found in nature and described with simplistic approximations. For instance, an unconfined floating ice shelf does not experience any basal drag on the ice-water interface which is needed to generate the shear stress and then a deformation speed component;

its internal velocity field can be approximated as vertically uniform sliding on the water interface (Figure 7-a). A glacier frozen at its base, which practically does not slide but experiences high basal shear stress, provides an opposite limit case; its flow can be approximated by the creep component alone (Figure 7-b).

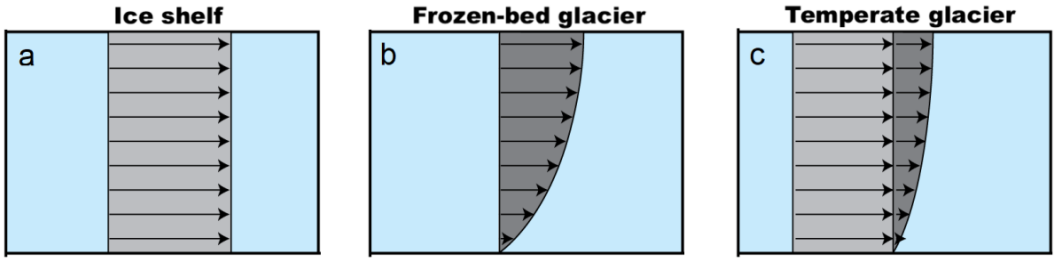

Figure 7 The simplified internal glacier velocity fields under varying conditions: (a) only sliding motion but no shear deformation, e.g. shelf slipping on the water face without basal drag; (b) only deformation motion but no basal sliding, e.g. glacier frozen to bedrock; (c) both components contribute to the ice surface motion, e.g. temperate glacier lying on the rocks.

As the motion-influencing factors are neither spatially uniform nor temporally stationary, the creep and basal sliding components can strongly vary in time and space, both in absolute magnitude and their relative contribution to the surface speed. This is observed, for example, in borehole measurements in Greenland (Maier et al., 2019; Young et al., 2019). It is commonly expected that the creep is the main motion mechanism of internal parts of the GrIS as they are most probably frozen to the bed (MacGregor et al., 2016), what explains why these regions move relatively slowly. The ice sheet periphery moves much faster (Mouginot et al., 2017), being mainly non-frozen at their base (MacGregor et al., 2016) and, thus, sliding-compatible. The range of speed can be very broad here, from tens of meters per year up to two tens of kilometers per year (Mouginot et al., 2017). As the majority of these velocities are much higher than the estimated creep-related scope (MacGregor et al., 2016), the basal sliding is expected to be dominating in the surface speed for many of these glaciers.

1.3 Drivers of velocity change over time

Remarkable variations of surface speed over different time scales have been widely observed across the GrIS on both land- and marine-terminating margins. Thereby, the questions of processes driving those variations are widely investigated.

To change the glacier's velocity over time, changes in the ice rheology properties and/or boundary conditions are required. Different factors affecting them evolve over different time scales, being thereby more or less important when a specific time scale is examined. Here, we will address the changes in the key factors affecting the ice rheology, geometry of glacier boundaries, or conditions in the bounding environments, including:

- ice temperature which affects the ice viscosity;
- ice thickness and surface slope which define the driving stress;
- grounding line and ice front displacement (mainly on tidewater glaciers) which changes the glacier geometry and thus the distribution of stresses;
- basal friction which usually is the major resistive stress on glaciers.

1.3.1 Ice temperature

The ice temperature is a parameter affecting ice viscosity and deformation rate, which increases with ice temperature. Thus, all other factors being equal, a warmer glacier deforms easier and so moves faster.

The temperature of a glacier depends on heat exchange at the top and bottom interfaces and on internal heat generated by ice deformation. The first point implies that usually temperature is not vertically uniform. Accurate description of the vertical profile, especially for the basal layers where the majority of shear deformation happens, is necessary to obtain the realistic simulations of other motion-related processes and conditions, for instance, the state of the basal environment (Habermann et al., 2017; Seroussi et al., 2013).

At the surface, the ice is at the air temperature. However, the low thermal conductivity of ice leads to the very slow propagation of surface temperature changes within the underlying layers. For instance, the typical greenlandic 50-degree amplitude of annual changes in air temperature does not propagate more than two tens of meters below the surface, while the mean annual air temperature is persistently kept deeper (Cuffey and Paterson, 2010). This means that the GrIS which is up to 3 km thick keeps in its current thermal regime the influence from the previous geological epochs; the deepest ice layers are only affected by air temperature changes on the millennium time scale (Dahl-Jensen et al., 1998; Goelzer et al., 2017).

The heat fluxes coming from the bottom – geothermal, frictional and dissipated by water – are more important for the greenlandic glaciers flow. They warm the basal glacier layers above the average temperature of the overlying ice. The geothermal heat component is usually assumed to evolve over very long time scales. The heat flux coming from the basal friction varies with the sliding speed. Finally, the thawing effect of infiltrating surface water is expected to exist along the margins, following the seasonal melt cycle (Karlsson et al., 2021). Between these three heat sources, friction is estimated to be the major source under the Greenlandic margins, while the

geothermal flux is the only one existing under the central parts (Karlsson et al., 2021). However, because across the margins the lowest ice layers are already close to the melting point (Doyle et al., 2018; Harrington et al., 2015; Hills et al., 2017; MacGregor et al., 2016), the possible small seasonal variations of basal ice temperature are commonly ignored. Generalizing, if no outstanding flow acceleration happens, one could consider the long-time absence of flow acceleration provoked by changes in external heat fluxes.

Besides the externaly-induced temperature changes, the process of ice deformation itself is accompanied by heat emission. In case of a newly emerging persistent and intense deformation, this source is able to change the temperature profile of the ice column at a relatively important rate. For instance, it has been modeled that Jakobshavn Isbræ's margin warmed up by almost 2° due to the twenty-year enhanced strain after the front disintegration and velocity acceleration by about +5 km/yr (Bondzio et al., 2017). Nevertheless, when the deformations have the short and alternating character, like seasonal speedups do, no significant or widespread changes in temperature would occur.

1.3.2 Ice thickness and surface slope

Changes in thickness and surface slope affect directly the driving stress and, thus, the basal stress. All factors being equal, first of all, effective pressure on the bed, a thicker glacier has a higher surface speed; in the same way, a steeper glacier moves faster.

While the bed topography under grounded ice can be considered unchanged over centuries (Goelzer et al., 2017), the upper free surface evolves with time. For the GrIS, thickness variations due to evolution of the SMB or flow dynamics are widely observed within the timeframe of several years (Csatho et al., 2014; Helm et al., 2014). On the same time scale an increase of an average glacier slope can be provoked.

It has been shown for mountain glaciers (Dehecq et al., 2019) and several Greenlandic regions (Joughin et al., 2012) that persistent thickness change trend on time frames of several years is able to impact significantly the surface speed. However, depending on the leading influence of creep or basal sliding motion components in the displacement of glaciers' surface, the net effect can be opposite. For instance, Dehecq et al. (2019) found that the ~5-7 m thinning in ~20 years was translated into ~5% decreases in driving stress and thus is responsible for 20-30 % speed slowdown in some sectors of High Mountain Asia. Meanwhile, Joughin et al. (2012) attributed the 100 m net thinning on the downstream section of Jakobshavn Isbrae as responsible for ~30 % of the total 30-year speed acceleration, as the basal friction decreased due to an effective pressure decrease.

Seasonal changes of ice thickness of a few tens of meters have been observed as well (e.g. Joughin et al., 2019). In the regions with very high summer melting rates and seasonal *dynamic thinning*, usually coming together, they are able to cause summer flow acceleration (Bevan et al., 2015; Joughin et al., 2012; Yang et al., 2019). Such thinning-induced speedups are observed on grounded tidewater glaciers, but do not appear on land-terminating glaciers. Outside of such extreme locations, the annual amplitude of surface topography changes in Greenland is orders of magnitude smaller than ice thickness. Thereby, its short-term influence on ice velocity is usually less important compared to other drivers (Joughin et al., 2012; Nienow et al., 2017).

1.3.3 Grounding line and ice front displacement

Figure 8 Retreat of ice front on Karale Glacier, Greenland, from 1933 to 2013 (by Natural History Museum of Denmark/University of Copenhagen)

A strong driver of flow speed changes in marine-terminating glaciers is the change in the force balance near the terminus (ice front or grounding line). Stresses acting on ice are subject to change whenever a glacier retreats or advances, thins or thickens, or reduces buttressing effects. These geometrical changes reduce or increase resistive and flow-driving stresses acting on the terminus, which can be significant enough to cause flow acceleration or deceleration.

As the **grounding line** (GL) of a glacier with an ice shelf extension is the limit of ice buoyancy, thinning or thickening can lead to the GL retreat or advance, respectively. The thinning which leads to the floatation of the previously grounded section can be driven by dynamic thinning, increased surface ablation or increased submarine melting. The latter seems to be the most frequent reason triggering GL retreats.

On glaciers with the marine floor inclined towards the open ocean (prograde bed), the GL retreat towards a shallower sea floor usually does not induce any additional feedbacks. On the other hand, for glaciers with deeper bedrock elevation inland (retrograde slope), when the GL moves to the location with deeper floor, volumetric ice flux across the GL increases strongly with depth, under the rising pulling stress which exerts on the glacier side face and drives the ice flow across the GL (Schoof, 2007). To satisfy this requirement, the glacier may respond by a speed acceleration and therefore dynamic thinning. Thus, when submarine melting causes the GL to retreat on a retrograde bed, the ice flux becomes imbalanced and the GL retreat becomes self-sustained as with each step a higher ice flux is required (Figure 9). This effect is called Marine Ice Sheet Instability (MISI) and is assumed to be the main possible way of rapid ice sheet collapse, because many large tidewater glaciers have large sections below sea level and a retrograde bed near GL (Morlighem et al., 2014). However, when it comes to specific glaciers, the behavior of GL is also controlled by the fjord geometry which not only prescribes the sea floor inclination but also determines the access of warm deep water to the glacier's GL and lateral drag (Åkesson et al., 2018; Millan et al., 2018; Wood et al., 2021).

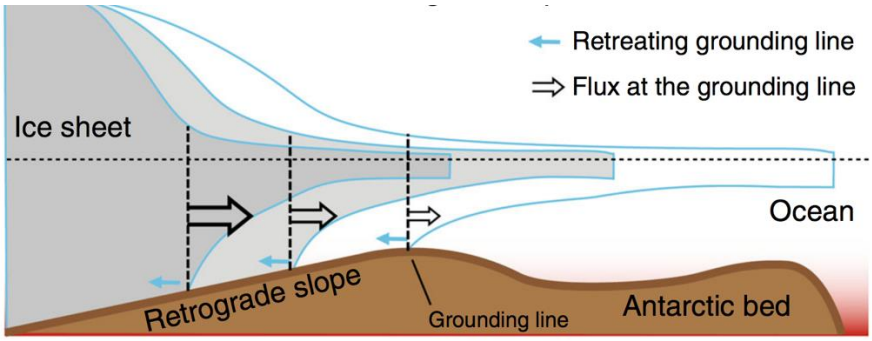

Figure 9 Marine Ice Sheet Instability (MISI) on the marine floor with retrograde inclination. Adapted from (Pattyn, 2018).

The thinning of a glacier in the grounding zone area can occur from both the surface and bed faces. The intensity and time frames of surface evolution are described in Section 1.3.2. It was estimated that the bottom interface experiences much more intensive ocean-induced melting compared to the surface. This has a strong impact on the ice shelf thickness or can "undercut" the ice at the GL over a few years (Beckmann et al., 2019; Rignot et al., 2010; Wilson et al., 2017). While submarine melting is difficult to observe and investigate due to the hard accessibility of the this environment, some understandings about its temporal variability were achieved. For instance, it has been shown that melting rate primarily depends on the ocean thermal forcing (difference between water and ice pressure-dependent melting temperatures) (Cook et al., 2016; Rignot et al., 2012; Wood et al., 2021; Xu et al., 2012), and increase of subglacial runoff in the summer time can enhance submarine melting by several times, due to intensification of water circulation (Sciascia et al., 2013; Slater et al., 2015; Xu et al., 2012). Seasonal air temperature changes do not directly affect ocean water at depths of hundreds of meters, which is a typical location of greenlandic tidewater glaciers' bottom. However, water from warm deep currents can reach Greenland coasts, and under favorable fjord geometry penetrate towards the glaciers' GL. This thermal forcing increase can happen from multiyear to seasonal time scales (Rignot et al., 2012; Wood et al., 2021).

GL retreats are clearly observed at interannual scales and are usually accompanied with an ice flow acceleration (Hogg et al., 2016; Mouginot et al., 2015; Rosenau et al., 2013). Up to now, no observations clearly confirm GL seasonal migration although they seem physically possible under the summer intensification of submarine melting. At the same time, GL migration by about one kilometer is observed as a response to the ocean tides (Milillo et al., 2017; Rosenau et al., 2013), as well as the short-term flow accelerations at tidal frequency (Echelmeyer and Harrison, 1990).

When a tidewater glacier ends by a grounded calving cliff, the displacement of the **front line** (FL) is equivalent to GL migrations in its effect. Advance of FL happens when the incoming flux of ice is greater than its discharge by calving and submarine melting; in turn, retreat means that calving/melt intensity prevails.

Iceberg calving is caused by different processes enhancing the fracture initiation or propagation through the ice. These forcings can be ice stretching under its own weight near the front, hydro-fracturing, submarine melting undercutting (Figure 10-left), buoyancy of the terminus section (Figure 10-right), etc. In favorable conditions of increasing ice thickness and

independently of the bed slope, the Marine Ice Cliff Instability (MICI) can take place on a retreating FL: each calving event exposes a thicker cross-section, which is more likely to calve under its own weight. Thereby, similar to MISI, MICI can potentially lead to the rapid sheet collapse or retreat. The retreat of the FL is commonly associated with the glacier flow acceleration (e.g. Sakakibara and Sugiyama, 2018; Walsh et al., 2012), while its advance is usually accompanied by the flow deceleration (Moon et al., 2014; Vijay et al., 2019).

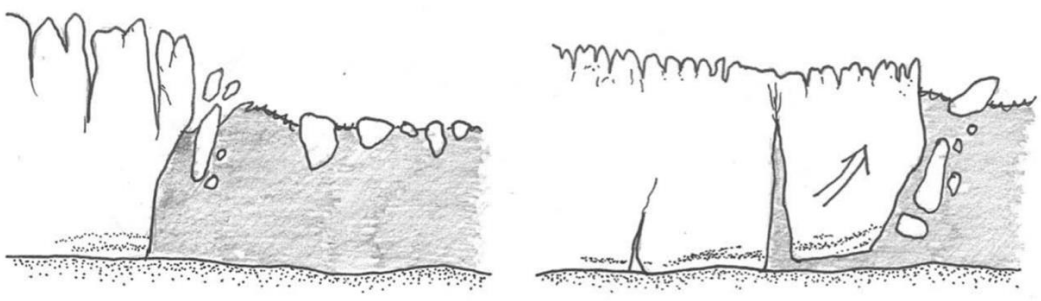

Figure 10 Illustration of some types of calving mechanism: ocean melt undercutting (left) and full-thickness buoyancy (right). Adapted from (Benn and Åström, 2018)

Large FL migrations associated to velocity changes have been widely observed across Greenland on decadal (Bjørk et al., 2012; Khan et al., 2014b; Lemos et al., 2018a; Moon and Joughin, 2008; Novoa Gautier, 2012; Schild and Hamilton, 2013) to seasonal time scale (Bunce et al., 2018; Joughin et al., 2012; Moon et al., 2014, 2015; Walsh et al., 2012). Leaving aside the exceptional events of large calving that can trigger the multiannual speed perturbations, we will consider further the link between the "normal" calving rate and glacier dynamics over a typical year.

The seasonal link between the FL migration and the flow acceleration has been observed and described for several tens of grounded tidewater glaciers across Greenland (Moon et al., 2014; Vijay et al., 2019). According to these studies, glaciers advance mostly during the winter due to the absence of calving, with a relatively slow or even slowing down speed. In summer, the FL retreats due to an enhanced calving rate, causing the flow speed to accelerate. Glacier speed can stay elevated for some time after the calving activity settles. Studies of calving physical mechanisms reveal that many of them are controlled by the processes or conditions that experience seasonal variability themselves. For instance, the surface hydrofracturing depends on runoff availability and air temperatures (Benn and Åström, 2018; Joughin et al., 2008a; King et al., 2018), additional backforce on the front face provided by sea ice and ice melange potentially preventing calving during winter (Howat et al., 2010; Khan et al., 2014b; Moon et al., 2015), or submarine undercutting melt that depends on ocean thermal forcing and subglacial runoff which are much larger during the summer (Moon et al., 2015; Mouginot et al., 2015; Nienow et al., 2017; Rignot et al., 2010; Slater et al., 2015). Note that the latter influences ice front evolution in the same way as described above for GL, including the importance of fjord geometry.

The displacement of **shelf's front line**, which also results from the unbalance between ice flux and calving rates, is able to lead to velocity changes as well. It acts on the upstream-located grounded ice through another mechanism than displacements of GL or grounded FL. This is

because no basal drag occurs on the ice-water interface. Instead, the drag comes from the lateral borders in contact with the surrounding topography. That provides retention of flow for a grounding-line cross-section, which is also known as *buttressing effect*.

The total amount of provided buttressing depends on the contacting area (shelf thickness and sides' length), fjord geometry and rocks properties. In fact, as it was already mentioned in Section 1.2.2, this lateral drag acts in the same way as the basal drag. Its decrease due to calving of a shelf section usually induces glacier flow acceleration, sometimes dramatic in its rapidity and rate (Bunce et al., 2018; Csatho et al., 2014; Joughin et al., 2010; Walsh et al., 2012). However, some glaciers can demonstrate insensitivity to calving even for a quarter of its shelf lenght (Nick et al., 2012), meaning that their shelf sections close to the terminus do not contribute significantly to the flow buttressing of grounded ice (Fürst et al., 2016). Thickness of the floating ice can evolve at both the top and bottom boundaries. As it was previously mentioned, the top surface variability can be significant over long time, but is usually neglected for the short time frames, while the submarine melting is usually much more intense. Nevertheless, the influence of the latter is usually considered as minor to affect buttressing at annual intervals.

1.3.4 Basal friction

In Section 1.2, we explained that the term of "basal friction" refers to the ice flow resistance provided by the bedrocks' roughness features acting as obstacles that need to be overpassed or by the till resistance to deformation. The majority of this action is provided by small-scale roughness, and its intensity varies with the basal conditions.

Dependency on basal conditions

When considering a **hard bed** (non-deformable), the basal friction is provided by the instantaneous bedrock small-scale rugosity (Weertman, 1957). While the bedrock surface has an initial roughness, the *effective roughness* experienced by the ice bottom can evolve over time and space due to opening and closing of cavities around the flow-obstructive features. These cavities are usually maintained by the presence of pressurized water which fills or even creates them. Alternatively, they can occur without water when a glacier moves fast enough so that the basal ice has no time to fill the depressions. Intensive cavitation leads to the reduction of the effective roughness, therefore less traction is generated on average and, thus, a higher basal speed can develop for a given driving stress (Figure 11) (Gagliardini et al., 2007; Schoof, 2005). The local average difference between ice and water pressures (*effective pressure*) gives ideas about the instant water influence; in a limit case where the effective pressure is null, meaning that the glacier becomes afloat, no basal friction exists. Note that the null effective pressure everywhere would mean an immediate downward slip of the entire glacier. In practice, this does not happen, because the cavities' network extension evacuates the water, as discussed further.

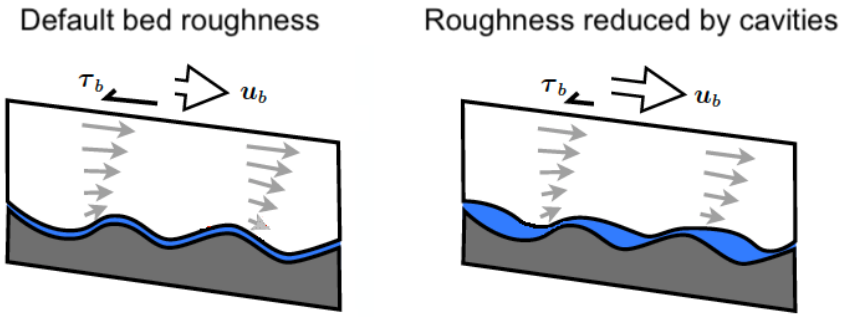

Figure 11 Ice flow across the default bed surface roughness (left) and "effective" roughness reduced by water-filled cavities (right). All factors equal, the basal friction τ_b is higher on the left, while the average basal velocity u_b is higher on the right. Credits: I. Howat.

When **soft sediments** are present, it is assumed that the bed offers less basal resistance compared to a hard bedrock and would therefore allow for a faster sliding. This is because on average they are more deformable than ice or rocks, thus, the sediments' surface under a glacier is sleek. Additionally, above a certain threshold of shear stress, the entire layer of underlying sediments can start to deform, offering an additional displacement for the overlying glacier. The stress threshold and the deformation rate of the sediments depend on the composing grain size and the amount of water between them, as this governs the inter-particle contacts and, thus, the sediment shear strength. The general hypothesis is that more water and a smaller grain size lead to a lower shearing threshold and higher deformation rate (Bougamont et al., 2014; Boulton, 1996; Davison et al., 2019; Nienow et al., 2017). It has been observed with observations and experiments that relatively low stress is required to trigger sediment deformation.

A number of *friction laws* have been proposed to establish the relationship between basal sliding and basal friction under varying subglacial conditions (see Section 3.2). The majority of the laws reflect the fact that the basal sliding speed increases together with basal friction and/or pressure of subglacial water; depending on the basic law's assumptions, this happens linearly or not, until a certain threshold or in an unlimited way.

Spatio-temporal variability of basal friction

Bed properties and/or the amount of water present at the bed can vary in space and time, as a result the basal friction can be highly variable as well. The **bed properties**, such as hard or soft, roughness, or sediments' grain size, evolve under the action of glacial erosion and so are assumed to be stable from decades to hundreds of years (Goelzer et al., 2017). Conversely, the amount of subglacial **water** can change significantly during a year and even a day across areas where the surface melting water has access to the bed. Simplifying, an increase in water pressure at the bed leads to a decrease in effective bedrock roughness causing a temporary flow acceleration.

In case of a non-frozen bed, the theory suggests a year-round presence of water under the glaciers (Cuffey and Paterson, 2010). The subglacial water can be a thin film between the bedrock and ice, water-filled cavities, or sediments saturated by water. The water network and pathways connecting them spatially constitute the *subglacial hydrological system*. When the system is in a steady

state, the water pressure remains relatively constant. When the water input to the bed increases faster than the hydrological system can adapt, it causes changes in the water pressure.

Water is continuously produced under the glacier due to different heat sources such as the geothermal heat flux and frictional heat, with the latter estimated to be responsible for about a half of the total basal melting water (Karlsson et al., 2021; Nienow et al., 2017). Across the areas hydrologically disconnected from the surface – or where surface runoff is insufficient – basal melting is the only source of water. The amount of basal water produced at the bed is assumed to vary slightly over a year, mainly due to increasing frictional heat during the summer flow acceleration (Karlsson et al., 2021). Such variability is usually considered as marginal and thus neglected when the ice flow processes are investigated (Echelmeyer and Harrison, 1990; Howat et al., 2010).

The second and main water source is the ice/snow melting at the surface, more specifically the part of melted water not captured by firn and called *runoff*. Usually, in the downstream region of a glacier basin, the surface is hydrologically connected to the bed by moulins and crevasses, thus, the spring/summer surface runoff has access to the subglacial hydrological system (Fountain and Walder, 1998). Surface melting is highly variable with seasons, clouds, and even fluctuates within a day (Bartholomew et al., 2012; Wright et al., 2016). Thereby, it is a key driver of the evolution of the basal hydrological system and, as a consequence, of changes in the sliding velocity within time scales ranging from hours to months. On average, in Greenland, the total amount of water produced at the surface is dominated by melt while rain is much less important (Fettweis, 2007). The seasonal speed variability begins with the melt season and continues for several months.

The changes in the subglacial amount of water, with all ensuing consequences in the basal environment, are considered to be the key factor behind the summer speedup of greenlandic land-terminating glaciers (Davison et al., 2019; Nienow et al., 2017). Indeed, speedups were observed with in-situ (Bartholomew et al., 2012; Sole et al., 2013; Tedstone et al., 2013; Zwally et al., 2002) and remote (Fitzpatrick et al., 2013; Joughin et al., 2008a; Lemos et al., 2018b; Sundal et al., 2011) methods across the majority of the land-terminating sectors. All altitudes at which melting occurs are affected, even far upstream from the equilibrium line altitude, where the melting rate is moderate (Doyle et al., 2014). The link between the surface runoff and water pressure changes was proven by in-situ measurements of water pressure in boreholes (Smeets et al., 2012; Van De Wal et al., 2015; Wright et al., 2016) and melt condition observations (Bartholomew et al., 2012; Sole et al., 2013; Van De Wal et al., 2015). When considering marine-terminating glaciers, this mechanism is also assumed to be an important driver of the annual velocity fluctuations on many glaciers (Howat et al., 2010; Lemos et al., 2018a; Luckman and Murray, 2005; Moon et al., 2015; Vijay et al., 2019), but the relation is more complex to establish as other drivers are at play as explained previously.

Annual cycle

Being interesting in this study by the time-scales accessible to remote sensing, we will leave aside the daily water-induced changes of basal friction and focus on the seasonal time frame.

Typically, for a **hard bed**, the annual cycle of the basal condition develops as follows (Davison et al., 2019; Nienow et al., 2017). When the spring melt begins, runoff infiltrates from the top surface to the bed through crevasses, moulins, etc. At this time, the subglacial

environment is still in winter state and is composed of areas with weakly- or non-developed drainage systems meaning that the routing capacity is relatively small and, thus, most likely is not enough to drain the enhanced amounts of water (Figure 12-a). This leads to an increase in water pressure at the bed, hence reducing the effective bed roughness and, consequently, the basal friction, allowing for a higher sliding speed. This phase of speed increase can last a few weeks until the subglacial drainage system adapts to the incoming water amount and becomes more efficient at draining the excess water (Figure 12-b). Depending on the capability of the network to adapt and variability of the water input rate, the sliding speed stabilizes for a while or immediately starts to decrease. The latter happens when the drainage efficiency of the subglacial

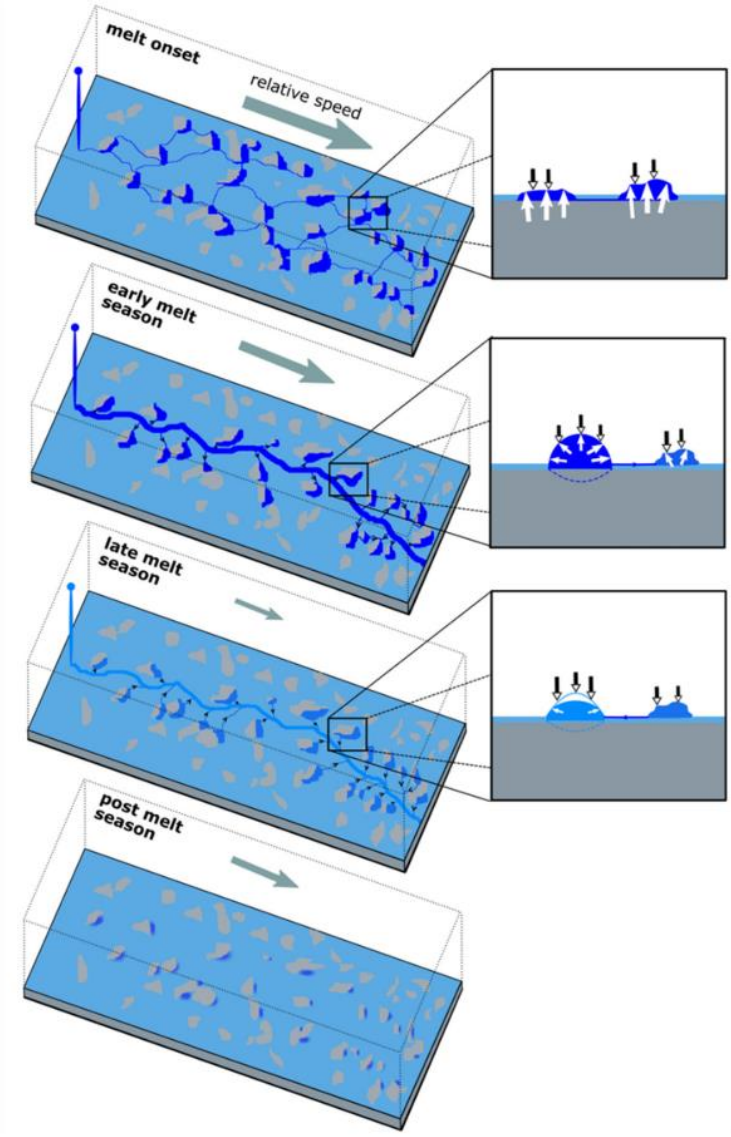

Figure 12 Stages of subglacial hydrological system development from early spring to late autumn. The main subplots present a planar view of the network, zoom subplots on the right show vertical cross-sections of the channels and water-filled cavities. The size of the gray arrows is proportional to the ice speed; white and black arrows in zoom subplots indicate the relative ice creep closure force and water pressure opening force, respectively. From Davison et al., 2019.

system exceeds the water input, which lowers the water pressure, increases the effective pressure and so causes more important basal friction (Figure 12-c). As a direct consequence, right after the end of the melt season, the ice velocity can decrease below the "initial" value (i.e. speed before the melt-driven acceleration) and maintain the slow speed during autumn to early winter. This happens because an established efficient hydrological system connects the majority of the bed surface, easily evacuating small volumes of present water coming from basal melting. Thus, the mean water pressure across the glacier is lower than at the end of winter when such a network does not exist anymore (Figure 12-d). During the winter, the subglacial network becomes again less efficient due to the closure of its conduits/channels/cavities by ice creep, because the low water production at the bed is not sufficient to keep them open.

In the case of a **soft bed**, the runoff infiltrates to the subglacial environment and makes the upper till layers more deformable due to saturation (Bougamont et al., 2014; Davison et al., 2019; Nienow et al., 2017): the initially present chaotic distribution of sediment grains has low porosity, which leads to a higher water pressure in the upper layers, with the possibility of water film formation on the sediment interface. This impacts both the deformation rate and threshold of deformation onset. With time, solid particles become arranged in a higher porosity structure, thereby water spreads more homogeneously across the vertical till profile and evacuates quicker, resulting in pressure drops.

To conclude on the relation between basal friction and sliding speed, the intensity and duration of seasonal speedups depend more on the initial state of the subglacial drainage system rather than the infiltration runoff rate, and depend more on its ability to adapt to the rising amount of water rather than the total volume of incoming water (Bartholomew et al., 2012). In an extreme case, when very little runoff water can access the bed compared to the amount of basal melt, it is possible that water pressure would be insignificantly affected and therefore a significant speedup would not happen. For instance, some studies suggest that starting with a certain sliding speed a glacier can generate so much basal melting water by friction heat that an efficient hydrological system will persistently exist for the whole year, resulting in summer melt not triggering a significant pressure rise (Echelmeyer and Harrison, 1990; Howat et al., 2010).

1.4 Summary

Between four drivers of glacier velocity changes described above, two – ice temperature (rheology) and thickness (driving stress) – are commonly assumed to act on relatively long time scales of few years at least. In contrast, changes in the basal traction from subglacial water pressure and in the force balance with GL/FL migrations can happen on short time scales (from hours to years). The glacier velocity reacts on them almost instantly (Van De Wal et al., 2015).

An acceleration provoked by any of these external forcings could lead to sustained mass loss. For instance, a marine-terminating glacier will discharge more ice into the ocean when the GL/FL retreats. On a land-terminating glacier, higher flow speed means that a larger ice volume is displaced towards the ablation zone. In both scenarios the positive feedback with topography lowering could lead to further acceleration and ablation increase (e.g. Joughin et al., 2012). Thus,

it could be speculated that even a short seasonal-scale acceleration above a certain threshold is able to lead to a self-sustaining glacier retreat and mass loss, if such acceleration is persistently repeated.

In practice, the interactions between ice motion and these acceleration mechanisms remain uncertain or not well constrained and so difficult to implement or parametrize in models. In addition, the impact of the short-term (seasonal) variability on the long-term (multi-decennial to centennial) is still poorly represented in numerical models. These current limitations impact our ability to "accurately" project the future evolution of the ice sheets. One of the main restrictions for that is still the deficit of suitable – widespread, precise, long and temporally frequent – observations that describe the glacier flow and geometry to constrain the physical processes associated with their changes (Vaughan and Arthern, 2007). Indeed, satellite observations only cover the last 2 or 3 decades, which is a relatively short period compared to the timescale of response of the ice sheets to perturbations. Conversely, the seasonal fluctuation in glacier flow offers the opportunity to observe important fluctuations over much shorter time scales and potentially to better understand the physical mechanisms at play.

The primary aim of this thesis is to explore the capabilities of satellite imagery to track ice speed changes over the shortest possible intervals. The imagery acquisition frequency by suitable sensors is currently about one week. Thereby, we expected to track successfully the speed changes caused by variability of basal stress and GL/FL position. The methodological developments, results and examples of these satellite-derived time-series are presented in Section 2. We expected as well to resolve the annual behavior of speed changes with a frequency sufficient for detailed investigation on the physical basis. The second aim is to investigate this new dense time-series using numerical modeling of the ice flow to better constrain the physical drivers of glacier velocity changes. The model setup, corresponding results and analysis are presented in Section 3.

2. Satellite observations of the surface ice speed

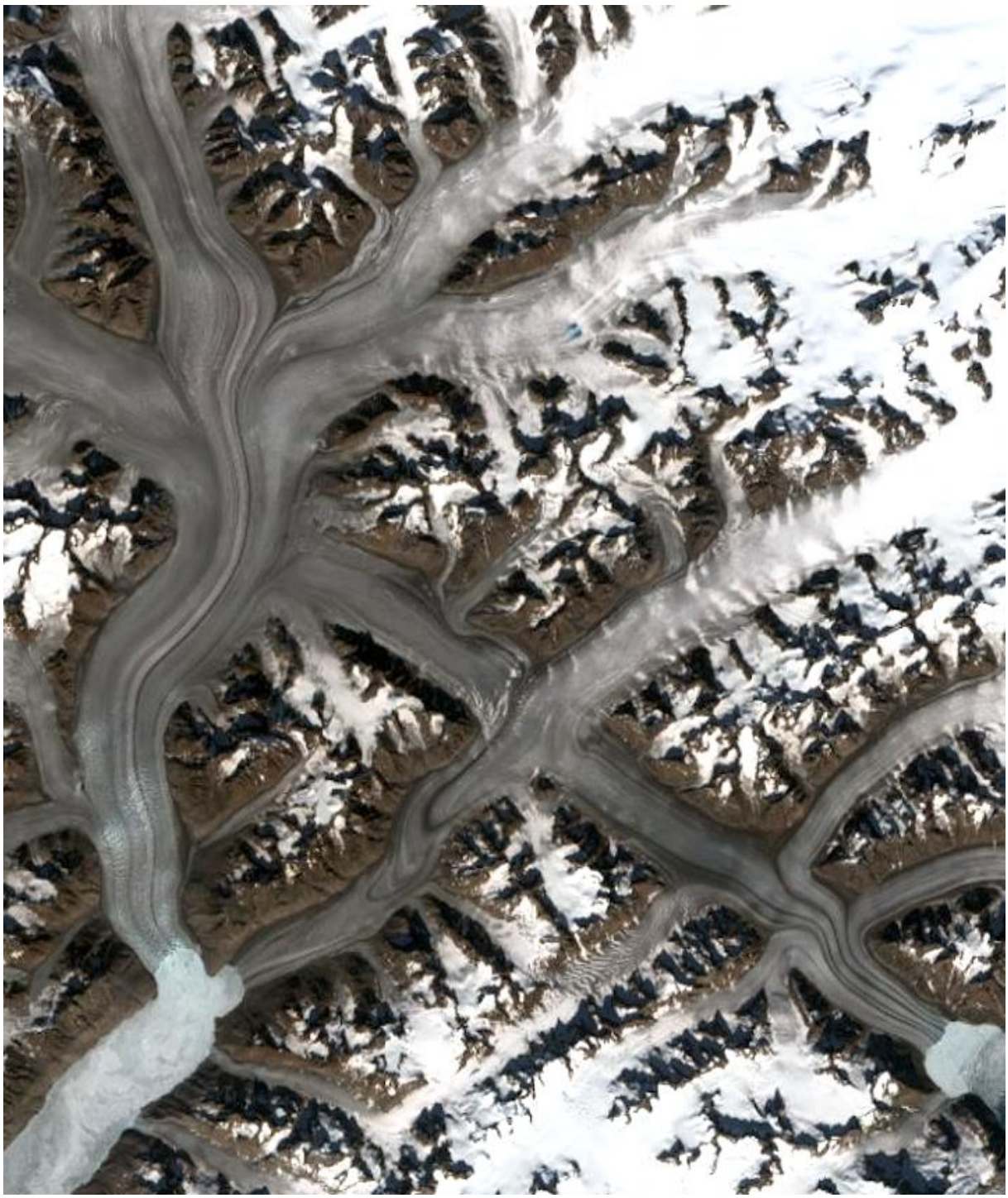

Midgard Gletscher, Greenland – Sentinel-2 satellite image, 16 Jul 2021

For a long time, airborne remote sensing imagery has been used for mapping of the ice surface speed of glaciers (Cheremnykh, 1962; Meier, 1979; Morgan, 1973). Satellite imagery started in the 1990th, with the launches of optical and radar instruments with suitable spatial resolution (Csatho et al., 1999; Joughin et al., 1996; Michel and Rignot, 1999). With the development of satellite-based instruments, the large-scale coverage, repeatability and low cost of the satellite data became largely beneficial compared to in-situ measurements or airborne surveys. In turn, this allowed for investigation of remote and hardly-accessible areas (Mouginot et al., 2012; Sattar et al., 2019), creation of the global overview maps (Joughin et al., 2010; Rignot and Mouginot, 2012), or implementation of repeated velocity observations to allow the monitoring of the glacier over time (Mouginot et al., 2019; Rignot et al., 2019). Since 2013, with the consecutive launches of Landsat-8, Sentinel-1 and Sentinel-2 satellites, relatively high-resolution imagery with high frequency has become routinely available, allowing to capture changes in the ice flow on shorter timescales (Armstrong et al., 2017; Millan et al., 2019).

However, it still remains challenging to capture subtle and/or rapid changes in the ice flow over the entire year and over relatively slowly moving areas by using the measurements from a single sensor and classical correlation techniques of speed retrieval (Fahnestock et al., 2015; Millan et al., 2019; Mouginot et al., 2017; Vijay et al., 2019). On one hand, this is due to the relatively high uncertainties in the displacement estimation associated with the spatial resolutions when short-time measurements are considered. Indeed, the tracking methods for velocity retrieval on optical data can achieve accuracy of surface displacement measurement of about 0.1-pixel (Millan et al., 2019; Mouginot et al., 2017). For the shortest Sentinel-2 (10 m/pix resolution) repeat cycle of 5 days this would correspond to uncertainty of about ±73 m/yr. This is more than a half of the average winter speed on a typical land-terminating sector of the Greenland ice sheet margin. In the same way, the precision of the nominal 16-day cycle is ±34 m/yr for Landsat-8 (15 m/pix resolution). On the other hand, the revisit time of individual sensors is a limiting factor to observe rapid events. For instance, the typical duration of the summer speed-up is about 6-8 weeks across the Greenland margin; this corresponds to 2-3 passes of Landsat-8. Unfavorable occasional natural conditions, such as cloudy weather for optical data or ionosphere storm for radar data, will additionally significantly reduce the quantity of suitable imagery (Ju and Roy, 2008). Finally, the gaps in data acquisition may persistently occur in the same moments of year and/or in the same location (Fahnestock et al., 2015; Joughin et al., 2018; Mouginot et al., 2017). Usually this is related to the sensor type (radar/optical), which causes the absence of source imagery (e.g. optical data during polar night) or repetitive correlation fails under certain conditions (e.g. melting season on radar data).

One of the ways to overcome such limitations is to combine observations from different sensors. This significantly increases the quantity of observations to resolve rapid dynamics and provides enhanced opportunities of measurement quality improvement with post-processing technics (Derkacheva et al., 2020; Tsai et al., 2019). Nevertheless, as each sensor is measuring surface displacements with its own unique characteristics (spatial resolution, time repeatability, etc.), it is technically and conceptually difficult to combine the data from different platforms. Thus, the integration of the derived velocity maps into a fused dataset, coherent in terms of numerical storage approach, metadata, and data specification, currently requires additional efforts.

To overcome these limitations, we establish the highly frequent and accurate tracking of ice velocity seasonal dynamics thanks to the joined usage of the satellite constellation Landsat-8, Sentinel-1, and Sentinel-2. For that, we create an operational workflow of the velocity maps production, design an outcoming data storage system and a corresponding data manipulation ecosystem. We test this workflow on three selected sites and evaluate the obtained database. We then test different regression methods of post-processing to accomplish the multi-sensor data fusion and their quality enhancement. The efficiency of those methods is evaluated against the simultaneous GPS measurements done on one of the observed sites. Finally, we describe and discuss the post-processed high-frequency time-series in terms of velocity spatio-temporal variations and physical mechanisms that are causing them.

2.1 Study areas

The Greenlandic outlet glaciers demonstrate the vast variability of situations. Differing by terminus type, speed range, geographical position, surface characteristics etc., they pose various challenges to derive surface velocity fields from satellite images. Herewith, an important range of seasonal speed changes from a few centimeters to several kilometers per year, as well as differing responsible drivers, can be found along the Greenlandic margin.

We selected three sectors – land-terminating, grounded tidewater, and floating tidewater – as the representative case studies with a diversified list of issues for remote sensing measurements of surface speed (Figure 13). All sectors have non-frozen beds over the lower half of their basin, and surface speeds largely exceed the values that can be explained by the shear deformation alone (MacGregor et al., 2016). Thereby, basal sliding contributes actively to the surface motion. Some of tidewater glaciers are also known for the relatively pronounced displacements of their fronts. Thus, being subjected to diverse seasonal forcings, these sectors additionally offer the diversity of behavior and the rate of ice flow seasonal dynamics.

The Russell sector is a land-terminating ice sheet margin which is representative of the ground-based South-West sector of Greenland. Having a relatively slow flowing speed, it remains a challenging area to track short-term events with a reasonable signal-to-noise ratio. Located in the Central West sector, Upernavik Isstrøm is a marine-terminating system that, in the recent years, shows three independent outlets glaciers terminated by calving fronts. It has a very fast-flowing speed up to several hundred of meters per month, therefore, it needs dedicated processing parameterization of the imagery processing chain to capture the rapid ice displacement. Petermann Gletscher has one of the largest basins in the North, and is one of the few tidewater glaciers in Greenland that still has an extended floating shelf. It requires large-scale observations and tracking of summer dynamics with a shorter live time than on more southern glaciers. Finally, according to our goal of continuous year-around observations, all case-studies provide an additional challenge, being located above the Polar Circle thereby in area of the Polar Night occurrence.

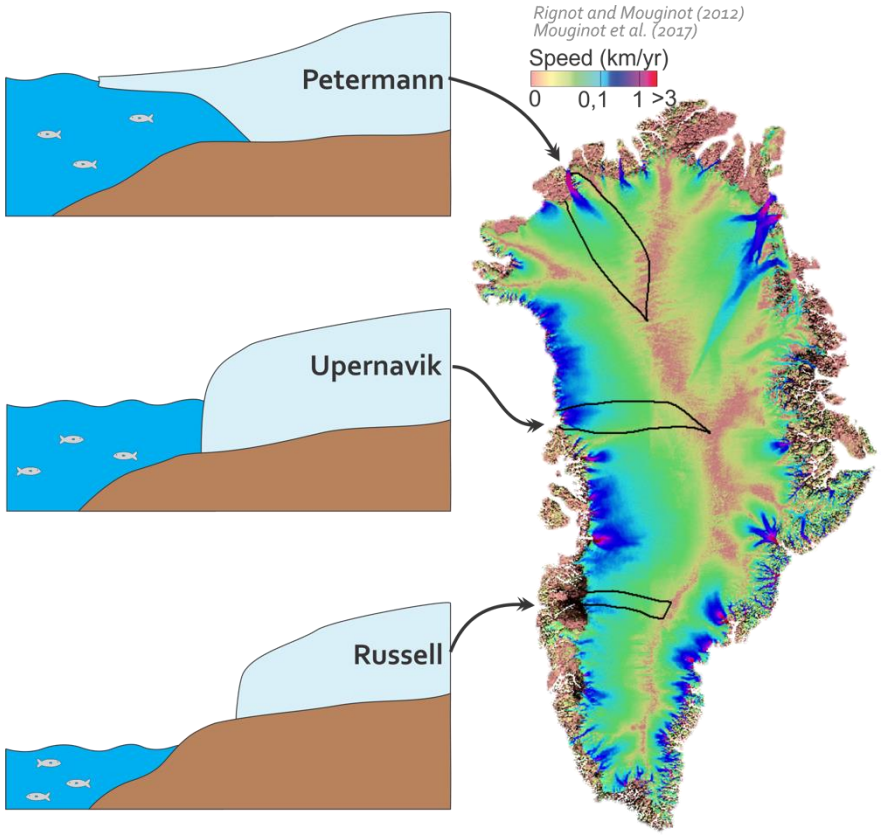

Figure 13 Location of Russell sector, Upernavik Isstrom and Petermann Gletscher basins in Greenland. Greenland velocity map is taken from (Mouginot et al., 2017).

The **Russell sector** is located in Western Greenland, slightly above the Polar circle, at 67°N 50°E, in a large land-terminating sector of the ice sheet, with a clear east-west orientation of ice flow (~275° from the north on average). We hereinafter refer to the Russell sector or basin as the area constituted by three glaciers – Insunnguata Sermia, Russell Gletcher, Ørkendalen Gletscher – and a portion of the ice margin located north of Insunnguata Sermia with no pronounced ice streams (Figure 14). Due to easy accessibility from the closest town, Kangerlussuaq, this is one of the most studied areas in Greenland. A number of investigations, experiments and in-situ observations have been made here, including: GPS surface velocity measurements (e.g. Bartholomew et al., 2012), maintaining of a long-term meteorological station (e.g. Van de Wal et al., 2005), borehole drilling (e.g. Harper et al., 2017; Maier et al., 2019), radar ice thickness surveys (e.g. Morlighem et al., 2011). Such an abundance of available data allows for a large-scale theoretical investigation, and, first of all, for modeling developments.

The Russell sector is known for its pronounced spatio-temporal ice velocity variations (Fitzpatrick et al., 2013; Joughin et al., 2008b; Lemos et al., 2018b; Palmer et al., 2011). The two northernmost glaciers follow topographical valleys in their downstream sections, and flow at speeds ranging from 100 to 250 m/yr during winter. Ørkendalen Gletscher has similar velocities, except at one downstream location where the ice flow overpasses a topographical ridge, which causes a tripling of the surface speed. The regions surrounding the named ice streams display ice speeds around 50–60 m/yr in winter. Seasonal ice speed fluctuations have been observed in a number of studies with GPS and space-based observations. Over a large area near the ice margin, speed-ups from +100 to +250% above the winter mean have been reported (Derkacheva et al.,

2020; Joughin et al., 2008b; Lemos et al., 2018b; Maier et al., 2019; Palmer et al., 2011), with the measured maximum of +360% in small isolated patches (Palmer et al., 2011).

The Russell mass balance equivalent here to SMB, which for a long time was almost zero, has been negative for the last two decades due to the surface melting intensification and enhancement in some years (Houtz et al., 2021; Van De Wal et al., 2012), with a value about -1.9 Gt/yr (Mouginot et al., 2019). This has led to surface elevation lowering, but the average thinning rate is moderate and does not exceed about -1 m/yr over the last decades (Csatho et al., 2014; Helm et al., 2014; Yang et al., 2019). At the same time, the observed ice front position has experienced negligible retreat.

The lower part of the basin, located below the long-term equilibrium line estimated to be at ~1500 m (Van De Wal et al., 2012), experiences a large-scale melting that generates a large amount of runoff water in summer (Hasholt et al., 2013). The produced water partly infiltrates towards the ice bed through multiple cracks and moulins (Bougamont et al., 2014; Christoffersen et al., 2018) and partly drains out on the ice surface (Smith et al., 2015).

The surface elevation changes smoothly across the basin from 300m to 2500m. However, the ice thickness also depends on the bed topography and is much more variable due to the deep channels (Morlighem et al., 2017). The main channel, followed by Insunnguata Sermia glacier, is about 300 m b.s.l. in the deepest section and 100 m a.s.l. near the glacier terminus.

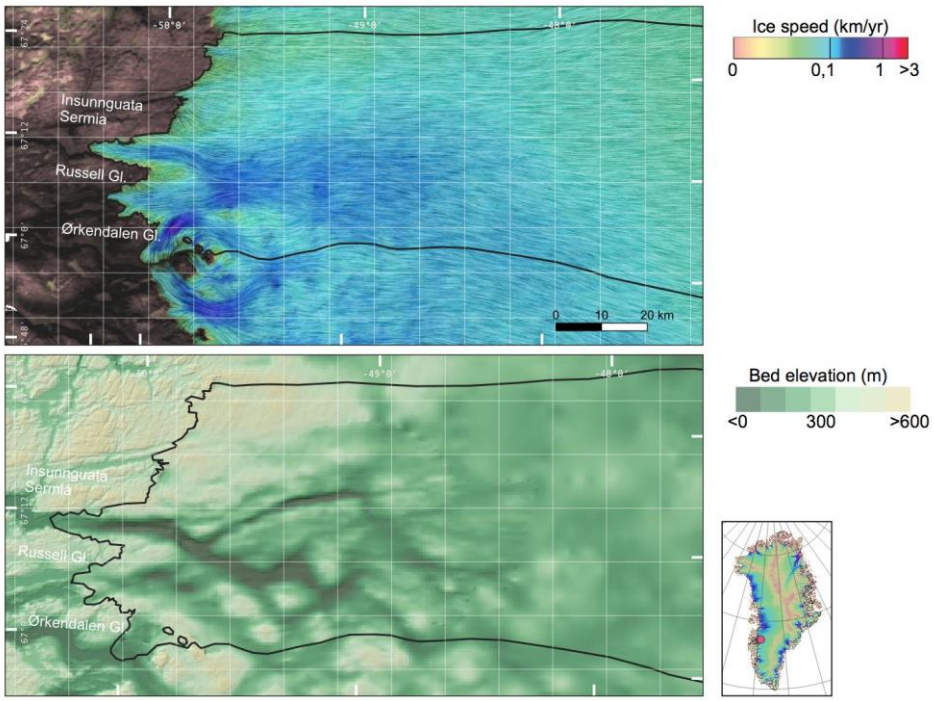

Figure 14 Downstream part of the Russell sector basin, composed of Insunnguata Sermia, Russell Gletcher, and Ørkendalen Gletscher. Top: mean multi-annual ice surface velocity (Mouginot et al., 2017). Bottom: Bedrock topography (Morlighem et al., 2017). Black contour follows the average glacier limits in 2015-2019.

Petermann Gletscher is one of the rare outlet glaciers of Greenland that still keeps a large floating ice tongue. Its basin, located in North Greenland at about 80°N and 58°W, is also one of the largest basins in Greenland in terms of surface (Figure 15). Alone, it drains about 4-6% of the ice sheet (Rignot and Kanagaratnam, 2006; Rignot and Steffen, 2008). The main ice stream

predefined by the subglacial topography drains the entire basin, and continues as a 50-km long and 15-20 km wide ice shelf after entering into a long fjord with sharp slopes.

The main stream has been showing mean winter surface speeds of about 1200 m/yr in the grounding line zone for two last decades (Ahlstrøm et al., 2013; Hill et al., 2018; Lemos et al., 2018a; Rignot and Kanagaratnam, 2006), with a slight but persistent acceleration about +2% per year since about 2010 (Mouginot et al., 2019). The seasonal speed variations are well pronounced in the downstream part of the basin, with summer speed-ups of around +300 m/yr at the GL (Ahlstrøm et al., 2013; Lemos et al., 2018a; Nick et al., 2012).

The surface elevation is slightly above sea level on the almost flat shelf and is smoothly increasing up to 2700 m far inland on the grounded part. The subglacial relief is more complex (Morlighem et al., 2014). In the downstream basin region, the glacier flows in a large depression, aligned towards the ocean and forming a continuous structure with the fjord. It has an estimated depth of ~500 m b.s.l. at the GL, which corresponds to an ice thickness of ~600m. From this depression, a narrow channel below sea level continues up to the internal greenlandic depression (Bamber et al., 2013). Therefore, up to 90% of Peterman's basin area is estimated to be below sea level (Johnson et al., 2011; Rignot and Steffen, 2008). Investigations on the grounding line location and displacements, done on a 1990s-2000s dataset, revealed its chaotic multiple retreat and advances by several kilometers, which had shaped an average net retreat of only ~0.5 km (Hogg et al., 2016). During the observed period 2015-2019, the glacier front position has advanced at a very homogenous speed of about 100 m/yr regardless of the season, meaning that the much faster flow speed is almost compensated by numerous and small calving events. The last large calving event was observed in 2012, shaping the current shelf length of about 55 km. Interestingly, the ice flow did not change significantly after this event as it has been observed in other places (Hill et al., 2018). This could suggest that only "passive" ice was removed (Fürst et al., 2016), i.e. the buttressing provided by the ice shelf remained unchanged.

Petermann glacier has been in an almost equilibrium state for a long time, meaning that positive surface mass balance with a dominating accumulation term is closely compensated by ice discharge to the ocean. The MB was on average -1 Gt/yr in 1970-2000 and about -2.5 Gt/yr in 2000-2017 (Mouginot et al., 2019). This decrease happened mainly due to the surface melt intensification, which changed the SMB from ~9.7 Gt/yr to ~8.6 Gt/yr for the same time intervals. The ice crosses the grounding line with a flux of ~11Gt/y and is then lost at 80% by submarine melt at the bottom of the shelf before reaching the calving front (Johnson et al., 2011; Rignot and Steffen, 2008). Being related to the MB, the surface elevation lowering is very limited here, about -0.5 to -1 m/yr, and does not propagates far inland (Helm et al., 2014; Yang et al., 2019). The surface melting generates a relatively small quantity of water. Herewith, the observed subglacial fresh water flux to the fjord at the GL (Johnson et al., 2011) significantly exceeds the estimated volume of basal ice melting (Karlsson et al., 2021). This means that the runoff has access to the bed through moulins or crevasses, which are primarily located in the lower part of the basin and on the shelf.

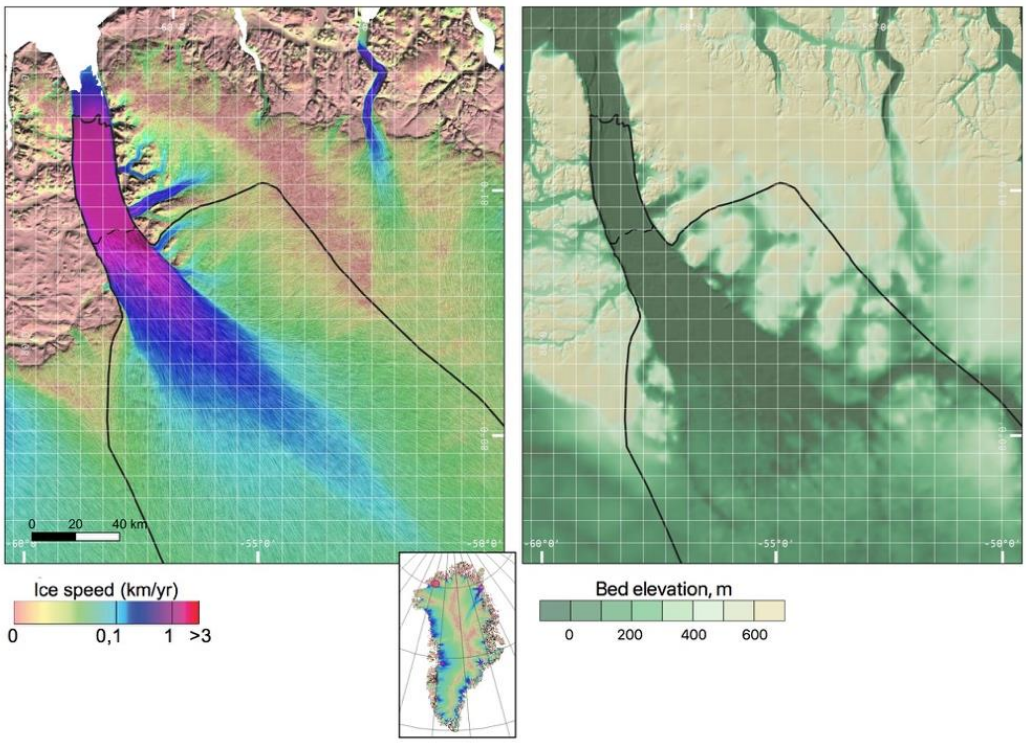

Figure 15 Downstream part of Petermann Gletscher basin. Left: mean multi-annual ice surface velocity (Mouginot et al., 2017). Right: Bedrocks topography (Morlighem et al., 2017). Black contour follows the average glacier limits in 2015-2019, dashed line shows the grounding line.

Upernavik Isstrøm is a tidewater glacier, located in Central Western Greenland, at about 73°N 54°W. It is in contact with the ocean by an ice cliff and has no floating tongues today. The current basin delimitation includes three independent branches – called here Northern, Central, and Southern – defined by the basal topography, which formed a single terminus some decades ago (Weidick, 1958) (Figure 16). This glacier belongs to the very fast flowing group with a speed range of several kilometers per year.

The three branches vary remarkably in terms of absolute velocity values, interannual and seasonal dynamics (Larsen et al., 2016; Vijay et al., 2019). The Northern stream's mean speed is about 4500 m/yr, with seasonal fluctuations of 100-300 m/yr in the target years 2015-2019 (+3% to +7% above the winter mean) and has a general multiannual slowdown trend. The Central stream has shown a significant interannual variability during the observation period with an average speed of 2800-3600 m/yr. It does not show pronounced seasonal-related pattern of speed change, just an insignificant short-term deceleration can be distinguished in the time series. The Southern stream is the only one among them where interannual variability is small and clear regular seasonal fluctuations happen. Contradictory to the "classical" dynamics with one summer peak, it has a "cardiogram" velocity curve: the mean winter velocity of about 1700-1800 m/yr increases in summer by nearly +7% and decreases by the same amount in autumn. While these oscillations are relatively small, they correspond to 100-150 m/yr in absolute values (Vijay et al., 2019).

The ice front positions also show non-uniform behaviors on the three branches (Larsen et al., 2016; Vijay et al., 2019). The Central stream has a well-pronounced seasonal cycle of advances and retreats. The margin of the Southern stream is very stable in space and does not move during

a year nor over the entire 2015-2019 period. The Northern stream's calving front is more dynamic, it developed a small displacement over the entire year regardless of the season; its multiyear location is overall stable. The basal topographical conditions are favorable for the calving, as the calving fronts have a height of about 500-700 m (Larsen et al., 2016). The ice streams follow the deep subglacial channels of several hundred meters below sea level that extend inland of the ice sheet for 30-50 km (Morlighem et al., 2014). The surface topography starts with a cliff elevation of less than 100m a.s.l and smoothly rises up to 3000 m.

The absolute values and the general trend of mass balance over the last decades are negative for all branches (Larsen et al., 2016; Mouginot et al., 2019). The SMB decreases due to the melt intensification, and was about 3.5, 3 and 0.5 Gt/yr in the 2010s on average for the three branches from north to south respectively (Mouginot et al., 2019). Ice discharge through the calving front is the main process of mass loss, being responsible for up to 80% of the total ice mass loss in certain years (Larsen et al., 2016; Mouginot et al., 2019). With the actual rates of about 10, 6, and 2.5 Gt/yr from north to south respectively in 2010s, they vary in time following the inter-annual speed trends. For instance, in the Northern branch, the brutal acceleration in the 2000s was accompanied by a doubling of the ice discharge (Mouginot et al., 2019) and a remarkable ice thinning at the rates up to tens of meters per year (Gray et al., 2019; Haubner et al., 2018; Nielsen et al., 2012). Even associated glacier uplifts were even observed in the downstream area in response to this large mass loss (Nielsen et al., 2012). On average across the last two decades, the elevation changes are a few meters per year inland of the mentioned branches and ~-1 m/yr on the Southern branch (Gray et al., 2019).

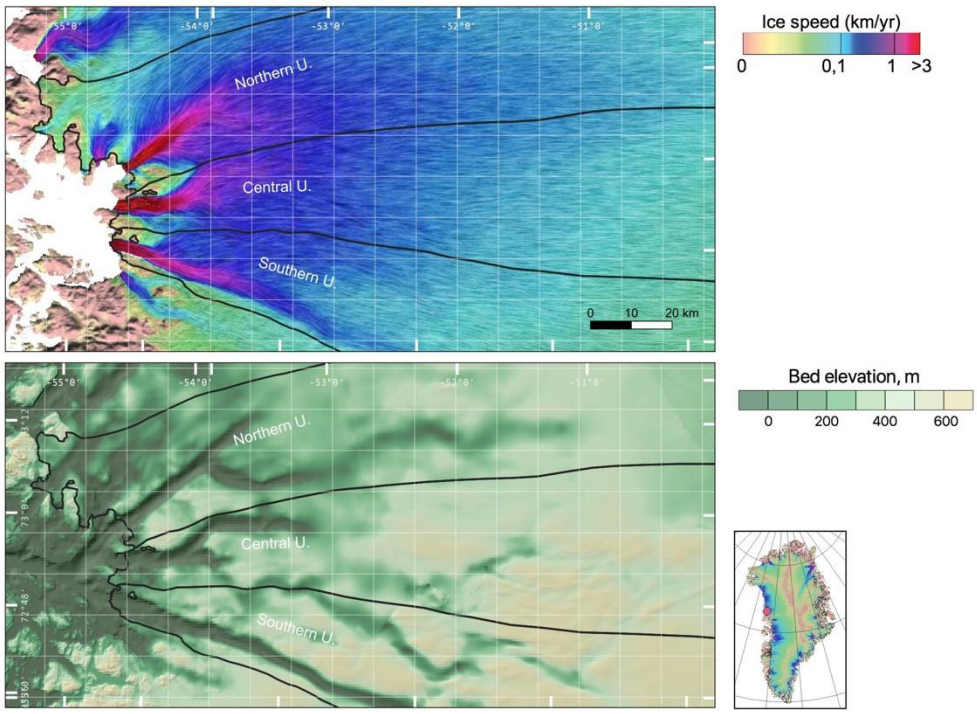

Figure 16 Downstream part of the Upernavik Isstrøm system composed of three glaciers. Top: mean multi-annual ice surface velocity (Mouginot et al., 2017). Bottom: Bedrock topography (Morlighem et al., 2017). Black contour follows the average glacier limits in 2015-2019.

2.2 Velocity database

2.2.1 State of the art methods for deriving glacier surface displacements

The general idea of the surface motion tracking in images is similar in a number of studies, independently from the thematical domain or used sensor (Altena and Kääb, 2021; Debella-Gilo and Kääb, 2011; Kraaijenbrink et al., 2016; Lacroix et al., 2018; Stumpf et al., 2017). The same surface pattern is searched in two images which are taken at different times; its displacement distance can be measured based on the known signal acquisition geometry and is converted into speed using the known time interval between the acquisitions (Konig et al., 2001). This approach was born in the era of Landsat constellation appearance and implied at first the visual inspection of optical images to find the easily distinguished surface features, like crevasse or moraine, and manually measure their displacement (Krimmel and Meier, 1975).

Since then, this idea has developed into two extensively explored groups of velocity-retrieval methods: *feature-tracking*, applied on both optical and Synthetic Aperture Radar (SAR) imagery, and *interferometry*, operating with specific type of SAR data. Initially applied over large-scale and fast-flowing streams in Antarctica and Greenland (Bindschadler and Scambos, 1991; Scambos et al., 1992), they have evolved together with sensors properties, and can be used to survey even the relatively small mountain glaciers now (Millan et al., 2019).

In this section, we provide a theoretical overview of different velocity-retrieval methods and limitations that influence velocity measurements. At the end, a vision on the current challenges in this scientific-technological domain is proposed.

2.2.1.1 Feature-tracking approaches and their limitations

Feature-tracking approaches can be applied on both – optical and radar – types of imagery. When the optical images are used, the proper name "feature tracking" algorithm is referred to. On radar imagery, either the amplitude signal ("intensity tracking" or "speckle tracking") or the phase signal ("coherence tracking") can be considered (Michel and Rignot, 1999; Strozzi et al., 2002). So, while in the majority of remote sensing thematical applications speckle is a noise, here it is useful content. All these methods are actively used to track ice displacements over huge ice sheets and small-size mountain glaciers (Fahnestock et al., 2015; Jeong and Howat, 2015; Michel and Rignot, 1999; Millan et al., 2019; Mouginot et al., 2017; Sakakibara and Sugiyama, 2018).

At the dawn of the computer methods development, the surface features were visually identified on **optical images** one-by-one and their positions were picked manually. In the 1990s, the development of algorithms based on optical images *matching* helped to automatize the processing and increased the efficiency and accuracy of the approach (Bindschadler and Scambos, 1991; Scambos et al., 1992). As a result, in modern processing utilities the visual feature

recognition is replaced by the fully automated search of the best matching between two sub-images called *master* and *slave chips* (Heid and Kääb, 2012; Konig et al., 2001) (Figure 17). The master chips, typically a few tens of pixels wide, are sequentially extracted from the master image and successively compared to the chips extracted from the slave image, moving step-by-step in a spatial neighborhood. A correlation score on the matching pixels is calculated for each chips' mutual position, forming a local *correlation map*. The highest score in the correlation map, meaning the maximum similarity between overlapping pixels for the given chips' mutual position, denote the ice surface displacement from the moment of the master image acquisition till the acquisition of the slave image.

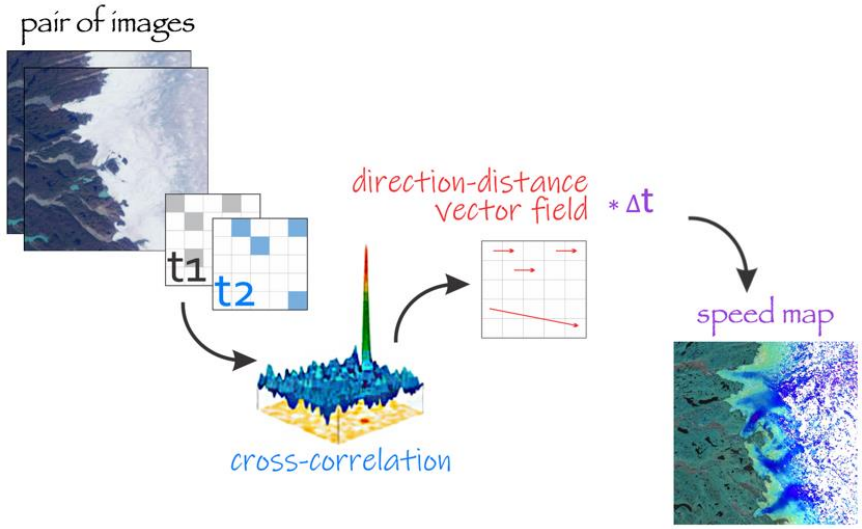

Figure 17 Feature-tracking algorithm of the ice surface velocity estimation from optical images.

Alternative, more sophisticated ways to do the matching have also been developed, aiming to increase the total area of successfully resolved velocity measurements or their accuracy. For instance, a few approaches now try to benefit from the high temporal redundancy by considering more than 2 successive images (Altena and Kääb, 2017; Hadhri et al., 2019b; Jeong et al., 2017).

In tracking algorithms, the size of the chips, their sampling step, offset step during the master-slave matching, and the search distance can be selected individually depending on the interval between images, sensor resolution, expected velocity range and the type/size of the object of interest (Debella-Gilo and Kääb, 2011). The similarity measure is classically implemented through normalized cross-correlation (NCC) (Bindschadler and Scambos, 1991), but some other metrics are also used (Heid and Kääb, 2012). According to Heid and Kääb (2012), each metrics presents an advantage compared to the others depending on the studied region, e.g. a flat wide ice cap against a narrow mountain glacier, but none is clearly better for worldwide application.

By default, optical-imagery-based tracking follows the displacements in a plane of image. Thereby, to accurately get the horizontal velocity, the *orthorectified images* (projected on horizontal plain without optical and topographical distortions) should be used. This is especially true for the steep mountain regions. The retrieved velocity can be presented as the v_x-v_y components, or horizontal magnitude v and direction α.

The images matching of the surface patterns expressed across many pixels, instead of the individual features or individual pixels, allowed to switch from few measurements across a glacier to full-cover velocity maps and to measure the surface displacements with accuracy below the pixel resolution. To achieve sub-pixel precision in NCC, two approaches can be used. The first option is to resample the chips to a higher spatial resolution through interpolation; the second is to interpolate the correlation maps (Debella-Gilo and Kääb, 2011). Roughly, the actual algorithms are able to achieve an accuracy of about 0.1-pixel in cross-correlation (Debella-Gilo and Kääb, 2011; Millan et al., 2019; Mouginot et al., 2017), which translates into the velocity precision of a few tens of meters per year for the shortest revisit time of contemporary satellites.

The speckle and coherence tracking techniques applied on **radar imagery** are conceptually close to those employed with optical images (Strozzi et al., 2002). In the same way, the chips extracted from both images are matched, and displacement in two axes is estimated. The speckle tracking operates with intensity property of the returned radar wave, and thus is more similar to the optical image; the coherence operates with a wave phase, assuming that the non-disturbing surface motion should preserve spatial patterns of returned phases. Commonly, the native geometry of radar images is kept during the entire processing, thus the initially retrieved velocity is in *azimuth* (along the satellite trajectory) and *slant-range (*perpendicular to it) coordinate space. The raw displacement map includes stereographic effects and the vertical displacements, due to sideways-looking geometry of the radar sensing. Thus, to obtain the true horizontal velocity of glacier surface, an external digital elevation model (DEM) is required to calculate stereographic effects and separate the horizontal motion from vertical. The latter is commonly done with an assumption that ice flows parallel to the surface. This step of vertical motion extraction is not an issue for the large and relatively flat ice sheets and ice caps, however, in the steeper mountains the minor errors of DEM or its co-registration with imagery can lead to large velocity errors.

As follows from the description, the spatial presence of well-distinguished features or patterns is critical for the optical data (Paul et al., 2017), which lead to less correlation over the smooth featureless inland areas of the ice sheets (Fahnestock et al., 2015; Mouginot et al., 2017). The radar speckle is independent from the objects, appearing over the relatively homogenic surface as well, and staying uniform from image to image under the relatively same surface conditions. It can be well treated with the cross-correlation methods and allows successful velocity estimation even on the featureless areas (Joughin et al., 2017; Mouginot et al., 2012). An opposite situation to the lack of features is their redundancy coupled with similarity, e.g. ogives or parallel crevasses fields: chips similarity is high in many positions so miscorrelation occurs (Paul et al., 2017).

Optical feature can be stable even for the long-time periods between images (e.g. – more than one year in Millan et al., 2019), but many effects can also lead to wrong correlation, even for short revisit, such as surface motion not related to glacier movement (e.g. snow dunes or sastruggi migration), semi-transparent clouds (Figure 18-c), or areas with contrast saturation (Fahnestock et al., 2015; Paul et al., 2017; Scambos et al., 1992). The radar-based tracking is more sensible to the surface changes and therefore requires the conditions with a high level of surface stability. For instance, the correlation significantly drops (or miscorrelation happens) when the surface rugosity or wetness changes due to melting, precipitation, or even wind redistribution of snow (Paul et al., 2017; Vijay et al., 2019; Weydahl, 2001) as this modifies the reflectance

properties of surface (Bevan et al., 2015; Konig et al., 2001). Among others factors, atmosphere humidity or ionospheric distortion may affect the radar data (Wegmüller et al., 2006). Note that while more robust, the speckle tracking is also affected when such surface or atmosphere changes are strong (Figure 18-a). Velocity mapping is also problematic near the fast-flowing marine-terminating fronts for any tracking algorithms, where after some time the frontal glacier section calves, therefore, no successful correlation is possible (Figure 18-b) (Nagler et al., 2015).

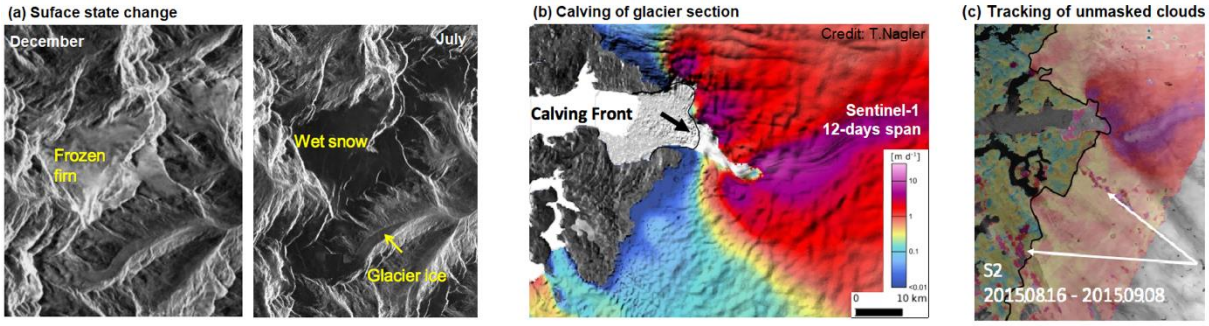

Figure 18 Examples of problematic situations for feature-tracking method: (a) Surface state change between radar intensity images taken in winter and summer; (b) unresolved velocity field near the calving front; (c) "successfully" derived velocity on unmasked clouds. Adapted from (Schwaizer, 2017).

The following specific issues can be listed for the tracking technics:

- The image matching methods use subset chips that are typically of several tens or a hundred of pixels for optical and radar data, respectively. This leads to a coarser spatial resolution and therefore to the loss of the small-scale spatial variability, which widely occurs in mountains, as well as to unresolved velocity field near calving fronts.
- The optimal matching parameters (chips size, sampling step, etc.) depend on glacier specificity and thus vary from site to site. Large-cover mapping with the same processing algorithm would requires adaptive parametrization to deal successfully with different regions.
- Topography-related corrections must be done using a DEM of compatible resolution and as temporarily close as possible to the images. The latter condition can be very important because the surface elevation may strongly change on glaciers, particularly in the ablation areas. Any errors in DEM elevation and its co-registration with a given image will propagate into a velocity error. Topographical issues are more important for radar imagery which has side-looking geometry than for down-looking optical imagery with relatively compact scenes.
- Regarding the optical data, significant changes in solar illumination and/or sun inclination can lead to large "visual" differences between images, directly impacting the correlation success. The correlation also fails in zones of radiometric saturation or across the featureless surfaces; both are common in accumulation areas of glaciers recovered by snow. In absence of solar illumination, e.g. polar night, or in cloud-cover conditions optical imagery cannot be used.
- Regarding the radar data, correlation diminishes rapidly with a longer revisit time. This can happen rapidly in the ablation areas at the onset of the melt season, where decorrelation occurs in a few days. The actual correlation durability partly depends on

the radar wavelength, because longer radar waves penetrate deeper into snow/firn/ice, thereby the "seen surface" can be longer preserved without changes. Radar imagery is independent from illumination and cloud problems, but the signal can be stochastically affected by the atmosphere.

2.2.1.2 SAR interferometry (InSAR) approaches

Although not considered in the following work of this thesis, repeat-pass SAR interferometry is commonly used to measure surface or infrastructure deformations with millimeter precision. Thus, it can be adapted for ice surface velocity measurements. The general idea consists in estimating the phase difference between radar waves returned by the same scatters of surface during two successive passes; this difference is directly proportional to the displacement.

The interferometry is sensitive only to displacements in the line-of-sight (i.e. the slant-range plane which is perpendicular to the flight trajectory) (Figure 19). Thereby, one *interferogram* (a map of waves' phase difference between two images) provides only a single-direction displacement component. To resolve the 2D motion of surface, at least two interferograms from different non-parallel tracks, e.g. from ascending and descending orbits, can be combined assuming that ice flows parallel to the surface (Joughin et al., 1998). Thus, four acquisitions (2 images per 2 sensor geometry) are necessary to get one velocity map. If more diverse line-of-sights are available for the same area, 3D velocity can be resolved. The task of obtaining several interferograms can become challenging during the seasons of rapid surface condition changes, as interferograms require high correlation between radar images.

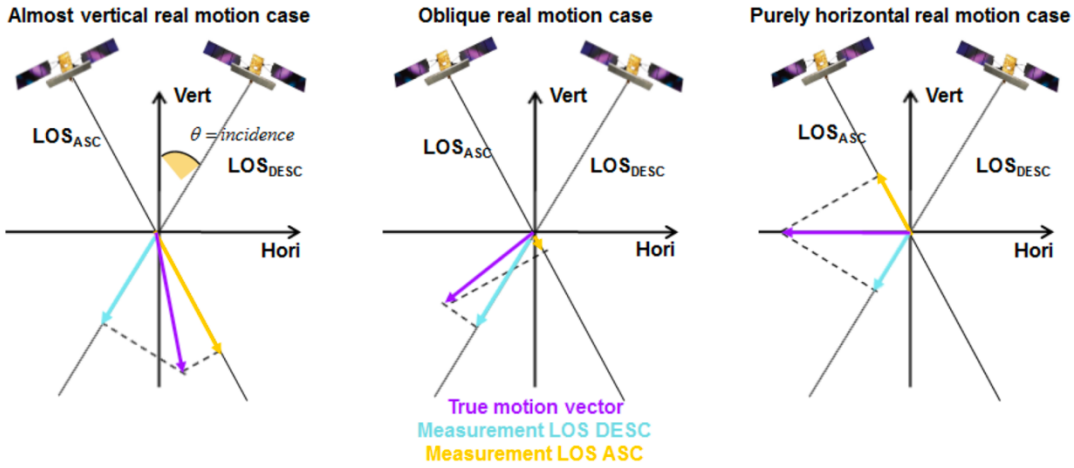

Figure 19 InSAR geometry of surface motion tracking (Duro et al., 2013). The true displacement (magenta arrows) is seen by SAR only in one of two components per track (blue and yellow arrows for descending and ascending orbits correspondingly). LOS – line of side (slant-range perpendicular to the orbit), incidence – angle of satellite orbit inclination, "Vert" and "Hori" – vertical and horizontal axes in the figure's plane.

The uncertainty sources and decorrelation conditions mentioned for the radar data above play important roles for InSAR as well. Thus, the interferometric phase is sensitive to the

stereoscopic effects from topography, which introduces a complementary term into the measured velocity and requires a precise DEM to be accounted for.

In contrast with speckle and feature tracking, the precision of the interferometric measurements is limited not by the spatial resolution but by the length of the radar wave, which is typically several centimeters (Massonnet and Feigl, 1998). On average, the InSAR method measures the ice deformation with a precision of one to two orders of magnitude better than tracking technics, i.e. at the centimeter level, which translates into a precision of less than 1 m/yr with a repeat cycle between interferograms of one to a few weeks. In cases of very "stable" ice plain like Central Antarctica, millimetric precision can be achieved, as images of few years span correlate well.

Regarding SAR interferometry, the following specific issues can be listed:

- The inaccuracy of InSAR velocity estimation is partly due to phase measurement errors (e.g. atmospheric distortion, interferogram decorrelation) and partly comes from processing steps (e.g. DEM-correction). On average, the InSAR precision is significantly better than tracking methods could achieve.
- Horizontal displacements can be reconstructed only using together images from non-parallel tracks (e.g. ascending/descending orbits) and an external DEM. This requires many successful acquisitions, which can be a problem over quickly decorrelating areas or regions rarely passed with varying orbits. The non-synchronous acquisitions can also be an issue for motion that changes rapidly over time.
- For the fastest glaciers or steep areas, if the temporal span exceeds a few days, the displacement gradient is larger than the threshold allowed by the wavelength to resolve interferometric fringes (2π-cycles of phase), so unwrapping fails (Strozzi et al., 2002). In contrast, on a very stable ice, the span can rise up to several years, providing an outstanding precision of measurements.

2.2.1.3 Axes of further development

The long-time development of velocity-retrieval algorithms has brought many various and highly-advanced implementations available for usage by the community. Thereby, other major **technical axes** of progress have been proposed to improve our ability to measure surface ice velocity more accurately (Heid and Kääb, 2012; Paul et al., 2015):

- **further development of pre-/post-processing technics**

Since the first automated workflows in the 1990s, many ideas have been proposed to improve the quality and accuracy of the results or to make image processing computationally efficient. First of all, it was quickly realized that two raw images are sometimes poorly suitable for correlation or accurate displacement estimation. Thereby, *pre-processing* of images has been introduced to improve the performances of the tracking algorithms. The major problem they should manage is inaccurate geospatial co-registration, which affects the value of retrieved displacement. At the source of the issue could be named satellite elevation drift, sensor distortion, inaccurate satellite positioning, bad orthorectification, etc. Another group of pre-processing technics addresses an increase in the amount of successfully-resolved correlations, as under some conditions, for instance changes in illumination, two images can hardly be

comparable. Edge filters to highlight the linear borders (Scambos et al., 1992) or the principal component analysis to extract the maximum diversity from spectral space (Dehecq et al., 2015) are examples of approaches to deal with this issue.

Post-processing techniques commonly focus on output data quality improvement (Paul et al., 2015). The most evident and oldest of them is filtering of pixels with too low correlation score which means that the displacement was technically estimated but is most probably wrong (Scambos et al., 1992). Nevertheless, other post-processing methods are emerging in order to detect and remove outliers (Skvarca et al., 2003), to statistically combine individual velocity maps into one time-average space-extended product (Fahnestock et al., 2015; Millan et al., 2019), to fill spatial and temporal gaps taking advantage of diversity in time intervals between acquisitions (Bontemps et al., 2018), or using regression approaches to reduce the raw datasets to corrected, ordered, and simplified time series (Derkacheva et al., 2020). Post-processing constitutes an essential base for construction of spatially-complete large-scale maps and temporally robust time-series.

- **intensive and extensive implementation of existing tracking algorithms**

The era of Big Data, where tens of terabits of images are generated every day, requires automated approaches for the treatment of large amounts of data. This includes both the aspects of vast regional coverage involving many tiles and of multi-temporal coverage involving multiple observations for the same tile. Such processing should consider the entire front-to-end workflows, including the questions of data download, pre- and post-processing, outputs storage and manipulation (e.g. Gardner et al., 2019; Millan et al., 2019). Additionally, the criteria of computational efficiency and minimal user interaction are more and more addressed when workflows are designed.

The simplest way to create a front-to-end workflow is to add the mentioned preceding and subsequent operations to a tracking algorithm with predefined fixed parameters, meaning that the same parametrization (chips size, correlation search distance, etc.) is used regardless of the image characteristics and/or geographical regions. It quickly became apparent that this did not provide optimal solutions when applied on a worldwide scale. Absence of parameters flexibility does not allow to deal successfully with site- or image-specific particularities, i.e. vast slow ice caps and narrow fast glaciers cannot be treated uniformly. This can lead to data gaps or inconsistencies persistently occurring over the same locations or at certain times (Fahnestock et al., 2015; Joughin et al., 2010; Millan et al., 2019; Rosenau et al., 2015). Currently, the more sophisticated implementations started to apply a flexible choice of parameters, which is adapted with respect to a geographical region or expected flow speed. Among other features for further development, an automatic choice of a better-suitable velocity-retrieval algorithm could be imagined (Heid and Kääb, 2012).

Here, both mentioned axes of post-processing and massive implementation of algorithms are addressed. First, we made the front-to-end workflow for automatic processing based on feature-/speckle-tracking, suitable on a big data amount and across different ice-covered regions (Section 2.2.2). With it, we create the spatio-temporally extended velocity datasets on the selected case-study sites (Section 2.2.3). After that, we investigate the question of time-series post-processing to perform fusion of multi-sensor data and diminish uncertainties (Section 2.2.4).

2.2.2 Implementation of the ice velocity retrieval workflow

2.2.2.1 Used sensors

The satellite constellations of Landsat-8, Sentinel-1, and Sentinel-2 are used in this survey. Designed for continuous observation of the Earth, they have suitable temporal and spatial resolutions for ice velocity measurements in Greenland. Presently, these satellites provide the best opportunities in the segment of routinely and publicly accessible images.

Landsat-8 (L8) (https://landsat.gsfc.nasa.gov/landsat-8/landsat-8-overview) is an American Earth observation satellite launched on February 11, 2013 by USGS and NASA as a continuation of the Landsat program started in 1972. The Operational Land Imager (OLI) sensor acquires global moderate-resolution images in the visible and infrared parts of the spectrum between 82.7° north and south latitudes. Space resolution is 30m for the spectrum channels and 15m for the panchromatic channel, which is used here for ice speed estimations. The satellite has a nominal revisit time (pass-by with the same looking geometry) of 16 days with 10:00 a.m. Mean Local Solar Time (MLST) of the descending orbit at equator. As toward the north the images footprints start to overlap on the borders, the same area in the middle latitude appears on images about twice as frequent, with local time deviating from MLST by several hours on side-looking acquisitions. Images are provided as orthorectified products by USGS, either in UTM or polar stereographic coordinates.

Sentinel-2 a&b (S2) (https://sentinel.esa.int/web/sentinel/missions/sentinel-2) are twin optical satellites developed under the European Commission Copernicus Program and launched into orbit in 2015 and 2017 respectively by the European Space Agency (ESA). They have identical orbit settings and a 180° shift of the orbital position. They provide moderate-resolution multi-spectral images, close to those of Landsat-8. Images in 4 spectral bands (RGB+NIR) are provided with 10 m resolution, and some additional spectral channels have 20 m or 60 m resolution. For the ice speed estimation, we use the green channel. Each of the Sentinel-2 satellites have a nominal revisit time of 10 days, but together the nominal cycle improves to 5 days. The real frequency of a middle-latitude area acquisition is about 2-3 days. The descending orbit MLST is 10:30 a.m. at the equator. The products are delivered to final users as orthorectified images in UTM projection.

Sentinel-1 a&b (S1) (https://sentinel.esa.int/web/sentinel/missions/sentinel-1) are twin right-looking C-band synthetic aperture radars (SAR) observing with an incidence angle ranging from 29° to 46°. Sentinel-1a was launched for the Copernicus Program by ESA in 2014, and was joined in the same orbit by Sentinel-1b in 2016. Nominal S1 revisit time is 12 days and 6 days for the constellation, with ascending orbit MSLT 6:00 p.m. on the equator. Acquisitions over land that we use are made with the interferometric wide swath mode (IW). We are preprocessing and mosaicking the IW bursts to form a single-look image with a ground resolution of about 15 m in azimuth and 8 m in slant-range directions. It should be noted that IW-mode does not operate over the entire globe (https://sentinel.esa.int/web/sentinel/missions/sentinel-1/observation-scenario). Following the recommendations by the international Polar Space Task Group, Sentinel-1 has been acquiring data continuously since June 2015 across a set of six tracks that cover the coast of Greenland, including the lower parts of Russell, Upernavik and Petermann

basins. In recent years, the interior part of the ice sheet is under continuous survey as well, however, the ice margin still receives more data.

2.2.2.2 Automated velocity-tracking workflow

We use feature-tracking algorithm with Normalized Cross-Correlation (NCC) metrics to retrieve the ice surface velocity. It is based on the implementation under Fortran-90 in the ROI_PAC package called AMPCOR (Rosen et al., 2004) which is now wrapped into a Python environment to maintain both efficiency and flexibility with the rest of the workflow. The Fortran-90 code calculates a standardized cross correlation map between the reference and slave chips, while the Python environment manages chips extraction. This allows to define adaptively processing parameters (window size, search distance, etc.), to define the mask of the areas of interest or to provide an initial guess of the surface displacements. Other python routines are then used to filter the correlation noise, and convert displacement to the speed units.

To deal with the big volumes of imagery in a routine automated way, a workflow was created at the facilities of the Grenoble Alpes University high performance computing center (GRICAD – Grenoble Alpes Recherche/Infrastructure de Calcul Intensif et de Données). The system searches for the metadata of all existing images for the requested region, filters it by cloudiness, matches the pairs for a required revisit time, launches the tracking algorithm, translates the output into a required projection, filters outliers and calibrates the results against the ground control points or areas. No human intervention is required during the processing, which allows for processing of hundreds of images per week. An expanded description of the adopted processing can be found (Millan et al., 2019) where the same workflow with adapted cross-correlation's parameters is applied on the mountain glaciers. Below is a detailed description of the workflow specifically used for this thesis focusing on Greenlandic glaciers.

At the first step, all images from the requested time period in the regions of interest are listed based on the data archives (ESA, NASA or Google). While we set a goal to process as much data as possible, only images with cloud cover below a user-defined threshold are considered. At first, we defined this threshold at 60% for all 3 regions considered, and then increased it to 90% on the Russell sector to gain more data for this slowly-moving sector and thereby increase quantity of successfully-derived measurements. On the next step, the listed images are matched with the requested time intervals to form all possible pairs for cross-correlation processing. Despite multiple track overlapping in high latitudes, we match only the images from the same orbits, to ensure the minimization of stereo-effect induced errors (Kääb et al., 2016; Paul et al., 2017). As this study focuses on the seasonal dynamics, longtime intervals are not useful and a period of one month was defined as a reasonable maximum. Thus, the used revisit times are 16 to 32 days for L8, 5 to 30 days for S2, 6 to 12 days for S1 (a few 24-day results were taken from the archives previously processed by J. Mouginot on the Russell sector, but this interval finally was not a part of the massive processing done here).

Cross-correlation is performed for each of the image pairs. For optical sensors, we use the 32×32-pixel (320×320-m for S2 and 480×480-m for L8) master and slave chips, 10-pix step of master chips sampling, and 4 pixel searching distance. For radar Sentinel-1 images, these parameters are 192×48-pixel (about 750×700-m) chips and 32×8-pixel searching distance. To

perform the initial placement of master and slave chips of optical images, a supporting "first-guess" map from mean multi-annual velocity maps (Mouginot et al., 2017) is used. This helps to increase the number of successfully correlated chips in fast-flowing regions without enlargement of the correlation-search area. Indeed, the maximum surface displacement which can be tracked with 4-pix offset on S2 image (10 m/pix resolution) would be only about 500 m/yr for a 30-days repeat cycle and about 3 km/yr for the shortest 5-days cycle. Without a first-guess map, we would not have been able to track the velocity near the North and Central Upernavik Isstrøm fronts, which moves at about 4-5 km/yr.

The resulting maps of surface displacement in pixel metrics and image-native geometry undergo calibration, filtering and translation to metric units and required geographical projection. The calibration step should remove the possible geometric distortions or geolocation errors; the corresponding bias is estimated over a stable ground or previous ice velocity mapping (Mouginot et al., 2017). Filtering is done using a 9×9-pixel median filter, which removes outliers above a 2-pixel threshold. Finally, the displacement is translated into v_x, v_y velocity maps in m/yr, using the Polar Stereographic projection (EPSG:3413).

2.2.2.3 Uncertainties assignment

Uncertainties in the ice velocity maps are usually estimated using a stable ground. According to the estimation of other studies, uncertainties for the nominal sensor repeat cycle should be about ±50 m/yr, ±40 m/yr, and ±20 m/yr for L8 (16 days), S2 (10 days), and S1 (12 days) satellites, respectively (Joughin et al., 2018a; Millan et al., 2019; Mouginot et al., 2017).

In our case, we have defined a theoretical uncertainty for each sensor and time interval by assuming that our correlation algorithm has an accuracy of about 0.1 pixel (Table 1). Thereby, error is $[365 * (0.1 * pixel\ resolution)/cycle]$. We use a unique value of 0.1 for all sensors, despite the fact that the real AMPCOR accuracy varies slightly between sensors and cycles (Millan et al., 2019). These values do not represent the real errors for each sensor or time interval but give a good overview of the typical noise that can be expected for each sensor and each cycle. Herewith, we expect that any georeferencing and geometrical problems are corrected by the calibration step. A better approach would be to take into account the other potential sources of errors mentioned in Section 2.2.1, but it remains difficult to setup for large-scale processing.

Table 1 Velocity estimation uncertainties assuming error in tracking of 0.1 pixel (two values are given for Sentinel-1 as it has non-squared native pixels).

Sentinel-1, 8×15 m/pix						
cycle, days	6	12				
error, m/yr	49×91	24×46				
Sentinel-2, 10×10 m/pix						
cycle, days	5	10	15	20	25	30
error, m/yr	73	37	24	18	15	12

Landsat-8, 15×15 m/pix						
cycle, days	16	32				
error, m/yr	34	17				

2.2.2.4 Data fusion and geo-database

As we use three different sensors that have various parameters of spatial and temporal resolution, the outcoming velocity maps are also heterogeneous in precision and revisit times along which the average velocity is estimated. To store the speed data in a unified way, the following solution has been implemented.

All processed maps regardless of the initial resolution are resampled to 150 m/pix without any spatial smoothing or averaging, and regrided on the common pixel grid. Each of them is added into a NetCDF file (*cube*) as an independent layer containing two maps of v_x and v_y velocity components with some associated metadata (dates of source images acquisition, time span, speed error, etc.). A number of such uniformly organized NetCDF files cover the entire region with a fixed grid, overlapping the neighboring cubes by 5 pixels for the spatial continuity of calculations (see below Fig.2 in Derkacheva et al., 2020, Section 2.2.4). This structure is easily compatible for matrix- or pixel-per-pixel based calculations, prevents too large files of varying spatial cover, and allows for an easy access to the data by spatial, temporal or source queries.

A Python module was developed to generate and manipulate these NetCDF cubes. It covers the functions of I/O operations, data management, query selection, visualization, and post-processing. While a number of NetCDF-oriented libraries already exist, including those oriented on the georeferenced data and capable to manage the temporal dimension, one particularity limits their application on our database: we have a description of the temporal dimension not as a precise moment or date but as a time interval of variable length, defined by two dates of master and slave images acquisition.

2.2.3 Overview of the obtained database

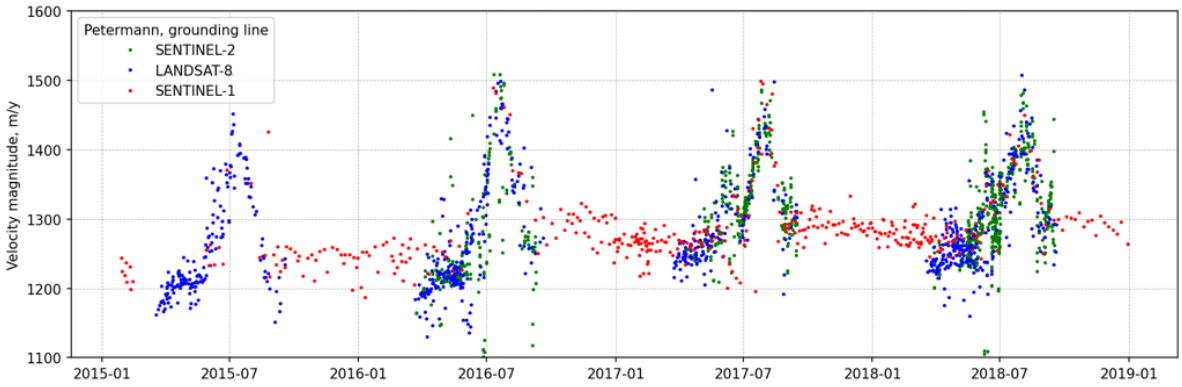

Figure 20 Example of an ice velocity time-series from our database for a location on Petermann Gletscher. The points are plotted in the center of master/slave images acquisition interval.

2.2.3.1 Data quantity

To create our velocity database, we focus on the period from 2015 to 2019. Thanks to three satellite constellations in use, more than several hundred velocity maps per year can be easily obtained in these regions, resolving well the seasonal-scale behavior of the glaciers flow velocity. The joint usage of optical and radar imagery ensures that the sites are continuously surveyed over the entire year (Figure 20).

In total, more than 50 000 image pairs were processed on the Russell, Upernavik, and Petermann sites. Nevertheless, the real average number of successfully derived velocity data per pixel is lower than the number of processed images and is highly uneven in time and space between the glaciers and across the same glacier. We show this with the year 2018 as an example by plotting the number of measurements obtained per pixel for each sensor and for 2 periods of 6 months centered on summer or winter. For the Russell sector this is Fig.3 from Derkacheva et al. (2020) located below in Section 2.2.4. The similar maps for Petermann Gletscher and Upernavik Isstrom are in Figure 21 and Figure 22, correspondingly.

The observed high variability in the measurement density comes from the points discussed previously:

- availability of the source imagery which is directly defined by the number of images taken by a satellite;
- suitability of source imagery for the processing (e.g. too much clouds);
- rate of cross-correlation successes or fails, when the feature tracking algorithm is not able to match successfully the surface patterns.

The availability of source imagery on the same glacier varies from winter to summer, mainly according to the specificity of the sensors, and is clearly visible in all figures. For instance, the number of measurements and their spatial cover change dramatically between winter and summer for optical sensors (Sentinel-2 and Landsat-8). The effect of overlapping imaging footprints in the polar regions is also clearly visible when comparing the Upernavik and Peterman

sites. Petermann glacier gets on average a few times more data than Upernavik (remember, that cloud threshold on Russell was different than there). Thus, the Petermann ice shelf can be observed up to several times per day with S2 (from different orbits with varying MLST), while the Upernavik and Russell sites are observed only once every 2-3 days (Li and Chen, 2020).

Regarding the suitability of source imagery for the processing, we can only estimate theoretically the influence of clouds on optical data. They are observed to appear without seasonal preferences but more frequently near the ice sheet margin (Van Tricht et al., 2016), which is our main area of interest. They are assumed to affect up to 40% of optical images done across our case-study glaciers (Li and Chen, 2020). In fact, the differences between the margins and the ice sheet interior in terms of measurement density are rather related to the success rate of correlations for different surfaces which is unambiguously lower on the featureless interior surfaces.

We can also observe that more S1 measurements are obtained in winter than in summer, which is due not only to the surface melting conditions that strongly affect the cross-correlation (Russell case, Figure 3 form the paper presented below), but also due to the planning of acquisitions that seem to be more spatially extensive in the winter half of year (Petermann and Upernavik cases, Figure 21 and Figure 22).

In summary, sensor type, location (geographic location of a glacier or pixel position on a glacier) and seasons are the important factors responsible for the observed variability in coverage. For the large-scale and intra-annual observations, the optical and radar sensors are highly complementary, one being more efficient in summer and the other in winter.

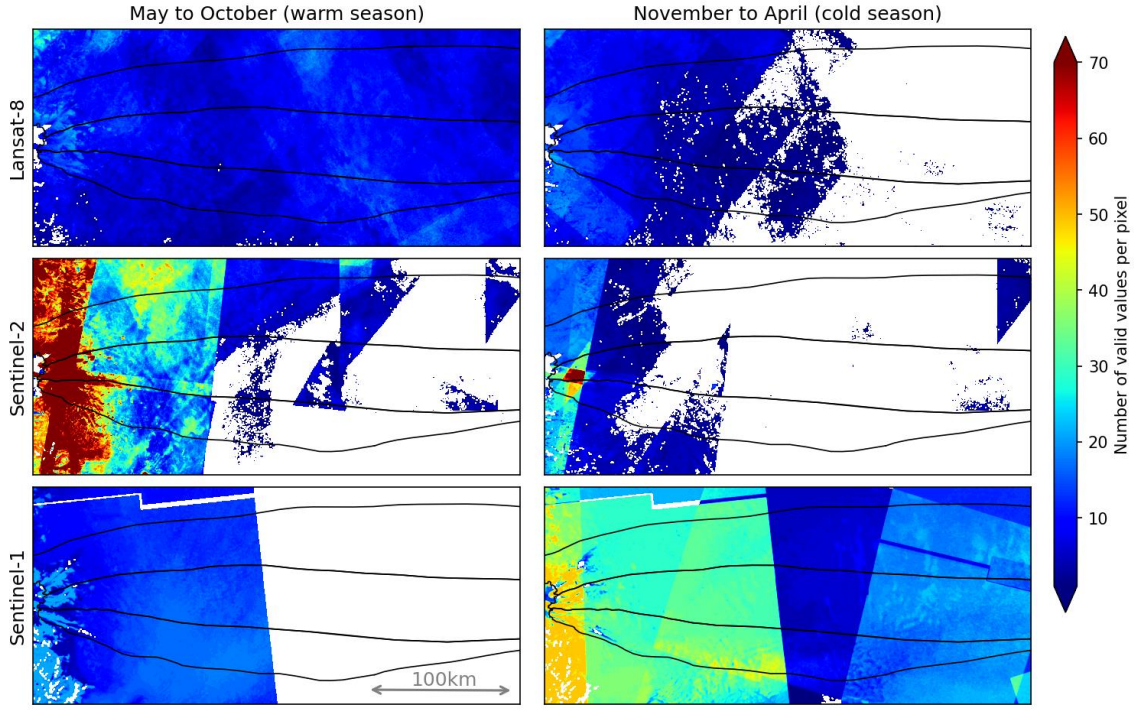

Figure 21 Upernavik Isstrøm: Number of successfully derived per pixel velocity measurements in 2018. Black contours are the basins of Northern, Central and Southern ice streams. White color indicates the absence of measurements.

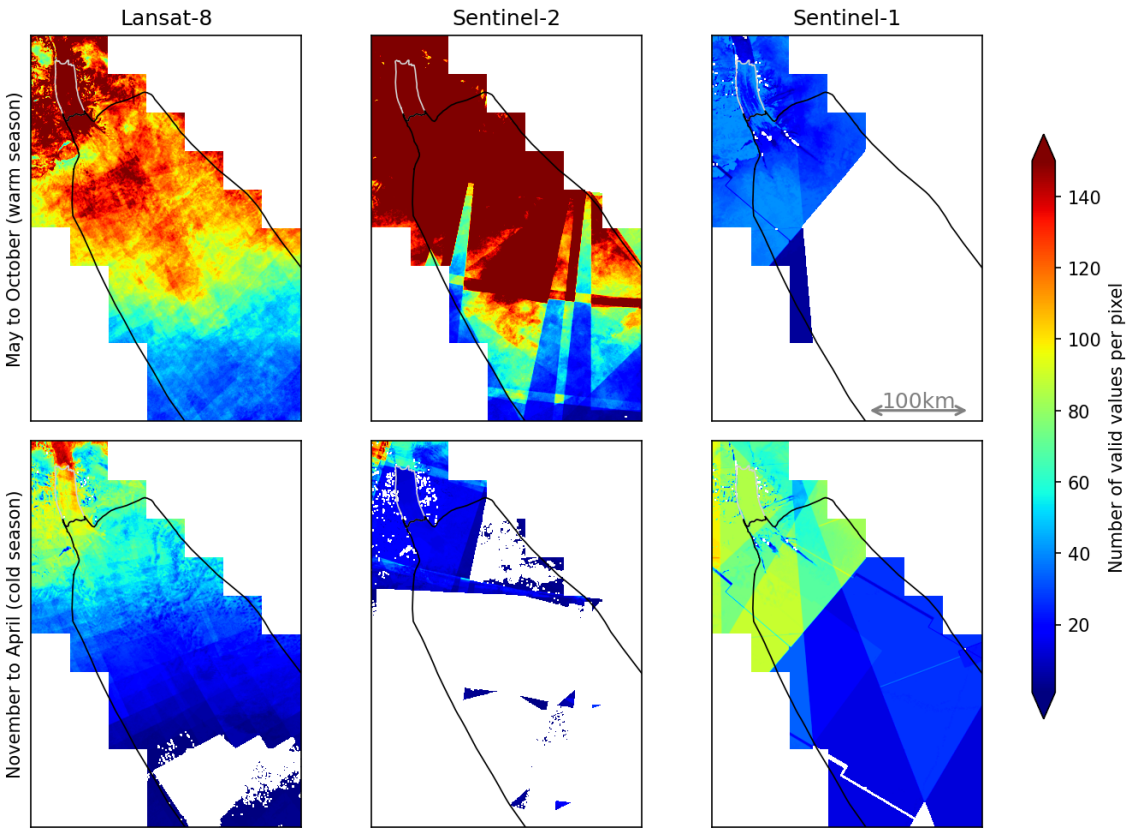

Figure 22 Petermann Gletscher: Number of successfully derived per pixel velocity measurements in 2018. The black contour is the glacier basin and the grey contour the floating shelf. White color inside the glacier basin indicates the absence of measurements; no data cubes were considered outside the basin limit.

2.2.3.2 Average precision and accuracy

It appears that the number and type of sensors that can be used over the course of a year vary if continuous measurements are to be obtained. As previously established, each of these sensors obtains velocity fields with a different theoretical accuracy stored in the metadata of our velocity maps. Gathered together, the maps keep the heterogeneity of both their theoretical and real quality. Thus, the precision (or dispersion) of the obtained measurements will vary over time, which may be important to take into account in the data usage and further post-processing.

In addition to the theoretical errors of each sensor presented above, here we take a look at the average dispersion of the measurements in different seasons. This dispersion seems to depend strongly on the locally-dominating sensor type (radar/optical) in combination with the surface conditions (i.e. season) and less on the dominating time span of velocity production. Thereby, we cannot address the issue by just filtering the presumably noisy velocity maps by metadata.

In Figure 23, we show the dispersion (standard deviation) of the speed measurements made by Sentinel-1 and Sentinel-2 over 2 periods of 2 weeks. The periods of early May and early September have been defined to highlight the standard deviation variability for the periods when the changes in the surface texture/state are most significant.

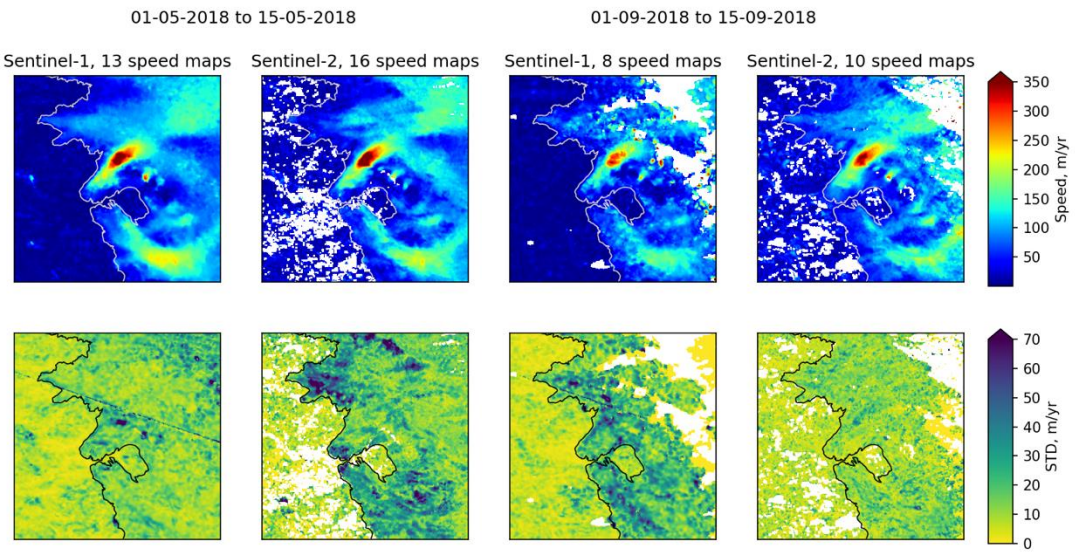

Figure 23 Mean and standard deviation (STD) of ice velocity measurements derived with Sentinel-1 and Sentinel-2 for 2 periods from 01-05-2018 to 15-05-2018 (left half), and from 01-09-2018 to 15-09-2018 (right half). The black line is the ice margin and the ice-free area is located on the left side of the maps.

The bottom line of the figure shows the pixels' standard deviation (STD) along the temporal axis as an approximation of individual measurements precision. In early spring, the radar speed measurements have a lower dispersion than the optical ones with an average STD on the ice of 39 m/yr against 46 m/yr. Conversely, the radar data demonstrate a larger dispersion with a spotted pattern in autumn, with STD of 49 m/yr against only 19 m/yr for the optical dataset.

Over these periods, Figure 23 also shows the median velocity (top panels), which should be identical between radar and optical datasets for similar periods and should always be zero on ice-free areas. These ice-free areas are recommended (Paul et al., 2017) and commonly used (Berthier et al., 2005; Derkacheva et al., 2020; Heid and Kääb, 2012; Millan et al., 2019; Sattar et al., 2019; Strozzi et al., 2020) as an approximation of the measurement accuracy. At our test site, for both time intervals the radar measurements display a better value than the optical results: the mean speed is respectively 8-9 m/yr and 24-30 m/yr for the S1 and S2 datasets, while the STD stays around 7 m/yr for both sensors. At the same time, it appears in Figure 23-top that the radar velocity field from September seems much noisier over the ice than the ice-free area and compared to the optical dataset. Thus, we have to keep in mind that the velocity values found on the ice-free area are only partially representative of the quality of ice velocity. This representativeness changes over the seasons depending on imagery nature, which seems understandable as the surface "texture" evolution over time is very different between the two areas.

According to our observations of the Russell sector, the average quality of our multi-sensor time-series degrades in spring and autumn compared to winter and summer seasons (Derkacheva et al., 2020, 2021). This implies that both radar and optical observations are strongly affected by rapid and pronounced changes of the ice surface that occurs during the periods by the transition between frozen and melting, and/or snow covered and bare ice. During winter, the SAR data are

the best source of measurements; in summer, they decorrelate more frequently than optical images due to the surface melting.

2.2.3.3 Comparison with similar databases

The closest public databases to our time-series are the GOLIVE https://nsidc.org/data/nsidc-0710 (Fahnestock et al., 2015) and ITS_LIVE https://its-live.jpl.nasa.gov/ (Gardner et al., 2018) archives. These are the worldwide long-term ice velocity databases using only the Landsat constellation, mainly L8 imagery. The latter is processed with many repeat cycles, including the 16 and 32-day cycles. Similar to our product, their surface displacement estimation is based on the normalized cross-correlation algorithms wrapped into a front-to-end automated workflow with the pre-/post-processing operations.

Here, we choose to compare these results with ours on the Russell sector as the major part of this area is relatively slow with an average winter speed of the order of a hundred meters per year in winter time and twice as high at the summer speed-up maximum. Such velocity range means that the cross-correlation uncertainties of the shortest L8 span (see Table 1) correspond to a third of the regional mean winter speed, thereby the signal-to-noise ratio is relatively low.

Figure 24 shows the time-series derived from all three databases for two selected locations (median value over 1500×1500 m area or 10×10 pixels in our cubes). Obviously, our time-series, represented by blue dots, has a much higher quantity of measurements, partly because we have combined three different sensors. Besides that, GOLIVE and ITS_LIVE do not seem to resolve properly the summer speed fluctuations on slowly-moving glaciers in the majority of compared years (Figure 24-a). For GOLIVE, the situation became better with a flow speed increase (Figure 24-b, Fig.10 from Fahnestock et al., 2015). ITS_LIVE seems to capture more accurately the high summer velocity, but the number of measurements remains insufficient to observe clearly the full cycle of speed fluctuations (Figure 24-b). It can also be noted that on average, our Landsat-derived observations are less noisy than GOLIVE or ITS_LIVE (Figure 24-c). It does not seem likely that our tracking algorithm is far better than those of Fahenstock et al. (2015) or Gardner et al. (2018). Presumably, we have included a calibration step in our processing pipeline that may not be part of the workflow from ITS_IVE or GOLIVE and allows for correcting or at least minimizing co-registration issues in Landsat-8. Finally, our time-series does not have an observation gap in winter thanks to the radar sensor, while Landsat-alone datasets cannot track displacement at this time.

This rapid comparison justifies the fact that the existing public archives do not seem adequate at capturing the seasonal flow fluctuation in Greenland and thereby cannot be used for the studding of these fluctuations.

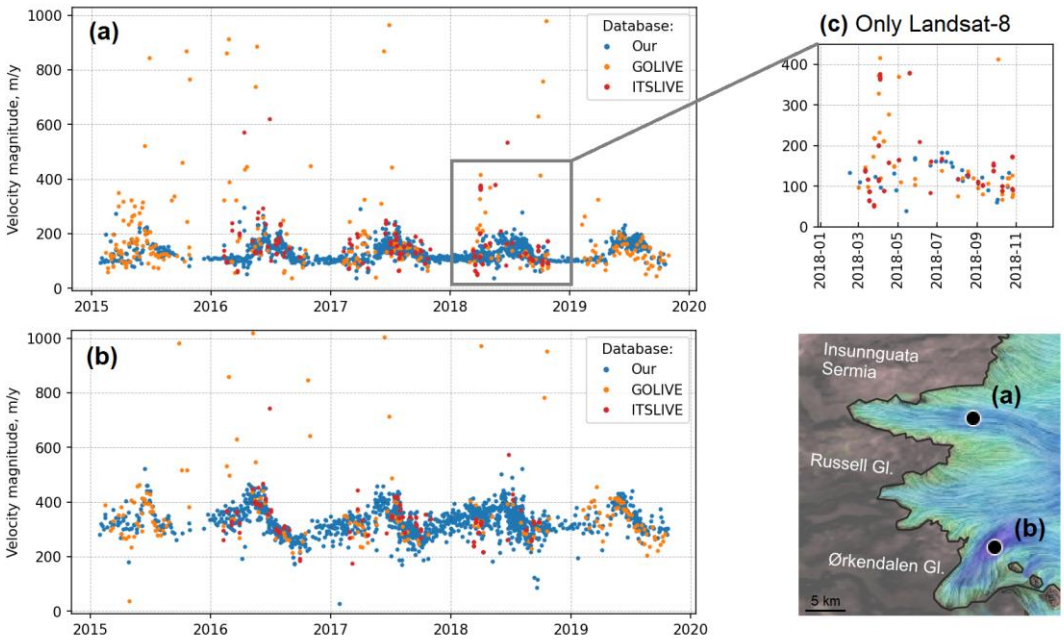

Figure 24 Comparison between speed time series processed by this study, GOLIVE and ITS_LIVE for two selected locations in the Russell sector: (a) Insunnguata Sermia; (b) Ørkendalen Gletscher. (c) The extraction of (a) subpanel with only Landsat-8 derived measurements.

2.2.3.4 Seasonal direction deviation

In some specific regions, we noticed that our time-series are affected by an important seasonal deviation of ice flow direction. The effect manifests as a change of average flow direction of about +30° in spring and -30° in autumn compared to summer/winter (Figure 25). The deviation persists even in the biweekly averaged velocities constructed from all available measurements in 2015-2019 (Derkacheva et al., 2021). It seems very unlikely that these observations of flow direction fluctuations would actually be provoked by large changes of the glacier ice flow. In addition, it appears that this effect affects only the optical results, and the radar Sentinel-1 does not display such variability. Among our three case studies, it clearly affects the major part of the Russell sector which is mainly flowing along the east-west direction with the speed range of 50-250 m/yr and the slow flowing parts of Upernavik (outside of the main streams) which are also flowing along the east-west direction. However, it is not observed for Petermann Gletscher that flows along the south-north direction or for Upernavik's outlet glaciers which follow the east-west direction with a speed of more than 2 km/yr).

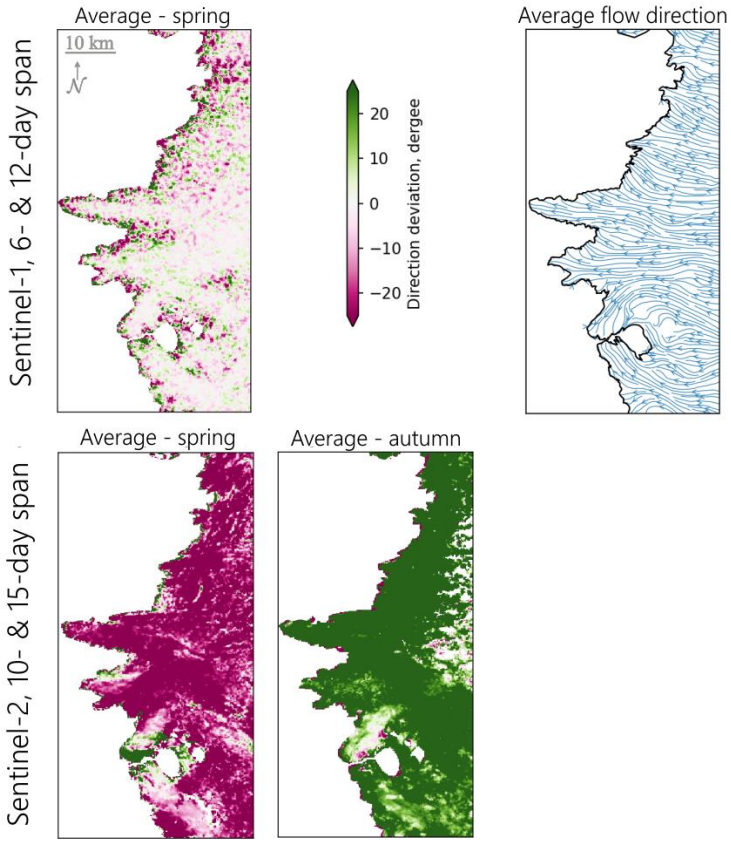

Figure 25 Direction deviation between a multi-annual database average and the radar Sentinel-1 or optical Sentinel-2 data in spring or autumn. Right: the average flow direction.

The origin of the problem could be in our processing workflow. For instance, radar and optical images are processed in their proper geometry and the derived maps are retranslated later into the required projection, which is accompanied by affine transformation of the velocity vectors. To verify this idea, the comparison with externally-processed optical databases is necessary. As we demonstrated in Section 2.2.3.3, there are no suitable sources for a proper comparison. Another possible reason for this issue could be the optical/radar nature of the data and the **sensitivity of our tracking algorithm to the changing illumination geometry** due to different solar elevation between the master and the slave images. We assume this assumption to be correct and demonstrate below how it may work.

To the best of our knowledge, no previous studies mentioning this kind of remote-sensing observations of the seasonal flow direction deviation in the literature. Only once, a theoretical remark was done without actual observations of this effect (Berthier et al., 2005). There could be two reasons why this effect is not mentioned in the literature: first, ice velocity datasets that resolve seasonal time-scale have just started to appear; second and even more important, specific ice flow conditions are required. As shown in Figure 25, the problem appears in spring and autumn in the optical measurements for areas with a relatively slow speed range (<100m/yr) and a dominant east-west flow orientation. At the same time, it is absent for all time and all regions in the radar velocity maps examined alone. Remember, that optical data dominate in our multi-sensor database in all seasons except winter, that is why the issue is observed even in all-data biweekly averaged maps.

The optical data are sensitive to the sun illumination geometry that defines the brightness distribution as well as the shadow locations and lengths. Thanks to this it is possible to derive the surface topography using photoclinometry methods from a single image for the surface displaying a homogeneous albedo (Dulova et al., 2008; Tang et al., 2019). As the sun elevation changes through the year, the surface illumination and the shadows can drift between the master and slave images, which may impact the estimation of the ice velocity. Such drift is assumed to happen along the South-North axis and to be relatively minor, but enough to influence v_y velocity component when it is close to zero and v_x component is also moderate. Depending on the time of year, the sun would be rising or falling between the master or slave images and so the displacements v_y in spring and autumn would go in opposite directions and symmetrically around the "true" value. Thus, the Sentinel-2 velocity maps (Figure 25) show the deviation from the mean v_y speed of about +50 m/yr and -40 m/yr in early spring and late autumn, respectively, while v_y derived from SAR always stays around +10 m/yr.

Figure 26 illustrates how the hypothesized mechanism would work. Note that even if the size of individual shadows is typically below the image resolution, the overall illumination of the surface changes, and this could be intensified by a local surface slope or crevasses geometry (Konig et al., 2001). The tracking algorithm "connects" similar features/patterns in the images from two consecutive dates *d1* and *d2* (master and slave images) with a velocity vector *v*. As the length *l* of a shadow depends on the date, it will differ at *d1* and *d2*. Thus, supposing a flow exactly along the east-west direction, the vector *v* will include a north-south component equal to $\Delta l = l(d1) - l(d2)$, which corresponds to a flow direction deviation a_v. In the northern hemisphere, this implies a deviation a_v towards the south in spring and towards the north in autumn; the relatively "true" flow direction can be observed around the winter and summer solstices due to the minimum sun elevation change over time.

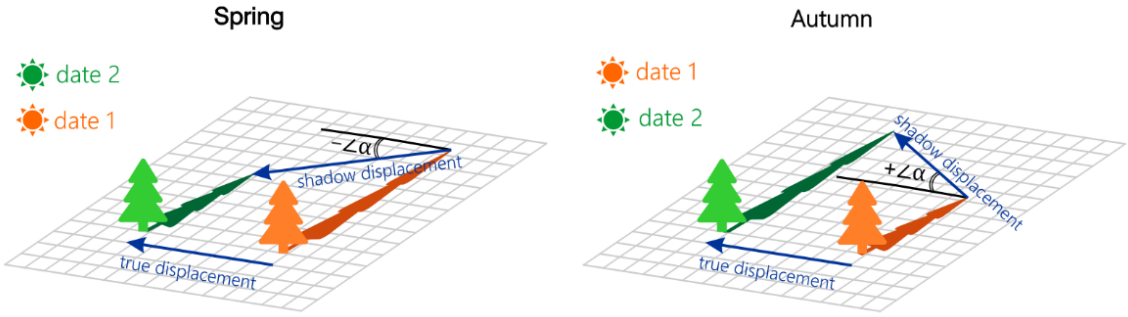

Figure 26 Scheme of the measured flow direction deviation induced by sun elevation change and shadows displacement from master to slave images. Sun ascent (left) and descent (right) cases.

To estimate the possible range of deviation induced by this mechanism, we compute the amplitude of this effect on a synthetic case at the Russell site latitude, for Sentinel-2 images taken on April 1st (*d1*) and 10th (*d2*) at 10 a.m., of a glacier flowing at 150 m/yr exactly along the east-west direction. Between these two dates, the sun elevation changes from 22.75° to 26.21°. For an isolated 1-m bump at a flat surface, Δl will therefore differ by 0.35 cm between *d1* and *d2* (equivalent to a speed of 12.7 m/yr), which corresponds to a deviation a_v of about 4° of the "measured" velocity. For an object or a surface undulation 3 m high, Δl would exceed 1 m and a_v

becomes about 13°. For a 5-m hill, the shadow length changes from 9 to 12 m, becomes comparable with S2 pixel size, and the a_v is 33° (or 12° between 1st to 20th April for the same conditions). It is worth noting that the deviation generated by similar conditions but in June-July would only be about 1-2°. Taking into account that a real glacier's surface is multi-bumpy, cracked, and inclined, even more significant influence of the shadow displacements can be expected over the favorable east-west oriented slopes, and the amplitude and direction of the deviations observed on the Russell sector correspond well with those theoretical values (Figure 25).

For the demonstrated Russell sector example, the resulting error in the velocity magnitude is estimated to be several times smaller than the other source errors in the final data and therefore can be neglected. Nevertheless, we have thought about the ways to correct this issue that affects the optical datasets. The ways to properly deal with it are not so trivial as they would include in an extreme case the image radiometric correction for light scattering on small-scale topography features. One of the easiest ways would be to assume that the flow does not change in direction over a year and use only the magnitude, imposing the flow direction found during the period when the effect is minimal. Such an approach would be suitable for the majority of glaciers if the flow direction does not change naturally over time.

It is important to highlight that, although the conditions required for direction deviation seem to be very specific, vast areas in Greenland could meet them and be affected by this bias. Indeed, many glaciers on the Western flank have the east-west orientation of flow and, being land-terminating like Russell, move with an average speed of one to two hundred meters per year. With the increasing number of the similar seasonal-scale datasets, the described issue should be carefully addressed.

2.2.4 Post-processing of dense ice velocity time-series

We demonstrated above that our multi-sensor multi-cycle database integrates together a large amount of velocity measurements where the seasonal signal is clearly visible even for slow moving regions. Usually, for a given location, a large and frequent number of measurements are available closely in time. At the same time, the uncertainty of individual observations remains significant and varies depending on the sensor or the considered repeat cycle. They are higher for the shorter time spans which are more useful to resolve the rapid flow speed fluctuations, and became significantly large compared to the speed magnitude in the slowly-moving regions. Taking advantage of the frequent sampling, it is possible to develop post-processing methods that can be used to significantly increase the quality of signal presented in our ice velocity time-series. Thereby, we tested, validated and applied post-processing algorithms on the "raw" velocity observations before moving towards their analysis.

The detailed study of several tested post-processing methods, their performance regarding our goal of investigating the seasonal-scale ice flow dynamics, and the quality estimation of the final post-processed time-series was published in Derkacheva et al. (2020). This paper is presented below.

remote sensing

MDPI

Article

Data Reduction Using Statistical and Regression Approaches for Ice Velocity Derived by Landsat-8, Sentinel-1 and Sentinel-2

Anna Derkacheva [1,*], Jeremie Mouginot [1,2], Romain Millan [1], Nathan Maier [1] and Fabien Gillet-Chaulet [1]

[1] Institut de Géosciences de l'Environnement—Université Grenoble Alpes, CNRS, IRD, INP, 38400 Grenoble, Isère, France; jeremie.mouginot@univ-grenoble-alpes.fr (J.M.); romain.millan@univ-grenoble-alpes.fr (R.M.); nathan.maier@univ-grenoble-alpes.fr (N.M.); fabien.gillet-chaulet@univ-grenoble-alpes.fr (F.G.-C.)

[2] Department of Earth System Science, University of California, Irvine, CA 92697, USA

* Correspondence: anna.derkacheva@univ-grenoble-alpes.fr or der_a@mail.ru

Received: 20 May 2020; Accepted: 11 June 2020; Published: 15 June 2020

check for updates

Abstract: During the last decade, the number of available satellite observations has increased significantly, allowing for far more frequent measurements of the glacier speed. Appropriate methods of post-processing need to be developed to efficiently deal with the large volumes of data generated and relatively large intrinsic errors associated with the measurements. Here, we process and combine together measurements of ice velocity of Russell Gletscher in Greenland from three satellites—Sentinel-1, Sentinel-2, and Landsat-8, creating a multi-year velocity database with high temporal and spatial resolution. We then investigate post-processing methodologies with the aim of generating corrected, ordered, and simplified time series. We tested rolling mean and median, cubic spline regression, and linear non-parametric local regression (LOWESS) smoothing algorithms to reduce data noise, evaluated the results against ground-based GPS in one location, and compared the results between two locations with different characteristics. We found that LOWESS provides the best solution for noisy measurements that are unevenly distributed in time. Using this methodology with these sensors, we can robustly derive time series with temporal resolution of 2–3 weeks and improve the accuracy on the ice velocity to about 10 m/yr, or a factor of three compared to the initial measurements. The presented methodology could be applied to the entire Greenland ice sheet with an aim of reconstructing comprehensive sub-seasonal ice flow dynamics and mass balance.

Keywords: ice velocity; time series; post-processing; data reduction; non-parametric regression; multi-sensor data

1. Introduction

Ice velocity is a key parameter for understanding of glaciological processes and thus is necessary for the projection of glaciers under climate change. The ice flow measurements are used to study ice speed variability [1,2] and the external drivers of that variability, such as terminus position [3,4], or to identify relationships between glacier speed and seasonal forcings, such as air temperature or runoff [5–7]. Furthermore, these measurements are necessary in order to determine the mass balance of ice sheets [8,9], are needed to evaluate the ice thickness through mass conservation techniques [10], serve as an input to numerical models, and are used to validate modeling studies [11,12]. As ice flow models are highly non-linear, surface ice velocity fields over large scale representing the tridimensional displacement of the ice are an essential observable to constrain them.

Between 1990 and 2010, the advent of spaceborne remote sensing allowed for the collection of large amounts of data over isolated places, such as ice sheets and generation of the first comprehensive mapping of the ice sheet dynamic [13–15]. Since about 2010, we have entered a new era where spaceborne observations are becoming routinely available. A new generation of medium-resolution optical sensors such as the American Landsat-8 and the European Sentinel-2, and the European synthetic aperture radar Sentinel-1 were launched, allowing for frequent observations of ice sheets and glaciers over large areas [16–21]. This increase in the spatiotemporal coverage is needed to capture the ice flow changes occurring at time-scales of a season, which is critical for our understanding of the physical processes controlling glacier dynamics. Indeed, changes in ice flow have been identified on monthly to weekly timescales when they are are relatively pronounced [2,3,22]. However, recent studies [19,21,23] have shown that it remains challenging to capture subtle changes in ice flow by using single individual measurements from these sensors and correlation techniques due to the relatively high uncertainties associated with the medium resolutions (∼10 m) and short revisit times of these sensors. In addition, each sensor is measuring displacements with its own unique characteristics (e.g., space resolution, time repeatability, etc.), making it difficult to combine the data from different platforms with different resolutions and repeat cycles. This is an important issue to overcome to create datasets of ice flow with high temporal resolution [24].

Data reduction is the transformation of empirically or experimentally derived numeric information into a corrected, ordered, and simplified form. Here, we explore the effectiveness of different regression methods used to perform data reduction on the cross-platform satellite-derived ice speed datasets. Our study area is a land-terminating sector around Russell Gletscher located along the southwest coast of Greenland. Ice motion is relatively slow here, with mean values of about 100–150 m/yr in winter. Further, strong decorrelation occurs in image matching algorithms due to surface saturation and the widespread presence of melt water in summer. Together, these factors make the retrieval of seasonal velocity variations quite challenging compared to many other sectors of Greenland. As a result, satellite-derived speeds have a relatively low signal to noise ratio, and thus statistical and regression methods may be useful for reducing the noise of the data.

In the following sections, we first describe the study area, the methodology used to derive the ice velocity from multiple satellite sources, and how we assemble them into a coherent database. We then explain the different regression methods applied to our datasets (rolling average, linear non-parametric local regression LOWESS, and cubic-spline regression), and compare their results with in-situ GPS measurements of ice velocity made in this sector of the ice sheet. We discuss further the results in terms of accuracy, robustness, temporal resolution, and limits. Finally, we conclude on the potential of such data reduction approaches for use in glaciological studies.

2. Data

2.1. Study Area

We focus our analysis on a land-terminating sector located along the southwest coast of Greenland at a latitude of 67°N and longitude of 50°E. The sector ends in multiple ice tongues, named from north to south: Insunnguata Sermia, Russell Gletcher, Ørkendalen Gletscher, Insorlersuup Gletscher (Figure 1). This is one of the most studied regions of Greenland due to the relatively easy accessibility from the town of Kangerlussuaq.

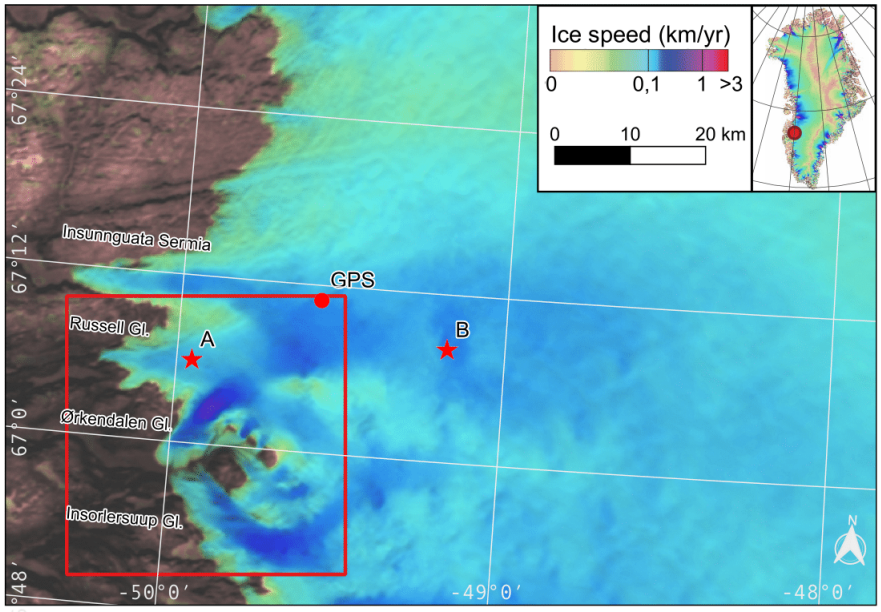

Figure 1. Mean ice velocity in Russell area, from [19]. Red stars indicate the locations for the points A and B mentioned in Sections 2.3 and 4.2 and Figures 4, 9 and 12; red circle indicates the GPS location mentioned in Sections 2.4 and 4.1 and Figures 5, 8, and 12. The red square indicates the location of maps in Figures 10 and 11.

The outlet glaciers in this region flow with speeds ranging from 100 to 250 m/yr during winter, while the surrounding regions display ice speeds around 50–60 m/yr in winter. Seasonal ice speed fluctuations have been observed in a number of studies in this region. They are commonly attributed to pressure changes in the subglacial drainage system [6,7,25–28]. When spring melt begins, ice speeds typically increase due to an influx of meltwater into the subglacial drainage system, which raises the subglacial water pressure and reduces the basal friction [25]. Ice speeds decrease later in the melt season (sometimes below its spring value) as the subglacial drainage system adapts with the establishment of efficient channels which accommodate the melt and so reduce water pressure at the bed. For the large area near the ice margin of the Russel sector, large accelerations from 100 to 250% above the winter mean, with the measured maximum of 360% in small isolated patches, have been reported [6].

2.2. Satellite-Derived Velocity Data

We use a combination of ice velocity measurements derived from satellite images collected between 2015 and 2019 by Landsat-8, Sentinel-1, and Sentinel-2. Landsat-8 (L8) is an American Earth observation satellite launched on 11 February 2013 by USGS and NASA as a continuation of the Landsat program started in 1972. The Operational Land Imager (OLI) on-board Landsat-8 acquires global moderate-resolution images (15 m for panchromatic channel or 30 m for spectral) in the visible and infrared parts of the spectrum with a revisit time of 16 days between 82.7° north and south latitude. Images are provided as geocoded products by USGS, either in UTM or polar stereographic coordinates. Optical imaging requires solar illumination, and correspondingly there are a large number of acquisitions during austral and boreal summers and few in winter.

Sentinel-2a and 2b (S2) are twin optical observation satellites developed under the European Commission Copernicus Program launched into orbit in 2015 and 2017 respectively by the European

Space Agency (ESA). They provide moderate-resolution multi-spectral images of Earth similar to that of Landsat-8. Images in 4 spectral bands (blue 490 nm, green 560 nm, red 670 nm, and near infrared 850 nm) are provided with 10 m resolution in UTM projection. Together the Sentinel-2 satellites have a revisit time of 5 days. Similar to L8, most of the acquisitions are made during the summer season when there is solar illumination.

Sentinel-1a was launched for the Copernicus Program by ESA on 3 April 2014, and was joined along the same orbit by Sentinel-1b on 25 April 2016. Sentinel-1 (S1) is a right-looking synthetic aperture radar (SAR) mission, observing with an incidence angle ranging from 29.1 to 46.0°. S1 is a C-band radar with a revisit time of 12 days per satellite and 6 days with the constellation. Acquisitions over land are made with the interferometric wide swath (IW) mode using progressive scans SAR (TOPS) technique. Using Gamma Software gamma-rs.ch, the bursts are de-ramped from their Doppler history and mosaicked together to form a single-look complex image with a ground resolution of 20 m in azimuth and 5 m in ground range [29]. Following the recommendations by PSTG, Sentinel-1 has acquired data continuously since June 2015 across a set of six tracks that cover the entire coast of Greenland, including the area of Russell Gletscher.

We use persistence surface features or speckle to track ice displacements between two images over the ice sheet [16,30,31] for optical data. We use the same methodology as presented in [19,23] to calculate a standardized cross-correlation between the reference image chip and the slave chips, which is based the Fortran code of `ampcor` [32]. For L8 [16], S2 [23], and S1 [18], sub-images of 32×32, 32×32, and 192×48 pixels are used respectively. The displacement maps in pixels are then converted to glacier surface velocity in meters per year and geocoded using the north polar stereographic projection. The final calibrated maps (see Figure 2) are resampled to a resolution of 150 m/pix; no spatial smoothing is applied at any of the steps for estimating speed. The x and y components of velocity in meters per year are stored independently as GeoTiff. We use the GDAL library gdal.org for all geographical transformations and formatting of the final files.

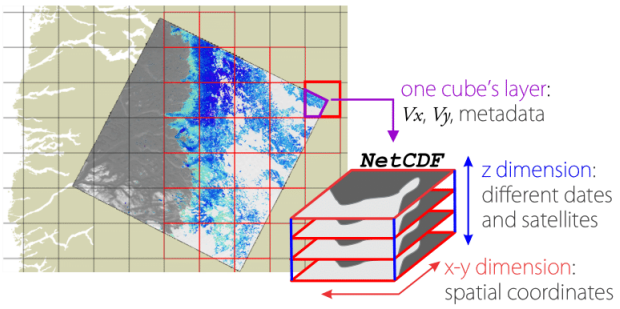

Figure 2. The schema of the cubes storage approach. On the left part: A preview of the speed map derived from the Landsat-8 18 September 2018 (master image) and 2 September 2018 (slave image) superposed on the outline of Greenland drawn with olive color. The black squares represent the entire regional cube grid; red squares are used to store the data from that particular image. On the Landsat image green and blue correspond to the successful speed estimation; black and white correspond to the areas without derived speed due to the ice-free ground or algorithm failure. On the right part: one NetCDF file consists of many layers (z dimension) that all cover the same area and correspond to the ice speeds derived from different images dates and sensors.

The estimated precision for the nominal cycle is about 50 m/yr, 40 m/yr, and around 20 m/yr for L8, S2, and S1 respectively, as reported by [19,21,23]. Shorter intervals are more sensitive to errors that are uncorrelated in time, such as those caused by the atmosphere or ionosphere, or errors from the correlation algorithm since surface displacement data are scaled by the observation interval used to

derive velocity. The entire range of velocity errors in our data varies from about 50 m/yr (nominal L8 cycle) to 5 m/yr (24-days S1 cycle).

2.3. Ice Velocity Database Creation

To facilitate post-processing, our velocity maps are divided into areas of equal size of 37.5 × 37.5 km with a resolution of 150 m (thus 250 × 250 pixels). For each area, we extract and stack the velocity maps and associated metadata into "cubes" where the 3rd dimension z corresponds to the number of calculated speed maps (Figure 2). To avoid edge problems during post processing, the cubes overlap by 5 pixels (750 m). Each cube is a standardized dataset where all maps are stored on a common grid and the time series of the surface velocity can be easily extracted to calculate time-averaged maps or apply time-oriented post-processing. The cubes are stored in the GDAL-compatible netCDF format following the Climate and Forecast metadata conventions cfconventions.org. A cube file contains metadata about the cube itself (dimensions, corner coordinates, number of speed maps, etc.), surface velocity maps in meters per year in x/y directions (v_x and v_y hereafter), associated errors, projection information, processing directory of source images, dates of master and slave images, repeat cycle, and sensor name.

ϵ_{v_x} and ϵ_{v_y}, which are the errors on v_x and v_y respectively, are independent in our processing chain. For the optical imagery with isotropic resolution, they are identical. However, in the case of Sentinel-1, we have a large difference between ϵ_{v_x} (east-west) and ϵ_{v_y} (north–south) components. This is due to the difference in pixel size between the azimuth and range and the fact that S1 tracks are more closely aligned with the north–south direction. The error on ice speed magnitude v is calculated as $\epsilon_v = \sqrt{v_x^2\epsilon_{v_x}^2 + v_y^2\epsilon_{v_y}^2}/v$.

We use speed measurements with time intervals shorter than 32 days (1 month) in order to capture rapid dynamic changes in ice flow, meaning that we use 16 and 32 day repeat cycles for L8, from 5 to 30 days for S2, and 6 to 24 days for S1. Longer time intervals would provide more precise velocity measurements but at the expense to temporal resolution, thereby limiting our ability to capture the seasonal velocity fluctuations we are interested in.

More than several hundred velocity maps per year can be obtained in our region of interest over the mentioned time spans, but the spatial coverage varies with sensor, location, and season: an example for year 2018 is given in Figure 3. The region above the equilibrium line about 30 km from ice margin has the poorest coverage because the surface is smooth and only a few surface features can be tracked with optical imagery. In this area, the S1 provides more measurements because the speckle tracking of SAR images does not require recognizable features on the glacier surface (e.g., crevasses) but is nevertheless limited by current acquisition plans that focus on marginal areas.

In summary, S1 is the main data source during the cold season (from November to April), particularly in the ice-sheet interior. However, its correlation drops significantly near the margin during the warm season when the glacier surface experiences melt. S2 and L8 optical sensors provide good correlation results along the ice margin where many surface features can be found, but perform poorly further inside the ice sheet where less features can be found, and provide no observations during the polar night (December-January) due to the absence of solar illumination.

Nevertheless, using the combination of all 3 sensors, we obtain a dense time series of ice surface velocity that allows us to investigate the seasonal ice flow dynamics. In Figure 4, we plot the time series for 2 different locations (point A and B, see Figure 1) with associated errors from January 2015 to September 2019 derived with 1308 (point A) and 908 (point B) individual velocity estimates by Sentinel-1, Landsat-8 and Sentinel-2. These time series are then used to evaluate the efficiency of different regression algorithms to create regularly sampled, filtered, and coherent time series of ice motion with reduced noise.

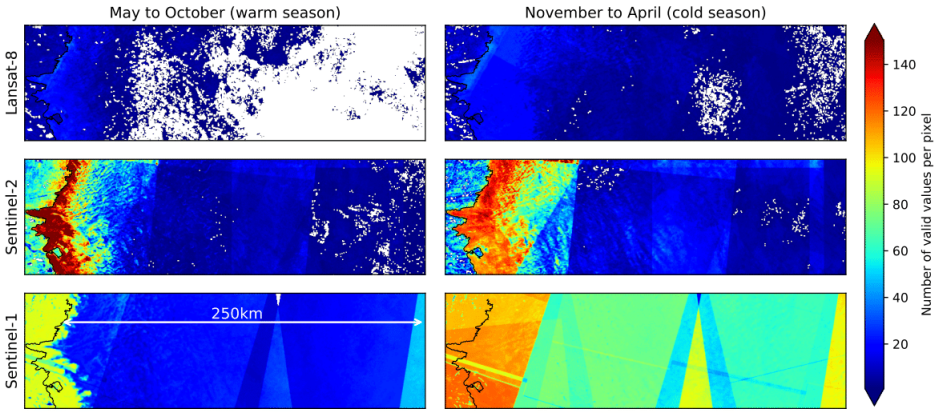

Figure 3. Number of valid speed estimates for year 2018 using Landsat-8, Sentinel-2, and Sentinel-1 sensors over the region of Russell Gletscher, West Greenland. White areas correspond to locations with no successful correlation between image pairs.

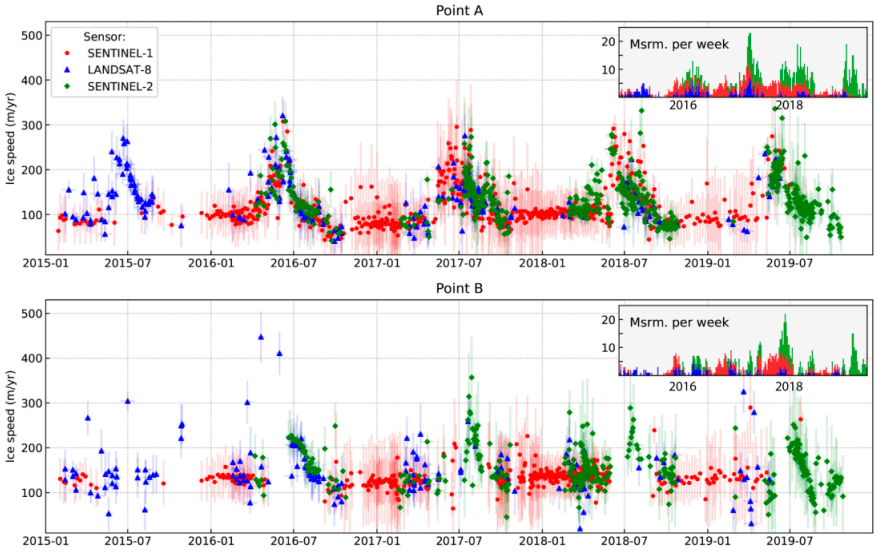

Figure 4. Velocity measurements from Landsat-8 (blue), Sentinel-2 (green), and Sentinel-1 (red) for 2 different locations (67.099°N, 49.953°W and 67.134°N, 49.177°W) as indicated by red stars in Figure 1. Vertical bars correspond to the estimated errors and horizontal bars correspond to the time-span between master and slave images used for tracking the displacement. Sub-plots show the number of available measurements per week; colors and temporal extent (*x*-axis) are the same as the main plot.

2.4. In-Situ GPS Measurements

We compare our satellite-derived speed measurements with GPS in-situ data made in one location between 15 July 2014 and 14 July 2017 collected as part of an ice dynamics study [33]. When first set up in July 2014, the GPS was located at the position 49.567°W and 67.182°N and moved by about 371 m over the course of the 3 years. GPS position was measured every 15 s, except when the system ran out of power during the winters. From the registered GPS locations we compute mean daily displacements (Figure 5), and then average them over 3 weeks to be comparable with our dataset (see Section 5.4 and Figure 8).

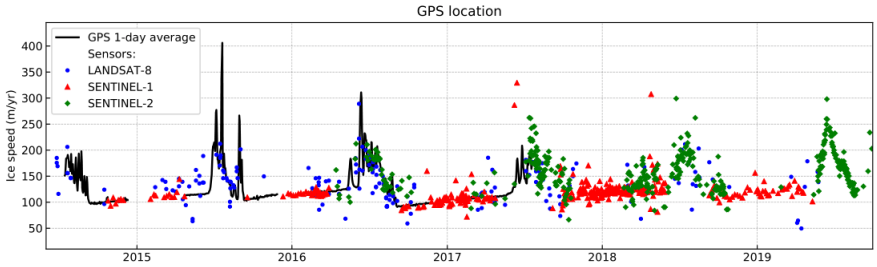

Figure 5. Ice velocity measurements from in-situ GPS station (black line) [33] and from satellite systems (colored dots) derived by us for location 67.182°N, 49.56°W as indicated by red dot at Figure 1. The color-coding for sensors is the same as in Figure 4.

3. Velocity Post-Processing/Data Reduction

The velocity dataset from multiple sensors contain a large number of incorrect or noisy displacements superimposed on the real variability of the ice flow. Despite the noise, sub-seasonal fluctuations in speed are clearly captured by Landsat and Sentinel satellites (see Figures 4 and 5). Here, we take advantage of dense data series and try several types of post-processing with the final goal of producing a filtered, continuous, and coherent time series of velocity with reduced noise compared to the individual measurements.

As detailed previously, we have generated ice speed data cubes from S1, S2, and L8 data, where every measurement is stored on a common spatial grid and the 3rd dimension corresponds to the discrete irregular time interval of the measurements. Thus, each pixel contains a velocity time series. For each time series, we independently apply and compare three different approaches of data smoothing and noise reduction: statistical rolling mean and median, cubic spline regression, and linear non-parametric local regression to obtain continuous filtered time series. The date of each measurement is assigned as the center between the first and second satellite images dates in the velocity estimation pair. Thus, we do not take into account the disparity of time spans of derived velocity (from 5 to 32 days). The regressions are performed on v_x and v_y separately, but implementation of regressions on the velocity magnitude v and direction a are discussed as well (see Section 5.2). We describe three data reduction approaches in detail in the following sections.

3.1. Rolling Mean or Median

Rolling mean, also called moving average, is the most simple statistical approach used to analyze series of ordered data. We use a weighted mean with the weights defined for each measurement individually as $1/\epsilon^2$, where ϵ is the error associated with a source velocity map. The increased size of the data subset used for the mean decreases the final error at the expense of the temporal resolution. Different subset sizes were tested from 1 to 4 weeks (see Sections 4.1 and 4.2, Figures 8 and 9a,b) to assess which subset sizes is best suited for our datasets.

Ice velocity sampling is not uniform in time (as explained in Section 2.3). There are periods with fewer measurements, which was the case before 2016, but more recent years have had more frequent sampling. Moving average generally implies that the time-series is continuous and evenly spaced in time, which is not the case for our time series. We note that having measurements that are not uniformly spaced across a subset window can introduce a bias in the final average.

From a statistical point of view, the moving average, when used to filter a time series, is likely to be biased by anomalies (outliers). A more robust estimate would be the rolling median with the disadvantage of not being able to use different weights depending on the measurement errors. We also tested the rolling median method and obtained the results that are very similar to the weighted rolling mean. Thus, only the rolling mean results are used in our analysis.

3.2. Linear Non-Parametric Local Regression: LOWESS

Locally weighted scatterplot smoothing (LOWESS) is a moving non-parametric regression that fits a regression model on the k closest samples. Local regression is a statistical method for robustly fitting smoothing curves without prior assumptions about the shape or form of the curve. This algorithm, which was specially designed for noisy and scattered datasets, was introduced by W.S. Cleveland in [34], and was further developed in [35]. It is now used for a wide range of applications, including the noise reduction in satellite derived measurements, most commonly for studies of seasonally evolving vegetation [36–38]. The basic principle of the method is to the fit the data points (independent variables) using a linear or quadratic function in a moving fashion analogous to that used for a moving average applied to a time series. The mathematical concept is illustrated in Figure 6. As shown in the sub-panel of Figure 6, a regression is performed using a low-order polynomial function on a localized subset of data centered around a particular point in the data series. The k closest neighboring points participate in the regression estimation with specific weights. The weighting is based on the idea that close points are more likely to be linked together in a simple way than distant points. Following this principle, greater weight is given to the points that are close to the local value. The procedure can be repeated several times; new weights are estimated, allowing one to remove outliers from the final solution, as illustrated with the green point in Figure 6. Depending on correspondence between data density and the subset size, some potentially correct measurements could be interpreted as outliers and ignored in the final solution, as with the orange point in Figure 6). These local regressions can be performed at any specified locations or for each input point. The final curve is the merge of all local regressions.

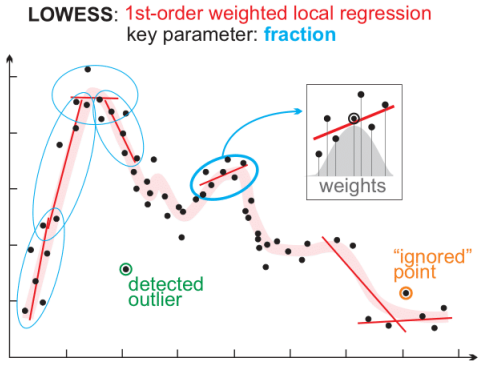

Figure 6. Principles of LOWESS (locally weighted scatterplot smoothing) method for a 1st-order polynomial. Black points are the source data; red narrow lines are the local regression solutions; the thick rose line is a final LOWESS solution. The gray area on the sub-panel represents a weight-defining function.

Here, we use the algorithms from Scipy has2k1.github.io/scikit-misc/ and Statmodels statsmodels.org adapted in Python by P. Gerard-Marchant. The first can provide additional statistics that are useful for experimental testing; however, the second seems to perform better for intense computation, and is therefore more useful given the large number of regressions performed in our analysis.

There are four key parameters that can be defined in the LOWESS algorithm. The fraction f, that is comprised between 0 and 1, defines the amount of smoothing and corresponds to the fraction of the time-series that is used for each local regression. Thus, large value of f will use more data points for each local estimation and provide a smoother solution, while a small value will reduce the number of data points used and so allows the regression to be closer to the initial data.

The weights w applied to measurements at each regression can also be specified. In the original paper [34] the author defines the optimal choice is a bell-shaped cubic function that gives maximum

weight to the closest points and diminishes quickly to zero with the distance from the evaluated point (as the gray-colored area represents on the sub-panel at Figure 6). This is an option by default for Python LOWESS implementations. Additionally, user-defined weights can be introduced into the `skmisc.loess` code, and in our analysis are based on the source data errors. Similarly to the rolling mean, we tested a case of weights defined as $1/\epsilon^2$, where ϵ is the error associated with each data point. We obtain a negligible change of fitted values with no clear improvement, indicating that the default weighting system is sufficient to obtain robust regressions. Thus, these additional weights are not used in our further tests.

To address data anomalies, several iterations of LOWESS can be applied to re-estimate neighbors' weights to identify and eliminate outliers. While the initial weights of a local fit rely only on x-axis distance to the neighbors, during the LOWESS iterations, data subsets with the largest deviation range are excluded to find a state with minimal root-mean-square deviation.

Linear and quadratic local regressions cover most cases [34] and the polynomial order of the local regression can be set to 0, 1, or 2. Using a zero degree polynomial turns LOWESS into a weighted moving average.

In our processing, we use a linear function, as the quadratic regression tends to be less robust against noisy datasets. We use 3 iterations to obtain the most robust results [34]. Weights are defined by the default cubic function as given in [34], and no additional error-based adjustment of weights is applied. The best choice of the smoothing parameter f depends on our initial data and is discussed on the following section (see Sections 4.1 and 4.2, Figures 8 and 9c,d).

3.3. Cubic Spline Regression

A cubic spline is a piecewise function that interpolates a set of data points with third-degree polynomic between neighbors in the way to guarantees smoothness of fitted curve and closeness to the source data points [39]. Its mathematical principles are illustrated in Figure 7. The "piecewise" function means that it fits data subsets as in the rolling mean and LOWESS, and thus is not a global fitting function. For each data subset that contains two neighboring points a cubic function is fitted with a constraint to satisfy the continuity of the global solution and its first and second derivatives. Here, we use a cubic smoothing spline designed specifically for noisy observations. Contrary to interpolation cubic splines, cubic smoothing splines have additional functional constraints: (i) to minimize the squared error between the dataset and spline, and (ii) to minimize the curvature. These two constraints are controlled by the smoothing parameter f, which varies from 0 to 1. When $f = 0$, the spline regression performs infinite smoothing, which corresponds to a linear least-squares fit on the entire dataset. When $f = 1$, the curve is the natural cubic spline that passes through all initial points.

When an outlier is located in a zone well-populated by "true" points, it can be successfully ignored by the spline regression (green point in the Figure 7). However, when a portion of the time series is less frequently sampled, the cubic spline is less constrained and can create unrealistic overshoots (orange part of the line in Figure 7).

We use the cubic spline approximation with a customizable smoothing parameter and weights from CSAPS github.com/espdev/csaps, which is based on [40]. Weights are provided in the same way as for the rolling mean ($1/\epsilon^2$, where ϵ is the error attributed to speed measurements). The best parameter of f will depend on data density and distribution of outliers, and could therefore change between regions. In the following sections, we discuss this choice of f that provides the best regression on our time series (see Sections 4.1 and 4.2, Figures 8 and 9e,f).

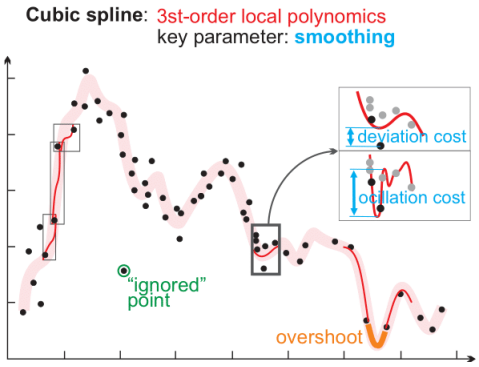

Figure 7. Cubic smoothing spline principles. Black points are the source data; red narrow lines are the local spline solutions; the thick rose line is a global spline solution for the smoothing parameter 0.05 (schema based on a real modeling).

4. Results

4.1. Comparison with GPS-Based Measurements

We first compare our initial and reduced ice speed time series with the 3-week moving average of ice speeds derived from GPS (Figure 8a). Over this averaging interval, the GPS best matches the satellite-derived data. (see Section 5.4 and Figure 12a). GPS ice speed is used as ground-truth since the velocity errors are less than 1 m/yr, while errors from satellite measurements are at best 7 m/yr and usually around 30 m/yr. The comparison is done by computing the root-mean-square error (RMSE) against the GPS for the individual measurements and then testing the sensitivity of different regression methods to parameter changes.

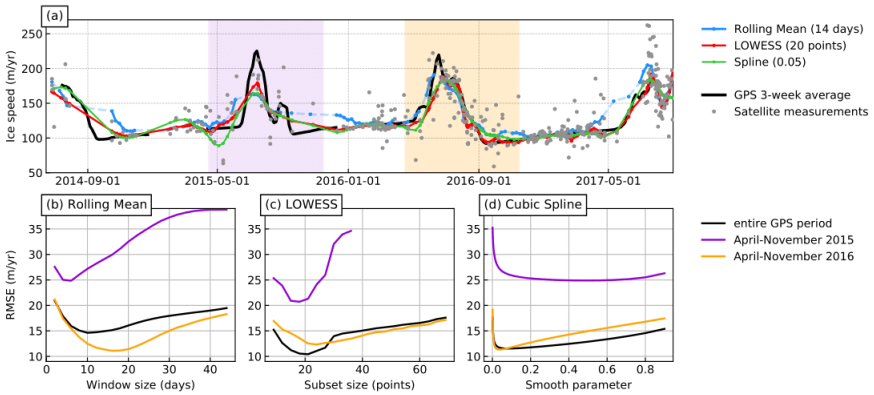

Figure 8. (**a**) Ice speed versus time from GPS (black line) and satellites (gray points) with reduction results (colored lines) from rolling mean, cubic spline, and LOWESS at the GPS location as indicated by the red dot at Figure 1. GPS-based ice speed is averaged over 3 weeks. (**b**–**d**) Root-mean-square error (RMSE) between ice velocity from averaged GPS and the different reduction approaches as functions of their adjustment parameters. For the rolling mean (**b**), LOWESS (**c**), and cubic spline regression (**d**), this adjustment parameter corresponds to the window size, the number of points in the subset, and the smoothing parameter, respectively. The black, violet, and orange curves show the RMSE for entire GPS period between 15 July 2014 and 14 July 2017, the part of 2015 for which few satellite measurements are available, and part of 2016 for which many satellite measurements are available, respectively.

We found that the RMSE of S1, S2, and L8 combined measurements versus 3-week moving average on GPS time series is about 27 m/yr when the entire time period is considered (see Figure 12a). For the data reduction methods, the minimum RMSE values (15, 12, and 10 m/yr) are found when the chosen adjustment parameters for the rolling mean, the cubic spline, and the LOWESS regressions, are a window size of 12 days, a smoothing parameter of 0.05, and a subset of 20 points, respectively (Figure 8b–d). We note that: (i) the RMSE is improved by the regressions compared to the original measurements, and (ii) LOWESS provides the best RMSE compared to the rolling mean and cubic spline.

We also tested two shorter periods, one from 15 April 2015 to 15 November 2015 and another from 15 April 2016 to 15 November 2016 (violet and orange colors respectively in Figure 8). These periods are both characterized by important speed fluctuations (while speeds are almost constant during winter) but differ by the number of acquisitions made, with only 38 for the first and more than 102 for the other. For the second period (2016), the RMSE is improved by a factor of two compared the first period. This shows the improvements gained by increasing the number of acquisitions in order to more precisely capture the seasonal variability. We also found that when the number of observations is low and they are not equally distributed through the time LOWESS performs better than the rolling mean and the cubic spline regression.

4.2. Time Series Post-Processing

Figure 9 presents the results using the different reduction methods on our time series for two locations (point A and point B) as shown at Figure 1. Point A (67.099°N, 49.953°W) is located relatively close to the ice-sheet margin in an area of relatively fast flow. This area experiences strong summer acceleration (see Figure 4). Winter speed from October to May is around 100 m/yr, with a minimum in October that increases slowly until May. In general, summer speed-ups start gradually in May and end in mid-July, and the maximum speed is about 170–200% faster than winter speeds, which equates to 270–300 m/yr. During the summer season, many surface features are present, allowing the correlation using optical sensors to work well, resulting in a dense velocity time-series. However, only S1 provides observations during winter.

Point B (67.134°N, 49.177°W) is located about 40 km from the ice margin in a flat smooth area with less surface features. This impacts the ability of the optical sensors to capture ice displacement during all seasons. Nevertheless, we found that, at this location, winter speed is around 120 m/yr and ice flow increases by about 70 to 90% during the summer season. The evaluation is more challenging than for point A because of fewer successful measurements during the melt season; however, it seems that the maximum ice speed is reached around mid-July which is later than for point A (mid-June).

Figure 9a,b presents the results of the weighted rolling mean using averaging windows of 2, 3, and 4 weeks. The rolling mean provides relatively good regression when the frequency of measurements is high. It is however impacted by outliers, which is especially true for point B where the speed magnitude sometimes jumps by hundreds of meters per year for periods with sparse and noisy measurements. As expected, by increasing the size of subsets used for averaging, we obtain a more robust results at the expense of temporal resolution. Given the data noise and time interval between master and slave images (5 to 30 days), a realistic balance between robustness of the regression and time resolution seems to be 3 weeks for dense time-series (as in location A), similar to the comparison made against GPS. However, we note that for sporadic time-series, even a window of 1 month is sensitive to outliers, as seen during July 2015 or 2016 for point B.

Figure 9c,d show the result for the LOWESS regression using various fraction parameters, corresponding to subsets used for the regression with 10, 20, and 50 points. Using the largest subset size (50 points) provides a smooth result at the expense of temporal resolution, while the smallest subset size (10 points) is less constrained and is sensitive to data noise. As expected, 50 point subsets tend to underestimate the amplitude of the summer speed-up the most. Therefore, the best comprise seems to be a fraction parameter using 20 points.

Figure 9e,f presents the cubic spline regressions for different smoothing parameters. Using a large value ($f = 0.5$, e.g., less smoothing) helps to capture the rapid accelerations during the summers, as seen for point A (Figure 9e). However, it also generates deep and unrealistic velocity deviations (overshoots) when few measurements are available as for point B (Figure 9f). On the contrary, using a low value ($f = 0.001$, strong smoothing) tends to provide a robust regression that is not impacted by the outliers but comes at the expense of temporal resolution and capturing the amplitude of the speed variations. An intermediate smoothing value around $f = 0.05$ seems to provide the best compromise between resolution and outlier impact for both locations.

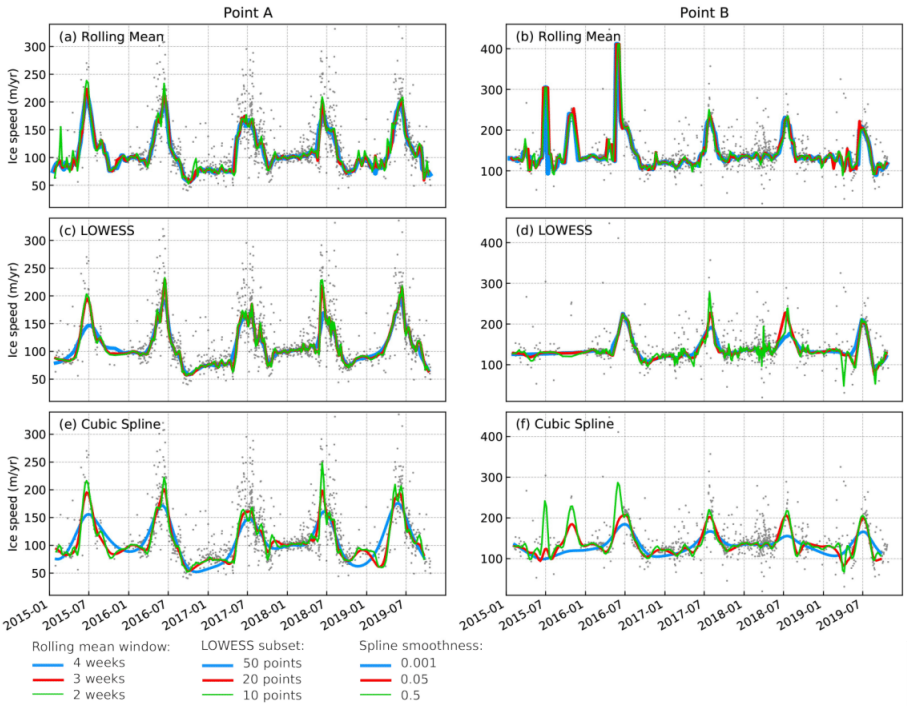

Figure 9. Statistical and regression approaches applied on our time series of ice velocity. (**a**,**b**) Rolling mean using subset window sizes of 1, 2, and 4 weeks on our time series. (**c**,**d**) Moving non-parametric regression (LOWESS) for different fraction parameters f corresponding to subsets of 10, 20, and 50 measurements applied on our time series. (**e**,**f**) Cubic spline regression using a smoothing parameter of $f = 0.001, 0.05, 0.5$. Left column correspond to the time series in point A and right column for point B as indicated by the red stars in Figure 1.

The data reduction using statistical and regression methods provides ice velocity in a corrected, ordered and simplified form. All tested methods using the fit with their optimized parameters more or less capture the seasonal velocity variations. Their solutions are very close when the source data are well populated, evenly distributed over time and contain few outliers as for point A (Figure 9). However, differences appear when times-series are less populated, like for point B (Figure 9). At this location where fewer and often noisy measurements are obtained, the simple statistical regression using rolling mean is much more sensitive to outliers, while more complex regressions such as spline and LOWESS still provide robust reconstructions. Point B is representative of results obtained in the ice-sheet interior.

Cubic spline seems less appropriate than LOWESS, especially in case of sporadic and noisy data. Indeed, we observe clear overshoot effects on the cubic spline solutions when the number of

measurements is limited, such as during February 2019 for point A or before January 2016 for point B (Figure 9), whereas LOWESS converges to a more realistic solution. This is also confirmed by the comparison with the GPS ice speeds, where the best RMSE is obtained by the LOWESS algorithm (Figure 8).

In Figure 10, we present the results in June and December of years 2016, 2017, and 2018 using the best adjustment parameters found previously for a complete data cube shaped as described in Section 2.3. The cube consists of 250 × 250 pixels corresponding to an area of 37.5 × 37.5 km (red square in Figure 1); thus, there are 62,500 regressions done for each approach. The black line corresponding to the ice margins delimits the boundary between ice-free (to the left) and ice-covered (to the right) area. As described previously, adjustment parameters are a 3-week window for the rolling mean, 0.05 smoothing for the cubic spline, and 20 points for the LOWESS. The standard deviation of the source measurements is calculated over 2 weeks. Although no spatial filtering or smoothing is applied, the results of each individual regression in a pixel are very consistent with their neighboring pixels, providing spatially more homogeneous results than original data. All methods capture the seasonal speed fluctuations; however, LOWESS provides the most robust and smooth solution with less visible noise and speeds closer to zero over the ice-free areas. This result is also highlighted in the sub-panels showing a zoom where ice is flowing around a nunatak. Here, LOWESS is the only method with speed close to zero over the entire rock surface (less than 3 m/yr in average), while the rolling mean and the cubic spline are much noisier and ice speeds approach 20 m/yr.

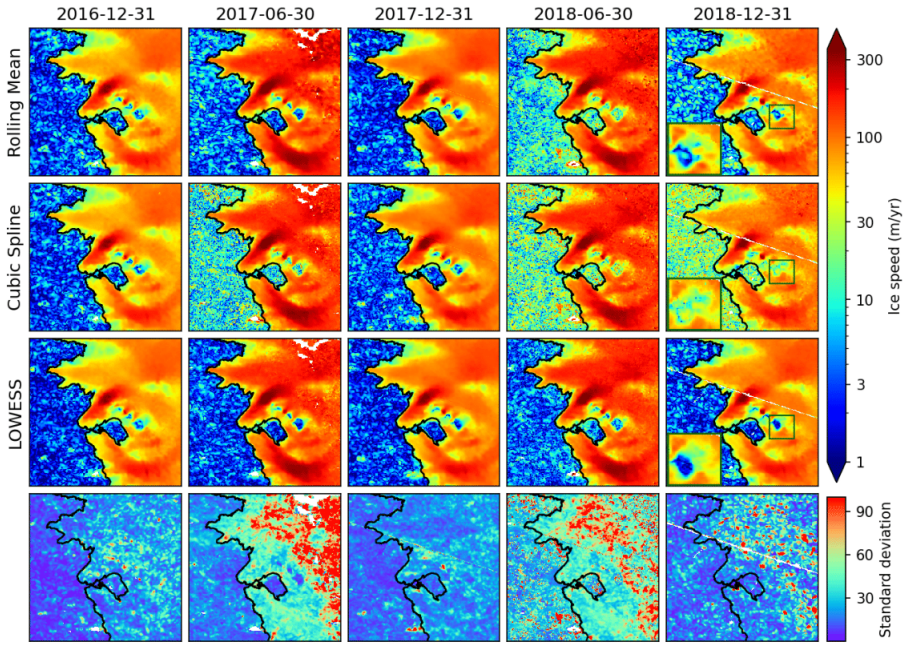

Figure 10. (Three top rows) Ice speeds for selected dates obtained by the different statistical and regression methods (3-weeks window for Rolling Mean and 2 weeks averaging for regressions). The right column sub-panel is a zoom-in for a nunatak area. Color coding is on logarithmic scale from blue (<1 m/yr) to red (>300 m/yr). (Bottom row) Standard deviation of the ice speed measurements for the combined dataset computed over an interval of 2 weeks for the shown dates. Maps are displayed in north polar stereographic projection and the area of the cube is 37.5 × 37.5 km. The black line corresponding to the ice margins delimits the boundary between ice-free (left) and ice-covered (right) areas.

5. Discussion

Since 2014, Landsat-8, Sentinel-2, and Sentinel-1 have acquired large amounts of data over Greenland. We have processed these spaceborne observations and generated maps of ice motion. Having seamless maps of ice velocity is crucial for the scientific community to study glacier dynamics and the evolution of ice sheets in a warmer climate. However, generating sub-seasonal velocity times series over large spatial scales is technically challenging using data from medium resolution sensors where the individual measurements can remain noisy.

Here, we show that (1) combining Landsat-8, Sentinel-2, and Sentinel-1 provides continuous estimate of ice velocity that one sensor alone would not; (2) using statistical or regression data reduction methods can help reducing the individual noisy measurements into filtered, ordered maps; (3) with LOWESS regression we are able to produce the reconstructions that agree well with ground-truth measurements from GPS even in slowly moving areas.

5.1. Multi-Sensor Time Series

The main reason why we rely on different sensors to obtain continuous times series is that each sensor contributes uniquely to the time series. The integration of S2 and L8 optical sensors and the SAR S1 provides continuous measurements through the entire year, as shown in Figure 4. Correlation drops significantly for Sentinel-1 due to surface melt during the summer months near the margin, but the use of S2 and L8 can over come this issue. Conversely, during the winter months, optical sensors are unable to observe due to the polar night and very smooth surface, yet S1 provides reliable observations. While optical sensors S2 and L8 replace S1 during summer month along the margin, we note that it remains challenging to capture the seasonal changes for the upper part of the glacier where fluctuations in speed are small compared the intrinsic errors of the tracking techniques. This is especially the case during the first part of summer season due to the limited number of S1 acquisitions in the ice-sheet interior and also because optical S2 and L8 fail to find surface features used for tracking (Figure 4, point B).

Comparing our time series to published results [1,6,26–28], we found the same range of values, spatial distribution, and general seasonal behavior of seasonal velocities. In general, summer speed-ups start gradually in May and ends in mid-July with acceleration up to 200% compared to winter speeds. The main differences come from the number of ice speed maps produced, where the number of ice speed maps generated by most studies is between 10 to 20 maps per year [1,6,26,27]. For example, the GoLIVE project nsidc.org/data/golive can at most provide 22 velocity maps using only Landsat-8 with a 16-day repeat cycle. We found the only study with high enough data density to capture seasonal fluctuations well is [28], which generated 96 velocity maps from Sentinel-1 between January 2016 and December 2017.

To summarize, the combined observations from Landsat-8, Sentinel-1, and Sentinel-2 produce surface velocity time series in the Russel sector with sub-seasonal resolution for the entire marginal area (about 50 km from the ice margin). Thus, making velocity time series derived from spaceborne data is not only possible for fast outlet glaciers, but also for slow areas such as the land-terminating sectors flowing at speeds of 70 m/yr. However, the number of observations, the accuracy, and the correlation success rate are lower farther inland, which still limits our ability to properly capture the more subtle seasonal signals. For these regions, additional SAR acquisitions would be an asset that could fill this data gap because they do not depend directly on surface features for correlation, as is the case for optical sensors. We therefore recommend extending the 6-day S1 repeat coverage of the Greenland coast to the entire Greenland ice sheet.

5.2. Which Variables to Fit?

Before we discuss the different approaches used to reduce our measurements, we would like to compare two different ways of using speed measurements. The satellite-derived ice velocity is defined

by the movement in x and y-direction independently (v_x and v_y) and our regressions is performed on these components. However, another strategy could be considered by using the speed magnitude v and flow direction α, where $v_x = v\cos(\alpha)$ and $v_y = v\sin(\alpha)$. We test both approaches in an ice free area where "ice speed" should be equal to zero. Deviations from zero in our observations comes from the random errors in the tracking algorithm and such non-moving regions can be used to evaluate the final precision of our measurements [19,23]. Here, we calculate the distribution of v from the original measurements as well as from the solutions given by LOWESS when used to adjust either (v_x, v_y) or (v, α). We found that the averaged values for v are 21 $\pm$ 19 m/yr from the original mixed satellite-derived measurements. After applying the LOWESS regression on the components v_x and v_y, we obtain an average value for v of 8 $\pm$ 4 m/yr, while being 17 $\pm$ 6 m/yr when using the direction α and magnitude v (Figure 11a).

It appears that fitting v_x, v_y gives a better solution by a factor of 2 with absolute speed v closer to 0, compared to fitting v and α. The difference between the solutions can be explained mathematically. Since $v_x, v_y \in \mathbb{R}$, when the ice speed approaches 0, v_x, v_y components with their associated errors are distributed around zero with positive or negative values, and thus averaging multiple independent measurements of v_x and v_y tend towards zero. While, as $v \in \mathbb{R}_+$ and errors can be only positive, the same averaging but on the velocity magnitude v tends toward the measurement error instead of zero. If absolute glacier speed is much higher than the intrinsic error of the measurement, then this is not an issue, as the distribution of v will not be truncated. However, when analyzing changes for areas flowing at a speed comparable to the measurement errors, one should use (v_x, v_y) rather than (v, α).

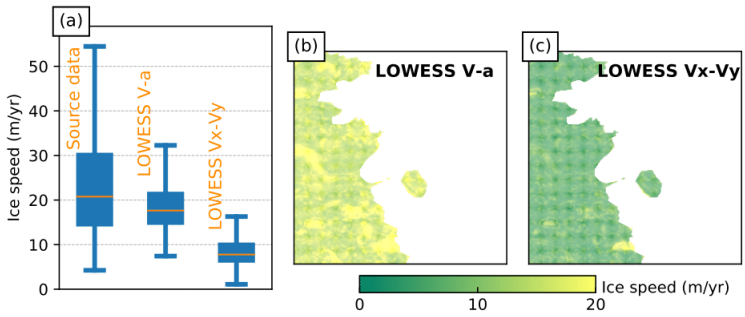

Figure 11. (**a**) Distribution of the average ice velocity for 2015–2019 on ice-free region for initial measurements and the LOWESS solutions using the components (v, α) or (v_x, v_y). (**b**,**c**) Maps of the average ice velocity on the ice-free region for the same time period from the LOWESS solutions using the components (v, α) or (v_x, v_y), respectively. Same spatial extent as for Figure 10 is used.

5.3. Data Reduction for Ice Velocity

Methodologies applied on the ice velocity time series to reduce data to a corrected, ordered, and simplified form have been very simple, and currently rely on statistical averaging on a monthly to annual basis [19,21,23,28] or using spatial filtering to remove outliers without any time context [4,41]. This partly comes from the limited number of available measurements or the use of more accurate sensors in previous studies (e.g., TerraSAR-X or TanDEM-X) [1,3]. As observations from medium resolution sensors (Landsat-8, Sentinel-1, or Sentinel-2) become routinely available, the need for more advanced methodologies is important and the results presented here are of interest to the glaciological community.

From the three different methods we tested (Figures 8–10), we found that a moving average (rolling mean or median) can be used only when the sampling of the time series is dense enough and homogeneous so that the mean can be computed on enough measurements to obtain statistically robust estimates (Figure 9a,b). That is usually the case for the ice-sheet margin but it is less true farther inland. Methods using local polynomial or spline regressions are more robust than the simple statistical rolling

mean. In our case, the non-parametric local regressions (spline and LOWESS) seem to be more adapted to reduce velocity time-series noise than global regression function that would require a specific mathematical description of the speed fluctuations. In other words, the flexibility of local regressions is able to describe a complex and highly non-linear processes for which no trivial mathematical models exist yet. However, we still observe differences between the regression approaches. Cubic spline regression has the tendency to provide inadequate solutions when poorly constrained, where LOWESS seems more robust. As for the moving average, when a piece of the time series is less populated by data, the solution of the cubic spline regression "overshoots." LOWESS does not have that limitation as the local regressions are based on the k nearest data points and thus the data subsets will adapt their time lengths.

Although LOWESS is a more robust tool, it comes at the cost of a longer computing time. LOWESS processing takes about 2 h on one CPU (Intel Core i5 2.30 GHz) for a cube of 250 × 250 pixels containing 1500 speed maps. This is 10 times longer than the computation of the moving average, or 5+five times longer than the cubic spline regression. Its large-scale application would therefore require further optimization of the code and/or the use of parallel computing. Thus, we support the use of rolling mean or cubic spline regression as a faster solution when measurements are frequent, accurate, and equally distributed in time, while we opt for LOWESS otherwise.

5.4. Temporal Resolution and Measurement Accuracy

It is important to evaluate at which temporal resolution the original and final reduced time series can represent the temporal variability of the ice flow. Here, we have mixed observations with repeated cycles of up to 32 days, making it difficult to assess at what typical temporal resolution our initial and fitted time series capture the fluctuations in ice velocity. For the combination of S1, S2, and L8 sensors, the temporal resolution is restricted by their own precision and the repeat cycles related to the observation frequency. According to estimations [19,21,23], every sensor can track ice displacement of roughly one-tenth (optical) or one-fiftieth (SAR) of a pixel with a temporal resolution corresponding to its shorter repeat cycle. This would correspond to ice speed changes of about 70, 35, and 30 m/yr over 5 days, 16 days, and 6 days for S2, L8, and S1, respectively. Such range is enough for the fastest glaciers of Greenland [1,21] but is a limiting factor for slower glaciers, such as the Russell sector. Therefore, when using the large number of acquisitions made by these sensors, we need to find the right balance in our regression approaches between (i) improving the speed estimation accuracy by increasing the size of the subset used to fit ice velocity at a specific date, and (ii) degrading the temporal resolution.

To evaluate the temporal resolution of the original satellite-derived time series, we average the GPS-based ice speed using different windows and calculate the root-mean-square deviation between the GPS and our space-based measurements (Figure 12a). We found the best agreement when GPS is smoothed with a window of 3 to 4 weeks (solid lines in Figure 12a), with a RMSE about 27 m/yr.

The GPS point is located more than 20 km from the ice margin. Closer to margin, more data are available and we can expect that the temporal resolution of our time-series would be slightly better. To prove this idea, we focus on a short period between July and August 2016 (dashed green line in Figure 12a), when the density of measurements in the GPS location is almost the same as for point A (Figure 12b). We found that the estimated temporal resolution is about 2 weeks when a dense time series is available with RMSE dropped to 22 m/yr.

As the LOWESS regression does not use a fixed window but the k nearest data point, the temporal resolution of regression solution will therefore vary depending on the rate of sampling of the input data. Previously, we evaluated that a subset of 20 measurements corresponds to the best adjustment parameter for LOWESS (Section 4.1). After 2015 (when Sentinel-2 and Sentinel-1b were introduced), an interval of 2–3 weeks always contained more than 20 measurements. In Figure 12b, we also evaluated the size of the weighted part of LOWESS subsets (weight > 0.5) for the regressions, which gives a good idea of the temporal resolution we can expect after the regression. Since 2016, the duration of the subsets used by LOWESS is always less than 40 days but often shorter than 20 days. This value

is comparable to the repeat cycles (up to 32 days) used here; therefore, we can expect that the temporal resolution of final reduced time-series is not degraded compared to the initial measurements by the LOWESS algorithm.

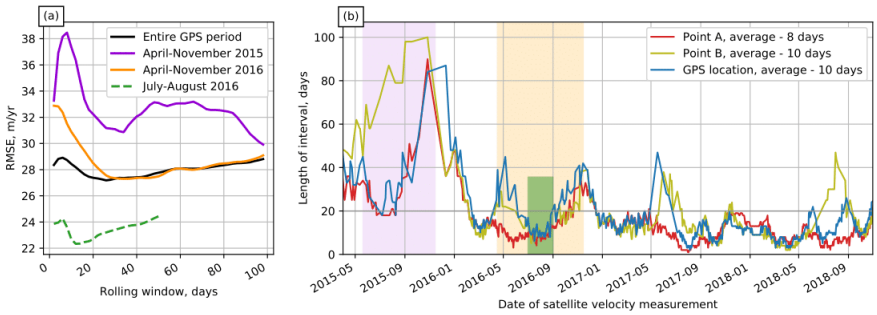

Figure 12. (**a**) Root-mean-square error (RMSE) between ice velocity from satellite and GPS as a function of the moving average's window size applied to the GPS data. The RMSE is calculated for the entire GPS period (black) and for time subsets of April to November 2015 (purple), April to November 2016 (orange), and July to August 2016 (dashed green). (**b**) Time length of LOWESS subset calculated for points having the weights greater than 0.5 versus point's date fitted by this subset for three locations indicated on Figure 1.

The comparison with the GPS also allows us to investigate the accuracy of our time-series. Speed estimations from images obtained by S1, S2, and L8 when combined have a RMSE of about 27 m/yr. After using the different regression approaches, the RMSE is improved by a factor 2 to 3: the best reconstruction is obtained by LOWESS with a RMSE of 10 m/yr. We note that this evaluation is performed at only one single location about 30 km inland from the ice margin and limited to the period from 2014 to 2017 when the GPS was installed. We think that the comparison would be better nearer to the ice margin where correlation success increases, yet lower further inland.

To summarize, it appears that using regression approaches on dense time-series improves significantly the precision of the ice speed maps without degrading the temporal resolution compared to the individual measurements.

5.5. Other Potential Ways of Improving Post-Processing

In our study, the algorithms applied to the data only use the temporal dimension independently between each point in space. It would be possible to take into account the physical spatial cohesion of the glacier and thus use the information contained in adjacent locations to locally improve the reconstruction of ice velocities (e.g., do spatial filtering or smoothing, fill gaps, or discriminate short speed-ups from outliers). Introducing adaptive parametrization depending on the number of measurements could improve the results as well, especially for capturing the sharp peak at the beginning of the summer speed-up. However, the significant increase in computational cost to test find the solution would need to be addressed. Here, we have treated the diverse revisit times indifferently (5 to 32 days, except for the error/weight estimation); advanced algorithms could more carefully use this information to obtain more precise reconstruction of the ice speed, as shown by [24,42].

We also could envision an application of "time-memory" techniques to our time-series, meaning that we could eventually take advantage of the seasonality of the ice motion fluctuations to improve locally in space and time our reconstruction. This would required long time memory to be properly used. Non-classical machine learning techniques such as ensembles or neural networks are now broadly proposed as time-memory methods (e.g., [43–45], but the questions regarding reproducibility or accurate learning should be treated carefully given the relatively short period with dense measurements we have obtained so far and the variability of velocity fluctuations from year

to year. Finally, one of the obvious advantages of our simple approaches is the robust reproducibility, meaning that such data reduction methodology could be applied on a much larger scale.

Another way to improve the final quality could be to directly refine the matching algorithm that derives the ice motion. For example, using reverse correlation [46,47], triangle closure [22], or more than two observations would prevent false correlation and improve single measurement accuracy. However, in all these cases, the obtained precision would be still limited by the resolution of the sensor and the distance moved by the glacier in a given period of time. Therefore, post-processing of the large spatio-temporal dataset would still be needed to improve the precision and temporal resolution to obtain corrected, ordered, and simplified reconstruction of the ice dynamics.

6. Conclusions

In this study we derived ice velocity from three different sensors over the sector of Russell Gletscher, Southwest Greenland, using data acquired between 2015 and 2019 by Landsat-8, Sentinel-2, and Sentinel-1, which all have repeat cycles of shorter than 32 days. These large datasets provide frequent estimation of the ice dynamics but are relatively noisy for the regions of ice flow where speeds are slower than a few hundreds of meters per year. We therefore investigated three different methodologies to post-process the ensemble of available data with a goal of reducing the initial measurements to a filtered, ordered, simplified form. We found that using linear non-parametric local regression (LOWESS) provides the best result compared to rolling mean and cubic spline regression in terms of robustness against data availability and precision of the reconstruction. For the slowly flowing land-terminating areas, such as the Russell sector, the processing results offer robust reconstruction at a temporal resolution between 2 and 3 weeks with a mean accuracy of about 10 m/yr on the annual time scale. As new observations become even more routinely available, post-processing analysis will become instrumental to providing reduced reanalysis of ice dynamics. In this context, the presented methodology could be applied to the entire Greenland ice sheet with an aim of reconstructing comprehensive sub-seasonal ice flow dynamics and mass balance.

Author Contributions: A.D. processed the data, performed the analysis, made the investigation, and wrote the article. J.M. provided supervision, designed the processing chain of source data, performed the analysis, and wrote the article. R.M. designed the processing chain of source data. N.M. processed the raw GPS data. All co-authors helped discussing and reviewing the article. All authors have read and agreed to the published version of the manuscript.

Funding: This work was performed at Institut des Géosciences de l'Environnement with support from the Centre National d'Etudes Spatiales (CNES) of France through the MaISON project and support through the project SOSIce ANR-19-CE01-0011-01 of the French National Research Agency (ANR).

Acknowledgments: We thank the space agencies (NASA, ESA) for making satellite observations of the polar regions free access to the scientific community. We also thank the PSTG for coordinating data acquisitions in the polar regions since the 2007–2008 International Polar Year. The computing/storage resources used for this work were provided by GRICAD (Grenoble Alpes Recherche—Infrastructure de Calcul Intensif et de Données). We thank Joel Harper for the GPS data which was collected under NSF Office of Polar Programs-Arctic Natural Sciences award #0909495. We thank Fedor Yakovlev as well for introducing us to the LOWESS method.

Conflicts of Interest: The authors declare no conflict of interest.

References

1. Moon, T.; Joughin, I.; Smith, B.; Van Den Broeke, M.R.; Van De Berg, W.J.; Noël, B.; Usher, M. Distinct patterns of seasonal Greenland glacier velocity. *Geophys. Res. Lett.* **2014**, *41*, 7209–7216. [CrossRef] [PubMed]
2. Armstrong, W.H.; Anderson, R.S.; Fahnestock, M.A. Spatial Patterns of Summer Speedup on South Central Alaska Glaciers. *Geophys. Res. Lett.* **2017**, *44*, 9379–9388. [CrossRef]
3. Moon, T.; Joughin, I.; Smith, B. Seasonal to multiyear variability of glacier surface velocity, terminus position, and sea ice/ice mélange in northwest Greenland. *J. Geophys. Res. Earth Surf.* **2015**, *120*, 818–833. [CrossRef]

4. Lemos, A.; Shepherd, A.; McMillan, M.; Hogg, A.E.; Hatton, E.; Joughin, I. Ice velocity of Jakobshavn Isbræ, Petermann Glacier, Nioghalvfjerdsfjorden, and Zachariæ Isstrøm, 2015–2017, from Sentinel 1-a/b SAR imagery. *Cryosphere* **2018**, *12*, 2087–2097. [CrossRef]
5. Shannon, S.R.; Payne, A.J.; Bartholomew, I.D.; Van Den Broeke, M.R.; Edwards, T.L.; Fettweis, X.; Gagliardini, O.; Gillet-Chaulet, F.; Goelzer, H.; Hoffman, M.J.; et al. Enhanced basal lubrication and the contribution of the Greenland ice sheet to future sea-level rise. *Proc. Natl. Acad. Sci. USA* **2013**, *110*, 14156–14161. [CrossRef]
6. Palmer, S.; Shepherd, A.; Nienow, P.; Joughin, I. Seasonal speedup of the Greenland Ice Sheet linked to routing of surface water. *Earth Planet. Sci. Lett.* **2011**, *302*, 423–428. [CrossRef]
7. Tedstone, A.J.; Nienow, P.W.; Sole, A.J.; Mair, D.W.F.; Cowton, T.R.; Bartholomew, I.D.; King, M.A. Greenland ice sheet motion insensitive to exceptional meltwater forcing. *Proc. Natl. Acad. Sci. USA* **2013**, *110*, 19719–19724. [CrossRef]
8. Rignot, E.; Mouginot, J.; Scheuchl, B.; Van Den Broeke, M.; Van Wessem, M.J.; Morlighem, M. Four decades of Antarctic ice sheet mass balance from 1979–2017. *Proc. Natl. Acad. Sci. USA* **2019**, *116*, 1095–1103. [CrossRef]
9. Mouginot, J.; Rignot, E.; Bjørk, A.A.; van den Broeke, M.; Millan, R.; Morlighem, M.; Noël, B.; Scheuchl, B.; Wood, M. Forty-six years of Greenland Ice Sheet mass balance from 1972 to 2018. *Proc. Natl. Acad. Sci. USA* **2019**, *116*, 9239–9244. [CrossRef]
10. Morlighem, M.; Rignot, E.; Seroussi, H.; Larour, E.; Ben Dhia, H.; Aubry, D. A mass conservation approach for mapping glacier ice thickness. *Geophys. Res. Lett.* **2011**, *38*, 1–6. [CrossRef]
11. Goelzer, H.; Nowicki, S.; Edwards, T.; Beckley, M.; Abe-Ouchi, A.; Aschwanden, A.; Calov, R.; Gagliardini, O.; Gillet-Chaulet, F.; Golledge, N.R.; et al. Design and results of the ice sheet model initialisation initMIP-Greenland: An ISMIP6 intercomparison. *Cryosphere* **2018**, *12*, 1433–1460. [CrossRef]
12. Seroussi, H.; Nowicki, S.; Simon, E.; Abe-Ouchi, A.; Albrecht, T.; Brondex, J.; Cornford, S.; Dumas, C.; Gillet-Chaulet, F.; Goelzer, H.; et al. initMIP-Antarctica: An ice sheet model initialization experiment of ISMIP6. *Cryosphere* **2019**, *13*, 1441–1471. [CrossRef]
13. Mouginot, J.; Scheuch, B.; Rignot, E. Mapping of ice motion in antarctica using synthetic-aperture radar data. *Remote Sens.* **2012**, *4*, 2753–2767. [CrossRef]
14. Rignot, E.; Mouginot, J. Ice flow in Greenland for the International Polar Year 2008–2009. *Geophys. Res. Lett.* **2012**, *39*, 1–7. [CrossRef]
15. Joughin, I.; Smith, B.E.; Howat, I.M.; Scambos, T.; Moon, T. Greenland flow variability from ice-sheet-wide velocity mapping. *J. Glaciol.* **2010**, *56*, 415–430. [CrossRef]
16. Fahnestock, M.; Scambos, T.; Moon, T.; Gardner, A.; Haran, T.; Klinger, M. Rapid large-area mapping of ice flow using Landsat 8. *Remote Sens. Environ.* **2016**, *185*, 84–94. [CrossRef]
17. Scambos, T.; Fahnestock, M.; Moon, T.; Gardner, A.; Klinger, M. *Global Land Ice Velocity Extraction from Landsat 8 (Go-LIVE)*; Version 1; NSIDC: National Snow and Ice Data Center: Boulder, CO, USA, 2016; Volume 10, p. N5ZP442B.
18. Nagler, T.; Rott, H.; Hetzenecker, M.; Wuite, J.; Potin, P. The Sentinel-1 mission: New opportunities for ice sheet observations. *Remote Sens.* **2015**, *7*, 9371–9389. [CrossRef]
19. Mouginot, J.; Rignot, E.; Scheuchl, B.; Millan, R. Comprehensive Annual Ice Sheet Velocity Mapping Using Landsat-8, Sentinel-1, and RADARSAT-2 Data. *Remote Sens.* **2017**, *9*, 364. [CrossRef]
20. Rosenau, R.; Scheinert, M.; Dietrich, R. A processing system to monitor Greenland outlet glacier velocity variations at decadal and seasonal time scales utilizing the Landsat imagery. *Remote Sens. Environ.* **2015**, *169*, 1–19. [CrossRef]
21. Joughin, I.; Smith, B.E.; Howat, I. Greenland Ice Mapping Project: Ice flow velocity variation at sub-monthly to decadal timescales. *Cryosphere* **2018**, *12*, 2211–2227. [CrossRef]
22. Altena, B.; Kääb, A. Weekly glacier flow estimation from dense satellite time series using adapted optical flow technology. *Front. Earth Sci.* **2017**, *5*, 1–12. [CrossRef]
23. Millan, R.; Mouginot, J.; Rabatel, A.; Jeong, S.; Cusicanqui, D.; Derkacheva, A.; Chekki, M. Mapping surface flow velocity of glaciers at regional scale using a multiple sensors approach. *Remote Sens.* **2019**, *11*, 2498. [CrossRef]

24. Altena, B.; Scambos, T.; Fahnestock, M.; Kääb, A. Extracting recent short-term glacier velocity evolution over southern Alaska and the Yukon from a large collection of Landsat data. *Cryosphere* **2019**, *13*, 795–814. [CrossRef]
25. de Fleurian, B.; Morlighem, M.; Seroussi, H.; Rignot, E.; van den Broeke, M.R.; Kuipers Munneke, P.; Mouginot, J.; Smeets, P.C.; Tedstone, A.J. A modeling study of the effect of runoff variability on the effective pressure beneath Russell Glacier, West Greenland. *J. Geophys. Res. Earth Surf.* **2016**, *121*, 1834–1848. doi:10.1002/2016JF003842. [CrossRef]
26. Fitzpatrick, A.A.W.; Hubbard, A.; Joughin, I.; Quincey, D.J.; As, D.V.A.N.; Mikkelsen, A.P.B.; Doyle, S.H.; Hasholt, B.; Jones, G.A. Ice flow dynamics and surface meltwater flux at a land-terminating sector of the Greenland ice sheet. *J. Glaciol.* **2013**, *59*, 687–696. [CrossRef]
27. Joughin, I.; Das, S.B.; King, M.A.; Smith, B.E.; Howat, I.W.; Moon, T. Seasonal Speedup Along the Western Flank of the Greenland Ice Sheet. *Science* **2008**, *320*, 781–783. [CrossRef]
28. Lemos, A.; Shepherd, A.; Mcmillan, M.; Hogg, A.E. Seasonal Variations in the Flow of Land-Terminating Glaciers in Central-West Greenland Using Sentinel-1 Imagery. *Remote Sens.* **2018**, *10*, 1878. [CrossRef]
29. Scheuchl, B.; Mouginot, J.; Rignot, E.; Morlighem, M.; Khazendar, A. Grounding line retreat of Pope, Smith, and Kohler Glaciers, West Antarctica, measured with Sentinel-1a radar interferometry data. *Geophys. Res. Lett.* **2016**, *43*, 8572–8579. [CrossRef]
30. Michel, R.; Rignot, E. Flow of Glaciar Moreno, Argentina, from repeat-pass Shuttle Imaging Radar images: Comparison of the phase correlation method with radar interferometry. *J. Glaciol.* **1994**, *45*, 93–100. [CrossRef]
31. Jeong, S.; Howat, I.M. Performance of Landsat 8 Operational Land Imager for mapping ice sheet velocity. *Remote Sens. Environ.* **2015**, *170*, 90–101. [CrossRef]
32. Rosen, P.A.; Hensley, S.; Peltzer, G.; Simons, M. Updated repeat orbit interferometry package released. *Eos* **2004**, *85*, 47. [CrossRef]
33. Maier, N.; Humphrey, N.; Harper, J.; Meierbachtol, T. Sliding dominates slow-flowing margin regions, Greenland Ice Sheet. *Sci. Adv.* **2019**, *5*, eaaw5406. [CrossRef] [PubMed]
34. Cleveland, W.S. Robust locally weighted regression and smoothing scatterplots. *J. Am. Stat. Assoc.* **1979**, *74*, 829–836. [CrossRef]
35. Cleveland, W.S.; Devlin, S.J. Locally weighted regression: An approach to regression analysis by local fitting. *J. Am. Stat. Assoc.* **1988**, *83*, 596–610. [CrossRef]
36. Gumbricht, T. Soil Moisture Dynamics Estimated from MODIS Time Series Images. *Multitemporal Remote Sens. Methods Appl.* **2016**, *20*, 233.
37. Cai, Z.; Jönsson, P.; Jin, H.; Eklundh, L. Performance of smoothing methods for reconstructing NDVI time-series and estimating vegetation phenology from MODIS data. *Remote Sens.* **2017**, *9*, 1271. [CrossRef]
38. Moreno, Á.; García-Haro, F.J.; Martínez, B.; Gilabert, M.A. Noise reduction and gap filling of fAPAR time series using an adapted local regression filter. *Remote Sens.* **2014**, *6*, 8238–8260. [CrossRef]
39. McClarren, R.G. *Computational Nuclear Engineering and Radiological Science Using Python*; Chapter 10—Interpolation; Academic Press: Cambridge, MA, USA, 2018; p. 460. [CrossRef]
40. de Boor, C. *A Practical Guide to Splines*; Springer: New York, NY, USA, 1978.
41. Paul, F.; Bolch, T.; Kääb, A.; Nagler, T.; Nuth, C.; Scharrer, K.; Shepherd, A.; Strozzi, T.; Ticconi, F.; Bhambri, R.; et al. The glaciers climate change initiative: Methods for creating glacier area, elevation change and velocity products. *Remote Sens. Environ.* **2015**, *162*, 408–426. [CrossRef]
42. Hadhri, H.; Vernier, F.; Atto, A.M.; Trouvé, E. Time-lapse optical flow regularization for geophysical complex phenomena monitoring. *ISPRS J. Photogramm. Remote Sens.* **2019**, *150*, 135–156. [CrossRef]
43. Ren, H.; Cromwell, E.; Kravitz, B.; Chen, X. Using deep learning to fill spatio-temporal data gaps in hydrological monitoring networks. *Hydrol. Earth Syst. Sci. Discuss.* **2019**, 1–20. [CrossRef]
44. Pashova, L.; Koprinkova-Hristova, P.; Popova, S. Gap filling of daily sea levels by artificial neural networks. *TransNav Int. J. Mar. Navig. Saf. Sea Trans.* **2013**, *7*. [CrossRef]
45. Rodriguez, H.; Flores, J.J.; Puig, V.; Morales, L.; Guerra, A.; Calderon, F. Wind speed time series reconstruction using a hybrid neural genetic approach. In *IOP Conference Series: Earth and Environmental Science*; IOP Publishing: Bristol, UK, 2017; Volume 93. [CrossRef]

46. Scambos, T.A.; Dutkiewicz, M.J.; Wilson, J.C.; Bindschadler, R.A. Application of image cross-correlation to the measurement of glacier velocity using satellite image data. *Remote Sens. Environ.* **1992**, *42*, 177–186. [CrossRef]
47. Jeong, S.; Howat, I.M.; Ahn, Y. Improved Multiple Matching Method for Observing Glacier Motion with Repeat Image Feature Tracking. *IEEE Trans. Geosci. Remote Sens.* **2017**, *55*, 2431–2441. [CrossRef] [PubMed]

2.2.5 Summary

Reliable and extensive observation data are required to conduct investigations on the processes controlling the ice flow. While the long-term ice velocity databases representing the interannual variability of ice flow have been widely established, it remains difficult to observe the short variability (seasonal) of glaciers on a large scale.

We show here that by combining multiple satellites with different sensing approaches, we can reconstruct accurately the seasonal dynamics of ice flow over large regions, even across relatively slowly moving ice margins.

To do so, we designed an automated processing pipeline to track the displacement of ice in a large number of observations and created a geo-database allowing for an easy consistent fusion/combination of these observations. We applied this process to 3 specific regions in Greenland. We discussed the associated errors and limitations that affect each sensor and showed that this large dataset provides frequent estimations of the ice dynamics but is relatively noisy for the regions of ice flow where speeds are slower than a few hundred meters per year.

We then investigated different methodologies to post-process the ensemble of available data with a goal of reducing the initial measurements to a filtered, ordered, and simplified form. If all methods improve the seasonal signal, we found that using linear non-parametric local regression (LOWESS) provides the best result compared to rolling mean and cubic spline regression. While other methodologies can indeed be envisioned to continue to improve post-processing, this result still shows that post-processing methodologies are now needed to handle the large amount of observations that are nowadays acquired and order it in a meaningful way, but also that these methodologies can improve the retrieved signal.

In the following sections, we demonstrate the capability of the final post-processed time-series to support the investigation of processes driving the glacier speed fluctuations on the examples of our case-study regions. In Section 2.3 we do that by means of time-series description and analysis, while in the Chapter 3 these data are used to launch the numerical model.

2.3 Seasonal variations in surface speed on selected glacier in 2015-2019

As shown in the previous section, Sentinel-2, Sentinel-1 and Landsat-8 data allow us to resolve the seasonal velocity fluctuations between 2015 and 2019 with a temporal resolution of about 2 weeks. In this section, the obtained velocity dynamics are described by considering both the "typical" seasonal behavior of our case studies, as well as the deviations from it. Herewith, for each glacier, we discuss the possible drivers and physical mechanisms causing the observed velocity variations. All presented speed data have been post-processed using the LOWESS regression methods described in the previous part of the chapter, and aggregated over 1 week for the time-series near the ice front and over 2 weeks for inland-extended profiles. When we refer to the interannual mean winter speed (MWS), it corresponds to the 5-year mean of the velocity fields derived for January, February and Mars.

2.3.1 Russell sector

The Russell sector is a well-studied area with many velocity observations conducted with both GPS and aerospace solutions. Up to now, details of the seasonal dynamics, like the inland propagation of the acceleration or the velocity double peaks, have only been observed in high-frequency but local GPS records. Thanks to our velocity dataset, merging spatial extension with high frequency and accuracy, we provide here some insights of the spatial distribution of such features.

2.3.1.1 Observed seasonal variations of the ice speed

Figure 27, Figure 28, and Figure 29 present the observations of the ice surface velocity on Insunnguata Sermia, Russell Gletscher, and Ørkendalen Gletscher, respectively. While the first two experience similar dynamics, the latter demonstrates an example of outstanding behavior.

Insunnguata Sermia and **Russell Gletscher** have a common upstream area and independent downstream ice tongues which flow following predefined valleys of the subglacial topography. They show relatively close speeds with MWS of hundred meters per year, and they show a similar seasonal behavior.

Ice speed increases quickly from mid-spring, depending on the site altitude. We observe a gradual inland propagation of acceleration onset, with a typical delay of about one month between the fronts and sites 30 km inland (Figure 27-b, Figure 28-b: time delay of the top border of reddish-colored patches). By late June to early July, ice velocity reaches its maximum, almost doubling compared to MWS across a vast area (+75-100 %, on average). The typical development of speedup in this sector, like Russell Gletscher experiences (Figure 28-a), consists of an acceleration immediately followed by deceleration; thus, a single speed maximum is observed. Herewith, the peaks with a longer duration or relatively pronounced double-peaks are

present across several localized areas (Figure 27-a, blue and orange curves). As for the acceleration, deceleration starts from the ice margin in mid-summer and progressively propagates inland during almost two months (Figure 27-b, Figure 28-b). Contradictory to the acceleration onset "wave", it spreads at a slower pace and on a shorter distance of about 10 km, which corresponds to the length of the glaciers' tongues. The speed deceleration stops in late September/early October with values that are equal or slightly lower than before the spring acceleration. In other words, the autumn speed (right after the end of the melt season) corresponds to the slowest speed observed over a year for the majority of the sector. Then gradual winter acceleration takes place until the next spring.

These patterns are well observed in our data up to 50-55 km inland from the Insunnguata Sermia and Russell Gletscher fronts. While some relevant variations are discernible from year to year even further inland up to the end of our profiles, neither their recurrence nor their signal-to-noise ratio allows us to confirm unambiguously the existence of the same behavior.

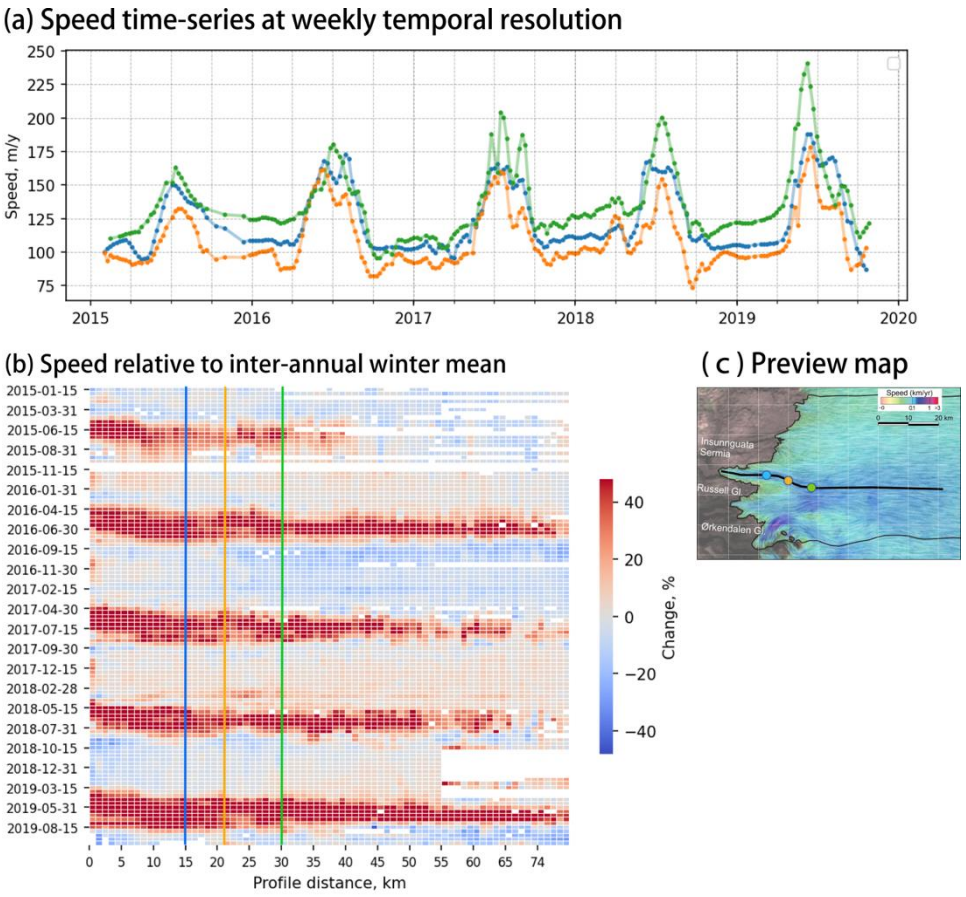

Figure 27 Insunnguata Sermia surface velocities: (a) time-series at selected locations; (b) heat map showing ice speed changes relative to the interannual mean winter speed (MWS) along profile; (c) multiyear mean ice velocity from Mouginot et al. (2017) showing the point locations and profile used in (a) and (b).

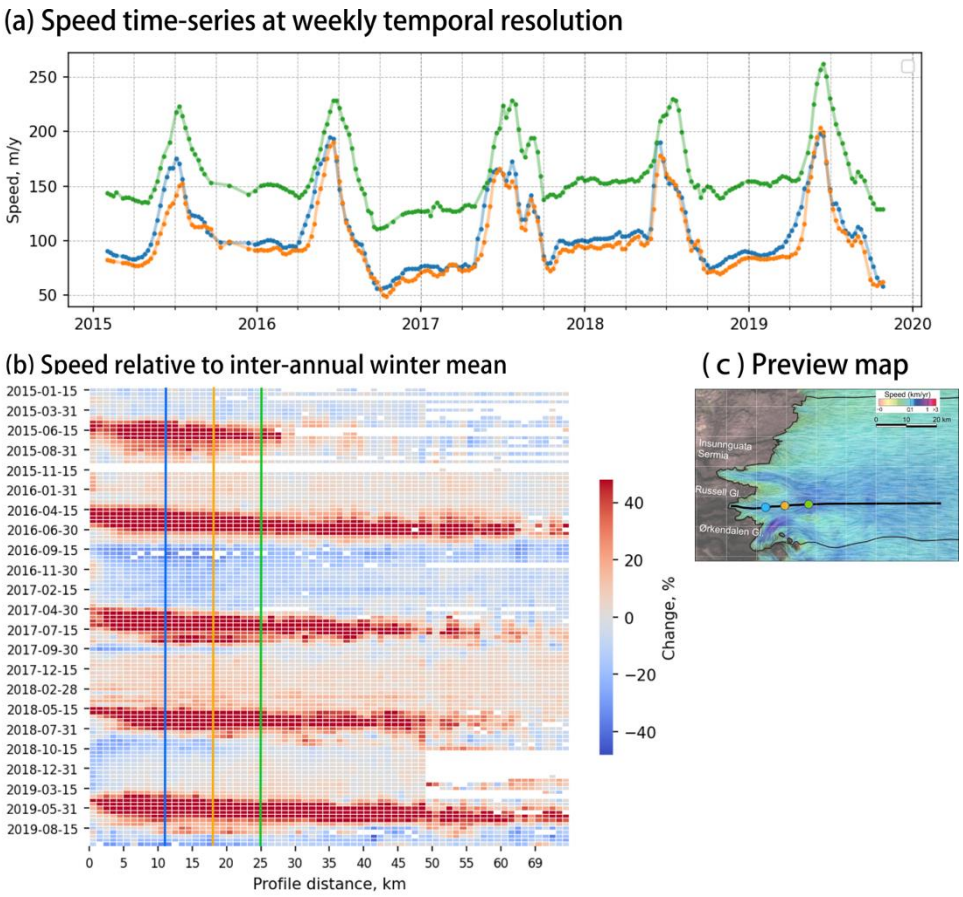

Figure 28 Russell Gletscher surface velocities: (a) time-series at selected locations; (b) heat map showing ice speed changes relative to the interannual mean winter speed (MWS) along profile; (c) multiyear mean ice velocity from Mouginot et al. (2017) showing the point locations and profile used in (a) and (b).

Ørkendalen Gletscher is located in a more complex topographical setting than Russell Gletscher and Insunnguata Sermia. From about 30 to 10 km upstream from the front, the glacier follows a subglacial depression, and at ~7 km from the front the ice has to overpass a topographical ridge, which is 200-300 m higher than the depression. At the ridge, the ice flows at 320-350 m/yr in winter, or about 3 to 4 times faster than elsewhere in this sector, and demonstrates the seasonal flow behavior differing from the rest of the sector area. The upper region's speed range and behavior are relatively similar to the other two glaciers at the equal distance from the fronts.

On the area close to the ridge, we observe that speed changes significantly during winter from about 270 m/yr at the end of the melt season to 350 m/yr at the onset of the next melt season, which corresponds to an increase of about +30% (Figure 29-a, blue curve). After a relatively calm pace in winter, the speed starts to rise more rapidly after the onset of the melt season as observed for other areas, but the maximum (around 430 m/yr) occurs a few weeks earlier compared to them. The deceleration that follows is very quick and pronounced, thus the flow velocity reaches a clear minimum at the end of the melt season around late September.

Much further upstream the ridge, Ørkendalen Gletscher experiences a "classical" single-peak speedup (Figure 29-a, green curve). The acceleration starts in mid- or late spring after a relatively stable winter time, reaches its maximum of about +75% to +100% from MWS around late June or early July, and ends slightly below the end-winter velocity level in late September.

Like for Russell Gletscher and Insunnguata Sermia, the gradual in space and time inland propagation of speed-up onset and end is observed on this glacier (Figure 29-b: time delay of the top and bottom borders of reddish-colored parches). The difference is that they are heading not from the front, but are related to two major topographical features along the profile. Thus, the acceleration launches almost simultaneously in the topographical depression (~10 to 27 km on the Figure 29-b), but its onset happens progressively over the distance further on the plateau. This is especially well seen in the spring of 2016. In turn, the gradual propagation of the deceleration phase end is noticeable only behind the ridge along 10 to 25 km, which roughly corresponds to the stretch of the topographical depression, while further inland this happens more or less simultaneously.

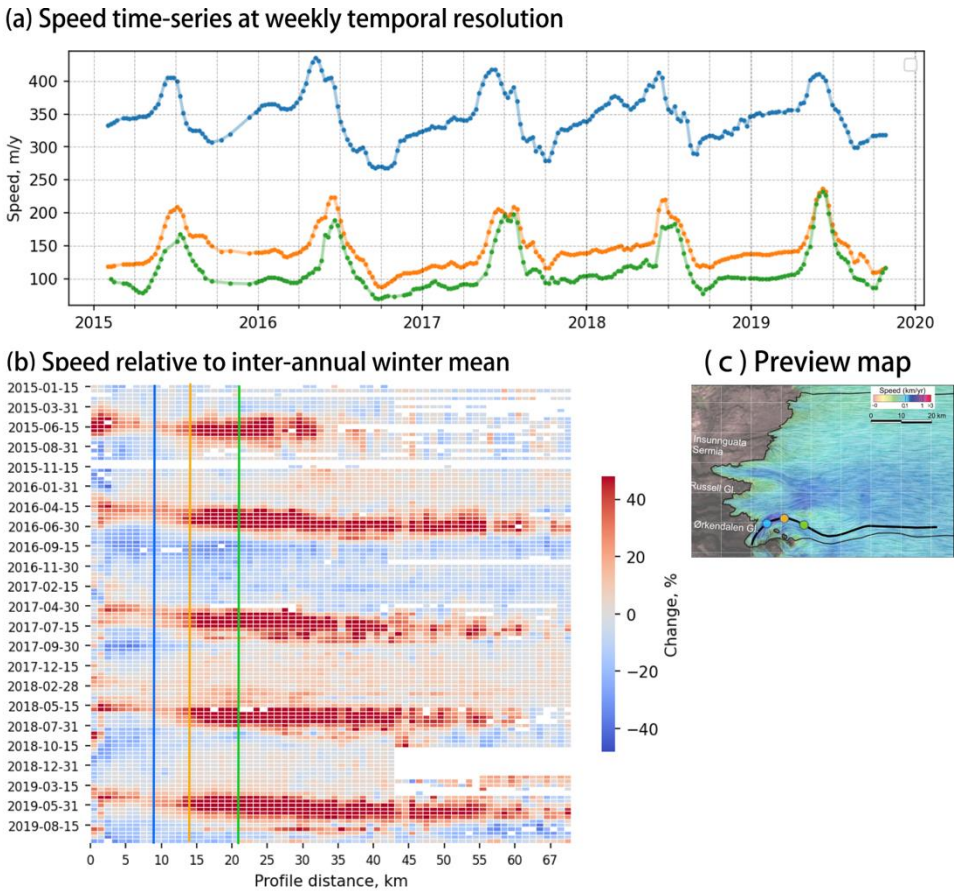

Figure 29 Ørkendalen Gletscher surface velocities: (a) Time-series of ice velocity on selected point locations; (b) heat map along profile showing the ice speed changes relative to interannual mean winter speed (MWS); (c) multiyear-mean ice velocity map showing the location points and profile used in (a) and (b), (Mouginot et al., 2017).

While intra-annual variability on all three glaciers is relatively stable (i.e. a similar seasonal behavior is observed each year), we do observe interannual changes. Thus, the vast majority of the inland areas experience a gradual increase in the speedup maximum. This is particularly well seen at 20-30 km from the glaciers' fronts (green curves on all "a" subplots). The average state of the flow in winter experiences a high variability as well, but without a uniform trend. For instance, we observe in the whole sector that the speed during the winter of 2016-2017 was particularly low compared to other winters, while in the next winter it was larger than the average. Generalizing, it seems that the winter speed is determined by the speed minimum reached at the

end of the melt season. The rate of sometimes occurring "excessive" deceleration below the pre-speedup state seems to be proportional to the acceleration magnitude. Indeed, the summers of 2016 and 2019 had a greater and more widespread acceleration of flow. This would suggest that not only the summer velocity is regulated by a physical driver which causes the accelerations, but the winter velocity depends on it as well, being influenced indirectly through the extent, duration and magnitude of the summer speedup.

2.3.1.2 Physical drivers of the seasonal dynamics

The Russell velocity fluctuations are commonly attributed to the production of surface water which infiltrates to the bed and causes a basal water pressure rise (Fitzpatrick et al., 2013; de Fleurian et al., 2016; Joughin et al., 2008b; Lemos et al., 2018b; Palmer et al., 2011). As it was described in Section 1.3.4, the current understanding of the subglacial hydrology system suggests that a rapid and important influx of water to the bed cannot be instantaneously accommodated by the subglacial drainage system, hence the water pressure raises facilitating the glacier motion; later increased drainage efficiency leads to a lowering in water pressure and, therefore, to the glacier deceleration (Davison et al., 2019; Nienow et al., 2017). This means that a glacier should respond by acceleration slightly after the melt onset and have a velocity peak not later than the maximum of the melting rate plus some infiltration-time delay.

To test this relationship in our time-series, we compared our speed observations with the surface water runoff simulated with the Regional Atmospheric Model (MAR v.3.1, https://mar.cnrs.fr/, Fettweis et al., 2020). Figure 30 illustrates both factors at a selected Insunnguata Sermia location that shows an extended double-peak speedup maximum. The comparison suggests that the physical mechanism proposed to explain the seasonal fluctuations fits well the speed observations presented above.

The timing of the speed acceleration corresponds closely to the onset of the melt season. This is also observed over the entire domain when the data fields are compared, thus the mentioned gradual propagation of speedup toward inland reflects the progression of surface melt at a higher altitude through the warm season. The speed deceleration usually starts before the maximum in runoff is reached, suggesting that the drainage system becomes highly efficient while the melt is still increasing. This also explains why the deceleration starts at the front and propagates latter towards upstream, which is contradictory to the expected direction of the cold season propagation: downstream, the hydrological system development starts earlier and happens more actively as the total water amount includes the runoff from the entire upstream basin. We also suggest that the velocity can stay elevated for some time, forming an extended or multi-peak speedup maximum, when the local routing capacity of the hydrological system is close to the incoming water flux, thus no rapid water pressure drop happens on the surrounding area.

Minimum speeds are reached at the end of the melt season, while the drainage system might still be efficient but the water input to the bed is minimal. Slow acceleration over winter is related to the transition from efficient to inefficient system during this period allowing for the water pressure to rise progressively. With this concept, the interannual variability in the mean winter speed is well explained by the intensity of the preceding melt season. In the years of more intense than usually melting, the subglacial drainage system becomes more developed than in the

"regular" years; less regions stay non-connected to the common network, which would allow them to keep an elevated pressure, and so the average regional basal drag increases more significantly resulting in a slower winter speed. This would correspond to the observations made by Tedstone et al. (2015) or Williams et al. (2020) that show inverse trends between runoff and annual mean speed.

In Section 3.2 we will come back to these velocity observations and investigate deeper the processes linking the surface runoff and speed dynamics using the numerical modelling.

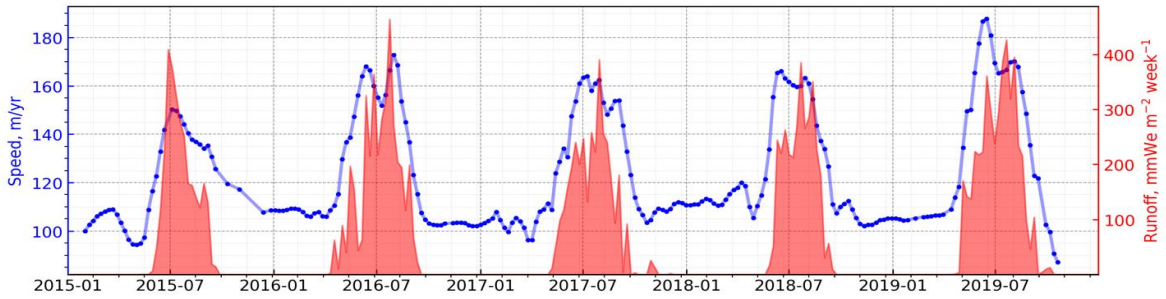

Figure 30 Satellite-derived ice surface velocity and the MAR modelled surface water runoff on the Insunnguata Sermia (blue point from Figure 27-c).

2.3.2 Petermann

Petermann Gletscher is a floating tidewater glacier located in the northern sector of Greenland. It is known for its high-amplitude seasonal speed fluctuations in the lower part of the basin. Our mean winter speeds, as well as the summer acceleration rate at the grounding line, fit well with those provided by previous studies (Hill et al., 2018; Lemos et al., 2018a; Nick et al., 2012; Rignot and Kanagaratnam, 2006). However, to our knowledge, no local time-series or maps with sufficient spatial and time resolutions to thoroughly discuss the seasonal dynamics of the ice flow have been published.

2.3.2.1 Observed seasonal dynamics of the ice speed

The mean observed winter speed is roughly about 1000-1200 m/yr at the grounding line which is the fastest zone over the grounded basin areas (Figure 31-a). Such a broad range of speed magnitude is due to the asymmetric subglacial topography with a pronounced narrow valley on the orographically-right side (Bamber et al., 2013), which leads to the displacement of the flowline with the maximum speed closer to the right border of the glacier tongue. In the grounded part, the MWS decreases gradually and relatively slowly to about 1000, 800 and 400 m/yr at the 10th, 20th and 40th km upstream from the GL, respectively.

During the summer months, a short and abrupt speedup takes place during 4-5 weeks (Figure 31-a, b), starting in late June and ending just before August. At the GL, the ice velocity increases evenly until mid-July to about 1400 m/yr, or +15 % above MWS, and slows down roughly to the winter state at the same even rate. A similar behavior is observed up to about 50 km from the GL (corresponding to a distance of about 100 km along the profile shown in Figure 31-b), and might continue further upstream, but our time-series become too noisy to resolve it

unambiguously. The relative amplitude of the acceleration shrinks with the distance from the GL; we observe a speedup of only +10 % and +5 % (+100 m/yr and +50 m/yr), 10 and 20 km upstream of the GL, respectively.

It can be noted in the presented time-series that the absolute speed range and dynamic behavior of the floating shelf mimic those of the grounded ice near the GL. The accelerations and decelerations happening on the GL propagate immediately onto the entire shelf up to the end. The tiny excess of absolute values towards the front can also be noted in the time-series (Figure 31-a), which is the effect of ice longitudinal stretching (Cuffey and Paterson, 2010).

The spatio-temporal propagation of the acceleration onset from the GL over the grounded ice can be noted in this region during several years at the first 20-30 km (Figure 31-b). Despite the temporal resolution of our time-series and a short speedup duration, we can estimate that the inner zone experiences a speed-up onset 2-4 weeks after the grounding line's surrounding.

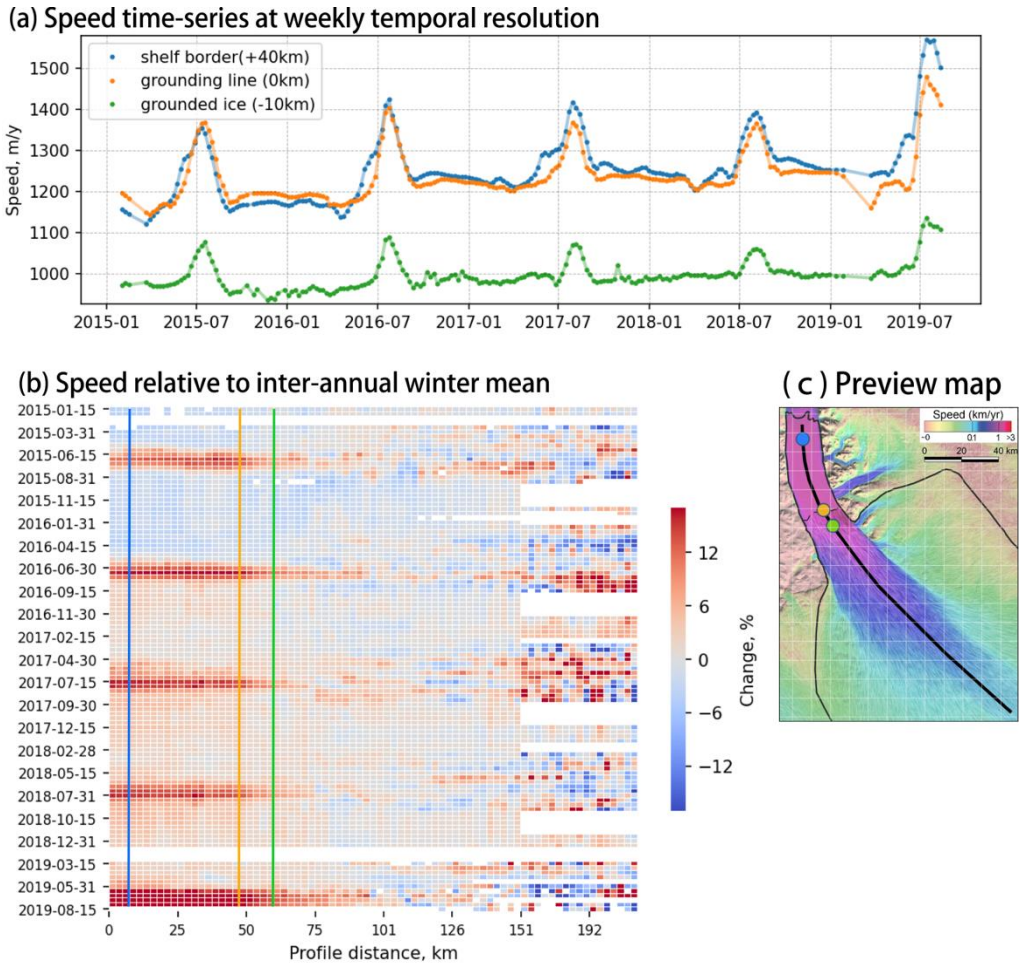

Figure 31 Petermann glacier surface velocities: (a) time-series at selected locations; (b) heat map showing ice speed changes relative to the interannual mean winter speed (MWS) along profile; (c) multiyear mean ice velocity from Mouginot et al. (2017) showing the point locations and profile used in (a) and (b).

Our dataset clearly reveals an interannual increase in winter speed during the considered 5 years. The mean annual acceleration rate is about +30 m/y near the GL (or +3%), similar to what was observed by Mouginot et al. (2019) in the annually-averaged data (Figure 31-a, -b). At the same time, except the summer of 2019, the average speedup amplitude is shrinking.

2.3.2.2 Physical drivers of the seasonal dynamics

Many of the Greenlandic marine-terminating glaciers have regular seasonal speed variations (Ahlstrøm et al., 2013; Hoffman et al., 2016; Howat et al., 2010; Vijay et al., 2019). Among them, there are those with a similar velocity range and temporal occurrence of changes as observed on Petermann: a single-peak pronounced acceleration of several hundred meters per year takes place in summer after the melt onset, while the rest of the year there is a stable speed magnitude (Moon et al., 2014; Vijay et al., 2019). On these glaciers, such a seasonal acceleration usually does not coincide with a displacement of the ice front; instead, the infiltration of the surface runoff to the bed is assumed to be the main speedup driver (Moon et al., 2014).

The winter and summer velocity ranges observed at Petermann in our dataset correspond well to those measured earlier (Ahlstrøm et al., 2013; Hill et al., 2018; Lemos et al., 2018a) meaning that the glacier dynamics has been relatively stable over the past decades. There were no fluctuations in the speed except for regular summer speedups during the 5 years of our observations; so, it seems reasonable to expect that the major control of summer acceleration is the melt water input to the bed, as some authors proposed based on the previous observations (Lemos et al., 2018a; Nick et al., 2012; Vijay et al., 2019). Note that in the surveyed time there was no seasonal variation of the ice front; however, it has gradually and evenly advanced, regardless of the season, seemingly without any back influence on the glacier speed. The absence of relation between the front position and speed here is explained by the low lateral friction offered by the sides of the terminus shelf section into the total forces balance (Hill et al., 2018; Lemos et al., 2018a; Nick et al., 2012). The small thickness of the terminus section, apparently responsible for the low drag, results from the intense submarine melt under the shelf (Hogg et al., 2016; Nick et al., 2012).

To verify the proposed hypothesis, we overlapped our speed time-series with the surface water runoff derived from the MAR climate model. A very good agreement between both fields was found (Figure 32). The start and end of the melt seasons coincide exactly with the start and end of the summer speedups. We can also assume that the drainage system has no time to develop much before the end of the melt season, as no summer-end slowdown compared to MWS happens and the velocity peak matches closely with the runoff maximum instead of getting ahead of it. Additionally, the amplitudes of the accelerations seem to correlate well with the intensity of the runoff, a lower runoff usually corresponding to a lower speedup. Thus, in 2017 and 2018, both the maximum runoff and speedup amplitude decreased, by about 15% and 40% respectively, compared to 2015 and 2016.

The speed variations on the ice shelf are driven by the dynamics occurring near the GL, as floating ice does not experience a basal drag. In turn, the weak lateral drag allows for the immediate and amplitude-lossless propagation of speed changes for the entire length of the shelf.

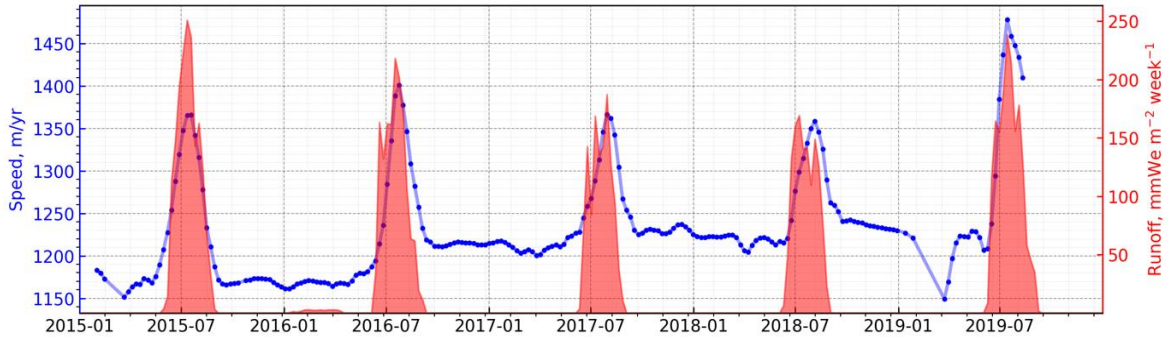

Figure 32 Satellite-derived ice surface velocity and the MAR modelled surface water runoff on the Petermann Gletscher near the front (orange point in Figure 31-c).

As the submarine melt intensifies in summer under the shelf (Washam et al., 2019), it could also be envisaged that the seasonal displacement of the grounding line would influence seasonal changes in speed as proposed for other glaciers (Beckmann et al., 2019; Katz and Worster, 2010; Miles et al., 2020). To our knowledge, there is no evaluation of the rate of GL displacement that would be necessary to cause the observed variability of ±200 m/yr. J. Mouginot has derived 35 grounding line positions from interferometry data for the year 2017. The positions have been determined before and after the melt season (15 in winter, 12 in spring and 8 in autumn). We found GL displacements of ±3-4 km in the subglacial channel and ±1-1.5 km outside, but with no seasonal patterns, fluctuations being larger within the individual months than from April to October. Regarding the good agreement of the speed fluctuations with the runoff we thus assume that this is the main driver of the seasonal fluctuations.

Herewith, numerical experiments have shown a very limited supplementary influence on the speedup rate coming from other seasonally varying factors sometimes mentioned in literature, such as ice shelf thickness modulated by the submarine melt rate, or the presence of the sea ice giving an additional back stress on the front (Nick et al., 2012).

2.3.3 Upernavik Isstrøm

Very few studies have looked at the seasonal speed fluctuations of Upernavik Isstrøm, and the majority are not site-specific but have a large regional cover (Vijay et al., 2019; Moon et al., 2014; Ahlstrøm et al., 2013). During the last two decades, two of the three glacier's branches have undergone high-amplitude (up to 30% per year) multi-annual velocity trends on which the seasonal changes have been superposed. Additionally, they now flow with a very high average speed. Because of these two points, Upernavik Isstrøm makes a challenging case study for satellite-based observations of seasonal events with a moderate relative amplitude. Here, we present the first high-frequency velocity datasets that successfully resolve the presence of seasonal velocity dynamics on all three branches of Upernavik Isstrøm.

2.3.3.1 Observed seasonal dynamics of the ice speed

The **northern branch of Upernavik Isstrøm** (UIN) has dramatically accelerated, almost twofold, in the 2000s (Larsen et al., 2016). Now it is a very fast flowing outlet glacier that shows mean annual speeds above 5 km/yr near its terminus (Figure 33-a). Farther inland, the average ice speed decreases gradually, to 4.5 and 2.5 km/yr at 5 km and 10 km upstream from the ice front. Currently the glacier is under a long-term slowdown. We found a decrease of about -10% between 2015 and 2019 in agreement with the rate obtained by Mouginot et al. for the same period (2019).

According to our time-series (Figure 33-a, -b), UIN clearly experiences summer speedups. The speed increases from late June to early August, with a maximum in mid-July. These events are well distinguishable up to 25 km upstream from the front (Figure 33-b). Farther inland, some relatively regular and spatially extended seasonal accelerations are still present, however, the uncertainties in our summer-time data become too large to draw any confident conclusion. Interestingly, it does not seem that the glacier accelerates gradually from the front towards the interior, as observed for the Russell sector or Petermann Gletscher, rather the acceleration is quasi-synchronous over the entire section under discussion. It can also be noted that across the inland areas the amplitude of the summer speedups does not change remarkably during the 5 observed years, being on average about +5% from the MWS. This corresponds to about +120 m/yr 10 km upstream from the front. However, the accelerations are more irregular both in magnitude and duration along the 1st km just near the front, where, in different years, they can vary from about +2% to +8% above winter speed (+100 m/yr to +400 m/yr, respectively).

Note that while the speed increases are noticeable in absolute values on UIN, the relative value is small. We speculate that such smallness of the relative value together with much more pronounced longer-term trends obstructed the segregation and observation of summer speedups in earlier studies which used sparse observations and declared absence of seasonal dynamics (Moon et al., 2014; Vijay et al., 2019).

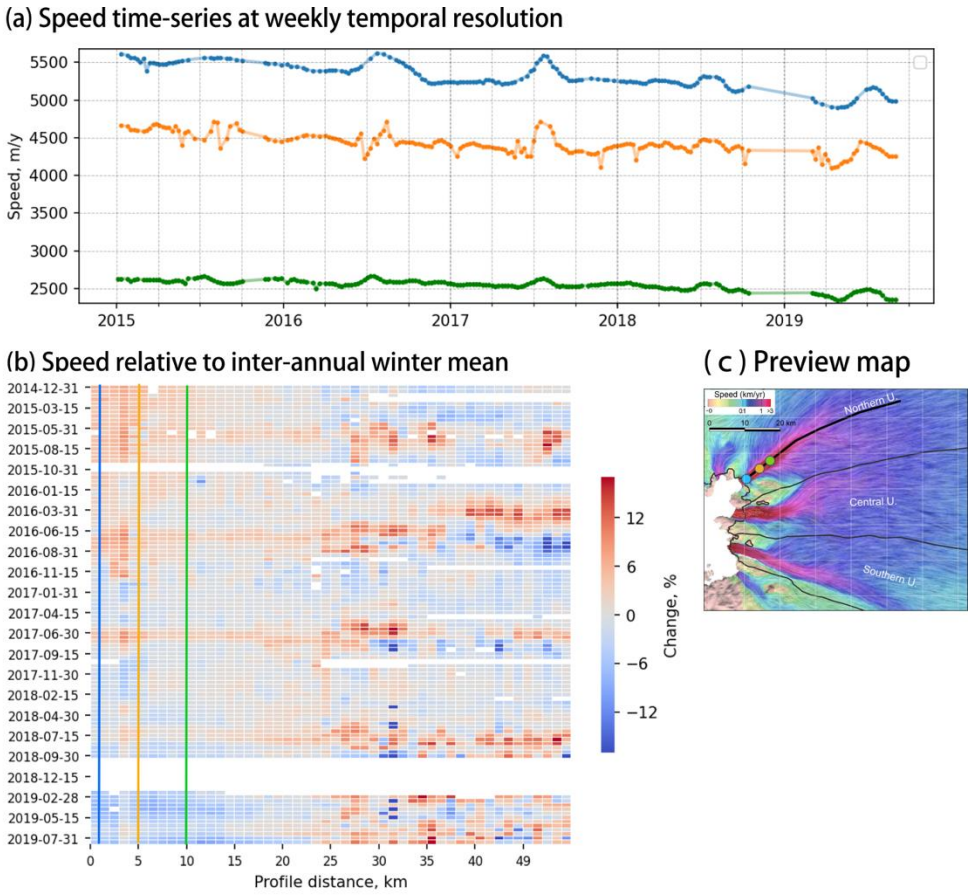

Figure 33 Surface velocities on the northern branch of Upernavik Isstrøm: (a) time-series at selected locations; (b) heat map showing ice speed changes relative to the interannual mean winter speed (MWS) along profile; (c) multiyear mean ice velocity from Mouginot et al. (2017) showing the point locations and profile used in (a) and (b).

The **central branch of Upernavik Isstrøm** (UIC) shows pronounced interannual fluctuations of speed (Figure 34-a). It significantly speeded up in the early 2010s (Larsen et al., 2016) and we still observe an increasing trend at the beginning of our time-series. At the end of 2016, after a sharp acceleration event, especially remarkable in the lowest 5 kilometers (almost +30% in less than one year), a general deceleration trend took place. Note that this outstanding event affected the MWS reference value used for Figure 34-b; therefore, some features observed near its terminus (e.g. strong spring deceleration in 2019) are artefacts.

Except the first kilometers near the front, UIC seasonal dynamics is characterized by regular mid-summer speedups with a maximum in mid-July. They happen simultaneously along at least 25 kilometers and, despite the data quality degradation farther inland, can be assumed up to 50 km upstream from the front. The typical magnitude of these speedups decreases in absolute values from the ice margin towards the ice sheet interior, but rises in relative values (Figure 34-a, -b): the acceleration peak reaches +150 m/yr above the pre-acceleration state at 10 km from the terminus, while it is about +50 m/yr at 20 km. At the same time, the relative rate changes a little, from about 5% in the downstream area to 8% along the rest of the stream.

The multi-month gentle speed rise and subsequent decrease, slowly happening in winter between October and April, is also observed in the majority of years in our observation across a vast area. However, we cannot be sure if it is a typical behavior or temporary perturbations caused by the 2016 acceleration event.

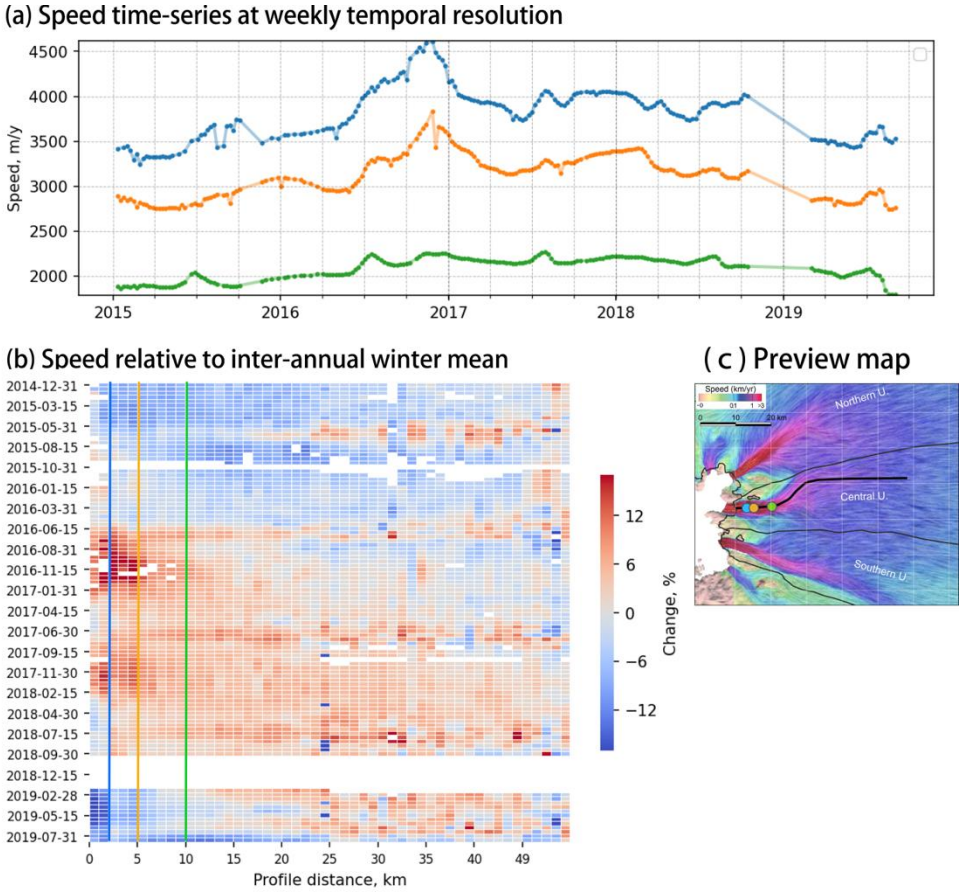

Figure 34 Surface velocities on the central branch of Upernavik Isstrøm: (a) time-series at selected locations; (b) heat map showing ice speed changes relative to the interannual mean winter speed (MWS) along profile; (c) multiyear mean ice velocity from Mouginot et al. (2017) showing the point locations and profile used in (a) and (b).

The Southern branch of Upernavik Isstrøm (UIS) differs significantly from the other two branches (Figure 35). It did not experience the long-term velocity trends over the last four decades (Larsen et al., 2016), flowing twice slower that its neighbors. Here, we observe only seasonal variations in speed. While in some years the annual speed extrema are greater than in others, this branch does not experience any remarkable multiannual trend. Finally, its seasonal behavior does not resemble the "classical" turn of events.

The UIS flows at about 2.4 km/yr near the front, slowing down to 100-200 m/yr per kilometer as we move inland. The seasonal variability of speed is visible along the entire length of the 50 km profile shown here. The behavior described below happens clearly along the first 20 km from the glacier front. Farther inland, the time-series became noisier and we cannot confidently discuss the behavior's nuances (Figure 35-b).

Here, the annual cycle of velocity changes is composed of asymmetric acceleration and slowdown phases which continuously replace each other almost without a speed stability phase (Figure 35-a). The speed slowly increases over the winter period, and then sharply rises up from late May until early July when the speed is maximal. After that, it decreases rapidly to reach values almost twice lower than those before the springtime acceleration by late August. From this minimum, the speed gradually grows up again until the next spring, relatively rapidly the first two

months and then slowly for the rest of winter. Near the terminus a typical range of velocity springtime acceleration is about +200 m/yr from the preceding winter (or +8%). The absolute magnitude drops to ~+100 m/yr from winter at 10 km further inland. However, the relative magnitude does not change a lot, still being about +7% relative to the preceding winter.

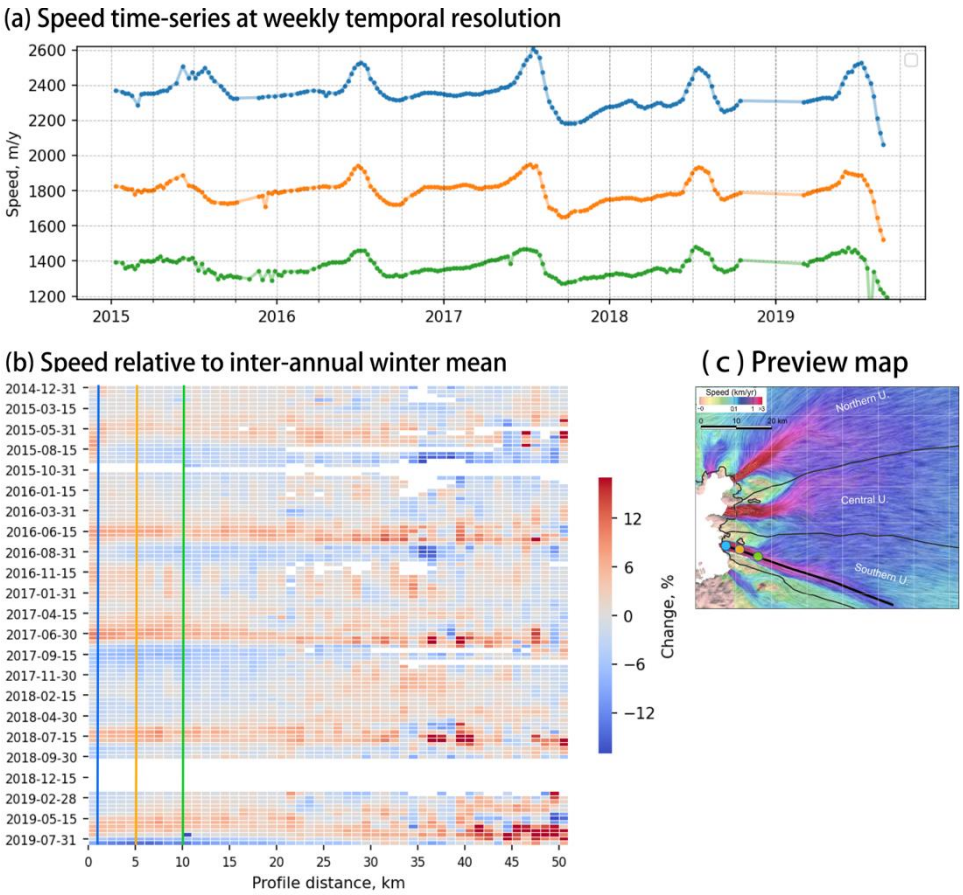

Figure 35 Surface velocities on the southern branch of Upernavik Isstrøm: (a) time-series at selected locations; (b) heat map showing ice speed changes relative to the interannual mean winter speed (MWS) along profile; (c) multiyear mean ice velocity from Mouginot et al. (2017) showing the point locations and profile used in (a) and (b). Measurements are absent from October 2018 to February 2019.

2.3.3.2 Physical drivers of the seasonal dynamics

As already mentioned, **UIN** seasonal behavior has not been identified in earlier studies (Moon et al., 2014; Vijay et al., 2019), therefore, the driving mechanisms have not yet been investigated. We compare the behavior of ice flow speed with those of front-line displacement and runoff.

While an important calving activity exists throughout a year (Andresen et al., 2014) and the ice front position is highly variable, we observe that on average the terminus is further back in mid-summer than the rest of the year (Figure 36-a). The velocity maximum occurs on average at this moment or 1-2 weeks later. The onset, intensity peak and termination of runoff also closely correspond to the speedup development. We speculate that both drivers are important for this

glacier, being separately dominant across the downstream or upper sections; additionally, it can be suspected that the synchronous acceleration along many tens of kilometers is the result of their simultaneous influence. Taking into account the mutual changes in magnitude of all three variables in different years, it seems that the terminus surrounding area is more influenced by the front displacement, while from about ten kilometers inland the runoff impact is more important. Indeed, the far front retreat in 2016 caused the largest response in our time-series along the first few kilometers but not inland. Across the inland area, the greatest speedup, both in magnitude and duration, happened in 2019 which is the year with the most intensive melting (e.g. see Figure 37 or Figure 38); nevertheless, downstream glacier sections demonstrated a moderate response. Such low sensitivity could result from the little resistance offered by the bed across this fastest glacier section, meaning that the runoff input to the hydrological system would have a limited impact on the average basal friction.

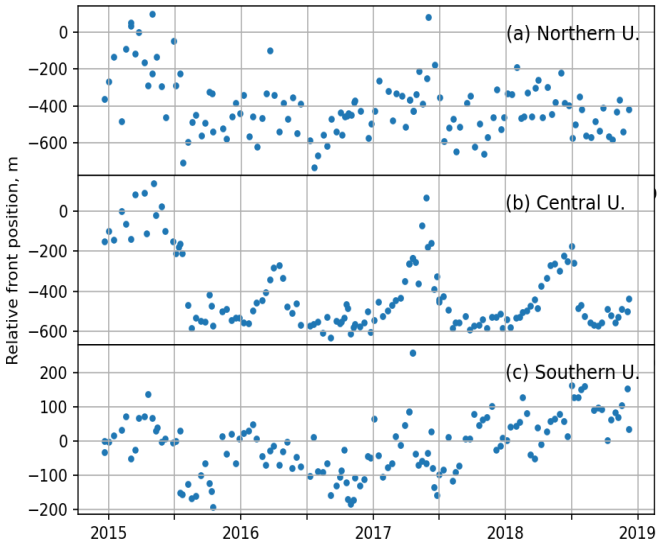

Figure 36 Time-series of the relative front positions of the Upernavik branches (collected and provided by J. Mouginot).

UIC is the only branch that demonstrates pronounced seasonal displacements of its front during the surveilled period in our observations (Figure 36-b), as well as in the twice shorter dataset of Vijay et al. (2019). On average, the front starts to advance in mid-winter and achieves the farthest position by late spring; once the melt onsets, the front retreats to its approximately pre-advance location and stabilizes by mid-summer. These displacements are assumed to be the major driver of the seasonal velocity dynamics (Vijay et al., 2019).

Due to the strong interannual variability, it is difficult to compare the velocity changes with the front and runoff dynamics. It seems that on average the terminus advances match with the periods of ice flow slowdown. What consider the summer speedup, it is less obvious. For many years, the acceleration has taken place slightly after the front retreat onset and stopped with the front position stabilization in some years or a few weeks after in other years. However, in 2018 the glacier velocity increased along many kilometers when the front was still advancing. At the same time, the occurrence, peak and duration of the speedups match well the surface runoff development in the observed years (Figure 37). Thereby, we speculate that both phenomena –

front displacements and surface runoff infiltration to the bed – would mutually drive the seasonal velocity changes at this glacier.

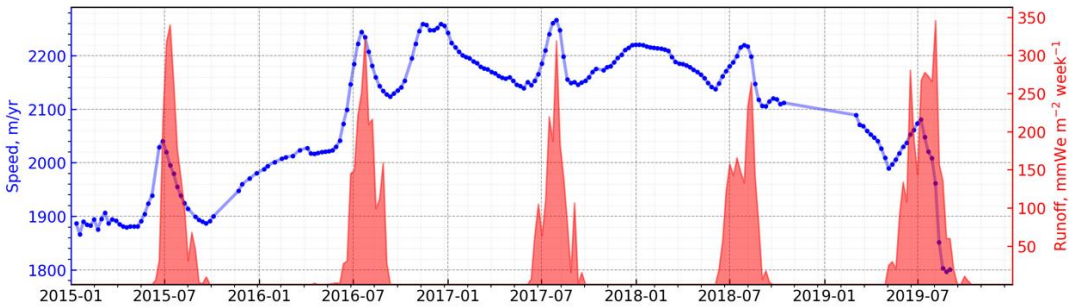

Figure 37 Satellite-derived ice surface velocity and the MAR modelled surface water runoff at the 10-km inland location on the central branch of Upernavik Isstrøm (green point in Figure 34-c).

For **UIS**, which presents clear and regular seasonal speed fluctuations, changes in subglacial water pressure are likely the leading forcing (Moon et al., 2014; Vijay et al., 2019), because the terminus does not show marked seasonal variations (Figure 36-c).

Comparison of our velocity time-series with MAR surface runoff demonstrates a correlated variability of both (Figure 38).The start of the sharpest spring part of the acceleration phase matches well with the runoff onset. The velocity peaks are reached before those of runoff, being more flatten and temporally extended if a series of multiple runoff increases took place, like in 2018 or 2019. Apparently, the duration of the deceleration phase and thus the resulting speed minimum are also related to the runoff cycle: if the latter continues for a longer time after the velocity slowdown onsets, a longer and deeper deceleration develops (e.g. 2017 against 2018). It has been hypothesized by Vijay et al. (2019) that the described specific relation between the speed and runoff phases is caused by the development of an efficient drainage system faster than typical, which is possible if high rates of basal melt prevent the channels extinction during winter. Indeed, the basal melt is estimated to be much more intensive at the Upernavik system than at the surrounding glaciers (Karlsson et al., 2021).

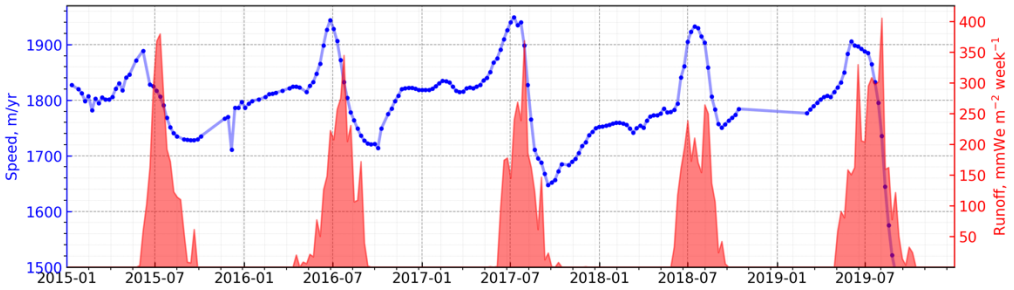

Figure 38 Satellite-derived ice surface velocity and the MAR modelled surface water runoff at the 5-km inland location on the southern branch of Upernavik Isstrøm (orange point in Figure 35-c).

3. Modelling of seasonal dynamics of glacier basal environment

Alexandra's Land, Franz Josef archipelago – Sentinel-2 satellite image, 23 Aug 2019

3.1 Modelling approaches

Here, we are considering *numerical modelling* as the computer-based solving of a set of mathematical equations. Contrary to pure "conceptualization models" describing phenomena, numerical models provide quantitative results. Usually, in glaciology the equations are based on physical conservation principles (e.g., conservation of mass and momentum) but also on parameterizations to describe certain processes (e.g., ice deformation under stresses). The required models' inputs can include physical constants, like ice thermal conductivity or gravity acceleration, observed environmental fields, like surface speed or topography, and uncertain coefficients for the processes that are parameterized, like sediment critical shear stress or bed slipperiness. Uncertainties in models come from different sources, such as the quality and quantity of input data, incompletely represented or missing physical processes, or inadequate simplification (e.g. unconstrained parameterization).

Regarding the devoted time and addressed questions, models are divided into diagnostic and prognostic. The *diagnostic* models focus on the actual conditions and state to investigate the system and its behavior, for instance the driving processes of an observed phenomenon. The *prognostic* models aim to predict and estimate the probability of the system's reaction to the certain conditions differing from the actual ones. Thereby, diagnostic models require, first of all, valid input data of the current state of a system, while the prognostic models need to be well constrained by the description of processes and their cross-interactions. Despite those two types of models address different questions, they are complementary. To make a robust projection using a prognostic model, we need first to obtain a reliable description of the system's processes with diagnostic models.

In this chapter, we aim to improve our understanding of subglacial processes governing the seasonal velocity changes. A diagnostic model is therefore used.

As described in Section 1.3.4, in Greenland the flow of outlet glaciers is strongly dependent on the subglacial water variability. Thereby, both systems – ice masses and underlying hydrology – attracted the attention of the modelling community. *Subglacial hydrological* models describe the state of water under a glacier and the corresponding evolution of the host environment, usually focusing on the water routing network and water pressure in it. Despite the intensive progress, these models are still difficult to set up as many input parametrizations are required. Moreover, the output results are hardly verifiable as the water state measurements are only possible locally in boreholes and a large-scale network location cannot be easily observed. *Ice flow* models are focused on a glacier itself, describing the ice body motion and geometry evolution. As inputs, they require the description of the initial conditions, e.g. surface and bed topography which are relatively easy to obtain over large areas. Also, those models can be rather easily validated by surface speed observations as velocity field is one of the major outputs.

For a realistic representation of the seasonal and/or long-term evolution of the glacier motion, subglacial hydrology and ice flow models can be coupled to simulate the interaction between the basal condition and the moving ice (Brinkerhoff et al., 2021; Flowers, 2015). In practice, the realistic coupling still remains difficult to achieve, because our understanding of the interaction between the ice and subglacial environment remains poorly constrained.

Here, we will use an ice flow model, forced with the temporally dense observations of ice surface velocity, established in Section 2, in order to improve the understanding about mutual influence between seasonal evolution of basal conditions and glacier motion.

Ice flow models estimate the velocity inside the ice from generic fluid mechanics equations based on the principles of mass and momentum conservation (Brinkerhoff and Johnson, 2013; Gillet-Chaulet et al., 2012). As described in Section 1.2, for the considered applications, ice behaves as a highly viscous non-Newtonian fluid so that inertial terms can be neglected and the internal velocity and pressure fields can be derived from the Stokes equations. Thus, at a given time, the glacier's 3D velocity field is fully determined by the glacier geometry, the ice material properties and the boundary conditions.

The most complex models (usually referred to as *Full Stokes model*) include all stresses described by the Stokes equations and solve the whole set of equation in 3D without approximations (Gillet-Chaulet et al., 2012; Mahaffy, 1976) (Figure 39). They are suitable for any flow conditions and glacier configurations. In return, they require intensive computations.

In certain flow conditions or glacier configurations, the Stokes equations can be simplified by neglecting some stress components.

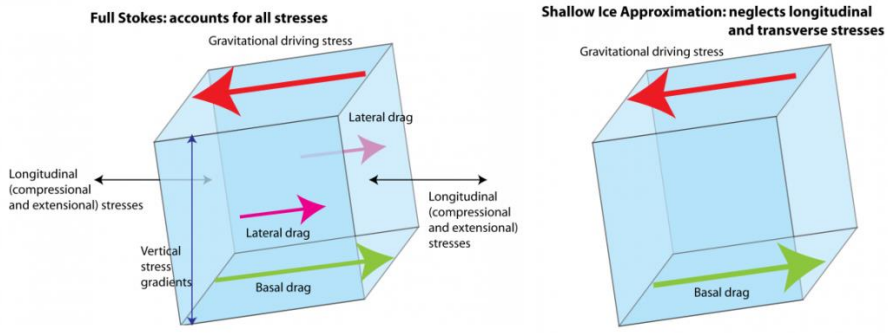

Figure 39 Full Stokes (left) and Shallow-Ice Approximation (right) models with stress components included. Adapted from *antarcticglaciers.org*.

For instance, the *Shallow-Ice Approximation* (SIA) is one of the simplest problem framing (Figure 39). It assumes that the driving stress is fully balanced by the basal drag alone, without any other stresses taken into account (Bueler, 2016; Winkelmann et al., 2011). In general, such simplification is allowed when horizontal dimensions of a glacier are much larger than its thickness, hence the name "shallow", and where the ice is frozen to the bed so that only the shear stresses in the horizontal plane are relevant. In such a case, the horizontal velocity only depends on the local surface slope and ice thickness. These are typical conditions when considering an ice-sheet interior. Another simplification is the *Shallow-Shelf Approximation* (SSA), which, contrary to the SIA, neglects horizontal shear and keep the other deviatoric stress components, i.e. longitudinal and vertical shear stresses (Bueler and Brown, 2009; Winkelmann et al., 2011). Its name refers to ice shelves as the drag is null on the water interface. As no or negligible horizontal shear stress occurs within the ice body, the horizontal speed is considered to be vertically uniform and the equations are vertically integrated.

The approach of how the spatial component is taken into account divides the flow models into *flowline* and *planar*. The former type makes the simulations along a single line, usually

following the glacier streamline (1D), and is suitable for long narrow valley glaciers (Jay-Allemand et al., 2011; Nick et al., 2012). The latter includes the two horizontal dimensions (i.e. plan-view and 3D models). Both types can average or neglect some processes vertically distributed across the ice column, like SSA do, and thus be *depth-integrated*. Simplified models are computationally more efficient. Models of intermediate complexity have also been developed, aiming to balance the usage universality with computational cost (Passalacqua et al., 2016).

3.2 Case study of the Russell sector: ice flow seasonal dynamics

In ice flow models the conditions at the base are usually prescribed by a friction law, i.e. boundary conditions that relate basal shear stress to the sliding velocity. Both components are thus solution of the problem. Basal conditions being particularly uncertain, most ice flow models are now equipped with *inverse methods* that allow to infer the friction parameters from observed surface speed.

Of our three case study glaciers, two are marine-terminating and one is land-terminating. As discussed in Section 1.3, the seasonal ice flow of the marine-terminating glaciers is influenced by changes in the terminus position and basal drag, while the land-terminating glaciers are only influenced by the latter. In the inverse problem, the marine-terminating glaciers consequently induce an additional level of complexity compared to the land-terminating glaciers.

In the context of this thesis, we chose to focus on the land-terminating Russell sector to have a first overview of the opportunities and limitations of inverse modelling in deriving the seasonal evolution of the basal conditions from the high-frequency observations described in Section 2.3.1.1. We decided to use a Full Stokes model rather than SIA or SSA approximations to keep the most precise description of the problem. Nevertheless, it could be interesting in the continuation of this work to evaluate the suitability of these approximations for the framing of the study.

The details of the model implementation, the integration of velocity observations, and the results obtained for the changes in the basal conditions (basal drag, water pressure) have been submitted for publication in *The Cryosphere* (Derkacheva et al., 2021) and therefore correspond to the continuation of this chapter.

The Cryosphere, 15, 5675–5704, 2021
https://doi.org/10.5194/tc-15-5675-2021

The Cryosphere Open Access EGU

Seasonal evolution of basal environment conditions of Russell sector, West Greenland, inverted from satellite observation of surface flow

Anna Derkacheva[1,★], **Fabien Gillet-Chaulet**[1,★], **Jeremie Mouginot**[1,2,★], **Eliot Jager**[1], **Nathan Maier**[1], **and Samuel Cook**[1]

[★]These authors contributed equally to this work.[1]Institute of Environmental Geosciences, Université Grenoble Alpes, CNRS, IRD, INP, 38400 Grenoble, Isère, France
[2]Department of Earth System Science, University of California, Irvine, 92697 CA, USA

Correspondence: Anna Derkacheva (anna.derkacheva@univ-grenoble-alpes.fr, der_a@mail.ru)

Received: 3 June 2021 – Discussion started: 16 June 2021
Revised: 2 November 2021 – Accepted: 15 November 2021 – Published: 17 December 2021

Abstract. Due to increasing surface melting on the Greenland ice sheet, better constraints on seasonally evolving basal water pressure and sliding speed are required by models. Here we assess the potential of using inverse methods on a dense time series of surface speeds to recover the seasonal evolution of the basal conditions in a well-documented region in southwest Greenland. Using data compiled from multiple satellite missions, we document seasonally evolving surface velocities with a temporal resolution of 2 weeks between 2015 and 2019. We then apply the inverse control method using the ice flow model Elmer/Ice to infer the basal sliding and friction corresponding to each of the 24 surface velocity data sets. Near the margin where the uncertainty in the velocity and bed topography are small, we obtain clear seasonal variations that can be mostly interpreted in terms of an effective-pressure-based hard-bed friction law. We find for valley bottoms or "troughs" in the bed topography that the changes in modelled basal conditions directly respond to local modelled water pressure variations, while the link is more complex for subglacial "ridges" which are often non-locally forced. At the catchment scale, in-phase variations in the water pressure, surface velocities, and surface runoff variations are found. Our results show that time series inversions of observed surface velocities can be used to understand the evolution of basal conditions over different timescales and could therefore serve as an intermediate validation for subglacial hydrology models to achieve better coupling with ice flow models.

1 Introduction

In recent decades, the Greenland ice sheet (GrIS) has been losing mass, reaching a negative mass balance of about $-286 \pm 20\,\mathrm{Gt\,yr^{-1}}$ in 2010–2018 (Mouginot et al., 2019). An important part of this loss comes from the ice-discharge acceleration of tidewater glaciers. In addition, ice dynamics also plays a significant role in land-terminating sectors as ice flow affects the flux of ice into the ablation area and the ice-sheet topography, with feedbacks between ice-sheet surface elevation and the atmosphere that can enhance mass loss in century-scale projections (Edwards et al., 2014; Le Clec'h et al., 2019).

Water pressure at the glacier base is considered to be a major control on basal sliding that affects ice dynamics over different timescales (Nienow et al., 2017; Davison et al., 2019). For instance, seasonal modulations of water input to the bed, induced by summer melt, are able to lead to peak glacier accelerations of up to +360 % locally compared to winter mean velocities (Palmer et al., 2011). Increased water pressure as melt drains through an inefficient drainage system is assumed by existing theories to be the mechanism driving the acceleration during the beginning of the melt season. However, increased drainage efficiency during the late melt season leads to a decrease in water pressures and causes a commensurate glacier deceleration. Moreover, during high melt years, higher early summer velocities are therefore supposed to be responsible for the slower velocities during the late melt and winter seasons, offsetting the higher initial ice flux (Tedstone et al., 2015). This suggests that the future of

Published by Copernicus Publications on behalf of the European Geosciences Union.

the GrIS will likely be affected by the evolution of the surface runoff discharge and its effect on the subglacial drainage system.

The rate of surface melting is already increasing due to warming of the air, as well as other factors amplifying this phenomenon such as the decrease in ice albedo (Box et al., 2012), decrease in the capacity of the firn to retain meltwater (Mikkelsen et al., 2016), or even change in the dominant weather type (Van Tricht et al., 2016). Climate models predict that this melting will continue to grow in the future. Surface runoff is also increasing in both observations and projection models (Ahlstrøm et al., 2017; Trusel et al., 2018). However, it is still debated how the ice flow velocity will respond to this enhancement in water production in the long term: with a continuous increase (Zwally et al., 2002; Greskowiak, 2014; Hewitt, 2013), an increase until a threshold (Tedstone et al., 2013, 2014; Poinar et al., 2015), or even a decrease (Tedstone et al., 2015; Stevens et al., 2016). A complete analysis of all these hypotheses suggests that different trends will dominate according to the timescale and altitudes considered (Nienow et al., 2017; Davison et al., 2019).

These questions have motivated the development of physical models to represent the subglacial environment and its interaction with ice dynamics. Basic ingredients of these models are (i) a subglacial hydrological model that computes effective pressure and (ii) a friction law that relates basal shear stress to the effective pressure and the basal sliding velocity. However, because of the limited accessibility to the basal environment, the processes at the bed remain difficult to characterize, limiting their understanding. Both components are still a matter of debate, and no consensus has emerged.

Flowers (2015) gives a review of available subglacial hydrology models and their theoretical background. A total of 13 models of various complexity have participated in a recent model intercomparison exercise that shows that physical approaches coupling several elements of the basal drainage system significantly differ from simpler approaches for short term, e.g. diurnal, variations (De Fleurian et al., 2018). To be run operationally, these physical models require highly detailed input data (e.g. basal topography, runoff forcing) that are often not available, and they suffer from a lack of direct and independent data for calibration and validation. The most direct way to access the basal hydrology system is to drill boreholes that allow direct measurements of the water pressure (Smeets et al., 2012; Meierbachtol et al., 2013; Van De Wal et al., 2015; Wright et al., 2016). While very valuable, these local measurements can show a high spatial variability depending on the element of the basal hydrology (e.g. active or inactive part of the subglacial drainage system) that is sampled (Wright et al., 2016), so these observations make the validation of subglacial hydrology models challenging, as they are not necessarily representative of the large-scale average basal conditions that are required to reproduce and predict the long-term evolution of the entire glacier. However, basal hydrology models have been applied in real settings, and the comparison with available observations has stimulated their development. For instance, in de Fleurian et al. (2016) the timing of the response of modelled water pressure broadly agrees with observations but with a significant difference in terms of magnitude. In addition to an efficient and inefficient drainage system, Hoffman et al. (2016) introduced a third weakly connected component to explain the decline of water pressure during the late melt season. Alternatively, Downs et al. (2018) suggest a reduction in hydraulic conductivity to explain the tendency of models to underpredict observed winter water pressure.

The second required component, the friction law, depends on the properties of the bed. Deformable basal sediments (commonly referred to as soft or weak beds) are usually modelled using a Mohr–Coulomb criterion to relate the basal shear stress to the effective pressure (Iverson et al., 1998; Fowler, 2003; Joughin et al., 2019; Helanow et al., 2021). For hard beds (rigid rocks or non-deformable till, as opposed to deformable till), the friction is controlled by the ice deformation over the small-scale basal roughness, inducing a relationship between the basal shear stress and the sliding velocity. Increasing the water pressure can open subglacial cavities, reducing the apparent bed roughness and the basal friction (also referred to as basal shear stress or basal traction). Several friction laws that incorporate the dependency on effective pressure have thus been developed from both theoretical (Schoof, 2005) and empirical considerations (Budd et al., 1984). Because of the inaccessibility of the basal environment, the bed properties of specific glaciers are generally poorly known. Additionally, geophysical investigations have shown evidence for the presence of deformable sediments and hard beds in relatively close proximity (Dow et al., 2013; Harper et al., 2017). Thus, in situ direct validation of the friction law is not possible, so models must be evaluated against surface velocities, necessarily inducing uncertainties in the basal hydrology and ice deformation.

Synthetic simulations of typical Greenlandic land-terminating glaciers using coupled basal hydrology–ice dynamics models have been able to reproduce the main observed features of the seasonal modulation of surface velocity (Hewitt, 2013; Gagliardini and Werder, 2018; Cook et al., 2020). Models have mostly been validated using velocity fluctuations recorded by GPS at the ice-sheet surface (Bougamont et al., 2014; Kulessa et al., 2017; Christoffersen et al., 2018; Koziol and Arnold, 2018). Again, being precise, these measurements are local and do not allow the spatial variability of the processes to be properly constrained.

Satellite imagery allows us to derive surface velocity fields with a good spatial resolution and coverage. During the last decade, the number of such observations has increased significantly with the launches of missions such as Landsat-8 or Sentinel-1 and Sentinel-2 (Fahnestock et al., 2016; Mouginot et al., 2017; Joughin et al., 2018; Lemos et al., 2018), allowing the reconstruction of flow variations at the seasonal

scale with a temporal resolution of days to weeks (Altena and Kääb, 2017; Vijay et al., 2019; Derkacheva et al., 2020).

Most recent ice flow models now include various inverse methods that make it possible to spatially constrain a free parameter that relates the basal friction to the sliding velocity using the observed geometry and surface velocity field (MacAyeal, 1993; Arthern and Gudmundsson, 2010). Several studies have then tried to validate or constrain the friction law from the inferred basal friction and velocity. As the velocities in ice sheets can range over several orders of magnitude, this can be assessed from the spatial variations in a single inversion, assuming that changes are mostly driven by the friction law and not by spatial variations in the bed properties. Thus, Arthern et al. (2015) found that the basal stress in Antarctica, on average, roughly agrees with a uniform value of ~ 100 kPa; however this can change locally by orders of magnitude. Spatially aggregating inversions with models of different complexity, Maier et al. (2021a) found that large areas under the Greenland ice sheet broadly agree with hard-bed physics. The other possibility to constrain the friction law is to use several inversions to study the temporal changes; however this can be done only where the changes are sufficiently large. For instance, Gillet-Chaulet et al. (2016) found that changes in the drainage basin of Pine Island Glacier in Antarctica over a 14-year period can be explained with a mostly plastic relation, where the basal friction is weakly sensitive to changes in sliding velocity.

Temporal variations in basal hydrology have been addressed by several studies using inferred velocity fields to constrain temporal variations in the basal water pressure by assuming a certain friction law that also includes effective pressure (Jay-Allemand et al., 2011; Minchew et al., 2016). The main objective of this paper is to assess the ability of existing inverse methods to use satellite-derived seasonal velocity maps to infer seasonal variations in the basal conditions.

We focus on a land-terminating sector of the southwest coast of Greenland located at 67° N, 50° E. This sector includes a slow-moving ice-sheet margin and three distinct glaciers (from north to south): Insunnguata Sermia, Russell Glacier, and Ørkendalen Gletscher (Fig. 1). Hereafter, this area is referred to as the Russell sector. Extensive measurements of the ice thickness were carried out over the study region using radar sounders, especially through NASA's Operation IceBridge mission (Morlighem et al., 2013; Lindbäck et al., 2014). This dense data set with an average radar-line spacing of less than 500 m is exceptional by Greenland standards, where most radar lines are generally separated by tens of kilometres. In addition, because of its relative accessibility, this sector has been the subject of numerous complementary geophysical investigations such as boreholes, seismometers, or GPS (Smeets et al., 2012; Dow et al., 2013; Wright et al., 2016; Harper et al., 2017; Kulessa et al., 2017; Maier et al., 2019), making it a privileged study site for numerical investigations (Bougamont et al., 2014; de Fleurian et al., 2016; Koziol and Arnold, 2017, 2018; Downs et al., 2018; Christoffersen et al., 2018; Brinkerhoff et al., 2021).

We use the three-dimensional finite-element full-Stokes ice flow model Elmer/Ice (Gagliardini et al., 2013) to invert for the seasonal evolution of the basal friction and sliding speed using surface velocity maps covering an entire year with a time step of 2 weeks. We address how best to integrate satellite-derived velocity into a model, as well as the sensitivity of the inverted basal friction fields to initial ice temperature and some commonly used model parameters. From the inverted basal fields, we estimate the corresponding evolution of the water pressure using a pressure-dependent friction law (Schoof, 2005; Gagliardini et al., 2007). Results are discussed using available in situ measurements and outputs from numerical models of subglacial hydrology and regional climate. Finally, we conclude with the usability of inverse-flow models with spatio-temporally dense observations of surface velocity to derive the seasonal evolution of the glacier basal environment.

2 Seasonal surface velocities

We have derived a time series of horizontal surface ice velocity of the Russell sector at a spatial resolution of 150 m using satellite images collected between 2015 and 2019 by Landsat-8, Sentinel-1, and Sentinel-2. The details on the data processing can be found in Derkacheva et al. (2020) and are summarized below.

Normalized cross-correlation is used to estimate the features' (or radar speckle) displacement between primary and secondary images taken on two different dates, which is further converted to the v_x (east–west direction) and v_y (north–south direction) surface flow speed components (Mouginot et al., 2017; Millan et al., 2019). Only the measurements with time intervals shorter than 32 d (1 month) are used in order to capture rapid dynamic changes in ice flow. To reduce the noise and relatively large errors associated with these short revisit times, a linear non-parametric smoothing algorithm LOWESS (locally weighted scatterplot smoothing; Cleveland, 1979; Cleveland and Devlin, 1988), also known as the locally weighted polynomial regression, is applied to the resulting time series (Derkacheva et al., 2020). The final accuracy of the product has been validated against in situ GPS measurements from Maier et al. (2019) showing that the product can be used to describe ice-velocity fluctuations with a temporal resolution of about 2 weeks over a large area.

To further minimize noise and increase spatial coverage, we also reduce this 5-year time series to a "typical year". To do so, we compute the median value for a given calendar interval over all 5 years simultaneously, averaging on a regular step of a half-month, referred to hereafter as "early" and "late" halves. We thus obtain a final product of 24 maps describing the median behaviour of annual ice flow variations. The two surface velocity components v_x and v_y for early July

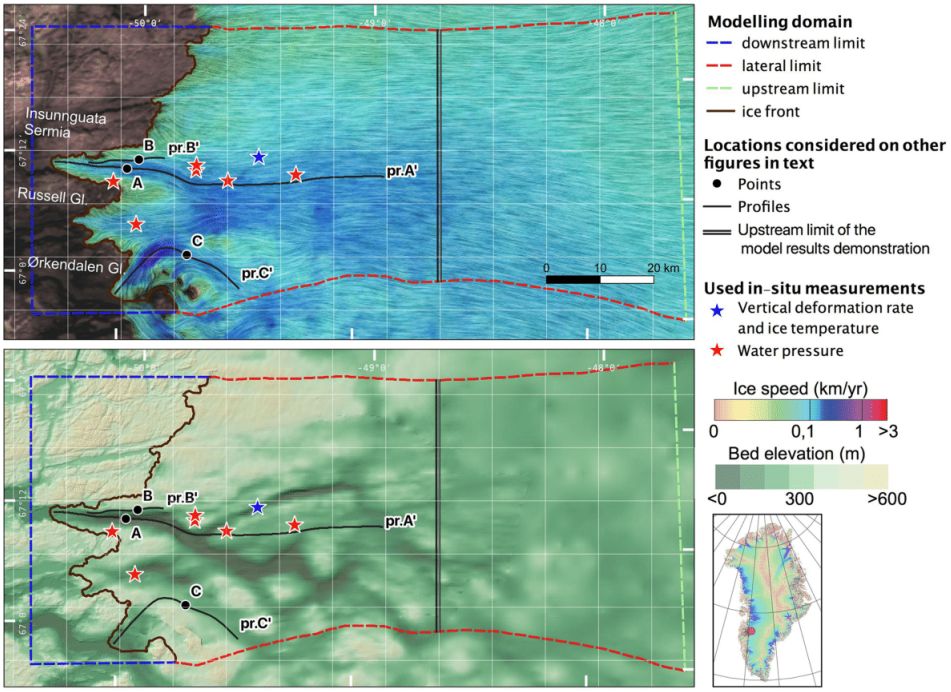

Figure 1. Study area with modelling domain. The points (A–C) and profiles (pr. A', pr. C') indicate locations considered later in the text, and the blue and red stars indicate locations of in situ measurements (Smeets et al., 2012; Meierbachtol et al., 2013; Wright et al., 2016; Hills et al., 2017; Maier et al., 2019). The top panel shows the surface ice velocity overlaid on the line integral convolution (Cabral and Leedom, 1993) to visualize the flow vector direction (Mouginot et al., 2017). The bottom panel displays the bed elevation from BedMachine (Morlighem et al., 2017). The white 10 km grid used here is identical in all figures in the article. The projection used is polar stereographic north with latitude of true scale at 70° N.

are shown in Fig. 2a and b. This temporal aggregation is justified by the fact that, between 2015 and 2019, this sector experienced a relatively similar pattern of speed variations each year without outstanding extremes. Thus the median year is fairly representative of the behaviour of this sector during the considered period. For instance, we compare in Fig. 2f the temporal evolution of the median speed with the annual data sets at a location on Insunnguata Sermia (point A in Fig. 1). The root-mean-squared deviation between the median and the annual data sets is about 10 m yr^{-1}, which is within 10 % of the mean winter speed. In addition to twice-monthly time series, we also calculated the mean velocity of early and late January, February, and March observations to produce a map of mean winter speed (MWS hereinafter).

Besides the velocity maps, we generate a spatially distributed estimate of the velocity uncertainties for each temporal step. This uncertainty σ is computed per pixel as $\sigma = \mathrm{SD}/\sqrt{n}$, where SD is the standard deviation of the averaged measurement in each time step and n is the number of averaged measurements. The typical range of n varies a lot in time and space (see Fig. 2e) due to the varying characteristics of the sensors and seasonal evolution of surface conditions (e.g. melting of snowfall). For instance close to the ice front it changes from few images in winter to more than 60 in summer. For the same reasons, the accuracy of the generated velocity maps varies over time and space. While for winter maps (January–April, December), the errors are generally below 10 m yr^{-1}, these values can rise 3- to 4-fold between May and November, especially for the most inland areas where fewer observations are available and the smooth terrain makes satellite speed tracking difficult (see Figs. 2c, d and A1).

Our averaged data set is consistent with previous satellite products and ground observations in the area (Joughin et al., 2008; Palmer et al., 2011; Fitzpatrick et al., 2013; Lemos et al., 2018), as we observe the same range of speed and seasonal changes. The average winter speed varies from 50 m yr^{-1} outside of the main glacier trunks to 100–250 m yr^{-1} at Insunnguata Sermia and Russell Glacier and up to 300 m yr^{-1} at Ørkendalen Gletscher. At the end of

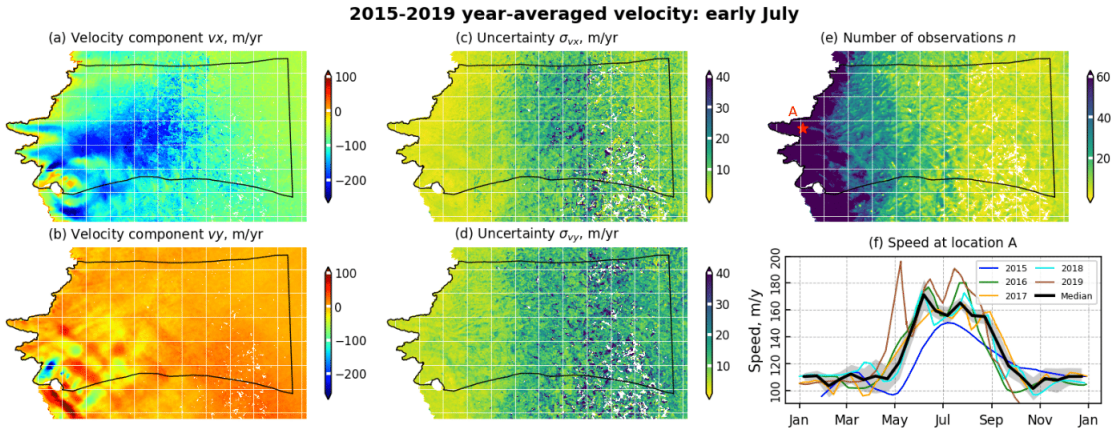

Figure 2. Year-averaged velocity data set. **(a–e)** Horizontal surface velocity components (v_x and v_y), associated uncertainties (σ_{v_x} and σ_{v_y}), and number of observations per pixel (n). **(f)** Comparison between the original speed observations for the years 2015 to 2019 and the year-averaged data set where the grey shading represents the 1σ interval at point A in **(e)** and in Fig. 1. White pixels in maps **(a, b, e)** correspond to areas that are ice-free or with no data and in maps **(c, d)** to pixels with fewer than two velocity observations. The white grid lines are spaced by 10 km.

spring and into summer, a pronounced speed-up is observed for the entire sector, with the acceleration starting at the ice margin and gradually moving upstream. As an extreme case, a short-term acceleration up to +360 % above MWS was observed over one small area (Palmer et al., 2011). However, the mean range of the speed acceleration spatially varies between +100 % and +250 % above MWS. Depending on the location, the deceleration starts in late June or July, continuing for 1 to 4 months. Consequently, the autumn velocity can be lower than the winter mean, which is especially typical for Ørkendalen Gletscher.

The ice in this sector flows in a clear east–west orientation with an averaged flow direction of about 275° from the north, except for Ørkendalen Gletscher. Therefore, the y-velocity component (v_y) is close to zero (Fig. 2b), and variations in order of magnitude of several tens of metres per year can induce relatively large changes in the estimated flow direction. We noted in our time series that the flow direction varies up to ±25° across the year. This effect is only observed in velocity fields derived from the optical images and not in the synthetic aperture radar images, suggesting that this phenomenon is not related to a real change in ice flow direction. We attribute this effect to changes in surface illumination and shadow length being a function of solar elevation change from March to October and assume that it can induce the supplementary displacements of the surface feature footprints tracked by cross-correlation algorithms. Indeed, on Insunnguata Sermia, the mean v_y velocity vector component changes from +60 to +10 and −40 m yr^{-1} between the velocity fields derived with Sentinel-2 optical images in early March (ascending low sun), late June (solstice), and early September (descending low sun) correspondingly. To deal with this phenomenon, we assume that the total magnitude of the majority of our time series was not severely affected. The most extreme case of the lowest sun angle and only optical imagery used with short time spans gives the magnitude overestimation by 10 % or about 10 m yr^{-1} for the average speed of 100 m yr^{-1} over the domain. So we only consider the norm of the velocity vector for the model inversions, keeping the vector direction to be defined by the model itself.

According to theoretical expectations, the ice flow is most likely to be affected by seasonal variations in surface runoff reaching the bed across the area that is under the equilibrium line. At Russell, the long-term equilibrium line is estimated to be at ∼ 1500 m (Van De Wal et al., 2012). Even so, the GPS records have shown the presence of a short summer speed-up further inland as well (Bartholomew et al., 2012; Greskowiak, 2014), with acceleration of about +5 % up to 50 km inland from the equilibrium line (Greskowiak, 2014). That corresponds to about +1 m yr^{-1} above the local MWS and is within the noise level in our velocity data set. For this reason the area of interest is limited to approximately 100 km upstream from the ice margin, which corresponds to a surface elevation of about 1400 m.

3 Methods and model description

We use the finite-element ice flow model Elmer/Ice (Gagliardini et al., 2013) to compute the 3D velocity field in the Russell sector and infer the basal conditions over an entire "typical" year using the 24 surface velocity maps.

We use the basal topography given by BedMachine version 3 (Morlighem et al., 2017). The surface elevation comes from the Greenland Ice Mapping Project (GIMP; Howat et al., 2014), which has a nominal date of 2007. This is 10 years earlier than our velocity observations. Thickness changes in this area are about $-1\,\mathrm{m\,yr^{-1}}$ near the margin (Helm et al., 2014; Csatho et al., 2014; Yang et al., 2019), which is relatively small compared to the ice thickness (see Fig. A2b); thereby we use it as it is. Over a single year the topography does not change significantly either. The average in situ observed rate is less than $\pm 1\,\mathrm{m\,yr^{-1}}$ and partly attributed to the summer uplift by pressurized water (Bartholomew et al., 2010; Cowton et al., 2016). We therefore keep the surface topography fixed for all inversions. In doing so, we assume that basal changes are the only drivers of the seasonal ice speed variations and that changes in driving stresses due to surface elevation variations are negligible.

In the remainder of this section we describe the modelling domain, the model set-up, and the inverse modelling method.

3.1 Modelling domain and mesh

Our model domain corresponds to the ice catchment basin of the three land-terminating glaciers mentioned above, reaching to about 100 km inland for the reasons explained in Sect. 2 (Fig. 1). The lateral borders of the domain are defined by flow lines derived from the mean multi-annual observed surface velocity (Rignot and Mouginot, 2012). As the margin is land-terminating and thus does not require special boundary conditions at the front, the model domain has been extended a few kilometres in front of the margin in expectation of future transient simulations, leaving the possibility of an advance of the glaciers open.

To create the mesh, we start by meshing the horizontal footprint of the domain using the Elmer/Ice anisotropic mesh capabilities that rely on the MMG library (https://www.mmgtools.org/, last access: 20 February 2020; Dapogny et al., 2014). The mesh adaptation scheme equi-distributes the interpolation error of the observed surface velocities and thickness. Because the domain is relatively small, the mesh resolution is allowed to vary between 150 m near the margin and 400 m up to 40 km inland, with a maximum value of 1 km attained progressively beyond this. The resulting two-dimensional irregular mesh consists of approximately 60 000 linear triangular elements and approximately 30 000 nodes. It is then vertically extruded into 20 layers to form the 3D mesh. As the vertical velocity gradients are expected to be higher near the bed, the vertical resolution increases following a geometric progression and is 2 times smaller at the bed than at the surface. The 3D mesh is then stretched vertically so that the top and bottom surfaces follow the topographies given by GIMP and BedMachine. The model does not support meshes that have null thickness. In order to include ice-free areas, we therefore impose the arbitrary value of 0.9 m thickness for them. This thickness is sufficiently small that the remaining "ice" in the ice-free areas will have no impact on the results of the inversions and will avoid crashing the model.

Note that our study area is well-constrained by the radar measurements of ice thickness in the lower half of the domain, while the upper part of the basin has been much less surveyed (see Fig. A2a). A mass conservation algorithm (Morlighem et al., 2011) has been used for the interpolation of the basal topography in the densely surveyed area, while kriging is used outside (Morlighem et al., 2017). The latter is used when mass conservation is not practicable due to sparse thickness measurement and/or slow surface motion; thereby the resulting bed topography is often less accurate. Reported uncertainties in the bed elevation over the lower part of our domain, except the steep-slope front line, are generally lower than 30 m or below 6 % of ice thickness, while on the upper part they can reach up to 300 m, or 20 % of the ice thickness. We also notice that a few small-scale features are not well captured in the BedMachine version used here (v3.10, 20 September 2017), such as the southwestern nunataks next to Ørkendalen Gletscher that are actually ice-free but for which the data display an ice thickness of 100–140 m. The surface data provided by GIMP (Greenland Ice Mapping Project) are constructed from a combination of digital elevation models derived with ASTER and SPOT-5 satellites for the ice-sheet periphery and margin and photoclinometry derived with the AVHRR (Advanced Very-High-Resolution Radiometer) space-borne sensor in the ice-sheet interior (Scambos and Haran, 2002). Their uncertainty has been estimated by comparing with spaceborne lidar altimetry from ICESat satellites and is about ±1 m over most areas of interest (Howat et al., 2014).

3.2 Direct model

3.2.1 Field equations

To compute the 3D ice velocity ($\boldsymbol{u}$) and ice pressure (p_i) fields, we solve the Stokes equations that express the conservation of momentum and mass for an incompressible fluid:

$$\begin{cases} \mathrm{div}(\boldsymbol{\sigma}) + \rho \boldsymbol{g} = 0 \\ \mathrm{div}(\boldsymbol{u}) = 0, \end{cases} \tag{1}$$

where ρ is the ice density, $\boldsymbol{g}$ is the gravity vector, and $\boldsymbol{\sigma} = \boldsymbol{\tau} - p_\mathrm{i}\mathbf{I}$ is the Cauchy stress tensor with $\boldsymbol{\tau}$ the deviatoric stress tensor and $\mathbf{I}$ the identity matrix.

To close the system, we use the classical viscous isotropic power law, known as Glen's flow law, that non-linearly relates the deviatoric stress tensor to the strain rate tensor $\dot{\boldsymbol{\epsilon}}$ as

$$\boldsymbol{\tau} = 2\eta\dot{\boldsymbol{\epsilon}}, \tag{2}$$

where the effective ice viscosity η is given by

$$\eta = \frac{1}{2}(EA)^{-1/n}\dot{\epsilon}_\mathrm{e}^{(1-n)/n}, \tag{3}$$

where the second invariant of the strain rate tensor is given by $\dot{\epsilon}_e^2 = \mathrm{tr}(\dot{\boldsymbol{\epsilon}}^2)/2$, n is the Glen exponent, and E is an enhancement factor, and the rate factor A depends on the ice temperature T following an Arrhenius relationship:

$$A = A_0 e^{-\frac{Q}{RT'}}, \tag{4}$$

where A_0 is the pre-exponential factor, Q is an activation energy, R is the gas constant, and $T' = T - T_\mathrm{p}$, where the pressure melting point is given by $T_\mathrm{p} = 273.15 - C_\mathrm{c} p_\mathrm{i}$ with C_c the Clausius–Clapeyron constant. The parameter values used by us are given in Table 1.

Initializing the temperature field is a difficult problem as the thermal state in an ice sheet has a long-term memory requiring multi-millennial spin-up simulations (Goelzer et al., 2017), and the heat sources are in general poorly constrained and make the thermo-mechanical problem nonlinear (Schäfer et al., 2014). Here we use the temperature field simulated by the ice-sheet model (http://www.sicopolis.net/, last access: 18 June 2019) for the present state of the Greenland ice sheet (Goelzer et al., 2020).

We have compared the temperature profiles to existing in situ borehole measurements from the ablation zones of Insunnguata Sermia (Harrington et al., 2015; Hills et al., 2017). Results are shown in Fig. A3. The modelled temperature appears to fit the observations better at higher altitudes around 40 km from the ice margin (Hills et al., 2017; Harrington et al., 2015, location S5) than at lower altitudes (Harrington et al., 2015, locations S2–S4). This is likely because SICOPOLIS does not have the resolution and processes to accurately capture the individual land-terminating glaciers. Within the first 40 km from the glacier terminus, observed temperatures are generally warmer than −6 °C across the entire ice column, while the model finds the temperature to be up to 6 °C cooler across the ice column. Further inland from the glacier terminus, both measurement campaigns found that the temperature decreases from −10° at the surface to −13 °C at a depth of about 200–300 m and then rises to near-melting temperature at the glacier base. Here the SICOPOLIS temperature follows a similar trend with a slight 1–2 °C warmer divergence over the ice column but becomes cooler about 200 m above the bedrock. At the glacier base, the model shows in all boreholes a deviation of 2–4 °C below the measurement, meaning that the measured temperature at the base is closer to the melting point than SICOPOLIS estimates. As deformation rates increase rapidly and non-linearly with increasing ice temperature (Eq. 4), the generally colder modelled ice could potentially cause the ice flow model to underestimate the internal deformation compared to reality. However, the investigation of the influence of temperature field uncertainties on the basal-friction inversions shows a more limited influence than, for instance, uncertainties in the basal topography (Habermann et al., 2017). As the temperature field reproduces part of the observed spatial variability sufficiently well, in the following, we briefly assess the sensitivity of the results to the ice rheology only by changing the value of the enhancement factor E. To validate the final rheology parameterization, the model-derived ice deformation profiles are compared further against in situ borehole measurements (Sect. 4.3).

3.2.2 Boundary condition

As we model only a part of the ice sheet, in addition to the conditions at the top and bottom surfaces we have to prescribe boundary conditions at the sides of the domain. Note that the lateral sides of the domain have been chosen to be sufficiently far from the regions of interest so that, for the diagnostic simulations presented here, the details of the boundary conditions should not affect the solution at distances greater than a few ice thicknesses. For all the boundaries, we denote by $\boldsymbol{n}$ the unit vector normal to the boundary and pointing outward from the model domain.

The lateral sides of the domain coincide with flow lines so there should be no ice flux entering the domain. We therefore impose the following condition:

$$\boldsymbol{u} \cdot \boldsymbol{n} = \boldsymbol{0}. \tag{5}$$

Along the tangential directions, we keep the natural stress-free condition and thus neglect the tangential shearing components along these boundaries. At the inflow boundary (Γ_i) we apply Dirichlet conditions for the horizontal components of the velocity vector ($\boldsymbol{u}_\mathrm{H} = (u_x, u_y)$) using the observed surface winter-mean velocities ($\boldsymbol{u}_\mathrm{s}^\mathrm{obs}$) (see Sect. 2):

$$\boldsymbol{u}_\mathrm{H} = \boldsymbol{u}_\mathrm{s}^\mathrm{obs}. \tag{6}$$

Note that we impose uniform velocities along the vertical direction and thus neglect the deformation profile at the starting point of the initialization model run. The deformation of the ice column occurring in the inland areas of the modelling domain are the modelled state adapted to the given boundary conditions. We expect that the results a few ice thicknesses from the border should be insensitive to the prescribed non-deforming vertical profile at the lateral borders (Mangeney et al., 1996; Gagliardini and Meyssonnier, 2002). This is consistent with observations in the area (Maier et al., 2019) and with our model results (Sect. 4.3), which show that the deformation profiles contribute to only a small portion of the surface velocities. We leave the natural stress-free condition for the vertical direction and thus neglect vertical shearing along this boundary.

The bottom and top surfaces correspond to natural interfaces of the ice. For the upper surface, Γ_s, we neglect the atmospheric pressure and impose a stress-free condition:

$$\boldsymbol{\sigma} \cdot \boldsymbol{n} = 0. \tag{7}$$

For the bottom boundary, Γ_b, we use a linear friction law that relates the tangential basal shear stress, $\boldsymbol{\tau}_\mathrm{b} = \mathbf{T} \cdot \boldsymbol{\sigma} \cdot \boldsymbol{n}$, to the basal sliding velocity $\boldsymbol{u}_\mathrm{b} = \mathbf{T} \cdot \boldsymbol{u}$ and a no-penetration condition for the normal velocity:

Table 1. List of the constants used in the model.

Description	Value	Units
Gravity constant $\boldsymbol{g}$	9.8	$\mathrm{m\,s^{-2}}$
Ice density ρ	910	$\mathrm{kg\,m^{-1}}$
Glen exponent n	3	
Pre-exponential factor A_0	2.84678×10^{-13} for $T'<10\,^{\circ}\mathrm{C}$ 2.35567×10^{-2} for $T'\geq-10\,^{\circ}\mathrm{C}$	$\mathrm{Pa^{-3}\,s^{-1}}$
Activation energy Q	60 for $T'<10\,^{\circ}\mathrm{C}$ 115 for $T'\geq-10\,^{\circ}\mathrm{C}$	$\mathrm{kJ\,mol^{-1}}$
Gas constant R	8.314	$\mathrm{J\,K^{-1}\,mol^{-1}}$
Clausius–Clapeyron constant C_c	9.8×10^{-2}	$\mathrm{K\,MPa^{-1}}$
Enhancement factor E	1	

$$\begin{cases} \boldsymbol{\tau}_\mathrm{b}+\beta\boldsymbol{u}_\mathrm{b}=0 \\ \boldsymbol{u}\cdot\boldsymbol{n}=0, \end{cases} \tag{8}$$

where $\mathbf{T}=\mathbf{I}-\boldsymbol{n}\otimes\boldsymbol{n}$ is the tangential operator, and β is an effective friction coefficient which is tuned using the inverse procedure described in the following section. Hereafter, we will mainly refer to the norm of the sliding velocity and basal friction denoted by $u_\mathrm{b}=|\boldsymbol{u}_\mathrm{b}|$ and $\tau_\mathrm{b}=|\boldsymbol{\tau}_\mathbf{b}|$.

The results of the inversions using a fixed geometry and a single velocity data set have been shown to be weakly sensitive to choice of friction law as the friction field must satisfy the global stress balance (Joughin et al., 2004). This has been confirmed in the area by Koziol and Arnold (2017), who found very small differences when comparing the basal shear stress fields inverted using three different friction laws.

3.3 Inverse model

Inverting for the basal friction coefficient using the observed surface velocities is now widespread in many ice-sheet models (Jay-Allemand et al., 2011; Gillet-Chaulet et al., 2012; Larour et al., 2014; Shapero et al., 2016; Maier et al., 2021a). Here, we use the variational control inverse method implemented in Elmer/Ice (Gagliardini et al., 2013), and in the following we highlight the main steps.

For a given observed surface velocity field, the optimal effective basal friction field β in Eq. (8) is found by minimizing the following cost function:

$$J_\mathrm{tot}=J_0+\lambda J_\mathrm{reg}, \tag{9}$$

where J_0 is an error term that measures the mismatch between model and observed surface velocities and J_reg is a regularization term weighted by the regularization parameter λ. As the effective friction coefficient must remain positive, we use the following change of variable $\beta=10^{\alpha}$, and the optimization is done on α.

We define J_0 as

$$J_0=\frac{1}{2}\sum_{1}^{N^\mathrm{obs}}\left(\frac{|\boldsymbol{u}_\mathrm{H}^\mathrm{mod}|-|\boldsymbol{u}_\mathrm{H}^\mathrm{obs}|}{|\boldsymbol{\sigma}_\mathbf{u}|}\right)^2, \tag{10}$$

where $|\boldsymbol{u}_\mathrm{H}^\mathrm{mod}|$ is the norm of the model horizontal surface velocity vector interpolated at the N^obs locations where we have an observation for the horizontal surface velocity $\boldsymbol{u}_\mathrm{H}^\mathrm{obs}$ (the nodes of the storage file grid, in fact), with $\boldsymbol{\sigma}_\mathbf{u}$ the norm of the vector composed by the estimated velocity uncertainties (see Sect. 2). Note that here we have chosen to compare only the norm of the vector and disregard the error on the flow direction, as the direction is mainly governed by the topography and, additionally, may be biased in our velocity observations, as explained in Sect. 2.

To regularize the inverse problem, J_reg is a Tikhonov regularization term that penalizes the horizontal derivatives of α as

$$J_\mathrm{reg}=\frac{1}{2}\int_{\Gamma_\mathrm{b}}\left(\frac{\mathrm{d}\alpha}{\mathrm{d}x}\right)^2+\left(\frac{\mathrm{d}\alpha}{\mathrm{d}y}\right)^2\mathrm{d}\gamma. \tag{11}$$

The gradients of J_tot with respect to the nodal values of α are computed by using the adjoint model, and the cost function is minimized using the limited-memory quasi-Newton routine M1QN3 (Gilbert and Lemaréchal, 1989).

4 Inferred basal sliding speed and friction

4.1 Mean winter state

4.1.1 Model set-up

We start with an inversion of the MWS velocity map to get the initialization state for our seasonal investigations. The friction coefficient is initialized using a previous inversion

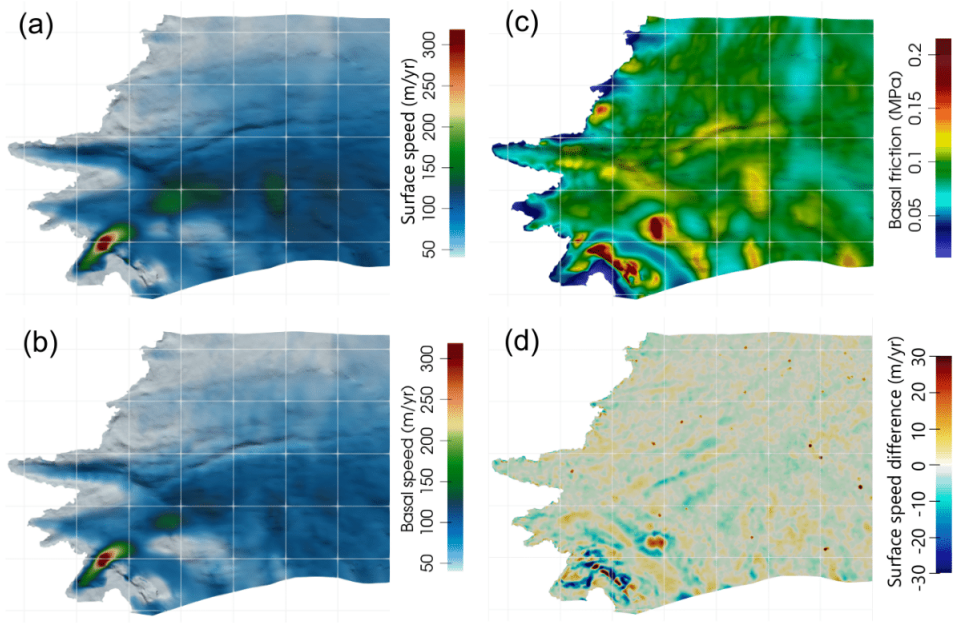

Figure 3. **(a)** Modelled horizontal surface speed, **(b)** basal sliding speed, and **(c)** basal friction inferred from the mean winter surface speed (MWS) overlaid on the basal topography hillshade. Panel **(d)** shows the difference between modelled and observed surface speed. The white grid lines are spaced by 10 km.

performed with Elmer/Ice for the whole Greenland ice sheet using the shallow-shelf equations for the force balance, and the minimization is stopped after 200 evaluations of the cost function. Based on such procedure, we run six inversions for different values of the regularization parameter λ. Following the L-curve method (Hansen, 2001), the optimal parameter is a compromise between fitting the observations and having a smooth solution which should correspond to the point of highest curvature in a log–log plot of the regularization term against the error term. We plot those L-curves and report the mean relative error $\overline{J_0} = \sqrt{(2J_0/N^{\text{obs}})}$ in Fig. A5a. The curves show the expected behaviour where $\overline{J_0}$ increases as λ and J_{reg} decreases. In the absence of model errors and for uncertainties accurately estimated and normally distributed, we should expect $\overline{J_0}$ to be close to 1. Here, for the smallest regularization we obtain a minimum $\overline{J_0} \sim 0.6$. For the following seasonal investigations, we choose the value $\lambda = 2500$, which gives a relative error just above 1 and is located in the area of highest curvature. Additionally, we observe that the results are weakly sensitive to the exact choice of λ as the standard deviation of the sliding speed and basal friction computed over all tested values of λ, except the smallest and the largest ones are generally below 5 % in 92 % and 91 % of nodes respectively.

4.1.2 Results

The modelled surface speed, sliding speed, and basal friction for the mean winter state are shown in Fig. 3. The modelled surface velocity shows a good agreement with the observations (Fig. 3d), with a root-mean-square error of about 3 m yr^{-1}, similar to the reported uncertainties (Fig. A5b). We notice however large differences (up to 30 m yr^{-1}) between the modelled and observed velocity for a few places. This is especially true near Ørkendalen Gletscher where some nunataks are not correctly represented in BedMachine. A similar issue with under-resolved subglacial features may also explain the speed mismatch on the other side of the Ørkendalen valley where BedMachine shows a large uncertainty (> 140 m). These areas appear with a particularly high friction compared to the rest of the domain (> 0.2 MPa) and nearly no sliding, meaning that the velocities resulting from vertical shear are already larger than the observations, likely because of the overestimated ice thicknesses. The areas of friction close to zero along the margin could be due to underestimation induced by BedMachine as well, as here, on the steep slopes of thin ice, the reported error-to-thickness ratio is larger than 50 % (Fig. A2a).

The spatial pattern of the basal velocity is very similar to that of the surface. We obtain a sliding ratio u_b/u_s of about 0.9 for most of the domain, consistent with defor-

mation profiles measured in the area (Maier et al., 2019). Deformation-induced speed estimated as $u_d = u_s - u_b$ is generally on the order of 10–15 m yr^{-1} and can locally increase to up to 30–50 m yr^{-1} in locations of high traction.

For most of the domain, the inferred basal friction τ_b is on the order of 0.1 MPa. These values are consistent with previous inversions in the same area performed by Koziol and Arnold (2017) using winter 2008–2009 velocities. Together with a typical sliding velocity of 100 m yr^{-1}, this falls in the velocity–traction relationship derived at the catchment scale by Maier et al. (2021a), which was interpreted as indicative of hard-bed conditions. However, Maier et al. (2021a) also found several patches in this catchment where the bed is weaker than the average. We also observe a few areas where relatively high sliding speeds correlate with particularly low friction compared to elsewhere, with values lower than 0.05 MPa. This is particularly true for a large fraction of Ørkendalen Gletscher, but can also be seen at the tongue of Russell Glacier. While for the glacier terminus we cannot rule out an under-estimation of the ice thickness that would be compensated for by higher inferred sliding speed, this would also be consistent with a "weak" bed offering less resistance due to the presence of deformable till or substantial cavitation. To our knowledge, no in situ measurements have been done on Ørkendalen Gletscher to confirm the presence of till, but seismic measurements suggest the presence of subglacial sediment within 13 km of the terminus of Russell Glacier (Dow et al., 2013), in agreement with the weak bed assumed by us.

There is no such low friction under Insunnguata Sermia, where the flow is well constrained by a subglacial valley for the first 25 km inland from the terminus. This is in agreement with Harper et al. (2017), who found no evidence of soft sediments at the bed of Isunnguata Sermia from their network of 32 boreholes. However, no borehole reached the bottom of the valley, where the friction is locally the lowest, it being higher on the adjacent sides. Higher upstream, the subglacial valleys are not aligned with the ice flow lines, and, in general, we have higher friction on the leeward sides of the valleys. The spatial heterogeneity of the basal friction shows that it is possible to reconcile opposite views on the nature of the bed in this sector (Booth et al., 2012; Dow et al., 2013; Kulessa et al., 2017; Harper et al., 2017), as the basal conditions of this sector are heterogeneous and can likely change from an inferred hard to weak bed over distances of a few ice thicknesses. Additionally, this could suggest that some specific conditions are required for till accumulation, for instance topographic depressions or lack of drainage efficiency, forming the non-uniform bed properties in the long run.

4.2 Seasonal inversions

4.2.1 Model set-up

To investigate the year-around behaviour of the basal friction and velocity fields, we perform the inversions for each of 24 velocity maps presented in Sect. 2 (hereafter called "time steps") in a similar way as described above for MWS.

As the observation errors are not uniform in time, to assess the sensitivity of the summer results to the regularization, we run a new L-curve analysis with the early July velocity data set. The results are shown in supplementary Fig. A5a. The minimal value of $\overline{J_0}$ is now close to 2. This could be due either to an under-estimation of the uncertainties on observed ice speed for these 2 weeks or to the model not being able to exactly match the summer observations. The latter could be due to model errors not taken into account or because reducing the observations to a standard year leads to more inconsistencies in summer as there is more variability during this period compared to winter. In addition, we found that the results are more sensitive to the choice of λ than for the MWS inversion, as the standard deviation on u_b and τ_b between the different tested λ, except the smallest and the biggest one, is about 15 %. However, we remark that the dependency of J_{reg} on λ is relatively similar to those obtained with the MWS data sets, and the value $\lambda = 2500$ seems consequently to also be a good compromise for this early July data set. Thereby, this λ value is used for inversions of all 24 time steps.

To reduce the computational burden for the independent twice-monthly inversions, the basal friction coefficient field is initialized each time using the solution obtained for MWS inversion. As we cannot guarantee in general that the given λ will be optimal for all the data sets, we stop the minimization after 30 evaluations of the cost function to avoid overfitting. This choice is motivated by the fact that in general the cost function decreases rapidly during the first iterations and then stagnates at a value close to the noise level where it may overfit the observations if regularization is not used (Arthern and Gudmundsson, 2010; Habermann et al., 2012). This can be clearly seen in Fig. A5b for the spring and summer months, where the error decreases during the first 10 to 20 iterations then stagnates. Note that the error can locally increase between two successive evaluations of the cost function, as the global convergence is enforced by a line-search phase so that the minimization routine effectively checks that the cost function decreases globally. As expected, because the velocities are relatively stable during the winter months and thus close to the MWS, the error is already very low when compared with the initial guess and stabilizes or eventually slightly increases (while J_{reg} decreases) during the iterations.

In Fig. A1, we show the misfit maps as the difference between observed and modelled surface ice speeds (only for the early half of the months as the second halves usually show a similar range of mismatch). The periods showing the largest misfit correspond to the transition between different surface

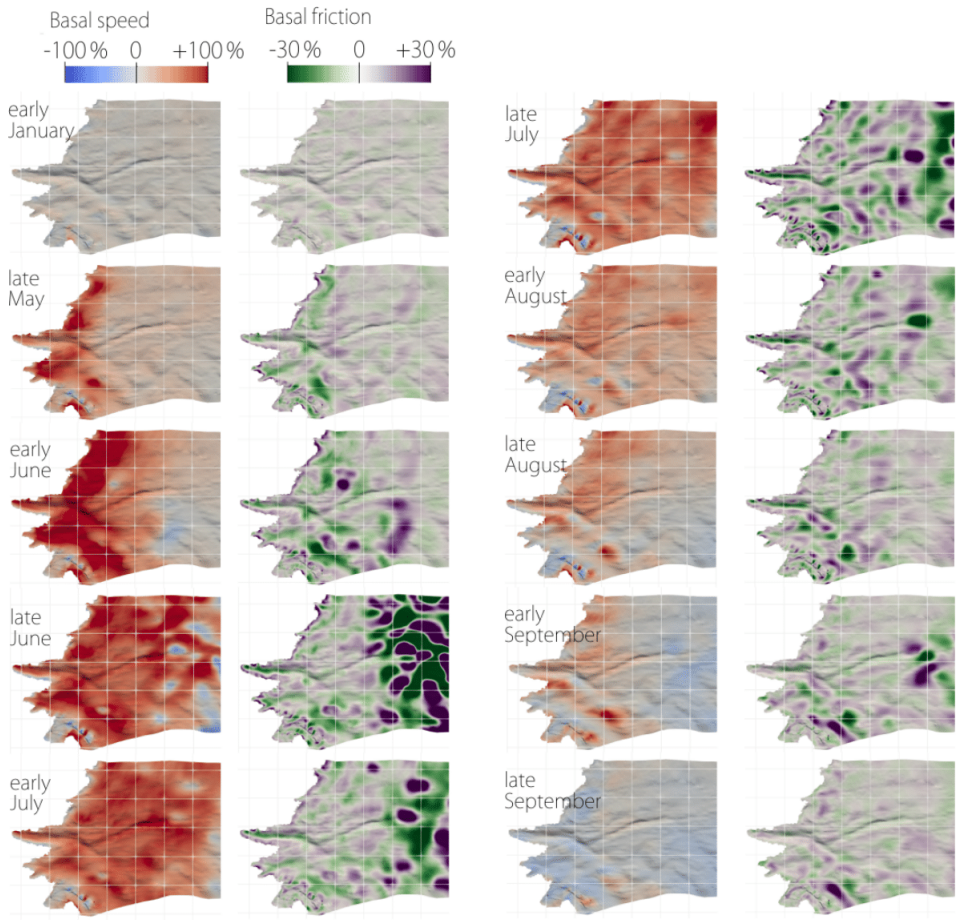

Figure 4. Seasonal change of basal sliding speed (left subcolumns) and basal friction (right subcolumns) relative to the winter mean state, with basal topography hillshade added. The white grid has a 10 km step.

conditions. This is especially true in June, July, and September, when the surface changes from snow-covered to melting ice or vice versa. Note that the November data set seems more likely to be corrupted by poor satellite imagery than by the surface conditions. The uncertainty in the observed velocity for these periods often exceeds 30 m yr^{-1}, which represents a significant relative uncertainty in the upper part of the domain where speed is below 100 m yr^{-1}. However, the surface velocity is captured relatively accurately in the first 50–70 km from the margin, and the inversions give a good match between the adjacent time steps, giving us confidence in the interpretation of the basal fields in these areas. Taking that into account, as well as the uncertainties in basal topography, we mainly discuss the results on the downstream half of the modelling domain.

4.2.2 Results

In Fig. 4, we present the ratio of the inverted basal friction τ_b and sliding speed u_b for 10 inversions (out of the 24) to their winter mean state. Results from early October to early March are fairly similar, so we show only early January as an example of this period. From late March to late September, the relative changes in τ_b and u_b are shown every 2 weeks. Note that the extreme τ_b variability in late June and early July over the upper shown area is most likely unrealistic and induced by the discussed quality of the input surface velocity fields.

These inversions demonstrate that u_b doubles first along the ice margin, and then the acceleration propagates inland until mid-July. Thus, in the first 20 km from the ice margin, the maximum sliding speed is reached by early June, whereas higher up the peak it only arrives later in early July. Similarly,

the sliding speed first decreases along the ice margin and then the deceleration propagates inland until the end of September. In late September, the velocity is generally lower than the MWS by about 10 % to 20 % in the first 10–15 km from the margin, while it is still slightly higher or equal further upstream.

Following changes in sliding speed, the basal friction τ_b first decreases along the ice margin in late May. Over time, this decrease then propagates higher up inland, mainly in subglacial valleys and depressions. Note that the lowering of τ_b is usually correlated with the highest increases in sliding speed. However, as the global force balance must be maintained, this decline cannot be widespread. Thus, the stresses are redistributed locally and simultaneously on higher parts of the bed or on the sides of subglacial valleys where the friction rises. The sliding speed here rises as well, but it is less pronounced. Both increases and decreases in τ_b over the domain are of the order of ± 30 %. By late September, τ_b returns to its winter state. One exception is Ørkendalen Gletscher where it remains higher and where we also have the most significant decrease in sliding speed in autumn compared to the mean winter value.

4.3 Ice deformation versus sliding speed

An interesting question is how the contributions of deformation and sliding to the surface speed change seasonally. Ice viscosity and surface topography are fixed in inversion set-ups; therefore the temporal variability in the ice deformation rate occurs only due to the change in the inferred basal friction (thus, in the shear stress). We found that in summer, on average across the domain, the magnitude of the deformation speed u_d increases, but the proportion of surface velocity it represents decreases. The mean winter value of u_d across the domain is about 8 m yr^{-1}, rising to about 20–30 m yr^{-1} in some topographically predefined locations (Fig. A4a). In early July it rises by +12 % above winter on average (Fig. A4b). At the same time, the contribution of deformation to glacier surface motion estimated as a fraction u_d/u_s slightly decreases from winter to summer over the majority of the domain (see Fig. A4c), with mean values of 10 % and 8 % respectively and an absolute change rate of a few metres per year. That means the sliding velocity represents about 90 % of the surface flow in winter and slightly more when velocities increase in summer. As expected, the summer acceleration observed on the surface is mainly due to enhanced sliding. In a full-Stokes model, the entire 3D velocity field depends on the material properties and boundary conditions, so that the deformation profiles are not constant in time. Here only model-inferred basal friction can influence the deformation profile, making it variable from one inversion to another. If the deformation changes remain small compared to changes in sliding velocities in magnitude (Fig. 5a), it is interesting to note that, by changing only the basal conditions in the model, the relative changes in deformation rate are important between winter and summer. Similar in situ observations have been made by Maier et al. (2021b) by examining spatio-temporal changes in deformation, sliding, and surface velocities over a 2-year period using GPS and a dense network of inclinometers installed in borehole grid drilled in Ørkendalen Gletscher.

Although direct measurements of sliding velocities and ice deformation rates are rare in Greenland, Maier et al. (2019) estimated them within a network of boreholes located approximately 20 km from the ice margin of the Insunnguata Sermia catchment (blue star in Fig. 1). These observations were made during the winter season 2015–2016 in boreholes spaced by about 150 m and include GPS (providing the surface velocity), temperature, and inclinometry (providing the deformation). At this site, the deformation was found to account for only 4 % of the surface velocities, and, thus, ice sliding was responsible for the overwhelming majority of surface velocity during the winter. In addition, their measurements show that the majority of deformation happens in the first 150 m above the bed and that almost no deformation occurs in the upper 75 % of the ice column.

We compare the measurements made by Maier et al. (2019) with the modelled fields at the same location in Fig. 5a and b, in the form of vertical profiles of the horizontal velocity magnitude $|\boldsymbol{u}_H|$ and shearing rates $\mathrm{d}|\boldsymbol{u}_H|/\mathrm{d}z$. The inverted sliding and surface velocities in winter of about 105 and 115 m yr^{-1} are in agreement with the in situ measurements of 110 and 114 m yr^{-1} respectively. It would appear that the model produces a slightly larger deformation speed u_d than observed (10 m yr^{-1} versus 4.6 m yr^{-1} in the in situ observations), with excess deformation mostly coming from the upper 75 % of the ice column and thus not expected to vary in time with changes in basal friction τ_b.

During the velocity peak in early July, the deformation speed u_d in our inversions rises up to 15 m yr^{-1} and thus increases relative to winter by about +50 % (maximum u_d is 19 m yr^{-1} in early August or +90 % from winter, Fig. 5a). At the same time, basal sliding speed u_b increases from 105 to 165 m yr^{-1} (+57 %), and surface speed u_s increases from 115 to 180 m yr^{-1} (+57 %). Consequently, at this specific point, the relative increase in surface flow velocities from winter to summer is about 8 % due to an increase in the deformation rate, and the remaining 92 % corresponds to the accelerated sliding. Note that the overall contribution of u_d to the surface speed is almost invariable from winter (9 %), being slightly lower at the moment of maximum glacier motion (8 %) and slightly higher when deformation of basal layers intensifies (10 %).

It should also be noted that the actual magnitude of modelled deformation and sliding velocity in this analysis depends on the constitutive law used for the ice rheology (here, Glen's flow law, Eq. 2). In this study, we assume a viscosity enhancement factor $E = 1$ (see Eq. 3) to describe the ability of ice to deform. This means we adopt Glen's rheology parameters constrained via laboratory experiments without

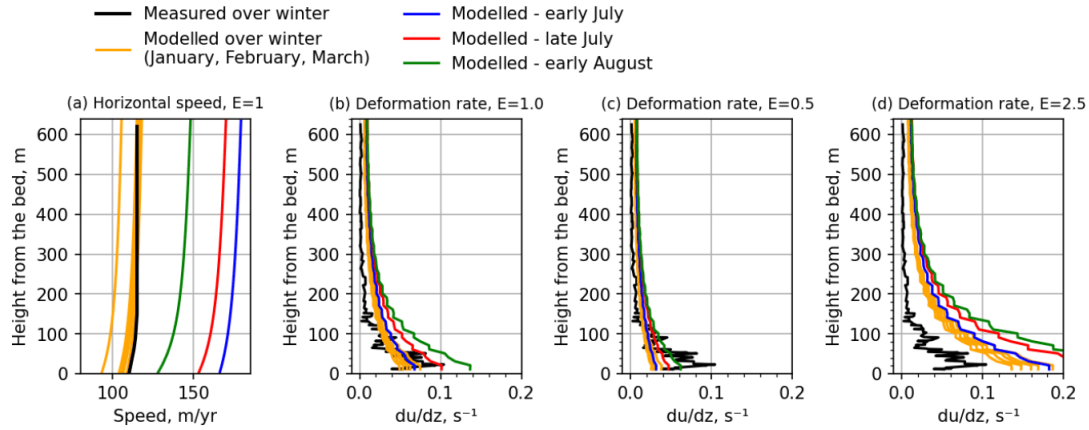

Figure 5. Vertical profiles of modelled **(a)** horizontal velocity magnitude $|\boldsymbol{u}_{\mathrm{H}}|$ and **(b–d)** vertical shear rate $\mathrm{d}|\boldsymbol{u}_{\mathrm{H}}|/\mathrm{d}z$ for varying enhancement factors E at the location of borehole measurements done by Maier et al. (2019), drawn here in black.

any modifications. Larger values of E would correspond to simulation of softer ice, while lower values of E represent stiffer ice, which provides the adjustment of viscosity imposed by laboratory parameters if required. In Fig. 5, we test different values of E against in situ observations from Maier et al. (2019) by comparing the vertical deformation rate obtained for inversions performed with $E = 0.5$, 1, and 2.5 with the mean measured winter deformation profile obtained over nine boreholes.

With $E = 0.5$, and thus stiffer ice, the model reproduces the winter deformation rate well over most of the ice column but underestimates it for the lower 100 m above the bedrock; there the majority of shearing happens according to observations. In this case, even with enhanced shearing in summer, modelled deformation does not reach the level observed in winter. With $E = 2.5$, the ice deformation is much larger over the entire ice column than observed, suggesting that the modelled ice is too soft. A value of $E = 1$ provides a good compromise where the deformation rate over the winter months near the bed is similar to that of the in situ measurements and does not deviate significantly at other depths.

4.4 Relation between τ_{b} and u_{b}

To further discuss the leading processes behind the seasonal variability of basal fields, we take a closer look at three different locations that are representative of the main types of τ_{b}-versus-u_{b} behaviour obtained across the modelled domain (Fig. 6). As the aim will be to interpret the results in terms of friction law, we show the seasonal evolution of τ_{b} as a function of u_{b} (bottom subplots) together with their evolution during the year (top subplots).

In the first case, at point A located at the Insunnguata valley floor about 10 km from the ice margin (see Fig. 1), we have a clear anti-correlation between friction and sliding speed. The friction slightly rises from January to May, but there is no clear trend for the velocity. Notable acceleration starts in early May in conjunction with a decrease in τ_{b}. High sliding velocities, 65 % above the winter average, are maintained until mid-July with some variability. At the same time, the basal friction continuously decreases until August, with a minimum at 30 % below the winter average. After that, u_{b} decreases and τ_{b} increases back to winter values. The seasonal evolution of τ_{b} as a function of u_{b} shows a clear hysteresis where for the same friction, the sliding speed is higher during the acceleration phase (spring) than during the deceleration phase (autumn). Such an effect, interpreted as an opening–closing of the subglacial water cavity and/or longitudinal stress coupling with the upper parts of the glacier, was already observed in situ (Sugiyama and Gudmundsson, 2004) and studied numerically (Iken, 1981). In our results, the regions that experience this type of behaviour are mainly the subglacial valley bottoms where the basal friction is not too low in winter (~ 0.1 MPa).

Point B is positioned on the northern valley slope of Insunnguata Sermia at about the same distance from the ice margin as point A. Here, during the warm season, the basal friction globally rises (+20 %) together with basal sliding (+80 %). However, there is a preceding phase from January to May where the sliding speed slightly increases in conjunction with decreasing friction. The clear acceleration in May correlates with an increase in friction. Further, the sliding velocity starts to diminish in June while the friction reaches its maximum only in August. This relation between τ_{b} and u_{b} is generally associated with valley sides and higher basal topography.

Point C is located at Ørkendalen Gletscher about 10 km along the glacier flow line from the ice margin (Fig. 1). This point is typical of areas with lower-than-average fric-

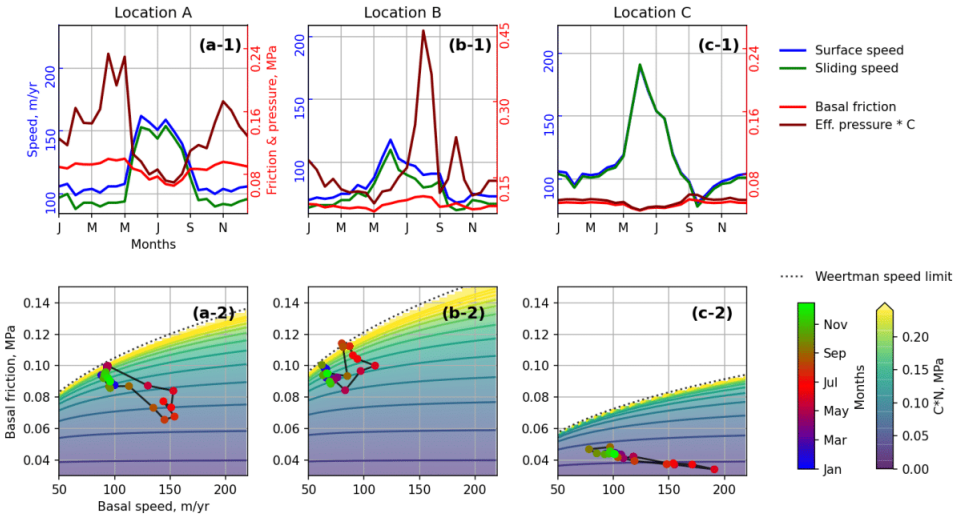

Figure 6. Surface speed u_s, sliding speed u_b, basal friction τ_b, and scaled effective pressure CN at three locations indicated in Fig. 1. **(a-1–c-1)** show the evolution of u_s, u_b, τ_b, and CN as a function of time. Panels **(a-2–c-2)** represent the evolution of the relation between τ_b and u_b throughout the year, where the coloured background shows the scaled effective pressure CN obtained from Eq. (12) with the solid lines corresponding to isovalues spaced by 0.02 MPa. The dotted line represents the upper limit corresponding to the Weertman regime (see Sect. 5.1).

tion values (< 0.05 MPa); i.e. the base offers little resistance throughout the entire year. Here, the velocity increases almost 2-fold from late April to late May and is associated with a relatively small absolute change in friction of about 0.01 MPa compared to point A where τ_b dropped by almost 0.04 MPa. For this point, it is also worth noting that the speed minimum appears in early September, clearly below the winter mean. As for point A, changes are mostly anti-correlated; i.e. sliding rises with decreasing friction and vice versa, and the maximum in u_b corresponds to a minimum in τ_b.

5 Basal water pressure

5.1 Water-dependent friction law

5.1.1 Definition of the friction law

To interpret the variations in the basal friction and velocity in terms of water pressure, we adopt a friction law that has been originally proposed to represent the flow of clean ice over a rough bedrock with cavitation (Schoof, 2005; Gagliardini et al., 2007). In its simplest form, this friction law relates the basal friction τ_b to the effective pressure N and the sliding velocity u_b and, following Gagliardini et al. (2007), is expressed as

$$\tau_b = CN\left(\frac{u_b}{C^n N^n A_s + u_b}\right)^{1/n}, \quad (12)$$

where A_s is the sliding parameter without cavities, C is a parameter related to the maximum bed slope, and the exponent n is usually equal to the flow law exponent in Eq. (2). The effective pressure N conceptually represents how frictional forces are reduced by the presence of pressurized water and is equal to the difference between the Cauchy compressive normal stress to the bed surface and the water pressure p_w. Here we approximate the normal stress by the ice pressure p_i solution of the Stokes system; thus $N = p_i - p_w$. In practice, p_i is close to the hydrostatic ice overburden pressure $p_i \approx \rho g H$, and this allows it to be consistent with observations of the water pressure that are reported as a fraction of the ice overburden pressure. A friction law of a type similar to Eq. (12) has been used by several ice flow models coupled with a subglacial hydrology model (Pimentel et al., 2010; Hewitt, 2013; Gagliardini and Werder, 2018; Cook et al., 2021). While Eq. (12) was primarily developed for hard beds, a similar expression has been proposed for deformable beds by Zoet and Iverson (2020). The main difference is that for a given basal friction, their expression predicts that u_b tends to zero at high effective pressure while it tends to the Weertman sliding velocity with Eq. (12). Similarly to account for the two friction regimes, a regularized Coulomb friction law where the dependency on N is not explicit but parameterized has been proposed by Joughin et al. (2019) and has been shown to provide a good fit to observations for Pine Island Glacier, Antarctica. Some authors (Koziol and Arnold, 2018, 2017; Brinkerhoff et al., 2021) have used a different

friction law where the dependency on N has been introduced in a mostly empirical manner (Budd et al., 1979). While Koziol and Arnold (2018) found that this last law gives a slightly better fit to observations than Eq. (12) in a coupled ice flow–hydrology model of a glacier, we do not consider this law as it has less physical background and does not satisfy Iken's bound (Iken, 1981).

Designing our workflow, we preferred to invert for the effective friction coefficient (β in Eq. 8) first and then interpret its temporal variations in terms of effective pressure in a second step. There are several reasons for this. First, it should be numerically more stable to use a linear relation in the numerical model. In winter, including the MWS case, the friction law involving the effective pressure is close to the Weertman regime and thus weakly sensitive to N, meaning that the modelling results would be much more sensitive to the regularization process described in Sect. 3.3. Second, this two-step approach allows us to carefully address the choices of A_s and C parameters of the effective pressure-based law.

From Eq. (12) it can be shown that the product CN can be expressed as a function of the fields τ_b and u_b, which are solutions of the inverse problem, and the parameter A_s as

$$CN = \tau_b \left(1 - \tau_b^n u_b^{-1} A_s\right)^{-1/n}. \quad (13)$$

Expressed this way, it is easy to see that this expression exhibits two asymptotic behaviours.

- When $\tau_b^n u_b^{-1} A_s \ll 1$, the relation tends to a Coulomb-type friction law $\tau_b = CN$, and the effective pressure does not depend on the sliding speed u_b anymore. That implies a lower bound for Eq. (13) $N > 0$, so we cannot get a water pressure exceeding the ice pressure. However, even if that is observed with local in situ measurements (Wright et al., 2016; Hoffman et al., 2016), the water pressure greatly exceeding ice overburden is very unlikely (Doyle et al., 2015). Thereby both very small positive and negative N values practically lead to the same outcome of near-zero friction in the model.

- When $\tau_b^n u_b^{-1} A_s \to 1$, $CN \to \infty$, and at the limit the basal friction is described by the classical Weertman friction law $\tau_b = (u_b/A_s)^{1/n}$. In practice N should satisfy the upper bound $N \leq p_i$, meaning that the water pressure must remain positive.

Finally, the case $\tau_b^n u_b^{-1} A_s \geq 1$ is incompatible with Eq. (13) and means that the inverted values are inconsistent with the choice of A_s as the bed is already too slippery even without water.

5.1.2 Choice of the sliding parameter A_s

The sliding parameter A_s should depend on the near-basal ice rheology and on the small-scale roughness of the bed and thus is likely to be variable in space. Large values of A_s correspond to a slippery bed even without water, while low values represent a bed that offers more frictional resistance to the flow. Thus, depending on the choice of A_s, one can approach the Weertman or Coulomb limits of the friction law defined in Eq. (12). This will obviously affect the effective pressure values N retrieved but also the amplitude of the seasonal changes expected to be observed.

Using a similar method to infer changes in water pressure from several inversions of the basal conditions under Variegated Glacier over a year, Jay-Allemand et al. (2011) compute a spatially varying A_s so that the upper bound $N \leq p_i$ is always fulfilled. In an application to the same area we investigate, Koziol and Arnold (2017) use winter velocities and a modelled winter basal water pressure field to invert for a single parameter in a friction law similar to Eq. (12). Their coefficient μ_b corresponds to our C, and they use a constant value for the product $A_s C^n$ (i.e. their $\lambda_b A_b$), so that for us this would correspond to spatially varying A_s and C. They found that the whole domain is close to the Weertman regime in winter.

Here, to spatially constrain A_s, we first compute the sliding coefficient A_s^W that would be obtained in the Weertman regime using u_b and τ_b from the MWS inversion. The derived coefficient corresponds to an "effective" A_s^W as it will reflect the effective winter state of the bed roughness which could include the smoothing effects of potentially existing cavities that are not closed or kept open by basal meltwater (Cook et al., 2020).

The distribution of A_s^W at the mesh nodes is shown in Fig. 7a. The median value is 4.04×10^{-21} m Pa^{-3} s^{-1}, corresponding approximately to a basal traction τ_b of 0.1 MPa for a sliding speed of about 100 m yr^{-1}. The same order of magnitude is found by looking at the relations between τ_b and u_b inferred by Maier et al. (2021a) at the scale of the GrIS catchments that are identified as being subject to hard-bed physics (see authors' Supplement, Fig. S9 and Table S1). Our A_s^W estimate also has a consistent order of magnitude with the value 1.66×10^{-21} used by Hewitt (2013) and Gagliardini and Werder (2018) in synthetic applications developed to represent a typical Greenlandic land-terminating glacier such as those in the Russell sector.

The spatial distribution of A_s^W mostly reflects the inferred winter basal friction (Fig.3c), where the areas with low friction would imply a very slippery bed. As mentioned previously, if we assume that these areas of weak bed might be underlain by deformable till or too many water-filled cavities maintained over the winter, the value of A_s^W has no meaning in its Weertman law sense, and these areas should be described with a Coulomb friction law. It is then reasonable to impose an upper bound for A_s. There is no obvious upper limit, and we arbitrarily choose $A_s^{MAX} = 8.3 \times 10^{-21}$ m Pa^{-3} s^{-1} (Fig. 7a). That limit covers 85 % of the mesh nodes and puts the areas of very likely assumed weak bed (Ørkendalen Gletscher valley, Russell Glacier tongue) in

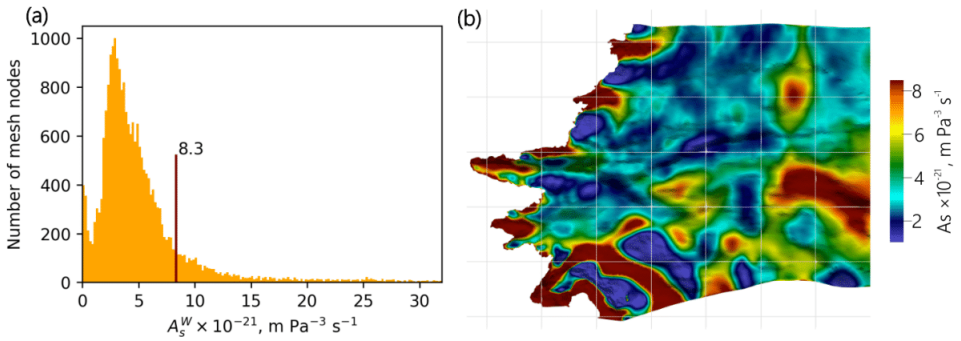

Figure 7. **(a)** Histogram of A_s^W. **(b)** Map of the A_s derived with Eq. (15) and used for water pressure calculation, with basal topography hillshade added. The white grid lines are spaced by 10 km.

the Coulomb regime while leaving the areas of strong bed in the Weertman one.

Directly taking A_s^W to compute N from Eq. (13) would lead to incompatibilities for some nodes in some inversions, i.e. $\tau_b^n u_b^{-1} A_s^W \geq 1$. We therefore choose to lower A_s as $A_s^W - 2\delta A_s^W$, where δA_s^W is the uncertainty on A_s^W estimated by uncertainty propagation of inferred u_b and τ_b computed as

$$\frac{\delta A_s^W}{A_s^W} = \frac{\delta u_b^W}{u_b^W} + n \frac{\delta \tau_b^W}{\tau_b^W}, \tag{14}$$

where δu_b^W and $\delta \tau_b^W$ are the standard deviation of the basal speed and friction obtained from the six inversions of the winter months from January to March, as we assume no significant changes in basal conditions over this period. Our winter velocity and friction uncertainties are about 4 % and 2 % respectively on median across the domain.

As more than 90 % of nodes have the January to March variability of τ_b and u_b values under $\pm 2\delta$ from mean winter state, we consider it sufficient to use $-2\delta A_s^W$ to avoid upper bound incompatibility of Eq. (13) (see Sect. 5.1.1) across the majority of the area. Therefore, A_s is taken as

$$A_s = \min\left(A_s^W - 2\delta A_s^W, A_s^{MAX}\right), \tag{15}$$

which brings together the initial slipperiness assumed under Weertman conditions, scaled down with respect to uncertainties in modelled basal velocity and friction and the arbitrary prescribed boundary to deal with weak-bed regions. Figure 7b represents the final field of A_s used further to infer water pressure, with maroon areas corresponding to the weak-bed regions restricted by A_s^{MAX}.

Reducing A_s compared to A_s^W is also consistent with observations in boreholes that suggest locations of relatively high water pressures p_w, above 80 % of the overburden pressure p_i, even in winter (Van De Wal et al., 2015; Wright et al., 2016). The latter means that our core assumption for winter-based A_s^W, which is a lack of pressurized water and a corresponding inhibition of sliding, would be invalid everywhere, and thus the estimated slipperiness of the bed in "dry" conditions would be higher than otherwise.

Note that even with accurately constrained A_s we are limited to confidently inferring the magnitude of winter pressure with the assumption of winter basal conditions close to the Weertman regime. As in this regime basal friction is weakly dependent on effective pressure, the small variations of inferred u_b or τ_b would have a large impact on the retrieved water pressure. To demonstrate that, we perform a pressure calculation with Eq. (13) using as the inputs the median value $A_s^W = 4.04 \times 10^{-21}$, typical in the Russell sector $\tau_b \sim 0.1$ MPa and $u_b \sim 100\,\mathrm{m\,a^{-1}}$, and a thickness of 1000 m. It shows that p_w values over a very large range, including > 80 % of p_i, which is usually appreciated as a high water pressure, can be obtained with variations in u_b and τ_b of only a few percent from the given values. Such a range of u_b and τ_b variations corresponds to the range of uncertainties on our inferred u_b and τ_b.

5.1.3 Choice of the bed roughness parameter C

Once CN has been inferred from the inversions, a value for C has to be prescribed to translate this in terms of basal water pressure. As shown by Schoof (2005), C should be lower than the maximum local positive slope of the bedrock topography at a decimetre to metre scale, so that the ratio $\tau_b/N \leq C$ fulfils Iken's bound (Iken, 1981). As there is no observational or experimental constraint for the value of C, most authors use values that are also consistent with the values that have been inferred to describe the Coulomb behaviour of deformable beds and that range between 0.17 and 0.84 (Iverson et al., 1998; Truffer et al., 2000; Cuffey and Paterson, 2010; Iverson, 2011).

Here we use a constant and uniform value and take $C = 0.16$ as in the synthetic applications for a typical Greenlandic land-terminating glacier by Hewitt (2013) and Gagliardini and Werder (2018). Using a value that might be considered a lower bound will underestimate the water pressures but over-

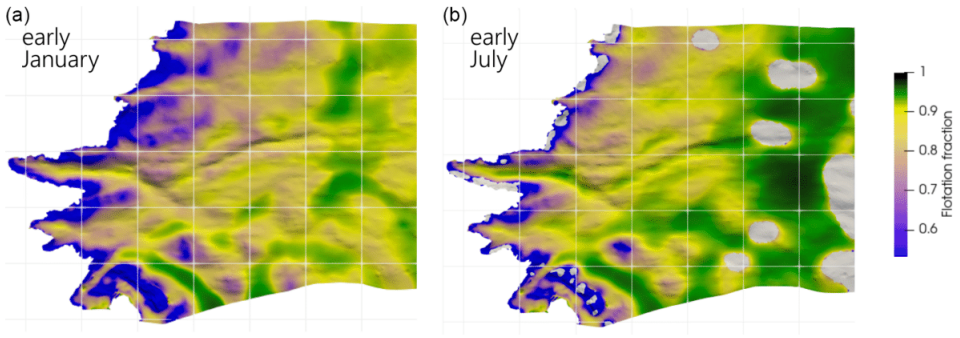

Figure 8. Flotation fraction maps obtained for early January **(b)** and July **(a)** using a regularized Coulomb friction law from Gagliardini et al. (2007), with basal topography hillshade added. The grey areas in the right panel have no value as they are outside the validity domain of Eq. (13) ($\tau_b^n u_b^{-1} A_s \geq 1$). The white grid lines are spaced by 10 km.

estimate the temporal variations, thus highlighting the areas where the changes are the most pronounced. In the following, the absolute values of N must then be regarded with caution; however the relative variations remain independent of C.

5.2 Seasonal changes in the modelled basal water pressure

5.2.1 Pressure fields

Using the A_s and C parameters discussed previously, the effective pressure obtained from Eq. (13) has been derived for the 24 dates and further unwrapped to water pressure $p_w = p_i - N$ and flotation fraction $FF = p_w/p_i$. The flotation fraction maps inferred for early January and early July are shown in Fig. 8. They correspond approximately to the months with the lowest and highest FF on average respectively.

Although the absolute pressure values obtained in winter are highly uncertain because we assumed the system to be close to the Weertman regime during this period, we obtain FF values above 0.8 for most of the domain in agreement with measurements obtained in boreholes in the range of 0.8–1.1 (Meierbachtol et al., 2013; Van De Wal et al., 2015; Wright et al., 2016). A good coherence between the variability of the spatio-temporal pressure fields and various constraints, e.g. basal topography or ice thickness, is successfully obtained as well. Between early January and July (Fig. 8), the FF increases globally by 7 % (median FF over the domain 0.83 and 0.88 respectively). The more pronounced increases happen mainly in valley floors and troughs, where the system comes very close to the flotation limit ($FF = 1$) during summer. This would be consistent with the idea that the water follows hydraulic potential gradients and concentrates in these topographic depressions (Wright et al., 2016; Downs et al., 2018). The weak-bedded areas, which are considered to be in a near-Coulomb regime in winter, have a higher flotation fraction than surrounding areas over the entire year. This is especially true for Ørkendalen Gletscher, where FF is already above 0.95 in early January. In summer, in those regions, FF cannot increase significantly as Eq. (13) shows CN is always positive, meaning that the water pressure is always lower than the ice overburden pressure. We also observe that FF generally rises with the distance to the ice margin. This is similar to the modelling of the water routing system in steady state by Meierbachtol et al. (2013), suggesting an increased drainage efficiency when approaching the terminus and vice versa when moving towards the interior of the ice sheet.

Modelling of the water pressure using subglacial hydrological models (de Fleurian et al., 2016; Koziol and Arnold, 2017; Downs et al., 2018) shows p_w spatial patterns similar to those obtained by us: the FF increases with the distance from the margin and is higher in large troughs in the glacier bed. We note however that such hydrological models generally obtain lower water pressure values than estimated here or observed in boreholes, with a typical range of winter FF values of 0.4 to 0.7 across the Russell sector. In de Fleurian et al. (2016), the modelled FF increases significantly in summer compared to the winter mean for altitudes above 1000 m (about 45 km inland from the Insunnguata front line), while below it changes are moderate and mainly concentrated in the Insunnguata valley. While it is difficult from our inversions to draw conclusions on the pressure changes above 1000 m, it seems that the pressure variations below it are more pronounced and systematically higher than modelled by de Fleurian et al. (2016) (this result can also be seen in Figs. 9 and 10), which might suggest that the subglacial hydrological system is not as efficient as assumed in this part of the ice sheet. In other similar work, Downs et al. (2018) reproduced even larger FF variability from summer to winter than we do, adjusting the seasonally evolving hydraulic con-

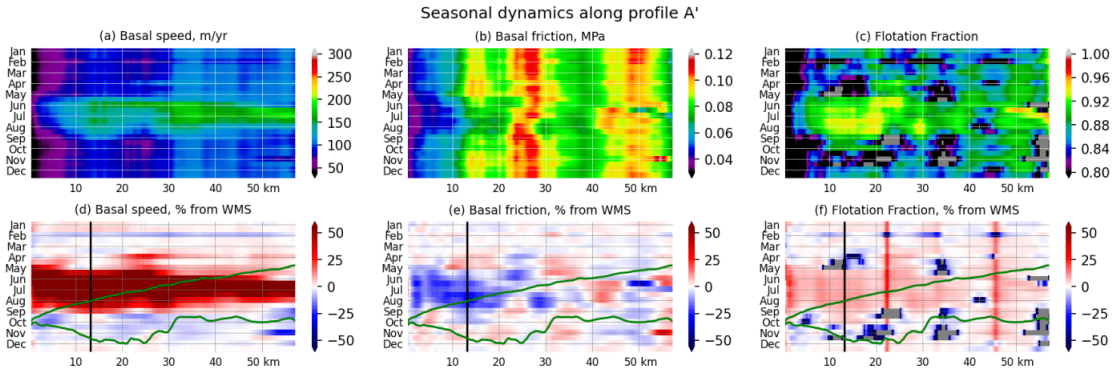

Figure 9. Modelled basal speed u_b, basal friction τ_b, and flotation fraction FF along profile A' (see Fig. 1). **(a–c)** Absolute units and **(d–f)** fraction relative to the mean winter values (average of January, February, March). In panels **(d–f)** the vertical black line represents the location of point A plotted in Fig. 6a (see Fig. 1), and the green lines represent the glacier top and bottom surfaces with 5× vertical scale factor. The dark-grey areas in **(c)** and **(f)** have no value as they are outside the validity domain of Eq. (13) ($\tau_b^n u_b^{-1} A_s \geq 1$).

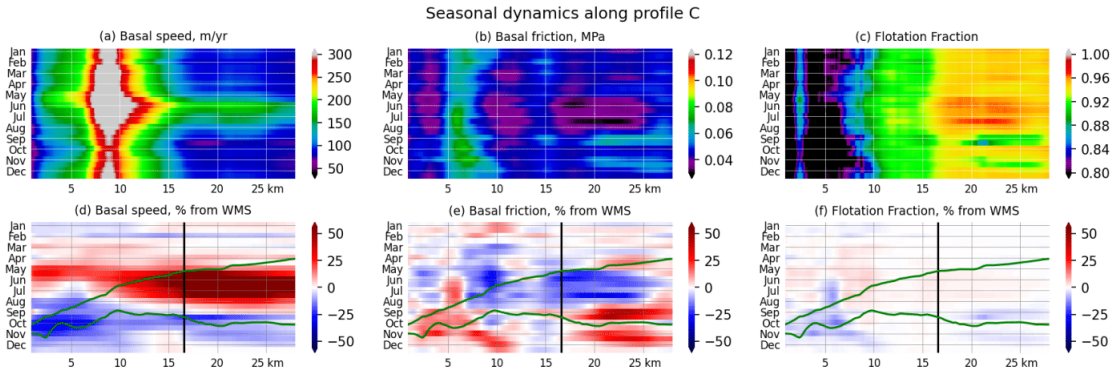

Figure 10. Modelled basal speed u_b, basal friction τ_b, and flotation fraction FF along the profile C' (see Fig. 1). **(a)–c)** Absolute units and **(d–f)** fraction relative to the mean winter values (average of January, February, March). In panels **(d–f)** the vertical black line represents the location of point C plotted in Fig. 6c (see Fig. 1), and the green lines represent the glacier top and bottom surfaces with 5× vertical scale factor.

ductivity. However, they still have absolute values of FF in winter that are almost half of those inferred by us.

5.2.2 Physical processes driving the seasonal dynamics

Isovalues of CN computed from Eq. (13) are reported in Fig. 6 (bottom subplots) for the three particular locations (points A, B, and C) discussed previously. In addition, we show in Figs. 9, 10, and A6 the seasonal evolution of basal velocity, friction, and flotation fraction along three profiles A', C', and B' that pass through points A, C, and B respectively (see Fig. 1).

Points A and B, which we have identified as having a hard bed, are, by assumption, close to the Weertman regime in winter, and they demonstrate that small variations in either u_b or τ_b have a large effect on the magnitude of the retrieved effective pressure.

At point A, the relationship between τ_b and u_b does not follow a power friction law where the evolution of τ_b would be proportional to $u_b^{1/n}$ such as in Weertman's law (Weertman, 1957). In summer, point A is in a regime closer to Coulomb where changes in N are mainly driven by changes in τ_b and are fairly insensitive to variations in u_b (Fig. 6). In profile A' (Fig. 9), the first 20 km seems to follow the same behaviour as point A, suggesting that the valley bottom behaviour is compatible with a response of the system to local variations in water pressure; i.e. the water pressure increases when the hydrological system is not able to drain the incoming amount of water efficiently and decreases later in the sea-

son as the system gets more efficient and/or the flux of water reduces.

In contrast to point A, point B (Fig. 6b) and its surroundings (Fig. A6) follow a power friction law. The variations inferred at point B are relatively compatible with the Weertman regime for the whole year, so it is difficult to discuss the temporal variations in N with confidence (including sharp peaks of CN in Fig. 6b-1). The most plausible hypothesis is that changes in point-B-like areas are mainly driven by changes in longitudinal stresses induced from the accelerating surroundings (such as point A) and are not a response to local variations in water pressure. In detail, we interpret annual friction and ice speed changes at point B as follows: from January to May, the gradual recharge of the subglacial water system locally reduces the friction, and the velocity slowly increases (Van De Wal et al., 2015; Harper et al., 2021). In May, when surface melting begins, local topography and/or organization of the hydrological system do not lead to an increase in water pressure and consequent facilitation of sliding. However, via longitudinal coupling to other accelerating areas such as point A, point B is forced to accelerate as well. Higher sliding speed for a relatively unchanging set of bed properties leads to a higher local friction. That could explain why the friction peak is observed in August at point B when it is the moment of lowest friction at point A. As such, the behaviours at points A and B could also be respectively related to the active and passive regions as have been observed and discussed by Ryser et al. (2014b) or Price et al. (2008). As for the slight increase in velocity from January to March correlated with a decrease in τ_b, this is consistent with a weakly connected hydrological system that slowly recharges in winter by basal meltwater (Hoffman et al., 2016; Cook et al., 2020).

Beyond 30 km inland, profile A' (Fig. 9) does not follow the bed trough from Insunnguata Sermia and covers higher basal topography where the basal drag alternates between reduced and increased summer values. Along this rugged terrain, the inverted behaviour is probably a mix between point A, where local variations in water pressure occur, and point B, which responds to non-local longitudinal stresses.

Point C is located in a region previously assumed to have a weak bed (see Sect. 5.1.2). The whole 30 km profile C' (Fig. 9) mainly exhibits the same conditions as were described for point C. It follows a topographical valley where the basal friction is very low (< 0.05 MPa), the exception being the ridge located at 3 km where basal drag is more important (~ 0.07 MPa). As τ_b and u_b are weakly connected to each other in this case, Coulomb-like behaviour is likely approached, where τ_b would be proportional to the effective pressure during the whole year. In the hypothesis of the hard bed physics used here, this could be consistent with cavitations and therefore low effective pressure throughout the year. Nevertheless, as some reasons should exist to explain the big and numerous cavities open even in winter while the sliding speed here is relatively moderate, we are more inclined to assume the local presence of deforming sediments below the glacier, like those observed in situ by Dow et al. (2013) for another location on Russell Glacier, which shows a τ_b-vs.-u_b relationship similar to our inversions. The exception to this in profile C' is the aforementioned ridge at 3 km, which appears to offer enhanced flow resistance, similar to point B where we have posited the existence of hard-bed physics adjusting to longitudinal stresses. As expected for weak beds, changes in effective pressure are mainly proportional to changes in τ_b and are weakly sensitive to u_b. We observe anti-correlated variations between u_b and τ_b with a maximum in velocity and water pressure in June and a minimum in September; during the winter months, water pressure and velocities increase slowly. As most of this valley is close to flotation throughout the year, the moderate relative increase in water pressure has a large impact on glacier flow in summer as would be expected for a bed described by a Coulomb friction law. These results are compatible with the model of Bougamont et al. (2014) for weak beds, where the water volume and pressure in the sediments increase in the early melt season, leading to a reduction of their shear strength. In late summer and autumn, grain rearrangement leads to increased porosity, reducing the water pressure and increasing inter-grain contact, resulting in an overall strengthening of the sediment relative to its pre-summer state and thus a maximum friction and a minimum sliding speed in autumn. It is interesting to note that the decrease in sliding velocity at the end of the melt season (August to October depending on the surface altitude) appears in general to be much more pronounced in areas where the bed is described as weak than in the rest of the domain where basal conditions appear to correspond to a hard bed.

5.2.3 Comparison with runoff: timing and maximum values

Water pressure variations in the system are globally controlled by the increase in surface runoff that percolates to the glacier bed continuously through moulins or crevasses or sporadically by the drainage of supraglacial lakes (Smith et al., 2015; Stevens et al., 2016). These water pressure variations are therefore closely related to runoff and drainage system evolution. Thus, we compare the seasonal evolution of the runoff obtained from the Regional Atmospheric Model (MAR, https://mar.cnrs.fr/, last access: 7 February 2020) with the inferred effective pressure variations and ice motion acceleration across different altitudes of our model domain (Fig. 11). The runoff is obtained from MAR v3.1, forced by the climate reanalysis ERA5, on a daily basis with a 15 km grid resolution downscaled to 1 km with respect to the surface topography (Fettweis et al., 2020). Further, the period from 2015 to 2019 is averaged in the same way as for the flow velocities (see Sect. 2).

As the domain mostly appears to obey hard-bed physics, the variations in Fig. 11 are most probably mainly characteristic of this type of bed. For all altitudes, the water pressure

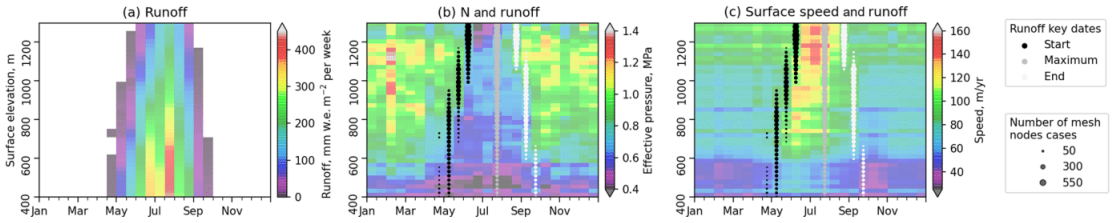

Figure 11. Evolution in time and space (averaged over 2 weeks and 20 m elevation bins) of MAR-modelled surface runoff **(a)**, effective pressure N **(b)**, and modelled surface speed u_s **(c)**. The black, dark grey, and light grey dots represent the onset, maximum, and end of the melting season in **(b)** and **(c)**. The size of the dots is proportional to the number of mesh nodes found for each state. We define the melting period as runoff > 10 mm w.e. m^{-2} per week.

peaks about 2–4 weeks after the start of the melt season as indicated by the MAR runoff. This delay may be due to water percolation duration (Fountain and Walder, 1998), a sliding activation threshold that is not yet reached (Davison et al., 2019), or simply the fact that the effective pressure changes are still too small to be observed in the 2-week-averaged surface velocities. Ice flow velocity begins to increase at about the same time as the effective pressure decreases. Ice speed quickly reaches its maximum a few weeks later, while runoff continues to increase and is maximal in late July at all altitudes. This probably illustrates the fact that the hydrological system became able to efficiently evacuate the additional meltwater inflow, which does not allow the effective pressure and thus sliding velocity to evolve any further. Once the melt season is over and runoff tends toward zero, the effective pressure quickly returns to its winter state and does not change significantly until next spring. Up to about 1000 m in surface elevation, ice flow experiences a minimum speed that always occurs after the end of the melting season around late September or early October. This seems to correspond to a minimum in water pressure, but, as we are getting closer to the Weertman regime, the pressure values obtained from the inverted basal friction are uncertain.

The overall evolution over the complete year of the surface speed and the water pressure obtained from the inversions corresponds well with the behaviour expected from previous observations and the current understanding of the interaction between the subglacial hydrological system and the ice flow (Nienow et al., 2017; Davison et al., 2019). For instance, the synchronous increase in basal water pressure and surface velocity demonstrated here at the beginning of the melt period fits well with the in situ observations (Bartholomew et al., 2010; Sole et al., 2013; Van De Wal et al., 2015). In our inferred fields the maximum water pressure and velocity are reached while surface runoff still continues to increase, which also corresponds to the local-scale (Bartholomew et al., 2010; Sole et al., 2013) and larger-scale (Sundal et al., 2011; Fitzpatrick et al., 2013) observations in this region, suggesting that a more efficient drainage system is limiting the increase in water pressure at the glacier bed. The drop in water pressure after the end of the melt season (Fig. 11b) corresponds to the presence of a more efficient drainage system established during summer that allows for easy evacuation of the remaining water inputs, chiefly the production of water at the bed as surface melting ceases. Finally, the water pressure slowly increases over winter as the hydrological system becomes inefficient at draining water. Both stages of this evolution have been observed with borehole measurements as well (Van De Wal et al., 2015).

Thus, we conclude that it is possible to obtain robust information on the seasonal evolution of friction and sliding at the base of glaciers by using inverse methods on dense time series of surface flow velocities. Using a pressure-dependent friction law in a suitable and well-restricted framework, it is also realistic to relate these changes in basal conditions to the evolution of the hydrological system and in particular basal water pressure.

5.3 Summary

Spatially extended time series of ice velocity can now be obtained at a time resolution of less than a month, allowing monitoring of glacier motion at a seasonal scale. This offers the opportunity to explore in much more detail the glacier physics driving these changes. Inversions of this time series in the Russell sector indicate that the basal friction changes are mostly consistent with hard-bed physics, which has implications for the choice of friction law in ice flow models and the development of subglacial hydrologic models. In some small areas, the relation between friction and basal sliding rather suggests the presence of weak beds. In such cases we are not able to confidently conclude from our inversions whether this indicates the presence of deformable till, explaining the low strength of the bed, as the results are still compatible with a hard bed with sustained and substantial cavitation.

To relate basal friction and sliding to water pressure, we use a regularized Coulomb friction law designed for a hard bed with cavitation, which seems to give realistic results despite an approximate knowledge of some of the flow

law parameters. The results highlight the presence of active (point A) and passive (point B) locations in terms of hydrology. This is similar to the in situ observations made by Ryser et al. (2014b, a) and Young et al. (2019), with the difference that the inversions offer new insight into the large-scale spatial distribution of active and passive sectors over an extended area. Thus, it is possible from such inversions to infer which regions are hydrologically forced during the melt season and relate it to the spatial evolution of the drainage system. It appears that in the Russell area, the main subglacial water pathways are located in the topographic troughs of the bed and thus correspond mainly to the active regions, while the ridges correspond to the passive regions, thus providing additional resistance to enhanced flow in the active regions.

Regardless of pressure assumptions, we show here that inversions of basal conditions from time series of seasonal flow velocity observations provide valuable information on sliding velocity and friction. These inversions could be used to better constrain the results obtained from subglacial hydrology models, as well as to couple these models with ice flow models. We note however that effort is still needed to obtain sufficiently accurate observational data to constrain seasonal variations in friction and sliding above the equilibrium line altitude (ELA) (about 50–60 km from the ice margin in this sector of the ice sheet). In addition, even though the spatial resolution and temporal resolution of the remotely sensed observations seem to be suitable for describing the weekly to monthly evolution of glaciers, it is important to note that the interactions between flow dynamics and subglacial hydrology still occur at much higher frequencies (hourly to daily) that satellite-sensed observations are currently unable to capture, a situation that seems unlikely to change in the coming years. On a more positive note, it nonetheless appears that the time-integrated results we obtain are coherent despite the fact that the effects of the variations are indeed at higher frequencies.

6 Conclusions

In this paper, we explore the ability of an existing inverse method to use satellite-derived seasonal velocity maps to infer seasonal variations in basal conditions. Based on the observations from multiple satellite missions, we reconstruct the fortnightly seasonal evolution of surface velocity in a land-terminating sector of the ice sheet in southwest Greenland. Then, we invert 24 fortnightly velocity fields to obtain the corresponding evolution of sliding speed and basal friction during a typical year, and we use them to infer the water pressure changes using a pressure-dependent friction law.

The uncertainties in the inverted fields are small compared to the amplitude of the observed variations, which allows the seasonal evolution to be reconstructed and the results to be interpreted in terms of water pressure variations. It seems from the winter inversions that this region of Greenland is globally dominated by a sliding regime described by the physics of hard-rock beds and similarly behaving non-deforming till, with small areas showing characteristics corresponding to beds with Coulomb-type sliding, which can be related to the presence of soft sediments or substantial year-round cavitation over a hard bed. This finding differs from previous results for this region by including both hard-bed (often modelled in a coupled hydrology–ice flow system with a general power law of the form $\tau_b = C_n N u_b^n$; see Koziol and Arnold, 2018) and soft-bed (usually modelled with a pure Coulomb law of the form $\tau_b = CN$; see Bougamont et al., 2014) physics. Indeed, with the proper set of coefficients, depending on their calibration, regularized "Coulomb" friction provides a complete description of both hard and weak regimes of the bed physics.

The obtained water pressure variations are consistent with those expected for both the Weertman-like and Coulomb-like bed and seem to be in phase with the independently derived runoff variations. Thus, we show that inversions of observed surface velocities could serve as an intermediate validation for subglacial hydrology models, assuming that the errors in observed ice dynamics and geometry are small enough to obtain robust inversions. Moreover, the current and future development of space missions suggests that we will be able to perform the observations with sufficient spatial and temporal resolution to describe the weekly to monthly evolution of glacier dynamics on a large scale.

Appendix A: Additional material

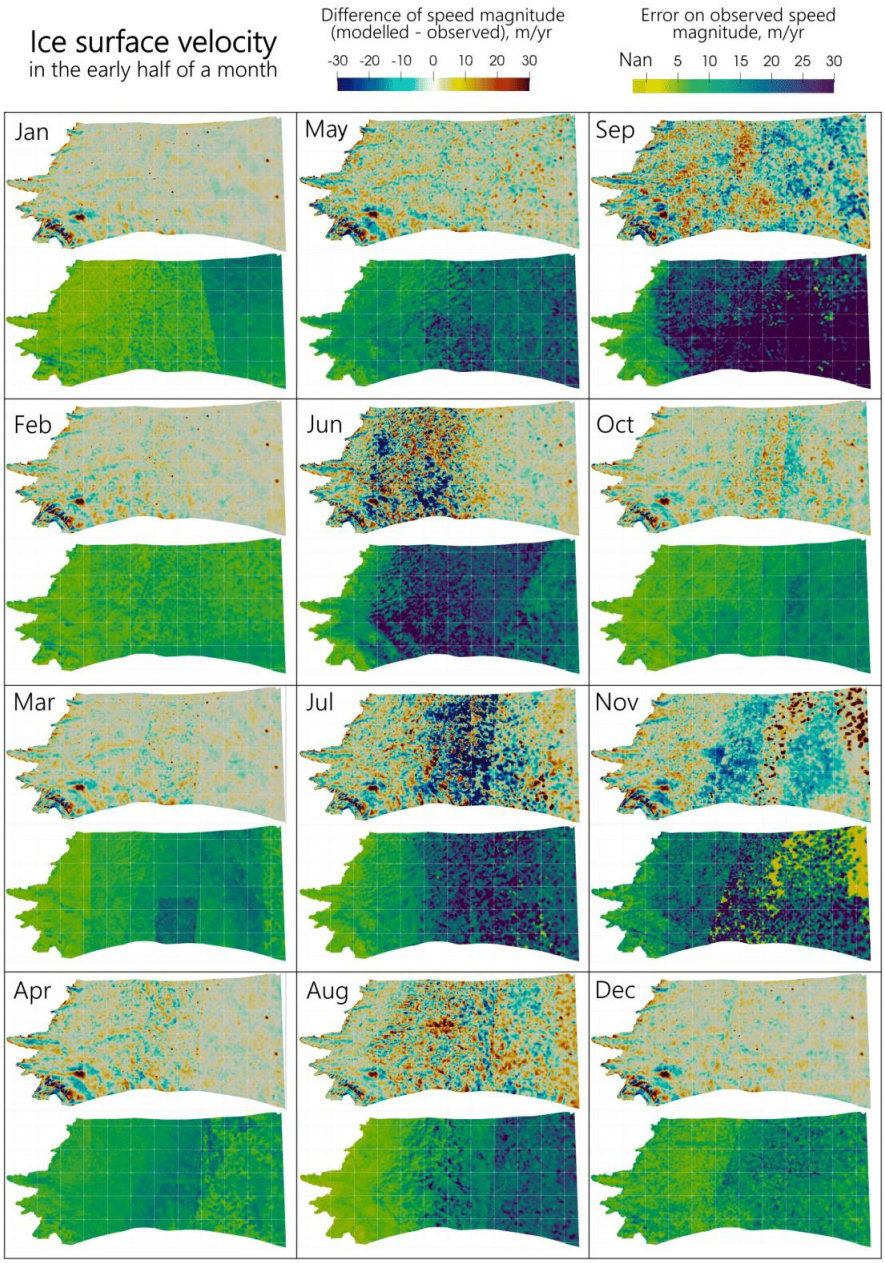

Figure A1. Mismatch between modelled and observed velocities (top subplots per section) and error on observed velocities (bottom subplot per section) for the first half of each month. The white grid lines are spaced by 10 km.

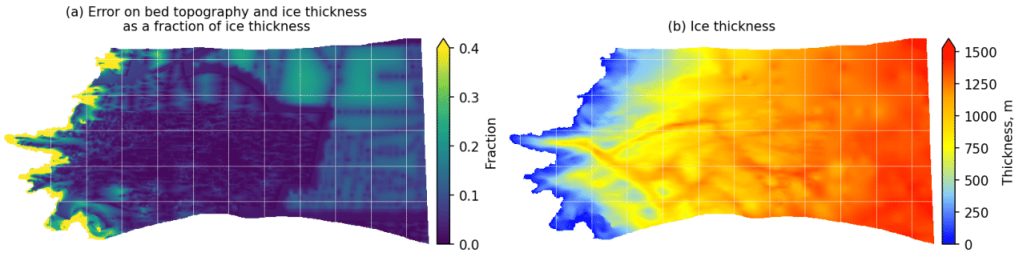

Figure A2. The data provided by BedMachine v3 (Morlighem et al., 2017): **(a)** errors on ice thickness and thus bed topography; **(b)** ice thickness. The white grid lines are spaced by 10 km.

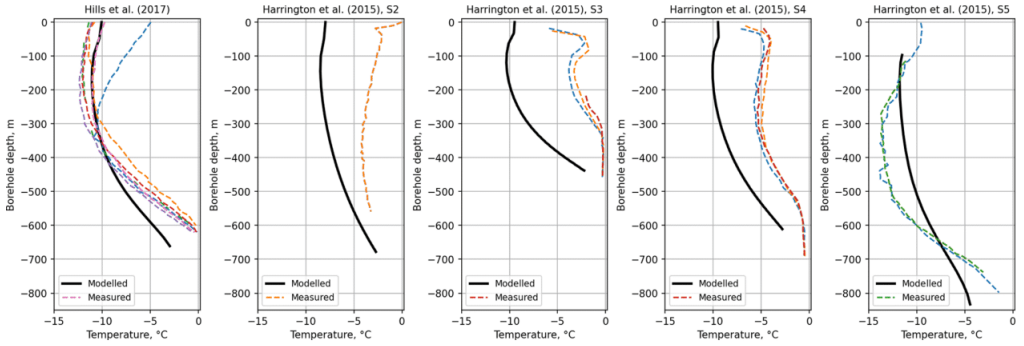

Figure A3. Comparison of ice temperature measured in boreholes (Hills et al., 2017; Harrington et al., 2015) with that modelled in SICOPOLIS (Goelzer et al., 2020).

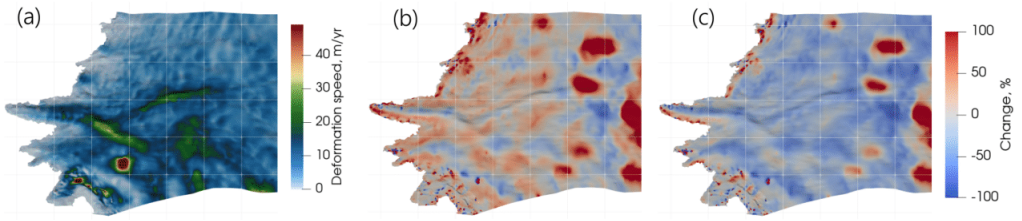

Figure A4. **(a)** Magnitude of modelled deformation velocity $u_d = u_s - u_b$ in early January. **(b)** Change in deformation velocity magnitude from early January to early July. **(c)** Change in fraction given by deformation velocity in total ice surface motion Frac $= u_d/u_s$ from early January to early July. All maps are with basal topography hillshade added. The white grid lines are spaced by 10 km.

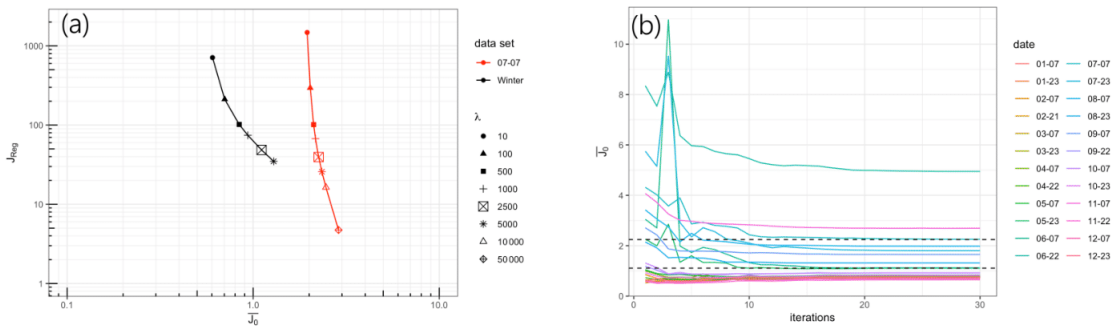

Figure A5. **(a)** L-curves: regularization term (J_{reg}) as a function of the mismatch between measured and modelled surface speed for different regularization parameters λ. **(b)** The change in mismatch between measured and modelled surface speed depending on the number of model regularization iterations per twice-monthly data set. Dotted lines represent the J_0 values obtained for the mean winter speed (MWS) and early July with chosen λ (2500).

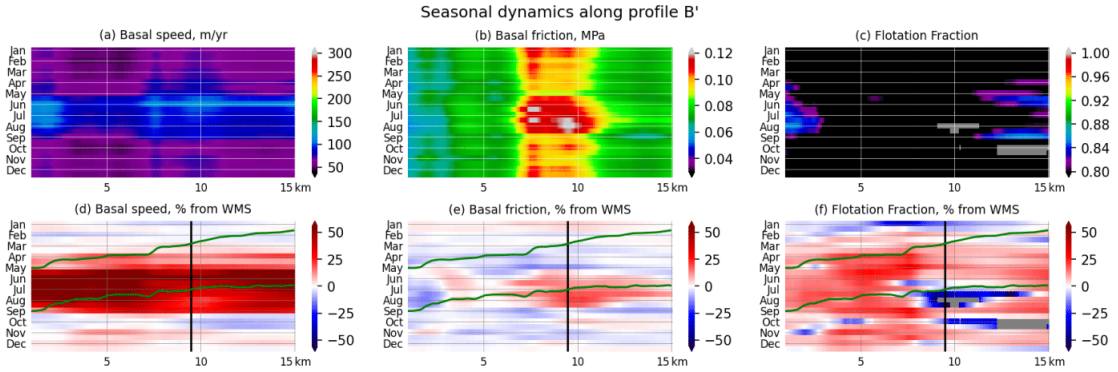

Figure A6. Modelled basal speed u_b, basal friction τ_b, and flotation fraction FF along profile B' (see Fig. 1). **(a–c)** Absolute units and **(d–f)** fraction relative to the mean winter values (average of January, February, March). In panels **(d–f)** the vertical black line represents the location of point B plotted in Fig. 6a (see Fig. 1), and the green lines represent the glacier top and bottom surfaces with 5× vertical scale factor. The dark-grey areas in **(c)** and **(f)** have no value as they are outside the validity domain of Eq. (13) ($\tau_b^n u_b^{-1} A_s \geq 1$).

Code and data availability. All data sets used here are publicly available. Elmer/Ice code is available here: http://elmerice.elmerfem.org/ (Elmer/Ice, 2020). BedMachine data are available from Morlighem et al. (2017). GIMP data are available here: https://doi.org/10.5067/NV34YUIXLP9W (Howat et al., 2015). Velocity time series are published at Zenodo (https://doi.org/10.5281/zenodo.5535532; Derkacheva et al., 2021a). Model results for 24 time steps are published at Zenodo (https://doi.org/10.5281/zenodo.5535624, Derkacheva et al., 2021b).

Author contributions. AD processed the velocity data, performed the analysis, wrote the article, and prepared the figures. JM provided supervision, performed the analysis, and wrote the article. FGC provided supervision, designed and performed the Elmer-related processing, and wrote the article. EJ helped to design the Elmer-related processing. NM processed the in situ deformation data and proofread a previous version of the article. SC proofread a previous version of the article. All co-authors helped with discussing and reviewing the article.

Competing interests. The contact author has declared that neither they nor their co-authors have any competing interests.

Disclaimer. Publisher's note: Copernicus Publications remains neutral with regard to jurisdictional claims in published maps and institutional affiliations.

Acknowledgements. Elmer/Ice computations and ice-velocity time series presented in this paper were performed using the https://gricad.univ-grenoble-alpes.fr (last access: 4 October 2021) infrastructure, which is supported by Grenoble research communities. We thank Neil Humphrey for the inclinometry data funded by the NSF Office of Polar Programs-Arctic Natural Sciences awards 1203451 and 0909495, SKB, NWMO, Posiva Oy, and NAGRA.

Financial support. This research has been supported by the Agence Nationale de la Recherche (grant no. ANR-19-CE01-0011-01) and the CNES MaISON research project.

Review statement. This paper was edited by Huw Horgan and reviewed by two anonymous referees.

References

Ahlstrøm, A. P., Petersen, D., Langen, P. L., Citterio, M., and Box, J. E.: Abrupt shift in the observed runoff from the southwestern Greenland ice sheet, Sci. Adv., 3, 1–8, https://doi.org/10.1126/sciadv.1701169, 2017.

Altena, B. and Kääb, A.: Weekly glacier flow estimation from dense satellite time series using adapted optical flow technology, Front. Earth Sci., 5, 1–12, https://doi.org/10.3389/feart.2017.00053, 2017.

Arthern, R. J. and Gudmundsson, G. H.: Initialization of ice-sheet forecasts viewed as an inverse Robin problem, J. Glaciol., 56, 527–533, https://doi.org/10.3189/002214310792447699, 2010.

Arthern, R. J., Hindmarsh, R. C. A., and Williams, C. R.: Flow speed within the Antarctic ice sheet and its controls inferred from satellite observations, J. Geophys. Res.-Earth, 120, 1171–1188, https://doi.org/10.1002/2014JF003239, 2015.

Bartholomew, I., Nienow, P., Mair, D., Hubbard, A., King, M. A., and Sole, A.: Seasonal evolution of subglacial drainage and acceleration in a Greenland outlet glacier, Nat. Geosci., 3, 408–411, https://doi.org/10.1038/ngeo863, 2010.

Bartholomew, I., Nienow, P., Sole, A., Mair, D., Cowton, T., and King, M. A.: Short-term variability in Greenland Ice Sheet motion forced by time-varying meltwater drainage: Implications for the relationship between subglacial drainage system behavior and ice velocity, J. Geophys. Res.-Earth, 117, 1–17, https://doi.org/10.1029/2011JF002220, 2012.

Booth, A. D., Clark, R. A., Kulessa, B., Murray, T., Carter, J., Doyle, S., and Hubbard, A.: Thin-layer effects in glaciological seismic amplitude-versus-angle (AVA) analysis: implications for characterising a subglacial till unit, Russell Glacier, West Greenland, The Cryosphere, 6, 909–922, https://doi.org/10.5194/tc-6-909-2012, 2012.

Bougamont, M., Christoffersen, P., Hubbard, A. L., Fitzpatrick, A. A., Doyle, S. H., and Carter, S. P.:Sensitive response of the Greenland Ice Sheet to surface melt drainage over a soft bed, Nat. Commun., 5, 5052, https://doi.org/10.1038/ncomms6052, 2014.

Box, J. E., Fettweis, X., Stroeve, J. C., Tedesco, M., Hall, D. K., and Steffen, K.: Greenland ice sheet albedo feedback: thermodynamics and atmospheric drivers, The Cryosphere, 6, 821–839, https://doi.org/10.5194/tc-6-821-2012, 2012.

Brinkerhoff, D., Aschwanden, A., and Fahnestock, M.: Constraining subglacial processes from surface velocity observations using surrogate-based Bayesian inference, J. Glaciol., 67, 385–403, https://doi.org/10.1017/jog.2020.112, 2021.

Budd, W. F., Keage, P., and Blundy, N.: Empirical study of ice sliding, J. Glaciol., 2, 157–170, https://doi.org/10.3189/S0022143000029804, 1979.

Budd, W. F., Jenssen, D., and Smith, I. N.: A Three-Dimensional Time-Dependent Model of the West Antarctic Ice Sheet, Ann. Glaciol., 5, 29–36, https://doi.org/10.3189/1984AoG5-1-29-36, 1984.

Cabral, B. and Leedom, L. C.: Imaging Vector Fields Using Line Integral Convolution, in: Proceedings of ACM SIGGRAPH'93, Anaheim, 263–270, https://doi.org/10.1145/166117.166151, 1993.

Christoffersen, P., Bougamont, M., Hubbard, A., Doyle, S. H., Grigsby, S., and Pettersson, R.: Cascading lake drainage on the Greenland Ice Sheet triggered by tensile shock and fracture, Nat. Commun., 9, 1064, https://doi.org/10.1038/s41467-018-03420-8, 2018.

Cleveland, W. S.: Robust locally weighted regression and smoothing scatterplots, J. Am. Stat. Assoc., 74, 829–836, https://doi.org/10.1080/01621459.1979.10481038, 1979.

Cleveland, W. S. and Devlin, S. J.: Locally weighted regression: An approach to regression analysis by local fitting, J. Am. Stat. Assoc., 83, 596–610, https://doi.org/10.1080/01621459.1988.10478639, 1988.

Cook, S. J., Christoffersen, P., Todd, J., Slater, D., and Chauché, N.: Coupled modelling of subglacial hydrology and calving-front melting at Store Glacier, West Greenland, The Cryosphere, 14, 905–924, https://doi.org/10.5194/tc-14-905-2020, 2020.

Cook, S. J., Christoffersen, P., and Todd, J.: A fully-coupled 3D model of a large Greenlandic outlet glacier with evolving subglacial hydrology, frontal plume melting and calving, J. Glaciol., https://doi.org/10.1017/jog.2021.109, in press, 2021.

Cowton, T., Sole, A., Nienow, P., Slater, D., Wilton, D., and Hanna, E.: Controls on the transport of oceanic heat to Kangerd-

lugssuaq Glacier, East Greenland, J. Glaciol., 62, 1167–1180, https://doi.org/10.1017/jog.2016.117, 2016.

Csatho, B. M., Schenka, A. F., Van Der Veen, C. J., Babonis, G., Duncan, K., Rezvanbehbahani, S., Van Den Broeke, M. R., Simonsen, S. B., Nagarajan, S., and Van Angelen, J. H.: Laser altimetry reveals complex pattern of Greenland Ice Sheet dynamics, P. Natl. Acad. Sci. USA, 111, 18478–18483, https://doi.org/10.1073/pnas.1411680112, 2014.

Cuffey, K. and Paterson, W.: The physics of glaciers, Academic Press, Amsterdam, 2010.

Dapogny, C., Dobrzynski, C., and Frey, P.: Three-dimensional adaptive domain remeshing, implicit domain meshing, and applications to free and moving boundary problems, J. Comput. Phys., 262, 358–378, https://doi.org/10.1016/j.jcp.2014.01.005, 2014.

Davison, B. J., Sole, A. J., Livingstone, S. J., Cowton, T. R., and Nienow, P. W.: The Influence of Hydrology on the Dynamics of Land-Terminating Sectors of the Greenland Ice Sheet, Front. Earth Sci., 7, 1–24, https://doi.org/10.3389/feart.2019.00010, 2019.

de Fleurian, B., Morlighem, M., Seroussi, H., Rignot, E., van den Broeke, M. R., Kuipers Munneke, P., Mouginot, J., Smeets, P. C. J. P., and Tedstone, A. J.: A modeling study of the effect of runoff variability on the effective pressure beneath Russell Glacier, West Greenland, J. Geophys. Res.-Earth, 121, 1834–1848, https://doi.org/10.1002/2016JF003842, 2016.

De Fleurian, B., Werder, M. A., Beyer, S., Brinkerhoff, D. J., Delaney, I., Dow, C. F., Downs, J., Gagliardini, O., Hoffman, M. J., Hooke, R. L., Seguinot, J., and Sommers, A. N.: SHMIP the subglacial hydrology model intercomparison Project, J. Glaciology, 64, 897–916, https://doi.org/10.1017/jog.2018.78, 2018.

Derkacheva, A., Mouginot, J., Millan, R., Maier, N., and Gillet-Chaulet, F.: Data Reduction Using Statistical and Regression Approaches for Ice Velocity Derived by Landsat-8, Sentinel-1 and Sentinel-2, Remote Sens., 12, 1935, https://doi.org/10.3390/rs12121935, 2020.

Derkacheva, A., Mouginot, J., and Millan, R.: Satellite-observed surface flow speed within Russell sector, West Greenland, bi-weekly average of 2015–2019 (1.0), Zenodo [data set], https://doi.org/10.5281/zenodo.5535532, 2021a.

Derkacheva, A., Gillet-Chaulet, F., and Mouginot, J.: Seasonal evolution of basal conditions within Russell sector, West Greenland, inverted from satellite observations of surface flow (1.0), Zenodo [data set], https://doi.org/10.5281/zenodo.5535624, 2021b.

Dow, C., Hubbard, A., Booth, A., Doyle, S., Gusmeroli, A., and Kulessa, B.: Seismic evidence of mechanically weak sediments underlying Russell Glacier, West Greenland, Ann. Glaciol., 54, 135–141, https://doi.org/10.3189/2013AoG64A032, 2013.

Downs, J. Z., Johnson, J. V., Harper, J. T., Meierbachtol, T., and Werder, M. A.: Dynamic Hydraulic Conductivity Reconciles Mismatch Between Modeled and Observed Winter Subglacial Water Pressure, J. Geophys. Res.-Earth, 123, 818–836, https://doi.org/10.1002/2017JF004522, 2018.

Doyle, S. H., Hubbard, A., Van De Wal, R. S., Box, J. E., Van As, D., Scharrer, K., Meierbachtol, T. W., Smeets, P. C., Harper, J. T., Johansson, E., Mottram, R. H., Mikkelsen, A. B., Wilhelms, F., Patton, H., Christoffersen, P., and Hubbard, B.: Amplified melt and flow of the Greenland ice sheet driven by late-summer cyclonic rainfall, Nat. Geosci., 8, 647–653, https://doi.org/10.1038/ngeo2482, 2015.

Edwards, T. L., Fettweis, X., Gagliardini, O., Gillet-Chaulet, F., Goelzer, H., Gregory, J. M., Hoffman, M., Huybrechts, P., Payne, A. J., Perego, M., Price, S., Quiquet, A., and Ritz, C.: Effect of uncertainty in surface mass balance-elevation feedback on projections of the future sea level contribution of the Greenland ice sheet, The Cryosphere, 8, 195–208, https://doi.org/10.5194/tc-8-195-2014, 2014.

Elmer/Ice: Open Source Finite Element Software for Ice Sheet, Glaciers and Ice Flow Modelling, Elmer/Ice [code], http://elmerice.elmerfem.org/, last access: 21 February 2020.

Fahnestock, M., Scambos, T., Moon, T., Gardner, A., Haran, T., and Klinger, M.: Rapid large-area mapping of ice flow using Landsat 8, Remote Sens. Environ., 185, 84–94, https://doi.org/10.1016/j.rse.2015.11.023, 2016.

Fettweis, X., Hofer, S., Krebs-Kanzow, U., Amory, C., Aoki, T., Berends, C. J., Born, A., Box, J. E., Delhasse, A., Fujita, K., Gierz, P., Goelzer, H., Hanna, E., Hashimoto, A., Huybrechts, P., Kapsch, M.-L., King, M. D., Kittel, C., Lang, C., Langen, P. L., Lenaerts, J. T. M., Liston, G. E., Lohmann, G., Mernild, S. H., Mikolajewicz, U., Modali, K., Mottram, R. H., Niwano, M., Noël, B., Ryan, J. C., Smith, A., Streffing, J., Tedesco, M., van de Berg, W. J., van den Broeke, M., van de Wal, R. S. W., van Kampenhout, L., Wilton, D., Wouters, B., Ziemen, F., and Zolles, T.: GrSMBMIP: intercomparison of the modelled 1980–2012 surface mass balance over the Greenland Ice Sheet, The Cryosphere, 14, 3935–3958, https://doi.org/10.5194/tc-14-3935-2020, 2020.

Fitzpatrick, A. A., Hubbard, A., Joughin, I., Quincey, D. J., As, D. V., Mikkelsen, A. P., Doyle, S. H., Hasholt, B., and Jones, G. A.: Ice flow dynamics and surface meltwater flux at a land-terminating sector of the Greenland ice sheet, J. Glaciol., 59, 687–696, https://doi.org/10.3189/2013JoG12J143, 2013.

Flowers, G. E.: Modelling water flow under glaciers and ice sheets, P. Roy. Soc. A, 471, 20140907, https://doi.org/10.1098/rspa.2014.0907, 2015.

Fountain, A. G. and Walder, J. S.: Water flow through temperate glaciers, Rev. Geophys., 36, 299–328, https://doi.org/10.1029/97RG03579, 1998.

Fowler, A. C.: On the rheology of till, Ann. Glaciol., 37, 55–59, https://doi.org/10.3189/172756403781815951, 2003.

Gagliardini, O. and Meyssonnier, J.: Lateral boundary conditions for a local anisotropic ice-flow model, Ann. Glaciol., 35, 503–509, https://doi.org/10.3189/172756402781817202, 2002.

Gagliardini, O. and Werder, M. A.: Influence of increasing surface melt over decadal timescales on land-terminating Greenland-type outlet glaciers, J. Glaciol., 64, 700–710, https://doi.org/10.1017/jog.2018.59, 2018.

Gagliardini, O., Cohen, D., Råback, P., and Zwinger, T.: Finite-element modeling of subglacial cavities and related friction law, J. Geophys. Res., 112, F02027, https://doi.org/10.1029/2006JF000576, 2007.

Gagliardini, O., Zwinger, T., Gillet-Chaulet, F., Durand, G., Favier, L., de Fleurian, B., Greve, R., Malinen, M., Martín, C., Råback, P., Ruokolainen, J., Sacchettini, M., Schäfer, M., Seddik, H., and Thies, J.: Capabilities and performance of Elmer/Ice, a new-generation ice sheet model, Geosci. Model Dev., 6, 1299–1318, https://doi.org/10.5194/gmd-6-1299-2013, 2013.

Gilbert, J. C. and Lemaréchal, C.: Some numerical experiments with variable-storage quasi-Newton algorithms, Math. Program., 45, 407–435, https://doi.org/10.1007/BF01589113, 1989.

Gillet-Chaulet, F., Gagliardini, O., Seddik, H., Nodet, M., Durand, G., Ritz, C., Zwinger, T., Greve, R., and Vaughan, D. G.: Greenland ice sheet contribution to sea-level rise from a new-generation ice-sheet model, The Cryosphere, 6, 1561–1576, https://doi.org/10.5194/tc-6-1561-2012, 2012.

Gillet-Chaulet, F., Durand, G., Gagliardini, O., Mosbeux, C., Mouginot, J., Rémy, F., and Ritz, C.: Assimilation of surface velocities acquired between 1996 and 2010 to constrain the form of the basal friction law under Pine Island Glacier, Geophys. Res. Lett., 43, 10311–10321, https://doi.org/10.1002/2016GL069937, 2016.

Goelzer, H., Robinson, A., Seroussi, H., and van de Wal, R. S.: Recent Progress in Greenland Ice Sheet Modelling, Curr. Clim. Change Rep., 3, 291–302, https://doi.org/10.1007/s40641-017-0073-y, 2017.

Goelzer, H., Nowicki, S., Payne, A., Larour, E., Seroussi, H., Lipscomb, W. H., Gregory, J., Abe-Ouchi, A., Shepherd, A., Simon, E., Agosta, C., Alexander, P., Aschwanden, A., Barthel, A., Calov, R., Chambers, C., Choi, Y., Cuzzone, J., Dumas, C., Edwards, T., Felikson, D., Fettweis, X., Golledge, N. R., Greve, R., Humbert, A., Huybrechts, P., Le Clec'h, S., Lee, V., Leguy, G., Little, C., Lowry, D., Morlighem, M., Nias, I., Quiquet, A., Rückamp, M., Schlegel, N. J., Slater, D. A., Smith, R., Straneo, F., Tarasov, L., Van De Wal, R., and Van Den Broeke, M.: The future sea-level contribution of the Greenland ice sheet: A multi-model ensemble study of ISMIP6, The Cryosphere, 14, 3071–3096, https://doi.org/10.5194/tc-14-3071-2020, 2020.

Greskowiak, J.: Tide-induced salt-fingering flow during submarine groundwater discharge, Geophys. Res. Lett., 41, 6413–6419, https://doi.org/10.1002/2014GL061184, 2014.

Habermann, M., Maxwell, D., and Truffer, M.: Reconstruction of basal properties in ice sheets using iterative inverse methods, J. Glaciol., 58, 795–807, https://doi.org/10.3189/2012JoG11J168, 2012.

Habermann, M., Truffer, M., and Maxwell, D.: Error sources in basal yield stress inversions for Jakobshavn Isbræ, Greenland, derived from residual patterns of misfit to observations, J. Glaciol., 63, 999–1011, https://doi.org/10.1017/jog.2017.61, 2017.

Hansen, P. C.: The L-Curve and its Use in the Numerical Treatment of Inverse Problems, in: Computational Inverse Problems in Electrocardiology, edited by: Johnston, P., WIT Press, 119–142, 2001.

Harper, J., Meierbachtol, T., Humphrey, N., Saito, J., and Stansberry, A.: Variability of Basal Meltwater Generation During Winter, Western Greenland Ice Sheet, The Cryosphere Discuss. [preprint], https://doi.org/10.5194/tc-2021-179, in review, 2021.

Harper, J. T., Humphrey, N. F., Meierbachtol, T. W., Graly, J. A., and Fischer, U. H.: Borehole measurements indicate hard bed conditions, Kangerlussuaq sector, western Greenland Ice Sheet, J. Geophys. Res.-Earth, 122, 1605–1618, https://doi.org/10.1002/2017JF004201, 2017.

Harrington, J. A., Humphrey, N. F., and Harper, J. T.: Temperature distribution and thermal anomalies along a flowline of the Greenland ice sheet, Ann. Glaciol., 56, 98–104, https://doi.org/10.3189/2015AoG70A945, 2015.

Helanow, C., Iverson, N. R., Woodard, J. B., and Zoet, L. K.: A slip law for hard-bedded glaciers derived from observed bed topography, Sci. Adv., 7, eabe7798, https://doi.org/10.1126/sciadv.abe7798, 2021.

Helm, V., Humbert, A., and Miller, H.: Elevation and elevation change of Greenland and Antarctica derived from CryoSat-2, The Cryosphere, 8, 1539–1559, https://doi.org/10.5194/tc-8-1539-2014, 2014.

Hewitt, I. J.: Seasonal changes in ice sheet motion due to melt water lubrication, Earth Planet. Sc. Lett., 371–372, 16–25, https://doi.org/10.1016/j.epsl.2013.04.022, 2013.

Hills, B. H., Harper, J. T., Humphrey, N. F., and Meierbachtol, T. W.: Measured Horizontal Temperature Gradients Constrain Heat Transfer Mechanisms in Greenland Ice, Geophys. Res. Lett., 44, 9778–9785, https://doi.org/10.1002/2017GL074917, 2017.

Hoffman, M. J., Andrews, L. C., Price, S. A., Catania, G. A., Neumann, T. A., Lüthi, M. P., Gulley, J., Ryser, C., Hawley, R. L., and Morriss, B.: Greenland subglacial drainage evolution regulated by weakly connected regions of the bed, Nat. Commun., 7, 13903, https://doi.org/10.1038/ncomms13903, 2016.

Howat, I., Negrete, A., and Smith, B.: MEaSUREs Greenland Ice Mapping Project (GIMP) Digital Elevation Model (2.1), NASA National Snow and Ice Data Center Distributed Active Archive Center, Boulder, Colorado, USA, [data set], https://doi.org/10.5067/NV34YUIXLP9W, 2015.

Howat, I. M., Negrete, A., and Smith, B. E.: The Greenland Ice Mapping Project (GIMP) land classification and surface elevation data sets, The Cryosphere, 8, 1509–1518, https://doi.org/10.5194/tc-8-1509-2014, 2014.

Iken, A.: The effect of the subglacial water pressure on the sliding velocity of a glacier in an idealized numerical model, J. Glaciol., 27, 407–421, https://doi.org/10.1017/S0022143000011448, 1981.

Iverson, N. R.: Shear resistance and continuity of subglacial till: Hydrology rules, J. Glaciol., 56, 1104–1114, https://doi.org/10.3189/002214311796406220, 2011.

Iverson, N. R., Hooyer, T. S., and Baker, R. W.: Ring-shear studies of till deformation: Coulomb-plastic behavior and distributed strain in glacier beds, J. Glaciol., 44, 634–642, https://doi.org/10.1017/S0022143000002136, 1998.

Jay-Allemand, M., Gillet-Chaulet, F., Gagliardini, O., and Nodet, M.: Investigating changes in basal conditions of Variegated Glacier prior to and during its 1982–1983 surge, The Cryosphere, 5, 659–672, https://doi.org/10.5194/tc-5-659-2011, 2011.

Joughin, I., MacAyeal, D. R., and Tulaczyk, S.: Basal shear stress of the Ross ice streams from control method inversions, J. Geophys. Res.-Solid, 109, 1–20, https://doi.org/10.1029/2003JB002960, 2004.

Joughin, I., Das, S. B., King, M. A., Smith, B. E., and Howat, I. M.: Seasonal Speedup Along the Western Flank of the Greenland Ice Sheet, Science, 320, 781–783, 2008.

Joughin, I., Smith, B. E., and Howat, I.: Greenland Ice Mapping Project: ice flow velocity variation at sub-monthly to decadal timescales, The Cryosphere, 12, 2211–2227, https://doi.org/10.5194/tc-12-2211-2018, 2018.

Joughin, I., Smith, B. E., and Schoof, C. G.: Regularized Coulomb Friction Laws for Ice Sheet Sliding: Application to Pine Is-

land Glacier, Antarctica, Geophys. Res. Lett., 46, 4764–4771, https://doi.org/10.1029/2019GL082526, 2019.

Koziol, C. P. and Arnold, N.: Incorporating modelled subglacial hydrology into inversions for basal drag, The Cryosphere, 11, 2783–2797, https://doi.org/10.5194/tc-11-2783-2017, 2017.

Koziol, C. P. and Arnold, N.: Modelling seasonal meltwater forcing of the velocity of land-terminating margins of the Greenland Ice Sheet, The Cryosphere, 12, 971–991, https://doi.org/10.5194/tc-12-971-2018, 2018.

Kulessa, B., Hubbard, A. L., Booth, A. D., Bougamont, M., Dow, C. F., Doyle, S. H., Christoffersen, P., Lindbäck, K., Pettersson, R., Fitzpatrick, A. A. W., and Jones, G. A.: Seismic evidence for complex sedimentary control of Greenland Ice Sheet flow, Sci. Adv., 3, e1603071, https://doi.org/10.1126/sciadv.1603071, 2017.

Larour, E., Utke, J., Csatho, B., Schenk, A., Seroussi, H., Morlighem, M., Rignot, E., Schlegel, N., and Khazendar, A.: Inferred basal friction and surface mass balance of the Northeast Greenland Ice Stream using data assimilation of ICESat (Ice Cloud and land Elevation Satellite) surface altimetry and ISSM (Ice Sheet System Model), The Cryosphere, 8, 2335–2351, https://doi.org/10.5194/tc-8-2335-2014, 2014.

Le Clec'h, S., Charbit, S., Quiquet, A., Fettweis, X., Dumas, C., Kageyama, M., Wyard, C., and Ritz, C.: Assessment of the Greenland ice sheet-atmosphere feedbacks for the next century with a regional atmospheric model coupled to an ice sheet model, The Cryosphere, 13, 373–395, https://doi.org/10.5194/tc-13-373-2019, 2019.

Lemos, A., Shepherd, A., McMillan, M., and Hogg, A.: Seasonal Variations in the Flow of Land-Terminating Glaciers in Central-West Greenland Using Sentinel-1 Imagery, Remote Sens., 10, 1878, https://doi.org/10.3390/rs10121878, 2018.

Lindbäck, K., Pettersson, R., Doyle, S. H., Helanow, C., Jansson, P., Kristensen, S. S., Stenseng, L., Forsberg, R., and Hubbard, A. L.: High-resolution ice thickness and bed topography of a land-terminating section of the Greenland Ice Sheet, Earth Syst. Sci. Data, 6, 331–338, https://doi.org/10.5194/essd-6-331-2014, 2014.

MacAyeal, D. R.: A tutorial on the use of control methods in ice-sheet modeling, J. Glaciol., 39, 91–98, https://doi.org/10.1017/S0022143000015744, 1993.

Maier, N., Humphrey, N., Harper, J., and Meierbachtol, T.: Sliding dominates slow-flowing margin regions, Greenland Ice Sheet, Sci. Adv., 5, eaaw5406, https://doi.org/10.1126/sciadv.aaw5406, 2019.

Maier, N., Gimbert, F., Gillet-Chaulet, F., and Gilbert, A.: Basal traction mainly dictated by hard-bed physics over grounded regions of Greenland, The Cryosphere, 15, 1435–1451, https://doi.org/10.5194/tc-15-1435-2021, 2021a.

Maier, N., Humphrey, N., Meierbachtol, T., and Harper, J.: Deformation motion tracks sliding changes through summer, western Greenland, J. Glaciol., https://doi.org/10.1017/jog.2021.87, in press, 2021b.

Mangeney, A., Califano, F., and Castelnau, O.: Isothermal flow of an anisotropic ice sheet in the vicinity of an ice divide, J. Geophys. Res.-Solid, 101, 28189–28204, https://doi.org/10.1029/96jb01924, 1996.

Meierbachtol, T., Harper, J., and Humphrey, N.: Basal drainage system response to increasing surface melt on the Greenland ice sheet, Science, 341, 777–779, https://doi.org/10.1126/science.1235905, 2013.

Mikkelsen, A. B., Hubbard, A., Macferrin, M., Box, J. E., Doyle, S. H., Fitzpatrick, A., Hasholt, B., Bailey, H. L., Lindbäck, K., and Pettersson, R.: Extraordinary runoff from the Greenland ice sheet in 2012 amplified by hypsometry and depleted firn retention, The Cryosphere, 10, 1147–1159, https://doi.org/10.5194/tc-10-1147-2016, 2016.

Millan, R., Mouginot, J., Rabatel, A., Jeong, S., Cusicanqui, D., Derkacheva, A., and Chekki, M.: Mapping surface flow velocity of glaciers at regional scale using a multiple sensors approach, Remote Sens., 11, 1–21, https://doi.org/10.3390/rs11212498, 2019.

Minchew, B., Simons, M., Björnsson, H., Pálsson, F., Morlighem, M., Seroussi, H., Larour, E., and Hensley, S.: Plastic bed beneath Hofsjökull ice cap, central Iceland, and the sensitivity of ice flow to surface meltwater flux, J. Glaciol., 62, 147–158, https://doi.org/10.1017/jog.2016.26, 2016.

Morlighem, M., Rignot, E., Seroussi, H., Larour, E., Ben Dhia, H., and Aubry, D.: A mass conservation approach for mapping glacier ice thickness, Geophys. Res. Lett., 38, 1–6, https://doi.org/10.1029/2011GL048659, 2011.

Morlighem, M., Rignot, E., Mouginot, J., Wu, X., Seroussi, H., Larour, E., and Paden, J.: High-resolution bed topography mapping of Russell Glacier, Greenland, inferred from Operation IceBridge data, J. Glaciol., 59, 1015–1023, https://doi.org/10.3189/2013JoG12J235, 2013.

Morlighem, M., Williams, C. N., Rignot, E., An, L., Arndt, J. E., Bamber, J. L., Catania, G., Chauché, N., Dowdeswell, J. A., Dorschel, B., Fenty, I., Hogan, K., Howat, I., Hubbard, A., Jakobsson, M., Jordan, T. M., Kjeldsen, K. K., Millan, R., Mayer, L., Mouginot, J., Noël, B. P., O'Cofaigh, C., Palmer, S., Rysgaard, S., Seroussi, H., Siegert, M. J., Slabon, P., Straneo, F., van den Broeke, M. R., Weinrebe, W., Wood, M., and Zinglersen, K. B.: BedMachine v3: Complete Bed Topography and Ocean Bathymetry Mapping of Greenland From Multibeam Echo Sounding Combined With Mass Conservation, Geophys. Res. Lett., 44, 11051–11061, https://doi.org/10.1002/2017GL074954, 2017.

Mouginot, J., Rignot, E., Scheuchl, B., and Millan, R.: Comprehensive Annual Ice Sheet Velocity Mapping Using Landsat-8, Sentinel-1, and RADARSAT-2 Data, Remote Sen., 9, 1–20, https://doi.org/10.3390/rs9040364, 2017.

Mouginot, J., Rignot, E., Bjørk, A. A., van den Broeke, M., Millan, R., Morlighem, M., Noël, B., Scheuchl, B., and Wood, M.: Forty-six years of Greenland Ice Sheet mass balance from 1972 to 2018, P. Natl. Acad. Sci. USA, 116, 9239–9244, https://doi.org/10.1073/pnas.1904242116, 2019.

Nienow, P. W., Sole, A. J., Slater, D. A., and Cowton, T. R.: Recent Advances in Our Understanding of the Role of Meltwater in the Greenland Ice Sheet System, Curr. Clim. Change Rep., 3, 330–344, https://doi.org/10.1007/s40641-017-0083-9, 2017.

Palmer, S., Shepherd, A., Nienow, P., and Joughin, I.: Seasonal speedup of the Greenland Ice Sheet linked to routing of surface water, Earth Planet. Sc. Lett., 302, 423–428, https://doi.org/10.1016/j.epsl.2010.12.037, 2011.

Pimentel, S., Flowers, G. E., and Schoof, C. G.: A hydrologically coupled higher-order flow-band model of ice dynamics with a

land Glacier, Antarctica, Geophys. Res. Lett., 46, 4764–4771, https://doi.org/10.1029/2019GL082526, 2019.

Koziol, C. P. and Arnold, N.: Incorporating modelled subglacial hydrology into inversions for basal drag, The Cryosphere, 11, 2783–2797, https://doi.org/10.5194/tc-11-2783-2017, 2017.

Koziol, C. P. and Arnold, N.: Modelling seasonal meltwater forcing of the velocity of land-terminating margins of the Greenland Ice Sheet, The Cryosphere, 12, 971–991, https://doi.org/10.5194/tc-12-971-2018, 2018.

Kulessa, B., Hubbard, A. L., Booth, A. D., Bougamont, M., Dow, C. F., Doyle, S. H., Christoffersen, P., Lindbäck, K., Pettersson, R., Fitzpatrick, A. A. W., and Jones, G. A.: Seismic evidence for complex sedimentary control of Greenland Ice Sheet flow, Sci. Adv., 3, e1603071, https://doi.org/10.1126/sciadv.1603071, 2017.

Larour, E., Utke, J., Csatho, B., Schenk, A., Seroussi, H., Morlighem, M., Rignot, E., Schlegel, N., and Khazendar, A.: Inferred basal friction and surface mass balance of the Northeast Greenland Ice Stream using data assimilation of ICESat (Ice Cloud and land Elevation Satellite) surface altimetry and ISSM (Ice Sheet System Model), The Cryosphere, 8, 2335–2351, https://doi.org/10.5194/tc-8-2335-2014, 2014.

Le Clec'h, S., Charbit, S., Quiquet, A., Fettweis, X., Dumas, C., Kageyama, M., Wyard, C., and Ritz, C.: Assessment of the Greenland ice sheet-atmosphere feedbacks for the next century with a regional atmospheric model coupled to an ice sheet model, The Cryosphere, 13, 373–395, https://doi.org/10.5194/tc-13-373-2019, 2019.

Lemos, A., Shepherd, A., McMillan, M., and Hogg, A.: Seasonal Variations in the Flow of Land-Terminating Glaciers in Central-West Greenland Using Sentinel-1 Imagery, Remote Sens., 10, 1878, https://doi.org/10.3390/rs10121878, 2018.

Lindbäck, K., Pettersson, R., Doyle, S. H., Helanow, C., Jansson, P., Kristensen, S. S., Stenseng, L., Forsberg, R., and Hubbard, A. L.: High-resolution ice thickness and bed topography of a land-terminating section of the Greenland Ice Sheet, Earth Syst. Sci. Data, 6, 331–338, https://doi.org/10.5194/essd-6-331-2014, 2014.

MacAyeal, D. R.: A tutorial on the use of control methods in ice-sheet modeling, J. Glaciol., 39, 91–98, https://doi.org/10.1017/S0022143000015744, 1993.

Maier, N., Humphrey, N., Harper, J., and Meierbachtol, T.: Sliding dominates slow-flowing margin regions, Greenland Ice Sheet, Sci. Adv., 5, eaaw5406, https://doi.org/10.1126/sciadv.aaw5406, 2019.

Maier, N., Gimbert, F., Gillet-Chaulet, F., and Gilbert, A.: Basal traction mainly dictated by hard-bed physics over grounded regions of Greenland, The Cryosphere, 15, 1435–1451, https://doi.org/10.5194/tc-15-1435-2021, 2021a.

Maier, N., Humphrey, N., Meierbachtol, T., and Harper, J.: Deformation motion tracks sliding changes through summer, western Greenland, J. Glaciol., https://doi.org/10.1017/jog.2021.87, in press, 2021b.

Mangeney, A., Califano, F., and Castelnau, O.: Isothermal flow of an anisotropic ice sheet in the vicinity of an ice divide, J. Geophys. Res.-Solid, 101, 28189–28204, https://doi.org/10.1029/96jb01924, 1996.

Meierbachtol, T., Harper, J., and Humphrey, N.: Basal drainage system response to increasing surface melt on the Greenland ice sheet, Science, 341, 777–779, https://doi.org/10.1126/science.1235905, 2013.

Mikkelsen, A. B., Hubbard, A., Macferrin, M., Box, J. E., Doyle, S. H., Fitzpatrick, A., Hasholt, B., Bailey, H. L., Lindbäck, K., and Pettersson, R.: Extraordinary runoff from the Greenland ice sheet in 2012 amplified by hypsometry and depleted firn retention, The Cryosphere, 10, 1147–1159, https://doi.org/10.5194/tc-10-1147-2016, 2016.

Millan, R., Mouginot, J., Rabatel, A., Jeong, S., Cusicanqui, D., Derkacheva, A., and Chekki, M.: Mapping surface flow velocity of glaciers at regional scale using a multiple sensors approach, Remote Sens., 11, 1–21, https://doi.org/10.3390/rs11212498, 2019.

Minchew, B., Simons, M., Björnsson, H., Pálsson, F., Morlighem, M., Seroussi, H., Larour, E., and Hensley, S.: Plastic bed beneath Hofsjökull ice cap, central Iceland, and the sensitivity of ice flow to surface meltwater flux, J. Glaciol., 62, 147–158, https://doi.org/10.1017/jog.2016.26, 2016.

Morlighem, M., Rignot, E., Seroussi, H., Larour, E., Ben Dhia, H., and Aubry, D.: A mass conservation approach for mapping glacier ice thickness, Geophys. Res. Lett., 38, 1–6, https://doi.org/10.1029/2011GL048659, 2011.

Morlighem, M., Rignot, E., Mouginot, J., Wu, X., Seroussi, H., Larour, E., and Paden, J.: High-resolution bed topography mapping of Russell Glacier, Greenland, inferred from Operation IceBridge data, J. Glaciol., 59, 1015–1023, https://doi.org/10.3189/2013JoG12J235, 2013.

Morlighem, M., Williams, C. N., Rignot, E., An, L., Arndt, J. E., Bamber, J. L., Catania, G., Chauché, N., Dowdeswell, J. A., Dorschel, B., Fenty, I., Hogan, K., Howat, I., Hubbard, A., Jakobsson, M., Jordan, T. M., Kjeldsen, K. K., Millan, R., Mayer, L., Mouginot, J., Noël, B. P., O'Cofaigh, C., Palmer, S., Rysgaard, S., Seroussi, H., Siegert, M. J., Slabon, P., Straneo, F., van den Broeke, M. R., Weinrebe, W., Wood, M., and Zinglersen, K. B.: BedMachine v3: Complete Bed Topography and Ocean Bathymetry Mapping of Greenland From Multibeam Echo Sounding Combined With Mass Conservation, Geophys. Res. Lett., 44, 11051–11061, https://doi.org/10.1002/2017GL074954, 2017.

Mouginot, J., Rignot, E., Scheuchl, B., and Millan, R.: Comprehensive Annual Ice Sheet Velocity Mapping Using Landsat-8, Sentinel-1, and RADARSAT-2 Data, Remote Sen., 9, 1–20, https://doi.org/10.3390/rs9040364, 2017.

Mouginot, J., Rignot, E., Bjørk, A. A., van den Broeke, M., Millan, R., Morlighem, M., Noël, B., Scheuchl, B., and Wood, M.: Forty-six years of Greenland Ice Sheet mass balance from 1972 to 2018, P. Natl. Acad. Sci. USA, 116, 9239–9244, https://doi.org/10.1073/pnas.1904242116, 2019.

Nienow, P. W., Sole, A. J., Slater, D. A., and Cowton, T. R.: Recent Advances in Our Understanding of the Role of Meltwater in the Greenland Ice Sheet System, Curr. Clim. Change Rep., 3, 330–344, https://doi.org/10.1007/s40641-017-0083-9, 2017.

Palmer, S., Shepherd, A., Nienow, P., and Joughin, I.: Seasonal speedup of the Greenland Ice Sheet linked to routing of surface water, Earth Planet. Sc. Lett., 302, 423–428, https://doi.org/10.1016/j.epsl.2010.12.037, 2011.

Pimentel, S., Flowers, G. E., and Schoof, C. G.: A hydrologically coupled higher-order flow-band model of ice dynamics with a

Coulomb friction sliding law, J. Geophys. Res.-Earth, 115, 1–16, https://doi.org/10.1029/2009JF001621, 2010.

Poinar, K., Joughin, I., Das, S. B., Behn, M. D., Lenaerts, J. T., and Van Den Broeke, M. R.: Limits to future expansion of surface-melt-enhanced ice flow into the interior of western Greenland, Geophys. Res. Lett., 42, 1800–1807, https://doi.org/10.1002/2015GL063192, 2015.

Price, S. F., Payne, A. J., Catania, G. A., and Neumann, T. A.: Seasonal acceleration of inland ice via longitudinal coupling to marginal ice, J. Glaciol., 54, 213–219, https://doi.org/10.3189/002214308784886117, 2008.

Rignot, E. and Mouginot, J.: Ice flow in Greenland for the International Polar Year 2008–2009, Geophys. Res. Lett., 39, 1–7, https://doi.org/10.1029/2012GL051634, 2012.

Ryser, C., Lüthi, M. P., Andrews, L. C., Catania, G. A., Funk, M., and Hawley, R.: Caterpillar-like ice motion in the ablation zone of the Greenland ice sheet, J. Geophys. Res.-Earth, 119, 2258–2271, https://doi.org/10.1002/2013JF003067, 2014a.

Ryser, C., Luthi, M. P., Andrews, L. C., Hoffman, M. J., Catania, G. A., Hawley, R. L., Neumann, T. A., and Kristensen, S. S.: Sustained high basal motion of the Greenland ice sheet revealed by borehole deformation, J. Glaciol., 60, 647–660, https://doi.org/10.3189/2014JoG13J196, 2014b.

Scambos, T. A. and Haran, T.: An image-enhanced DEM of the Greenland ice sheet, Ann. Glaciol., 34, 291–298, https://doi.org/10.3189/172756402781817969, 2002.

Schäfer, M., Gillet-Chaulet, F., Gladstone, R., Pettersson, R., Pohjola, V. A., Strozzi, T., and Zwinger, T.: Assessment of heat sources on the control of fast flow of Vestfonna ice cap, Svalbard, The Cryosphere, 8, 1951–1973, https://doi.org/10.5194/tc-8-1951-2014, 2014.

Schoof, C.: The effect of cavitation on glacier sliding, P. Roy. Soc. A, 461, 609–627, https://doi.org/10.1098/rspa.2004.1350, 2005.

Shapero, D. R., Joughin, I. R., Poinar, K., Morlighem, M., and Gillet-Chaulet, F.: Basal resistance for three of the largest Greenland outlet glaciers, J. Geophys. Res.-Earth, 121, 168–180, https://doi.org/10.1002/2015JF003643, 2016.

Smeets, C. J. P. P., Boot, W., Hubbard, A., Pettersson, R., Wilhelms, F., Van Den Broeke, M. R., and Van De Wal, R. S. W.: A wireless subglacial probe for deep ice applications, Instrum. Meth., 58, 841–848, https://doi.org/10.3189/2012JoG11J130, 2012.

Smith, L. C., Chu, V. W., Yang, K., Gleason, C. J., Pitcher, L. H., Rennermalm, A. K., Legleiter, C. J., Behar, A. E., Overstreet, B. T., Moustafa, S. E., Tedesco, M., Forster, R. R., LeWinter, A. L., Finnegan, D. C., Sheng, Y., and Balog, J.: Efficient meltwater drainage through supraglacial streams and rivers on the southwest Greenland ice sheet, P. Natl. Acad. Sci. USA, 112, 1001–1006, https://doi.org/10.1073/pnas.1413024112, 2015.

Sole, A., Nienow, P., Bartholomew, I., Mair, D., Cowton, T., Tedstone, A., and King, M. A.: Winter motion mediates dynamic response of the Greenland Ice Sheet to warmer summers, Geophys. Res. Lett., 40, 3940–3944, https://doi.org/10.1002/grl.50764, 2013.

Stevens, L. A., Behn, M. D., Das, S. B., Joughin, I., Noël, B. P., van den Broeke, M. R., and Herring, T.: Greenland Ice Sheet flow response to runoff variability, Geophys. Res. Lett., 43, 11295–11303, https://doi.org/10.1002/2016GL070414, 2016.

Sugiyama, S. and Gudmundsson, G. H.: Short-term variations in glacier flow controlled by subglacial water pressure at Lauteraargletscher, Bernese Alps, Switzerland, J. Glaciol., 50, 353–362, https://doi.org/10.3189/172756504781829846, 2004.

Sundal, A. V., Shepherd, A., Nienow, P., Hanna, E., Palmer, S., and Huybrechts, P.: Melt-induced speed-up of Greenland ice sheet offset by efficient subglacial drainage, Nature, 469, 521–524, https://doi.org/10.1038/nature09740, 2011.

Tedstone, A., Nienow, P. W., Gourmelen, N., Dehecq, A., Goldberg, D., and Hanna, E.: Decadal slowdown of a land-terminating sector of the Greenland Ice Sheet despite warming, Nature, 526, 692–695, https://doi.org/10.1038/nature15722, 2015.

Tedstone, A. J., Nienow, P. W., Sole, A. J., Mair, D. W. F., Cowton, T. R., Bartholomew, I. D., and King, M. A.: Greenland ice sheet motion insensitive to exceptional meltwater forcing, P. Natl. Acad. Sci. USA, 110, 19719–19724, https://doi.org/10.1073/pnas.1315843110, 2013.

Tedstone, A. J., Nienow, P. W., Gourmelen, N., and Sole, A. J.: Greenland ice sheet annual motion insensitive to spatial variations in subglacial hydraulic structure, Geophys. Res. Lett., 41, 8910–8917, https://doi.org/10.1002/2014GL062386, 2014.

Truffer, M., Harrison, W. D., and Echelmeyer, K. A.: Glacier motion dominated by processes deep in underlying till, J. Glaciol., 46, 213–221, https://doi.org/10.3189/172756500781832909, 2000.

Trusel, L. D., Das, S. B., Osman, M. B., Evans, M. J., Smith, B. E., Fettweis, X., McConnell, J. R., Noël, B. P., and van den Broeke, M. R.: Nonlinear rise in Greenland runoff in response to post-industrial Arctic warming, Nature, 564, 104–108, https://doi.org/10.1038/s41586-018-0752-4, 2018.

Van De Wal, R. S., Boot, W., Smeets, C. J., Snellen, H., Van Den Broeke, M. R., and Oerlemans, J.: Twenty-one years of mass balance observations along the K-transect, West Greenland, Earth Syst. Sci. Data, 4, 31–35, https://doi.org/10.5194/essd-4-31-2012, 2012.

Van De Wal, R. S., Smeets, C. J., Boot, W., Stoffelen, M., Van Kampen, R., Doyle, S. H., Wilhelms, F., Van Den Broeke, M. R., Reijmer, C. H., Oerlemans, J., and Hubbard, A.: Self-regulation of ice flow varies across the ablation area in south-west Greenland, The Cryosphere, 9, 603–611, https://doi.org/10.5194/tc-9-603-2015, 2015.

Van Tricht, K., Lhermitte, S., Lenaerts, J. T., Gorodetskaya, I. V., L'Ecuyer, T. S., Noël, B., Van Den Broeke, M. R., Turner, D. D., and Van Lipzig, N. P.: Clouds enhance Greenland ice sheet meltwater runoff, Nat. Commun., 7, 10266, https://doi.org/10.1038/ncomms10266, 2016.

Vijay, S., Khan, S. A., Kusk, A., Solgaard, A. M., Moon, T., and Bjørk, A. A.: Resolving Seasonal Ice Velocity of 45 Greenlandic Glaciers With Very High Temporal Details, Geophys. Res. Lett., 46, 1485–1495, https://doi.org/10.1029/2018GL081503, 2019.

Weertman, J.: On the sliding of glaciers, J. Glaciol., 3, 33–38, https://doi.org/10.1007/978-94-015-8705-1_19, 1957.

Wright, P., Harper, J., Humphrey, N., and Meierbachtol, T.: Measured basal water pressure variability of the western Greenland Ice Sheet: Implications for hydraulic potential, J. Geophys. Res.-Earth, 121, 1134–1147, https://doi.org/10.1002/2016JF003819, 2016.

Yang, Y., Li, F., Hwang, C., Ding, M., and Ran, J.: Space-Time Evolution of Greenland Ice Sheet Elevation and Mass From En-

visat and GRACE Data, J. Geophys. Res.-Earth, 124, 2079–2100, https://doi.org/10.1029/2018JF004765, 2019.

Young, T. J., Christoffersen, P., Doyle, S. H., Nicholls, K. W., Stewart, C. L., Hubbard, B., Hubbard, A., Lok, L. B., Brennan, P. V., Benn, D. I., Luckman, A., and Bougamont, M.: Physical Conditions of Fast Glacier Flow: 3. Seasonally-Evolving Ice Deformation on Store Glacier, West Greenland, J. Geophys. Res.-Earth, 124, 245–267, https://doi.org/10.1029/2018JF004821, 2019.

Zoet, L. K. and Iverson, N. R.: A slip law for glaciers on deformable beds, Science, 368, 76–78, https://doi.org/10.1126/science.aaz1183, 2020.

Zwally, H. J., Abdalati, W., Herring, T., Larson, K., Saba, J., and Steffen, K.: Surface melt-induced acceleration of Greenland ice-sheet flow, Science, 297, 218–222, https://doi.org/10.1126/science.1072708, 2002.

Conclusion & perspectives

In this thesis, we addressed the problems of lack of frequent, spatially-extended and precise observation of glaciers surface speed and of the resulting limitations in investigations of speed fluctuations driving processes.

Our results of the first part (Section 2) show that the joint use of images from multiple satellites allows the creation of velocity time-series with temporal resolution and uncertainties suitable for seasonal observation of dynamics across the entire GrIS margin. Developing post-processing analysis improved the accuracy of our time series and the final datasets have a temporal resolution of about 2-weeks and an accuracy of about 10 m/yr, hence improving the quality of raw measurements by a factor three. With such datasets, we reveal the detailed spatio-temporal behavior of seasonal flow dynamic of three glaciers in Greenland; for the first time we resolved the presence of seasonal velocity fluctuation on Upernavik glacier northern and central branches, where the previous studies declared lack thereof. The satellite data reveal a complex seasonal behavior for each of the studied glaciers, which comes from the mixed effects of different forcings acting on a seasonal basis.

Nevertheless, it is good to mention that our time-series still suffer from gaps in observations and cross-correlation results. This issue was not been fully solved during this study. Two ways of further improvements could be proposed to deal with these issues. First, a finer choice of the cross-correlation parameters with respect to the specificity of site, season, or sensor type could potentially improve the feature-tracking robustness. Second, more advanced post-processing algorithms would take into account the redundancy of measurements to fill the gaps in sophisticated way with the respect to the local dynamics. Besides that, a more detailed and realistic estimation of uncertainties in the derived time-series is crucial in order to tend toward data assimilation in models, which would help to produce an optimal estimate of the evolving state of the system. As shown here, the theoretically estimated values assigned to the raw measurements are not uniformly suitable for measurements done in various seasons; moreover, the unique value per velocity map hides the spatial heterogeneity of the measurement's quality. Further, on the LOWESS post-processing step, we do not take into account even those theoretically uncertainty values and do not evaluate the uncertainties of output data. The proper manipulation by the uncertainties in the post-processing would be realized by adding several intermediate calculations in a used routine.

In the second part of the thesis (Section 3), we assess the potential of modelling use on a dense time series to recover the seasonal evolution of the external forcings and so improve our understanding of its interaction with the glacier dynamic. Our diagnostic model-based study showed that the retrieved surface speed measurements can provide a new level of details on the evolution of basal conditions. The temporal richness of the input data became an important benefitting point for the created modelling workflow, providing a better constrain of the model's procedures and parameterization. As a result, we achieved to describe with great detailes the seasonal evolution of subglacial environment conditions and responsible drivers, including hydrological processes, based on the observations of ice surface speed. It was also possible to

identify areas of differing responses of ice motion, or to make the assumptions on the bedrock properties and presence of deformable sediments.

This experiment has been done for the land-terminating Russell site, for which many studies have been previously conducted and the major velocity driver has already been conceptualized. The time-series generated for marine-terminating Upernavik Isstrøm and Petermann Gletscher, where the mutual role of more numerous processes is less clear and will be difficult to entangle, would also allow similar detailed investigations of the seasonal drivers. The incorporation of grounding/front lines displacement will require an additional level of complicity of the model and results analysis. Besides that, the access to the velocity observations with fine temporal resolution open the large possibilities for a list of questions that were previously investigated only on synthetic case studies. For instance, it has not yet been examined if the usage of a constant mean annual velocity or the velocity fields containing seasonal fluctuations would lead to changes in the results of a multi-decennial prognostic modelling.

Thanks to the currently operational satellite constellation and image processing facilities, it is possible to produce frequent, accurate, and spatially extended measurements of glacier flow. It can be stated that the lack of observations, which has been a limiting factor until recently, is now overcoming. However, a careful attention must be paid to how these time series will be made available to the glaciological community, including questions of post-processing and errors budget assessment. In any case, this era of Big Data makes possible the new series of advances in modelling and, consequently, refinement of the understanding of processes driving the ice flow.

Bibliography

Ahlstrøm, A. P., Andersen, S. B., Andersen, M. L., Machguth, H., Nick, F. M., Joughin, I., Reijmer, C. H., van de Wal, R. S. W., Merryman Boncori, J. P., Box, J. E., Citterio, M., van As, D., Fausto, R. S. and Hubbard, A.: Seasonal velocities of eight major marine-terminating outlet glaciers of the Greenland ice sheet from continuous in situ GPS instruments, Earth Syst. Sci. Data, 5(2), 277–287, doi:10.5194/essd-5-277-2013, 2013.

Åkesson, H., Nisancioglu, K. H. and Nick, F. M.: Impact of fjord geometry on grounding line stability, Front. Earth Sci., 6(June), 1–16, doi:10.3389/feart.2018.00071, 2018.

Altena, B. and Kääb, A.: Quantifying river ice movement through a combination of European satellite monitoring services, Int. J. Appl. Earth Obs. Geoinf., 98(January), 102315, doi:10.1016/j.jag.2021.102315, 2021.

Andresen, C. S., Kjeldsen, K. K., Harden, B., Nørgaard-Pedersen, N. and Kjær, K. H.: Outlet glacier dynamics and bathymetry at Upernavik Isstrøm and Upernavik Isfjord, North-West Greenland, Geol. Surv. Denmark Greenl. Bull., (31), 79–82, doi:10.34194/geusb.v31.4668, 2014.

Armstrong, W. H., Anderson, R. S. and Fahnestock, M. A.: Spatial Patterns of Summer Speedup on South Central Alaska Glaciers, Geophys. Res. Lett., 44(18), 9379–9388, doi:10.1002/2017GL074370, 2017.

Bamber, J. L., Siegert, M. J., Griggs, J. A., Marshall, S. J. and Spada, G.: Paleofluvial mega-canyon beneath the central Greenland ice sheet, Science (80-.)., 341(6149), 997–999, doi:10.1126/science.1239794, 2013.

Bartholomew, I., Nienow, P., Sole, A., Mair, D., Cowton, T. and King, M. A.: Short-term variability in Greenland Ice Sheet motion forced by time-varying meltwater drainage: Implications for the relationship between subglacial drainage system behavior and ice velocity, J. Geophys. Res. Earth Surf., 117(3), 1–17, doi:10.1029/2011JF002220, 2012.

Beckmann, J., Perrette, M., Beyer, S., Calov, R., Willeit, M. and Ganopolski, A.: Modeling the response of Greenland outlet glaciers to global warming using a coupled flow line-plume model, Cryosphere, 13(9), 2281–2301, doi:10.5194/tc-13-2281-2019, 2019.

Benn, D. and Evans, D.: Glaciers and glaciation, 2nd ed., Routledge, New York., 2010.

Benn, D. I. and Åström, J. A.: Calving glaciers and ice shelves, Adv. Phys. X, 3(1), 1048–1076, doi:10.1080/23746149.2018.1513819, 2018.

Berthier, E., Vadon, H., Baratoux, D., Arnaud, Y., Vincent, C., Feigl, K. L., Rémy, F. and Legrésy, B.: Surface motion of mountain glaciers derived from satellite optical imagery, Remote Sens. Environ., 95(1), 14–28, doi:10.1016/j.rse.2004.11.005, 2005.

Bevan, S. L., Luckman, A., Khan, S. A. and Murray, T.: Seasonal dynamic thinning at Helheim Glacier, Earth Planet. Sci. Lett., 415, 47–53, doi:10.1016/j.epsl.2015.01.031, 2015.

Bevis, M., Harig, C., Khan, S. A., Brown, A., Simons, F. J., Willis, M., Fettweis, X., Van Den Broeke, M. R., Madsen, F. B., Kendrick, E., Caccamise, D. J., Van Dam, T., Knudsen, P. and Nylen, T.: Accelerating changes in ice mass within Greenland, and the ice sheet's sensitivity to

atmospheric forcing, Proc. Natl. Acad. Sci. U. S. A., 116(6), 1934–1939, doi:10.1073/pnas.1806562116, 2018.

Bindschadler, R. A. and Scambos, T. A.: Satellite-Image-Derived Velocity Field of an Antarctic Ice Stream, Science (80-.)., 252(5003), 242–246, 1991.

Bjørk, A. A., Kjær, K. H., Korsgaard, N. J., Khan, S. A., Kjeldsen, K. K., Andresen, C. S., Box, J. E., Larsen, N. K. and Funder, S.: An aerial view of 80 years of climate-related glacier fluctuations in southeast Greenland, Nat. Geosci., 5(6), 427–432, doi:10.1038/ngeo1481, 2012.

Bondzio, J. H., Morlighem, M., Seroussi, H., Kleiner, T., Rückamp, M., Mouginot, J., Moon, T., Larour, E. Y. and Humbert, A.: The mechanisms behind Jakobshavn Isbræ's acceleration and mass loss: A 3-D thermomechanical model study, Geophys. Res. Lett., 44(12), 6252–6260, doi:10.1002/2017GL073309, 2017.

Bontemps, N., Lacroix, P. and Doin, M. P.: Inversion of deformation fields time-series from optical images, and application to the long term kinematics of slow-moving landslides in Peru, Remote Sens. Environ., 210(February), 144–158, doi:10.1016/j.rse.2018.02.023, 2018.

Bougamont, M., Christoffersen, P., Hubbard, A. L., Fitzpatrick, A. A., Doyle, S. H. and Carter, S. P.: Sensitive response of the Greenland Ice Sheet to surface melt drainage over a soft bed, Nat. Commun., 5, doi:10.1038/ncomms6052, 2014.

Boulton, G. S.: Theory of glacial erosion, transport and deposition as a consequence of subglacial sediment deformation, J. Glaciol., 42(140), 43–62, doi:10.1017/S0022143000030525, 1996.

Brinkerhoff, D., Aschwanden, A. and Fahnestock, M.: Constraining subglacial processes from surface velocity observations using surrogate-based Bayesian inference, J. Glaciol., 1–19, doi:10.1017/jog.2020.112, 2021.

Brinkerhoff, D. J. and Johnson, J. V.: Data assimilation and prognostic whole ice sheet modelling with the variationally derived, higher order, open source, and fully parallel ice sheet model VarGlaS, Cryosphere, 7(4), 1161–1184, doi:10.5194/tc-7-1161-2013, 2013.

Bueler, E.: Stable finite volume element schemes for the shallow-ice approximation, J. Glaciol., 62(232), 230–242, doi:10.1017/jog.2015.3, 2016.

Bueler, E. and Brown, J.: Shallow shelf approximation as a "sliding law" in a thermomechanically coupled ice sheet model, J. Geophys. Res. Solid Earth, 114(3), doi:10.1029/2008JF001179, 2009.

Bunce, C., Carr, J. R., Nienow, P. W., Ross, N. and Killick, R.: Ice front change of marine-terminating outlet glaciers in northwest and southeast Greenland during the 21st century, J. Glaciol., 64(246), 523–535, doi:10.1017/jog.2018.44, 2018.

Cazenave, A., Meyssignac, B., Ablain, M., Balmaseda, M., Bamber, J., Barletta, V., Beckley, B., Benveniste, J., Berthier, E., Blazquez, A., Boyer, T., Caceres, D., Chambers, D., Champollion, N., Chao, B., Chen, J., Cheng, L., Church, J. A., Chuter, S., Cogley, J. G., Dangendorf, S., Desbruyères, D., Döll, P., Domingues, C., Falk, U., Famiglietti, J., Fenoglio-Marc, L., Forsberg, R., Galassi, G., Gardner, A., Groh, A., Hamlington, B., Hogg, A., Horwath, M., Humphrey, V., Husson, L., Ishii, M., Jaeggi, A., Jevrejeva, S., Johnson, G., Kolodziejczyk, N., Kusche, J., Lambeck, K., Landerer, F., Leclercq, P., Legresy, B., Leuliette, E., Llovel, W., Longuevergne, L., Loomis, B. D., Luthcke, S. B., Marcos, M., Marzeion, B., Merchant, C., Merrifield, M., Milne, G., Mitchum, G., Mohajerani, Y., Monier, M., Monselesan, D., Nerem, S., Palanisamy, H., Paul, F.,

Perez, B., Piecuch, C. G., Ponte, R. M., Purkey, S. G., Reager, J. T., Rietbroek, R., Rignot, E., Riva, R., Roemmich, D. H., Sørensen, L. S., Sasgen, I., Schrama, E. J. O., Seneviratne, S. I., Shum, C. K., Spada, G., Stammer, D., van de Wal, R., Velicogna, I., Schuckmann, K. von, Wada, Y., Wang, Y., Watson, C., Wiese, D., Wijffels, S., Westaway, R., Woppelmann, G. and Wouters, B.: Global sea-level budget 1993-present, Earth Syst. Sci. Data, 10(3), 1551–1590, doi:10.5194/essd-10-1551-2018, 2018.

Cheremnykh, G. D.: New developments in the measurement of the rate of movement of ice in the surface parts of glaciers as shown by aerial photography, Geod. Aerophotogr., 5, 342–344, 1962.

Christoffersen, P., Bougamont, M., Hubbard, A., Doyle, S. H., Grigsby, S. and Pettersson, R.: Cascading lake drainage on the Greenland Ice Sheet triggered by tensile shock and fracture, Nat. Commun., 9(1), 1064, doi:10.1038/s41467-018-03420-8, 2018.

Chu, V. W.: Greenland ice sheet hydrology: A review., 2014.

Cook, A. J., Holland, P. R., Meredith, M. P., Murray, T., Luckman, A. and Vaughan, D. G.: Ocean forcing of glacier retreat in the western Antarctic Peninsula, Science (80-.)., 353(6296), 283–286, doi:10.1126/science.aae0017, 2016.

Csatho, B. M., Bolzan, J. F., van der Veen, C. J., Schenk, A. F. and Lee, D. C.: Surface velocities of a Greenland outlet glacier from high-resolution visible satellite imagery, Polar Geogr., 23(1), 71–82, doi:10.1080/10889379909377665, 1999.

Csatho, B. M., Schenka, A. F., Van Der Veen, C. J., Babonis, G., Duncan, K., Rezvanbehbahani, S., Van Den Broeke, M. R., Simonsen, S. B., Nagarajan, S. and Van Angelen, J. H.: Laser altimetry reveals complex pattern of Greenland Ice Sheet dynamics, Proc. Natl. Acad. Sci. U. S. A., 111(52), 18478–18483, doi:10.1073/pnas.1411680112, 2014.

Cuffey, K. M. and Paterson, W. S. B.: The physics of glaciers, Academic Press., Amsterdam., 2010.

Davison, B. J., Sole, A. J., Livingstone, S. J., Cowton, T. R. and Nienow, P. W.: The Influence of Hydrology on the Dynamics of Land-Terminating Sectors of the Greenland Ice Sheet, Front. Earth Sci., 7(February), 1–24, doi:10.3389/feart.2019.00010, 2019.

Debella-Gilo, M. and Kääb, A.: Sub-pixel precision image matching for measuring surface displacements on mass movements using normalized cross-correlation, Remote Sens. Environ., 115(1), 130–142, 2011.

Dehecq, A., Gourmelen, N. and Trouve, E.: Deriving large-scale glacier velocities from a complete satellite archive: Application to the Pamir-Karakoram-Himalaya, Remote Sens. Environ., 162, 55–66, doi:10.1016/j.rse.2015.01.031, 2015.

Dehecq, A., Gourmelen, N., Gardner, A. S., Brun, F., Goldberg, D., Nienow, P. W., Berthier, E., Vincent, C., Wagnon, P. and Trouvé, E.: Twenty-first century glacier slowdown driven by mass loss in High Mountain Asia, Nat. Geosci., 12(January), doi:10.1038/s41561-018-0271-9, 2019.

Derkacheva, A., Mouginot, J., Millan, R., Maier, N. and Gillet-Chaulet, F.: Data Reduction Using Statistical and Regression Approaches for Ice Velocity Derived by Landsat-8, Sentinel-1 and Sentinel-2, Remote Sens., 12(12), 1935, doi:10.3390/rs12121935, 2020.

Derkacheva, A., Gillet-chaulet, F., Mouginot, J., Jager, E., Maier, N. and Cook, S.: Seasonal evolution of basal environment conditions of Russell sector , West Greenland , inverted from satellite observation of surface flow, Cryosph. Discuss., (June), 1–41, 2021.

Doyle, S. H., Hubbard, A., Fitzpatrick, A. A. W., van As, D., Mikkelsen, A. B., Pettersson, R. and Hubbard, B.: Persistent flow acceleration within the interior of the Greenland ice sheet, Geophys. Res. Lett., 41(18), 6413–6419, 2014.

Doyle, S. H., Hubbard, B., Christoffersen, P., Young, T. J., Hofstede, C., Bougamont, M., Box, J. E. and Hubbard, A.: Physical Conditions of Fast Glacier Flow : 1 . Measurements From Boreholes Drilled to the Bed of Store, J. Geophys. Res., 324–348, 2018.

Dulova, I. A., Skuratovsky, S. I., Bondarenko, N. V. and Kornienko, Y. V.: Reconstruction of the surface topography from single images with the photometric method, Sol. Syst. Res., 42(6), 522–535, doi:10.1134/S0038094608060051, 2008.

Duro, J., Albiol, D., Mora, O. and Payas, B.: Application of advanced InSAR techniques for the measurement of vertical and horizontal ground motion in longwall minings, 13th Coal Oper. Conf. Univ. Wollongong, Australas. Inst. Min. Metall. Mine Manag. Assoc. Aust., 99–106, 2013.

Echelmeyer, K. and Harrison, W. D.: Jakobshavns Isbrae, West Greenland: seasonal variations in velocity - or lack thereof, J. Glaciol., 36(122), 82–88, doi:10.1017/S0022143000005591, 1990.

Fahnestock, M., Scambos, T., Moon, T., Gardner, A., Haran, T. and Klinger, M.: Rapid large-area mapping of ice flow using Landsat 8, Remote Sens. Environ., 185, 84–94, doi:10.1016/j.rse.2015.11.023, 2015.

Fettweis, X.: Reconstruction of the 1979-2006 Greenland ice sheet surface mass balance using the regional climate model MAR, Cryosphere, 1(1), 21–40, doi:10.5194/tc-1-21-2007, 2007.

Fitzpatrick, A. A. W., Hubbard, A., Joughin, I., Quincey, D. J., As, D. Van, Mikkelsen, A. P. B., Doyle, S. H., Hasholt, B. and Jones, G. A.: Ice flow dynamics and surface meltwater flux at a land-terminating sector of the Greenland ice sheet, J. Glaciol., 59(216), 687–696, doi:10.3189/2013JoG12J143, 2013.

de Fleurian, B., Morlighem, M., Seroussi, H., Rignot, E., van den Broeke, M. R., Kuipers Munneke, P., Mouginot, J., Smeets, P. C. J. P. and Tedstone, A. J.: A modeling study of the effect of runoff variability on the effective pressure beneath Russell Glacier, West Greenland, J. Geophys. Res. Earth Surf., 121(10), 1834–1848, doi:10.1002/2016JF003842, 2016.

Flowers, G. E.: Modelling water flow under glaciers and ice sheets, Proc. R. Soc. A Math. Phys. Eng. Sci., 471(2176), doi:10.1098/rspa.2014.0907, 2015.

Fountain, A. G. and Walder, J. S.: Water flow through temperate glaciers, Rev. Geophys., 36(3), 299–328, doi:10.1029/97RG03579, 1998.

Fürst, J. J., Durand, G., Gillet-Chaulet, F., Tavard, L., Rankl, M., Braun, M. and Gagliardini, O.: The safety band of Antarctic ice shelves, Nat. Clim. Chang., 6(5), 479–482, doi:10.1038/nclimate2912, 2016.

Gagliardini, O., Cohen, D., Råback, P. and Zwinger, T.: Finite-element modeling of subglacial cavities and related friction law, J. Geophys. Res., 112(F2), F02027, doi:10.1029/2006JF000576, 2007.

Gardner, A. S., Moholdt, G., Scambos, T., Fahnstock, M., Ligtenberg, S., Van Den Broeke, M. and Nilsson, J.: Increased West Antarctic and unchanged East Antarctic ice discharge over the last 7 years, Cryosphere, 12(2), 521–547, doi:10.5194/tc-12-521-2018, 2018.

Gardner, A. S., Fahnestock, M. A. and Scambos, T. A.: ITS_LIVE Regional Glacier and Ice Sheet Surface Velocities. Data archived at National Snow and Ice Data Center, , doi:10.5067/6II6VW8LLWJ7, 2019.

Gillet-Chaulet, F., Gagliardini, O., Seddik, H., Nodet, M., Durand, G., Ritz, C., Zwinger, T., Greve, R. and Vaughan, D. G.: Greenland ice sheet contribution to sea-level rise from a new-generation ice-sheet model, Cryosphere, 6(6), 1561–1576, doi:10.5194/tc-6-1561-2012, 2012.

Goelzer, H., Robinson, A., Seroussi, H. and van de Wal, R. S. W.: Recent Progress in Greenland Ice Sheet Modelling, Curr. Clim. Chang. Reports, 3(4), 291–302, doi:10.1007/s40641-017-0073-y, 2017.

Gray, L., Burgess, D., Copland, L., Langley, K., Gogineni, P., Paden, J., Leuschen, C., van As, D., Fausto, R., Joughin, I. and Smith, B.: Measuring height change around the periphery of the greenland ice sheet with radar altimetry, Front. Earth Sci., 7(June), 1–14, doi:10.3389/feart.2019.00146, 2019.

Habermann, M., Truffer, M. and Maxwell, D.: Error sources in basal yield stress inversions for Jakobshavn Isbræ, Greenland, derived from residual patterns of misfit to observations, J. Glaciol., 63(242), 999–1011, doi:10.1017/jog.2017.61, 2017.

Harper, J. T., Humphrey, N. F., Meierbachtol, T. W., Graly, J. A. and Fischer, U. H.: Borehole measurements indicate hard bed conditions, Kangerlussuaq sector, western Greenland Ice Sheet, J. Geophys. Res. Earth Surf., 122(9), 1605–1618, doi:10.1002/2017JF004201, 2017.

Harrington, J. A., Humphrey, N. F. and Harper, J. T.: Temperature distribution and thermal anomalies along a flowline of the Greenland ice sheet, Ann. Glaciol., 56(70), 98–104, doi:10.3189/2015AoG70A945, 2015.

Hasholt, B., Mikkelsen, A. B., Nielsen, M. H. and Larsen, M. A. D.: Observations of runoff and sediment and dissolved loads from the Greenland ice sheet at kangerlussuaq, West Greenland, 2007 to 2010, Zeitschrift fur Geomorphol., 57(July), 3–27, doi:10.1127/0372-8854/2012/S-00121, 2013.

Haubner, K., Box, J. E., Schlegel, N. J., Larour, E. Y., Morlighem, M., Solgaard, A. M., Kjeldsen, K. K., Larsen, S. H., Rignot, E., Dupont, T. K. and Kjær, K. H.: Simulating ice thickness and velocity evolution of Upernavik Isstrøm 1849-2012 by forcing prescribed terminus positions in ISSM, Cryosphere, 12(4), 1511–1522, doi:10.5194/tc-12-1511-2018, 2018.

Heid, T. and Kääb, A.: Evaluation of existing image matching methods for deriving glacier surface displacements globally from optical satellite imagery, Remote Sens. Environ., 118, 339–355, doi:10.1016/j.rse.2011.11.024, 2012.

Helm, V., Humbert, A. and Miller, H.: Elevation and elevation change of Greenland and Antarctica derived from CryoSat-2, Cryosphere, 8(4), 1539–1559, doi:10.5194/tc-8-1539-2014, 2014.

Hill, E. A., Hilmar Gudmundsson, G., Rachel Carr, J. and Stokes, C. R.: Velocity response of Petermann Glacier, northwest Greenland, to past and future calving events, Cryosphere, 12(12),

3907–3921, doi:10.5194/tc-12-3907-2018, 2018.

Hills, B. H., Harper, J. T., Humphrey, N. F. and Meierbachtol, T. W.: Measured Horizontal Temperature Gradients Constrain Heat Transfer Mechanisms in Greenland Ice, Geophys. Res. Lett., 44(19), 9778–9785, doi:10.1002/2017GL074917, 2017.

Hoffman, M. J., Andrews, L. C., Price, S. A., Catania, G. A., Neumann, T. A., Lüthi, M. P., Gulley, J., Ryser, C., Hawley, R. L. and Morriss, B.: Greenland subglacial drainage evolution regulated by weakly connected regions of the bed, Nat. Commun., 7, doi:10.1038/ncomms13903, 2016.

Hogg, A. E., Shepherd, A., Gourmelen, N. and Engdahl, M.: Grounding line migration from 1992 to 2011 on Petermann Glacier, North-West Greenland, J. Glaciol., 62(236), 1104–1114, doi:10.1017/jog.2016.83, 2016.

Houtz, D., Mätzler, C., Naderpour, R., Schwank, M. and Steffen, K.: Quantifying Surface Melt and Liquid Water on the Greenland Ice Sheet using L-band Radiometry, Remote Sens. Environ., 256(December 2020), doi:10.1016/j.rse.2021.112341, 2021.

Howat, I. M., Box, J. E., Ahn, Y., Herrington, A. and McFadden, E. M.: Seasonal variability in the dynamics of marine-terminating outlet glaciers in Greenland, J. Glaciol., 56(198), 601–613, doi:10.3189/002214310793146232, 2010.

IPCC Working Group 1, Stocker, T. F., Qin, D., Plattner, G.-K., Tignor, M., Allen, S. K., Boschung, J., Nauels, A., Xia, Y., Bex, V. and Midgley, P. M.: IPCC, 2013: Climate Change 2013: The Physical Science Basis. Contribution of Working Group I to the Fifth Assessment Report of the Intergovernmental Panel on Climate Change., 2013.

Jay-Allemand, M., Gillet-Chaulet, F., Gagliardini, O. and Nodet, M.: Investigating changes in basal conditions of Variegated Glacier prior to and during its 1982–1983 surge, Cryosph., 5(3), 659–672, doi:10.5194/tc-5-659-2011, 2011.

Jeong, S. and Howat, I. M.: Performance of Landsat 8 Operational Land Imager for mapping ice sheet velocity, Remote Sens. Environ., 170(8), 90–101, doi:10.1016/j.rse.2015.08.023, 2015.

Johnson, H. L., Münchow, A., Falkner, K. K. and Melling, H.: Ocean circulation and properties in Petermann Fjord, Greenland, J. Geophys. Res. Ocean., 116(1), 1–18, doi:10.1029/2010JC006519, 2011.

Joughin, I., Tulaczyk, S., Fahnestock, M. and Kwok, R.: A mini-surge on the Ryder Glacier, Greenland, observed by satellite radar interferometry, Science (80-.)., 274(5285), 228–230, doi:10.1126/science.274.5285.228, 1996.

Joughin, I., Das, S. B., King, M. A., Smith, B. E. and Howat, I. M.: Seasonal Speedup Along the Western Flank of the Greenland Ice Sheet, Science (80-.)., 320(5877), 781–783, 2008a.

Joughin, I., Das, S. B., King, M. A., Smith, B. E., Howat, I. W. and Moon, T.: Seasonal Speedup Along the Western Flank of the Greenland Ice Sheet, Science (80-.)., 320 (5877)(May), 781–783, 2008b.

Joughin, I., Smith, B. E., Howat, I. M., Scambos, T. and Moon, T.: Greenland flow variability from ice-sheet-wide velocity mapping, J. Glaciol., 56(197), 415–430, doi:10.3189/002214310792447734, 2010.

Joughin, I., Smith, B. E., Howat, I. M., Floricioiu, D., Alley, R. B., Truffer, M. and Fahnestock, M.: Seasonal to decadal scale variations in the surface velocity of Jakobshavn Isbrae, Greenland: Observation and model-based analysis, J. Geophys. Res. Earth Surf., 117(2), 1–20, doi:10.1029/2011JF002110, 2012.

Joughin, I., Smith, B., Howat, I. and Scambos, T.: Greenland Ice Mapping Project 2 (GIMP-2) Algorithm. Theoretical Basis Document. [online] Available from: https://nsidc.org/data/measures/gimp/technical-references, 2017.

Joughin, I., Smith, B. E. and Howat, I.: Greenland Ice Mapping Project: Ice flow velocity variation at sub-monthly to decadal timescales, Cryosphere, 12(7), 2211–2227, doi:10.5194/tc-12-2211-2018, 2018.

Joughin, I., Shean, D., Smith, B. and Floricioiu, D.: A Decade of Variability on Jakobshavn Isbrae: Ocean Temperatures Pace Speed Through Influence on Mélange Rigidity, Cryosph. Discuss., 1–27, doi:10.5194/tc-2019-197, 2019.

Joughin, I. R., Kwok, R. and Fahnestock, M. A.: Interferometric estimation of threedimensional ice-flow using ascending and descending passes., IEEE Trans. Geosci. Remote Sens., 36(1), 25–37, 1998.

Ju, J. and Roy, D. P.: The availability of cloud-free Landsat ETM+ data over the conterminous United States and globally, Remote Sens. Environ., 112(3), 1196–1211, doi:10.1016/j.rse.2007.08.011, 2008.

Kääb, A., Winsvold, S. H., Altena, B., Nuth, C., Nagler, T. and Wuite, J.: Glacier remote sensing using Sentinel-2. part I: Radiometric and geometric performance, and application to ice velocity, Remote Sens., 8(7), doi:10.3390/rs8070598, 2016.

Karlsson, N. B., Solgaard, A. M., Mankoff, K. D., Gillet-Chaulet, F., MacGregor, J. A., Box, J. E., Citterio, M., Colgan, W. T., Larsen, S. H., Kjeldsen, K. K., Korsgaard, N. J., Benn, D. I., Hewitt, I. J. and Fausto, R. S.: A first constraint on basal melt-water production of the Greenland ice sheet, Nat. Commun., 12, 1–10, doi:10.1038/s41467-021-23739-z, 2021.

Katz, R. F. and Worster, M. G.: Stability of ice-sheet grounding lines, Proc. R. Soc. A Math. Phys. Eng. Sci., 466(2118), 1597–1620, doi:10.1098/rspa.2009.0434, 2010.

Khan, S. A., Kjær, K. H., Bevi, M., Bamber, J. L. and All., E.: Sustained mass loss of the northeast Greenland ice sheet triggered by regional warming, Nat. Clim. Chang., doi:10.1038/nclimate2161, 2014a.

Khan, S. A., Kjær, K. H., Bevi, M., Bamber, J. L. and All, E.: Sustained mass loss of the northeast Greenland ice sheet triggered by regional warming, Nat. Clim. Chang., doi:10.1038/nclimate2161, 2014b.

King, M. D., Howat, I. M., Jeong, S., Noh, M. J., Wouters, B., Nöel, B. and van den Broeke, M. R.: Seasonal to decadal variability in ice discharge from the Greenland Ice Sheet, Cryosph. Discuss., 1–28, doi:10.5194/tc-2018-177, 2018.

Konig, M., Winther, J. and Isaksson, E.: Measuring snow and glacier ice properties from satellite, Rev. Geophys., 29(1), 1–27, 2001.

Kraaijenbrink, P., Meijer, S. W., Shea, J. M., Pellicciotti, F., De Jong, S. M. and Immerzeel, W. W.:

Seasonal surface velocities of a Himalayan glacier derived by automated correlation of unmanned aerial vehicle imagery, Ann. Glaciol., 57(71), 103–113, doi:10.3189/2016AoG71A072, 2016.

Krimmel, R. M. and Meier, M. F.: Glacier applications of ERTS images, J. Glaciol., 15(73), 391–402, 1975.

Lacroix, P., Bièvre, G., Pathier, E., Kniess, U. and Jongmans, D.: Use of Sentinel-2 images for the detection of precursory motions before landslide failures, Remote Sens. Environ., 215(July 2017), 507–516, doi:10.1016/j.rse.2018.03.042, 2018.

Larsen, S. H., Khan, S. A., Ahlstrøm, A. P., Hvidberg, C. S., Willis, M. J. and Andersen, S. B.: Increased mass loss and asynchronous behavior of marine-terminating outlet glaciers at Upernavik Isstrøm, NW Greenland, J. Geophys. Res. Earth Surf., 121(2), 241–256, doi:10.1002/2015JF003507, 2016.

Lemos, A., Shepherd, A., McMillan, M., Hogg, A. E., Hatton, E. and Joughin, I.: Ice velocity of Jakobshavn Isbræ, Petermann Glacier, Nioghalvfjerdsfjorden, and Zachariæ Isstrøm, 2015–2017, from Sentinel 1-a/b SAR imagery, Cryosph., 12(6), 2087–2097, doi:10.5194/tc-12-2087-2018, 2018a.

Lemos, A., Shepherd, A., McMillan, M. and Hogg, A.: Seasonal Variations in the Flow of Land-Terminating Glaciers in Central-West Greenland Using Sentinel-1 Imagery, Remote Sens., 10(12), 1878, doi:10.3390/rs10121878, 2018b.

Li, J. and Chen, B.: Global Revisit Interval Analysis of Landsat-8 -9 and Sentinel-2A -2B Data for Terrestrial Monitoring, Sensors, 20, 1–15, doi:10.3390/s20226631, 2020.

Luckman, A. and Murray, T.: Seasonal variation in velocity before retreat of Jakobshavn Isbræ, Greenland, Geophys. Res. Lett., 32(8), 1–4, doi:10.1029/2005GL022519, 2005.

MacGregor, J. A., Fahnestock, M. A., Catania, G. A., Aschwanden, A., Clow, G. D., Colgan, W. T., Gogineni, S. P., Morlighem, M., Nowicki, S. M. J., Paden, J. D., Price, S. F. and Seroussi, H.: A synthesis of the basal thermal state of the Greenland Ice Sheet, , 300–316, 2016.

Mahaffy, M. W.: A three-dimensional numerical model of ice sheets: Tests on the Barnes Ice Cap, Northwest Territories, J. Geophys. Res., 81(6), 1059–1066, doi:10.1029/jc081i006p01059, 1976.

Maier, N., Humphrey, N., Harper, J. and Meierbachtol, T.: Sliding dominates slow-flowing margin regions, Greenland Ice Sheet, Sci. Adv., 5(7), eaaw5406, 2019.

Massonnet, D. and Feigl, K. L.: Radar interferometry and its application to changes in the earth's surface, Rev. Geophys., 36(4), 441–500, doi:10.1029/97RG03139, 1998.

Meier, M. F.: Variations in Time and Space of the Velocity of Lower Columbia Glacier, Alaska, J. Glaciol., 23(89), 408–408, doi:10.3189/S0022143000030057, 1979.

Michel, R. and Rignot, E.: Flow of Glaciar Moreno, Argentina, from repeat-pass Shuttle Imaging Radar images: Comparison of the phase correlation method with radar interferometry, J. Glaciol., 45(149), 93–100, doi:10.1017/S0022143000003075, 1999.

Miles, B., Jordan, J., Stokes, C., Jamieson, S., Gudmundsson, G. H. and Jenkins, A.: Recent acceleration of Denman Glacier (1972–2017), East Antarctica, driven by grounding line retreat and changes in ice tongue configuration, Cryosph. Discuss., 1–26, doi:10.5194/tc-2020-162,

2020.

Milillo, P., Rignot, E., Mouginot, J., Scheuchl, B., Morlighem, M., Li, X. and Salzer, J. T.: On the Short-term Grounding Zone Dynamics of Pine Island Glacier, West Antarctica, Observed With COSMO-SkyMed Interferometric Data, Geophys. Res. Lett., 44(20), 10,436-10,444, doi:10.1002/2017GL074320, 2017.

Millan, R., Rignot, E., Mouginot, J., Wood, M., Bjørk, A. A. and Morlighem, M.: Vulnerability of Southeast Greenland Glaciers to Warm Atlantic Water From Operation IceBridge and Ocean Melting Greenland Data, Geophys. Res. Lett., 45(6), 2688–2696, doi:10.1002/2017GL076561, 2018.

Millan, R., Mouginot, J., Rabatel, A., Jeong, S., Cusicanqui, D., Derkacheva, A. and Chekki, M.: Mapping surface flow velocity of glaciers at regional scale using a multiple sensors approach, Remote Sens., 11(21), 1–21, doi:10.3390/rs11212498, 2019.

Moon, T. and Joughin, I.: Changes in ice front position on Greenland's outlet glaciers from 1992 to 2007, J. Geophys. Res. Earth Surf., 113(2), 1–10, doi:10.1029/2007JF000927, 2008.

Moon, T., Joughin, I., Smith, B., Van Den Broeke, M. R., Van De Berg, W. J., Noël, B. and Usher, M.: Distinct patterns of seasonal Greenland glacier velocity, Geophys. Res. Lett., 41(20), 7209–7216, doi:10.1002/2014GL061836, 2014.

Moon, T., Joughin, I. and Smith, B.: Seasonal to multiyear variability of glacier surface velocity, terminus position, and sea ice/ice mélange in northwest Greenland, J. Geophys. Res. Earth Surf., 818–833, doi:10.1002/2015JF003494, 2015.

Morgan, P. J.: A Photogrammetric Survey of Hoseason Glacier, Kemp Coast, Antarctica, J. Glaciol., 12(64), 113–120, doi:10.3189/S0022143000022759, 1973.

Morlighem, M., Rignot, E., Seroussi, H., Larour, E., Ben Dhia, H. and Aubry, D.: A mass conservation approach for mapping glacier ice thickness, Geophys. Res. Lett., 38(19), 1–6, doi:10.1029/2011GL048659, 2011.

Morlighem, M., Rignot, E., Mouginot, J., Seroussi, H. and Larour, E.: Deeply incised submarine glacial valleys beneath the Greenland ice sheet, Nat. Geosci., 7(6), 418–422, doi:10.1038/ngeo2167, 2014.

Morlighem, M., Williams, C. N., Rignot, E., An, L., Arndt, J. E., Bamber, J. L., Catania, G., Chauché, N., Dowdeswell, J. A., Dorschel, B., Fenty, I., Hogan, K., Howat, I., Hubbard, A., Jakobsson, M., Jordan, T. M., Kjeldsen, K. K., Millan, R., Mayer, L., Mouginot, J., Noël, B. P. Y., O'Cofaigh, C., Palmer, S., Rysgaard, S., Seroussi, H., Siegert, M. J., Slabon, P., Straneo, F., van den Broeke, M. R., Weinrebe, W., Wood, M. and Zinglersen, K. B.: BedMachine v3: Complete Bed Topography and Ocean Bathymetry Mapping of Greenland From Multibeam Echo Sounding Combined With Mass Conservation, Geophys. Res. Lett., 44(21), 11,051-11,061, doi:10.1002/2017GL074954, 2017.

Mouginot, J., Scheuch, B. and Rignot, E.: Mapping of ice motion in Antarctica using synthetic-aperture radar data, Remote Sens., 4(9), 2753–2767, doi:10.3390/rs4092753, 2012.

Mouginot, J., Rignot, E., Scheuchl, B., Fenty, I., Khazendar, A., Morlighem, M., Buzzi, A. and Paden, J.: Fast retreat of Zachariæ Isstrøm, northeast Greenland, Science (80-.)., 350(6266), 1357–1361, 2015.

Mouginot, J., Rignot, E., Scheuchl, B. and Millan, R.: Comprehensive Annual Ice Sheet Velocity Mapping Using Landsat-8, Sentinel-1, and RADARSAT-2 Data, Remote Sens., 9(364), 1–20, doi:10.3390/rs9040364, 2017.

Mouginot, J., Rignot, E., Bjørk, A. A., van den Broeke, M., Millan, R., Morlighem, M., Noël, B., Scheuchl, B. and Wood, M.: Forty-six years of Greenland Ice Sheet mass balance from 1972 to 2018, Proc. Natl. Acad. Sci. U. S. A., 116(19), 9239–9244, doi:10.1073/pnas.1904242116, 2019.

Nagler, T., Rott, H., Hetzenecker, M., Wuite, J. and Potin, P.: The Sentinel-1 mission: New opportunities for ice sheet observations, Remote Sens., 7(7), 9371–9389, doi:10.3390/rs70709371, 2015.

Nick, F. M., Luckman, A., Vieli, A., Van Der Veen, C. J., Van As, D., Van De Wal, R. S. W., Pattyn, F., Hubbard, A. L. and Floricioiu, D.: The response of Petermann Glacier, Greenland, to large calving events, and its future stability in the context of atmospheric and oceanic warming, J. Glaciol., 58(208), 229–239, doi:10.3189/2012JoG11J242, 2012.

Nielsen, K., Khan, S. A., Korsgaard, N. J., Kjær, K. H., Wahr, J., Bevis, M., Stearns, L. A. and Timm, L. H.: Crustal uplift due to ice mass variability on Upernavik Isstrøm, west Greenland, Earth Planet. Sci. Lett., 353–354(April 2011), 182–189, doi:10.1016/j.epsl.2012.08.024, 2012.

Nienow, P. W., Sole, A. J., Slater, D. A. and Cowton, T. R.: Recent Advances in Our Understanding of the Role of Meltwater in the Greenland Ice Sheet System, Curr. Clim. Chang. Reports, 3(4), 330–344, doi:10.1007/s40641-017-0083-9, 2017.

Novoa Gautier, S.: Water quality assessment and characterisation of chlorophyll-a variability related to river discharges, within the southeastern Bay of Biscay: Evaluation and development of chlorophyll-a algorithms for MODIS and MERIS imagery, Universidad del Pais Vasco, PhD these., 2012.

Palmer, S., Shepherd, A., Nienow, P. and Joughin, I.: Seasonal speedup of the Greenland Ice Sheet linked to routing of surface water, Earth Planet. Sci. Lett., 302(3–4), 423–428, doi:10.1016/j.epsl.2010.12.037, 2011.

Passalacqua, O., Gagliardini, O., Parrenin, F., Todd, J., Gillet-Chaulet, F. and Ritz, C.: Performance and applicability of a 2.5D ice-flow model in the vicinity of a dome, Geosci. Model Dev. Discuss., 0(February), 1–21, doi:10.5194/gmd-2016-18, 2016.

Pattyn, F.: The paradigm shift in Antarctic ice sheet modelling, Nat. Commun., 9(1), 10–12, doi:10.1038/s41467-018-05003-z, 2018.

Paul, F., Bolch, T., Kääb, A., Nagler, T., Nuth, C., Scharrer, K., Shepherd, A., Strozzi, T., Ticconi, F., Bhambri, R., Berthier, E., Bevan, S., Gourmelen, N., Heid, T., Jeong, S., Kunz, M., Lauknes, T. R., Luckman, A., Merryman Boncori, J. P., Moholdt, G., Muir, A., Neelmeijer, J., Rankl, M., VanLooy, J. and Van Niel, T.: The glaciers climate change initiative: Methods for creating glacier area, elevation change and velocity products, Remote Sens. Environ., 162, 408–426, doi:10.1016/j.rse.2013.07.043, 2015.

Paul, F., Bolch, T., Briggs, K., Kääb, A., McMillan, M., McNabb, R., Nagler, T., Nuth, C., Rastner, P., Strozzi, T. and Wuite, J.: Error sources and guidelines for quality assessment of glacier area, elevation change, and velocity products derived from satellite data in the Glaciers_cci project, Remote Sens. Environ., 203(August 2017), 256–275, doi:10.1016/j.rse.2017.08.038, 2017.

Rignot, E. and Kanagaratnam, P.: Changes in the Velocity Structure of the Greenland Ice Sheet, Science (80-.)., 311, 986–990, 2006.

Rignot, E. and Mouginot, J.: Ice flow in Greenland for the International Polar Year 2008-2009, Geophys. Res. Lett., 39(11), 1–7, doi:10.1029/2012GL051634, 2012.

Rignot, E. and Steffen, K.: Channelized bottom melting and stability of floating ice shelves, Geophys. Res. Lett., 35(2), 2–6, doi:10.1029/2007GL031765, 2008.

Rignot, E., Koppes, M. and Velicogna, I.: Rapid submarine melting of the calving faces of West Greenland glaciers, Nat. Geosci., 3(3), 187–191, doi:10.1038/ngeo765, 2010.

Rignot, E., Fenty, I., Menemenlis, D. and Xu, Y.: Spreading of warm ocean waters around Greenland as a possible cause for glacier acceleration, Ann. Glaciol., 53(60), 257–266, doi:10.3189/2012AoG60A136, 2012.

Rignot, E., Mouginot, J., Scheuchl, B., Van Den Broeke, M., Van Wessem, M. J. and Morlighem, M.: Four decades of Antarctic ice sheet mass balance from 1979–2017, Proc. Natl. Acad. Sci. U. S. A., 116(4), 1095–1103, doi:10.1073/pnas.1812883116, 2019.

Rosen, P. A., Hensley, S., Peltzer, G. and Simons, M.: Updated repeat orbit interferometry package released, Eos (Washington. DC)., 85(5), 47, doi:10.1029/2004EO050004, 2004.

Rosenau, R., Schwalbe, E., Maas, H. G., Baessler, M. and Dietrich, R.: Grounding line migration and high-resolution calving dynamics of Jakobshavn Isbræ, West Greenland, J. Geophys. Res. Earth Surf., 118(2), 382–395, doi:10.1029/2012JF002515, 2013.

Rosenau, R., Scheinert, M. and Dietrich, R.: A processing system to monitor Greenland outlet glacier velocity variations at decadal and seasonal time scales utilizing the Landsat imagery, Remote Sens. Environ., 169, 1–19, doi:10.1016/j.rse.2015.07.012, 2015.

Sakakibara, D. and Sugiyama, S.: Ice front and flow speed variations of marine-terminating outlet glaciers along the coast of Prudhoe Land, northwestern Greenland, J. Glaciol., 64(244), 300–310, doi:10.1017/jog.2018.20, 2018.

Sattar, A., Goswami, A., Kulkarni, A. V. and Das, P.: Glacier-surface velocity derived ice volume and retreat assessment in the Dhauliganga basin, Central Himalaya – A remote sensing and modeling based approach, Front. Earth Sci., 7(May), 1–15, doi:10.3389/feart.2019.00105, 2019.

Scambos, T. A., Dutkiewicz, M. J., Wilson, J. C. and Bindschadler, R. A.: Application of image cross-correlation to the measurement of glacier velocity using satellite image data, Remote Sens. Environ., 42(3), 177–186, doi:10.1016/0034-4257(92)90101-O, 1992.

Schild, K. M. and Hamilton, G. S.: Seasonal variations of outlet glacier terminus position in Greenland, J. Glaciol., 59(216), 759–770, doi:10.3189/2013JoG12J238, 2013.

Schoof, C.: The effect of cavitation on glacier sliding, Proc. R. Soc. A Math. Phys. Eng. Sci., 461(2055), 609–627, doi:10.1098/rspa.2004.1350, 2005.

Schoof, C.: Ice sheet grounding line dynamics: Steady states, stability, and hysteresis, J. Geophys. Res. Earth Surf., 112(3), 1–19, doi:10.1029/2006JF000664, 2007.

Schwaizer, G.: ESA Training Course: SAR / Optical Applications to Ice and Snow, , 1–172, 2017.

Sciascia, R., Straneo, F., Cenedese, C. and Heimbach, P.: Seasonal variability of submarine melt rate and circulation in an East Greenland fjord, J. Geophys. Res. Ocean., 118(5), 2492–2506, doi:10.1002/jgrc.20142, 2013.

Seroussi, H., Morlighem, M., Rignot, E., Khazendar, A., Larour, E. and Mouginot, J.: Dependence of century-scale projections of the Greenland ice sheet on its thermal regime, J. Glaciol., 59(218), 1024–1034, doi:10.3189/2013JoG13J054, 2013.

Shepherd, A., Ivins, E., Rignot, E., Smith, B., van den Broeke, M., Velicogna, I., Whitehouse, P., Briggs, K., Joughin, I., Krinner, G., Nowicki, S., Payne, T., Scambos, T., Schlegel, N., A, G., Agosta, C., Ahlstrøm, A., Babonis, G., Barletta, V. R., Bjørk, A. A., Blazquez, A., Bonin, J., Colgan, W., Csatho, B., Cullather, R., Engdahl, M. E., Felikson, D., Fettweis, X., Forsberg, R., Hogg, A. E., Gallee, H., Gardner, A., Gilbert, L., Gourmelen, N., Groh, A., Gunter, B., Hanna, E., Harig, C., Helm, V., Horvath, A., Horwath, M., Khan, S., Kjeldsen, K. K., Konrad, H., Langen, P. L., Lecavalier, B., Loomis, B., Luthcke, S., McMillan, M., Melini, D., Mernild, S., Mohajerani, Y., Moore, P., Mottram, R., Mouginot, J., Moyano, G., Muir, A., Nagler, T., Nield, G., Nilsson, J., Noël, B., Otosaka, I., Pattle, M. E., Peltier, W. R., Pie, N., Rietbroek, R., Rott, H., Sandberg Sørensen, L., Sasgen, I., Save, H., Scheuchl, B., Schrama, E., Schröder, L., Seo, K. W., Simonsen, S. B., Slater, T., Spada, G., Sutterley, T., Talpe, M., Tarasov, L., van de Berg, W. J., van der Wal, W., van Wessem, M., Vishwakarma, B. D., Wiese, D., Wilton, D., Wagner, T., Wouters, B. and Wuite, J.: Mass balance of the Greenland Ice Sheet from 1992 to 2018, Nature, 579(7798), 233–239, doi:10.1038/s41586-019-1855-2, 2020.

Skvarca, P., Raup, B. and De Angelis, H.: Recent behaviour of Glaciar Upsala, a fast-flowing calving glacier in Lago Argentino, southern Patagonia, Ann. Glaciol., 36(October 2000), 184–188, doi:10.3189/172756403781816202, 2003.

Slater, D. A., Nienow, P. W., Cowton, T. R., Goldberg, D. N. and Sole, A. J.: Effect of near-terminus subglacial hydrology on tidewater glacier submarine melt rates, Geophys. Res. Lett., 42(8), 2861–2868, doi:10.1002/2014GL062494, 2015.

Smeets, C. J. P. P., Boot, W., Hubbard, A., Pettersson, R., Wilhelms, F., Van Den Broeke, M. R. and Van De Wal, R. S. W.: A wireless subglacial probe for deep ice applications, Instruments and Methods, 58(211), 841–848, doi:10.3189/2012JoG11J130, 2012.

Smith, L. C., Chu, V. W., Yang, K., Gleason, C. J., Pitcher, L. H., Rennermalm, A. K., Legleiter, C. J., Behar, A. E., Overstreet, B. T., Moustafa, S. E., Tedesco, M., Forster, R. R., LeWinter, A. L., Finnegan, D. C., Sheng, Y. and Balog, J.: Efficient meltwater drainage through supraglacial streams and rivers on the southwest Greenland ice sheet, Proc. Natl. Acad. Sci. U. S. A., 112(4), 1001–1006, doi:10.1073/pnas.1413024112, 2015.

Sole, A., Nienow, P., Bartholomew, I., Mair, D., Cowton, T., Tedstone, A. and King, M. A.: Winter motion mediates dynamic response of the Greenland Ice Sheet to warmer summers, Geophys. Res. Lett., 40(15), 3940–3944, doi:10.1002/grl.50764, 2013.

Strozzi, T., Luckman, A., Murray, T., Wegmüller, U. and Werner, C. L.: Glacier motion estimation using SAR offset-tracking procedures, IEEE Trans. Geosci. Remote Sens., 40(11), 2384–2391, doi:10.1109/TGRS.2002.805079, 2002.

Strozzi, T., Caduff, R., Jones, N., Barboux, C., Delaloye, R., Bodin, X., Kääb, A., Mätzler, E. and Schrott, L.: Monitoring rock glacier kinematics with satellite synthetic aperture radar, Remote Sens., 12(3), 1–24, doi:10.3390/rs12030559, 2020.

Stumpf, A., Malet, J. P. and Delacourt, C.: Correlation of satellite image time-series for the detection and monitoring of slow-moving landslides, Remote Sens. Environ., 189, 40–55, doi:10.1016/j.rse.2016.11.007, 2017.

Sundal, A. V., Shepherd, A., Nienow, P., Hanna, E., Palmer, S. and Huybrechts, P.: Melt-induced speed-up of Greenland ice sheet offset by efficient subglacial drainage, Nature, 469(7331), 521–524, doi:10.1038/nature09740, 2011.

Tang, Y., Birch, S. P. D., Hayes, A. G., Kirk, R., Kutsop, N., Vincent, J. B. and Squyres, S.: Generation of photoclinometric DTMs for application to transient changes on the surface of comet 67P/Churyumov-Gerasimenko, Astron. Astrophys., 630, 1–8, doi:10.1051/0004-6361/201834127, 2019.

Tedstone, A., Nienow, P. W., Gourmelen, N., Dehecq, A., Goldberg, D. and Hanna, E.: Decadal slowdown of a land-terminating sector of the Greenland Ice Sheet despite warming, Nature, 526, 692–695, doi:10.1038/nature15722, 2015.

Tedstone, A. J., Nienow, P. W., Sole, A. J., Mair, D. W. F., Cowton, T. R., Bartholomew, I. D. and King, M. A.: Greenland ice sheet motion insensitive to exceptional meltwater forcing, Proc. Natl. Acad. Sci., 110(49), 19719–19724, doi:10.1073/pnas.1315843110, 2013.

Van Tricht, K., Lhermitte, S., Lenaerts, J. T. M., Gorodetskaya, I. V., L'Ecuyer, T. S., Noël, B., Van Den Broeke, M. R., Turner, D. D. and Van Lipzig, N. P. M.: Clouds enhance Greenland ice sheet meltwater runoff, Nat. Commun., 7(May 2015), doi:10.1038/ncomms10266, 2016.

Tsai, Y. L. S., Lin, S. Y., Kim, J. R. and Choi, Y. S.: Analysis of the seasonal velocity difference of the Greenland Russell glacier using multi-sensor data, Terr. Atmos. Ocean. Sci., 30(4), 541–562, doi:10.3319/TAO.2019.06.03.01, 2019.

Vaughan, D. G. and Arthern, R.: Why is it hard to predict the future of ice sheets?, Science (80-.)., 315(5818), 1503–1504, doi:10.1126/science.1141111, 2007.

Van Der Veen, C. J. and Whillans, I. M.: Force budget: I. theory and numerical methods, , 35(119), 53–60, 1989.

Vijay, S., Khan, S. A., Kusk, A., Solgaard, A. M., Moon, T. and Bjørk, A. A.: Resolving Seasonal Ice Velocity of 45 Greenlandic Glaciers With Very High Temporal Details, Geophys. Res. Lett., 46(3), 1485–1495, doi:10.1029/2018GL081503, 2019.

Van de Wal, R. S. W., Greuell, W., Van den Broeke, M. R., Reijmer, C. J. and Oerlemans, J.: Surface mass-balance observations and automatic weather station data along a transect near Kangerlussuaq, West Greenland, Ann. Glaciol., 42(August 2004), 311–316, doi:10.3189/172756405781812529, 2005.

Van De Wal, R. S. W., Boot, W., Smeets, C. J. P. P., Snellen, H., Van Den Broeke, M. R. and Oerlemans, J.: Twenty-one years of mass balance observations along the K-transect, West Greenland, Earth Syst. Sci. Data, 4(1), 31–35, doi:10.5194/essd-4-31-2012, 2012.

Van De Wal, R. S. W., Smeets, C. J. P. P., Boot, W., Stoffelen, M., Van Kampen, R., Doyle, S. H., Wilhelms, F., Van Den Broeke, M. R., Reijmer, C. H., Oerlemans, J. and Hubbard, A.: Self-regulation of ice flow varies across the ablation area in south-west Greenland, Cryosphere, 9(2), 603–611, doi:10.5194/tc-9-603-2015, 2015.

Walsh, K. M., Howat, I. M., Ahn, Y. and Enderlin, E. M.: Changes in the marine-terminating glaciers of central east Greenland, 2000-2010, Cryosphere, 6(1), 211–220, doi:10.5194/tc-6-211-2012, 2012.

Washam, P., Nicholls, K. W., Münchow, A. and Padman, L.: Summer surface melt thins Petermann Gletscher Ice Shelf by enhancing channelized basal melt, J. Glaciol., 65(252), 662–674, doi:10.1017/jog.2019.43, 2019.

Weertman, J.: The sliding of glaciers, J. Glaciol., 33–38, doi:10.1007/978-94-015-8705-1_19, 1957.

Wegmüller, U., Werner, C., Strozzi, T. and Wiesmann, A.: Ionospheric electron concentration effects on SAR and INSAR, Int. Geosci. Remote Sens. Symp., 3714–3717, doi:10.1109/IGARSS.2006.956, 2006.

Weidick, A.: Frontal variations at Upernaviks Isstrøm in the last 100 years, Meddelser fra Dansk Geol. Foren., (14), 52–60, doi:10.1016/j.yqres.2013.09.008, 1958.

Weydahl, D. J.: Analysis of ERS tandem SAR coherence from glaciers, valleys, and fjord ice on Svalbard, IEEE Trans. Geosci. Remote Sens., 39(9), 2029–2039, doi:10.1109/36.951093, 2001.

Williams, J. J., Gourmelen, N. and Nienow, P.: Dynamic response of the Greenland ice sheet to recent cooling, Sci. Rep., 10(1), 1–11, doi:10.1038/s41598-020-58355-2, 2020.

Wilson, N., Straneo, F. and Heimbach, P.: Satellite-derived submarine melt rates and mass balance (2011–2015) for Greenland's largest remaining ice tongues, Cryosph. Discuss., (2015), 1–17, doi:10.5194/tc-2017-99, 2017.

Winkelmann, R., Martin, M. A., Haseloff, M., Albrecht, T., Bueler, E., Khroulev, C. and Levermann, A.: The Potsdam Parallel Ice Sheet Model (PISM-PIK) - Part 1: Model description, Cryosphere, 5(3), 715–726, doi:10.5194/tc-5-715-2011, 2011.

Wood, M., Rignot, E., Fenty, I., An, L., Bjørk, A., van den Broeke, M., Cai, C., Kane, E., Menemenlis, D., Millan, R., Morlighem, M., Mouginot, J., Noël, B., Scheuchl, B., Velicogna, I., Willis, J. K. and Zhang, H.: Ocean forcing drives glacier retreat in Greenland, Sci. Adv., 7(1), 1–11, doi:10.1126/sciadv.aba7282, 2021.

Wright, P., Harper, J., Humphrey, N. and Meierbachtol, T.: Measured basal water pressure variability of the western Greenland Ice Sheet: Implications for hydraulic potential, J. Geophys. Res. Earth Surf., 121, 1134–1147, doi:10.1002/2016JF003819.Received, 2016.

Xu, Y., Rignot, E., Menemenlis, D. and Koppes, M.: Numerical experiments on subaqueous melting of greenland tidewater glaciers in response to ocean warming and enhanced subglacial discharge, Ann. Glaciol., 53(60), 229–234, doi:10.3189/2012AoG60A139, 2012.

Yang, Y., Li, F., Hwang, C., Ding, M. and Ran, J.: Space-Time Evolution of Greenland Ice Sheet Elevation and Mass From Envisat and GRACE Data, J. Geophys. Res. Earth Surf., 124(8), 2079–2100, doi:10.1029/2018JF004765, 2019.

Young, T. J., Christoffersen, P., Doyle, S. H., Nicholls, K. W., Stewart, C. L., Hubbard, B., Hubbard, A., Lok, L. B., Brennan, P. V., Benn, D. I., Luckman, A. and Bougamont, M.: Physical Conditions of Fast Glacier Flow: 3. Seasonally-Evolving Ice Deformation on Store Glacier, West Greenland, J. Geophys. Res. Earth Surf., 124(1), 245–267, doi:10.1029/2018JF004821, 2019.

Zwally, H. J., Abdalati, W., Herring, T., Larson, K., Saba, J. and Steffen, K.: Surface melt-induced acceleration of Greenland ice-sheet flow, Science (80-.)., 297(5579), 218–222, doi:10.1126/science.1072708, 2002.